Source Term Modeling of Vortex Generators

Master Thesis

Cornelis Jan Stam

June 2016

DTU Mechanical Engineering
Department of Mechanical Engineering

DTU Mechanical Engineering
Section of Fluid Mechanics, Coastal and Maritime Engineering
Technical University of Denmark

Nils Koppels Allé, Bld. 403
DK-2800 Kgs. Lyngby
Denmark
Phone (+45) 4525 1360
Fax (+45) 4588 4325

www.mek.dtu.dk

Summary

The purpose of this thesis concerns the validation of a vortex generator model that can be used for parameter studies on wind turbine airfoils. In order to accomplish this the validation has been broken down into three parts, covering both flow parameters and model inputs. The vortex generator model has been chosen based on extensive literature study on boundary layer control and published papers on such models. A qualitative table revealed that the model of Bender, Anderson, and Yagle[1], hence referred to as the BAY model, should be the most suitable for the purpose of this thesis.

The BAY model is based on the lifting line theory. It contains an expression for the lift force generated by the vortex generator based on its geometry and the model constant. Mesh nodes need to be assigned to the vortex generator volume in order to apply this force to the fluid domain. This has been accomplished by defining a volume that is based on the vortex generator geometry. A FORTRAN algorithm scans the mesh and assigns a portion of the lift force if the corresponding mesh node is inside this predefined volume. This method has been validated and shown to be able to represent both rectangular and triangular vortex generators. Cambered vanes are also possible, but they require additional adaptation to the BAY model lift force expression, which has not been investigated further.

The first validation case compared the BAY model to a vortex generator shape study conducted in the Turbulent Boundary Layer tunnel in Lille, France. The flow featured a high Reynolds Momentum Thickness number of 17000 at the inlet. It has been shown that the BAY model is capable of accurately replicating the effects of different shapes of vortex generators. Furthermore, testing several model inputs showed that the BAY model is not very sensitive to the aforementioned predefined volume. However, the fluid volume that contains the vortex generator needs to have a minimal resolution in order to accurately capture the peak vorticity development.

A comparison with a similar measurement campaign conducted in the Boundary Layer Tunnel in Delft at a lower Reynolds Momentum Thickness of 3124 showed that the gap between the BAY model and experimental values seems to reduce as the Reynolds number increases. This could be explained by the fact that at higher Reynolds numbers the assumptions on which turbulence models are build are more valid. Further studies should be conducted to confirm this tendency.

The second validation case showed that the BAY model could be used for a parameter study. It has been compared to experimental data from a parameter study of vortex generators on a bump in the same wind tunnel as the first case. The bump caused an adverse pressure gradient. Efforts to validate the base flow proved to be difficult due to a lack of crucial information with regard to the bump and conspicuous assumptions of the design of the bump. Nonetheless, the trends and optimal values shown by experiments were matched quite well by the results produced by the BAY model.

In the third study the BAY model was further tested in an adverse pressure gradient situation by reproducing the polars of lift and drag on the DU-97-W-300 and the DU-93-W-210, at a Reynolds number of 3e6 and 1e6 respectively. The main effort was focused on the DU-97-W-300 and the DU-93-W-210 was used to confirm trends spotted in the main effort. The vortex generators on the DU-97-W-300 simulated by the BAY model exhibited a delay in stall and general increase in lift that matched the experimental data. There is an overprediction of the stall angle of 1 degree, which resulted in an overprediction of lift. This overprediction had been observed previously in the polar without the vortex generators. Furthermore, the BAY model also showed a slight increase in drag though the effect of the base plate meant that the total drag was still underpredicted. For the DU-93-W-210 close agreement for the linear region of lift was found as well as close agreement for drag for the same angles of attack. The stall angle was overpredicted slightly due to overprediction in the base flow, as was the case with the DU-97-W-300.

In conclusion, it has been shown that the BAY model is capable of accurately modeling the flow behind a vortex generator at high Reynolds numbers. The BAY model has also shown the capability to perform parameter studies, but this requires further validation to reduce uncertainties. It can also be used to simulate the influence a vortex generator has on thick and thin airfoils such as the DU-97-W-300 and the DU-93-W-210. An increased accuracy as the Reynolds number increases has been observed. Nevertheless, it requires additional validation to be confirmed.

Acknowledgements

My time in the European Wind Energy Master and graduating at Siemens Wind Power has been one of the most gratifying parts of my academic journey. I certainly wandered around a little and I could not have done that without the heartfelt support from my parents. I cannot thank them enough for the opportunity.

During this thesis I have been very lucky to receive feedback and help from many people. I especially want to thank Nando Timmer, Clara Velte, Martin Hansen, and Busra Akay for being my supervisors. I could not have completed my thesis without their contributions and feedback. The setup of my thesis did not always make things easy but each and every one of them have been there for me regardless. The experimental data they shared with me is a key part of this thesis.

I want to thank Alex Loeven and his team at Siemens Wind Power for giving me this opportunity and welcoming me with open arms. The interest in my work and kindness that everyone there showed me means a lot to me.

Lastly, I would like to thank my sister, Marcella Stam, for making the wonderful cover.

Cornelis Jan Stam
Gjellerup, Denmark
2016, June 7th

List of Figures

List of Tables

Nomenclature

Symbol	Units	Description
a_{ij}		Anisotropy Tensor
$\hat{b}$	$-$	Cross Product of Normal and Tangential Unit Vector
C_p	$-$	Coefficient of Power
C_f	$-$	Skin Friction Coefficient
C_{vg}	$-$	BAY Model Constant
g_i	$\mathrm{m\,s^{-2}}$	Gravity Einstein Notation
g_p	$-$	Error Coefficient [unit depends on input]
G	$-$	Görtler number
h	m	Vortex Generator Height
h_s	m	Distance between limiting streamlines
H	$-$	Schlichting Shape Factor
H_{12}	$-$	Shape Factor
H_{23}	$-$	Shape Factor
k	$\mathrm{m^2\,s^{-2}}$	Turbulent Kinetic Energy
$\mathbf{L_i}$	$\mathrm{kg\,m^{-2}\,s^{2}}$	BAY Model Body Force
$\hat{n}$	$-$	Normal Unit Vector
$\hat{p}$	$-$	Observed Order of Accuracy
P	W	Aerodynamic power of a wind turbine
Q	$\mathrm{s^{-2}}$	Q Criterion or Second Invariant of ∇u
r	m	Vortex Radial Location
r_{mn}	$-$	Refinement Ratio
R_c	m	Radius of Curvature
R	m	Rotor Radius
S	$\mathrm{s^{-1}}$	Symmetrical Matrix of ∇u or Strain Rate Tensor
S_{vg}	$\mathrm{m^2}$	Vortex Generator Surface Area
t	s	Time
$\hat{t}$	$-$	Tangential Unit Vector
u	$\mathrm{m\,s^{-1}}$	Streamwise Local Velocity
u_i	$\mathrm{m\,s^{-1}}$	Flow Velocity Einstein Notation
u_ζ	$\mathrm{m\,s^{-1}}$	Axial Velocity
u_θ	$\mathrm{m\,s^{-1}}$	Azimuthall Velocity
u_r	$\mathrm{m\,s^{-1}}$	Radial Velocity
U	$\mathrm{m\,s^{-1}}$	Streamwise External Velocity
v	$\mathrm{m\,s^{-1}}$	Vertical Local Velocity
V_m	$\mathrm{m^3}$	Total Numerical Volume of Vortex Generator
$\dot{V}$	$\mathrm{m^3\,s^{-1}}$	Volumetric Flow Rate
ΔV_i	$\mathrm{m^3}$	Local Volume of Cell Inhabiting Vortex Generator
w	$\mathrm{m\,s^{-1}}$	Spanwise Local Velocity
x	m	Streamwise Location
x_i	m	Cartesian Einstein Notation
y	m	Vertical Location
$y+$	$-$	Non-Dimensionalised Wall Height
z	m	Spanwise Location

Greek Symbols

Symbol	Units	Description
β	$^\circ$	Vortex Generator Angle
Γ	$\mathrm{m^2\,s^{-1}}$	Circulation
δ_*	m	Displacement Thickness
δ_{**}	m	Energy Thickness
δ_τ	m	Boundary layer reference length
ϵ	m	Vortex Core Radius
ϵ	$\mathrm{m^2\,s^{-3}}$	Turbulent Dissipation
ϵ_{mn}	$-$	Numerical Error [unit depends on input]
θ	m	Momentum Thickness
λ_n	$-$	The nth Eigenvalue
μ	Pa s	Dynamic Viscosity
ν	$\mathrm{m^2\,s^{-1}}$	Kinematic Viscosity
ν_τ	$\mathrm{m^2\,s^{-1}}$	Kinematic Eddy Viscosity
ρ	$\mathrm{kg\,m^{-3}}$	Density
τ_{ij}	$\mathrm{m^2\,s^{-2}}$	Reynolds Stress Tensor
τ_w	Pa	Local Wall Shear Stress
ω	$\mathrm{s^{-1}}$	Specific Dissipation Rate
ω_w	$\mathrm{s^{-1}}$	Wall vorticity
Ω	$\mathrm{s^{-1}}$	Anti-Symmetrical Matrix of ∇u or Vorticity Tensor

Acronyms

BAY	Bender, Anderson, and Yagle Vortex Generator Model
BSL EARSM	Baseline - Explicit Algebraic Reynolds Stress Model
CEL	CFX Expression Language
CFD	Computational Fluid Dynamics
CoE	Cost of Energy
GCI	Grid Convergence Index
HAWT	Horizontal Axis Wind Turbine
(S)PIV	(Stereo) Particle Image Velocimetry
RANS	Reynolds Averaged Navier Stokes
SST	Shear Stress Transport
SBVG	Sub Boundary-layer Vortex Generator
VG	Vortex Generator

Contents

Chapter 1

Introduction

1.1 Introduction

The wind energy industry has seen considerable growth in the past decade, as documented by the DTU International Energy Report 2014[2]. This growth is a result of the increasing demand of governments and citizens for a more sustainable energy production. However, both citizens and governments also demand that these renewable solutions are competitive in the energy market. This is often expressed in the Cost of Energy (CoE):

$$CoE = \frac{C + M}{E} \tag{1.1}$$

with C being the cost of the wind turbine and M the cost of maintaining it. It is then divided by the total energy that is produced by the wind turbine in its lifetime. The aim of wind turbine manufacturers is therefore to reduce the CoE in order to provide economically competitive and environmentally sustainable means of energy production.

In the wind energy industry this focus has led to two different streams of thought. In the offshore market the reduction of CoE has led the industry on a quest to build the largest wind turbine possible. This is because the wind turbine is not the driving cost for the offshore market, there the foundation is the most significant portion of C. That is why in the market of today you can find wind turbines such as the 154 meter diameter Siemens D7 and 180 meter diameter Adwen AD-8.

However, you will not find such large wind turbines on the onshore market. This is because their size makes the logistics of installing them at onshore sites very expensive. Further more, the new projects at onshore sites these days are categorised as low wind sites whereas the offshore sites are typically high wind sites. Sites with a low mean wind speed require a different approach to wind turbine design than the offshore market. Additionally, the onshore market also contains a large number of older wind turbines that have been designed 10 or even 20 years ago. This means that the onshore market tends to focus on upgrading existing wind turbines and designing new wind turbines that can extract more energy out of lower wind speeds.

One of those upgrades for the onshore market are vortex generators. Vortex generators have been researched since the 1960s[3]. In those days research focused on examining how vortex generators influenced the performance of airfoils. It revealed this influence is determined by several vortex generators parameters. Optimisation of those parameters can be made efficient by the use of models. One of the first models was introduced in 1999, known as the Bender-Anderson-Yagle (BAY) model[1], derived from the lifting line theory. It has seen been verified and enhanced[4][5][6][7]. However, these papers do not mention if the BAY model is capable of distinguishing between different vortex generator geometries. This might become particularly interesting as the vortex generator shapes become more intricate, as highlighted in a recent paper[8].

There have been attempts to approach modeling vortex generators in different ways. Methods such as immersed boundary layer[9], statistical descriptions[10], or the modeling of the generated vortex instead of the vortex generator itself[11][12]. Once again though, the variation of geometry is discussed. Some different types of vortex generators are investigated, for instance Zhang[12] looks specifically into the delta wing type vortex generator. However, this led to a significant adaptation instead of expanding existing functionality of the vortex generator model.

In addition to the ambiguity with respect to the geometrical representation there is also inconsistency in validating the aforementioned models and their adaptations. In some studies, the peak vorticity is the parameter in the validation process[5], other studies look at axial velocity[13], or at the tangential velocity[14]. These studies all can see that the model lacks in some parameters at certain phases of the flow, but none are able to establish a complete picture of its performance. Perhaps this is due to the complex nature of the flow behind a vortex generator and how that relates to its performance.

1.2 Project Aim

The Introduction has shown that vortex modeling has been done successfully in some applications, such as S-ducts and flat plates. Though in all these studies some aspects, such as varying geometry, have not been adequately researched yet.

Therefore, this thesis aims to highlight one such model and validate its performance thoroughly. This will be accomplished by breaking down the validation in stages, such as flow parameters, model parameter study, and flow dynamics. This will provide a more nuanced analysis of the model. Furthermore, data at high Reynolds numbers can provide new insights, as previous studies have not explicitly looked into the effect of high Reynolds numbers on the models.

1.3 Research Questions

The main research question of this study is whether or not the effects of (an array of) vortex generators have on the boundary layer can be predicted accurately by a model. This can be divided into the following questions and sub-questions.

- How does a vortex generator accomplish boundary layer control and how can this be expressed in quantifiable parameters?
- What are the types of models that are used for vortex generators?
- Can such a model accurately model different shapes of vortex generators?
- Can such a model be used for a parameter study?
- Can such a model predict the flow physics of the wake of a vortex generator in zero pressure gradient flow?
- Can such a model predict the flow physics of the wake of a vortex generator in adverse pressure gradient flow?
- How sensitive is such a model with respect to model inputs and flow setup?

The sequence of sub-questions leads to a first attempt to validate the model by running a computational fluid dynamics case for a flat plate with the model and comparing it to experimental data of a similar flat plate. Upon a successful comparison the transition will then be made to a 2-D airfoil, both numerically and experimentally, in order to validate the model further. The numerical case will mimic the conditions of the case from which the experimental data is obtained. This way the capabilities of the model can be more accurately described, with respect to its application. In all cases the effect of changes in mesh geometry will also be investigated. This means checking how refinement of the mesh impacts the performance and whether or not the type of meshing, structure or unstructured, has an effect.

The goal of the present study is to model the effects of a vortex generator on an airfoil. An effective model will allow expensive computational cases, such as a full 3-D wind turbine blade analysis, to incorporate the effects of vortex generators with minimal addition to the computational time. Though the computational efficiency of the BAY model is not part of this thesis itself. Initial validation will be limited to minimal cases, such as flow over the floor of a wind tunnel. Therefore complexity can be limited to the model and its implementation. The use of data from the LML wind tunnel[15], which has unique features that enable detailed research into turbulent boundary layers, enables a new approach to verifying the vortex generator model. Subsequent cases will test the model in adverse pressure gradient flow and check the capability of the model to reproduce parameter studies.

1.4 Methodology

In order to answer the research questions in a consistent and thorough manner a literature research has been conducted to obtain the necessary background information. Considering the essence of this thesis is the investigation of the performance of a model theoretical background of the context of the model is also required. Additionally, analysis of such models will provide benchmarks and points of improvement. It will also provide analysis that can be used to choose a model to validate with experimental data.

In order to chose the model applied in this thesis, all the information gathered during the literature review will be collected in a table for a qualitative trade-off. A quantitative trade-off is outside the scope and time frame of a master thesis. A conceptual setup for such a trade-off table can be seen in Tab 1.1. Each model in the table will be denoted by the primary author of the paper or book it is found in. Then its type will be denoted

Table 1.1: Concept qualitative trade-off table

	Type	Representation	Differentiation	Computation	Implementation	Calibration
Benchmark	Fully resolved RANS	o	o	o	o	o
Author 1	Actuator	−	−	++	+	−
Author 2		++	−	+	+	−
Author 3		+	+	−	+	−−

and consequently judged on how well it can represent the effects of vortex generators, if it can distinguish between different geometries, what the impact is on the computational time, how easy it is to implement it, and how much work is required to calibrate the model. The grades of each characteristic are determined through the reports made by the author or external author. This introduces some degree of uncertainty, hence the use of '+/−' as grades.

The main research question cannot be falsified, but it is possible to verify and validate it. Therefore the chosen model will be applied to several cases. These numerical cases will be chosen in a way that allows direct comparison with experimental data where possible. The initial case will limit the external variables as much as possible, in order to focus on the performance of the model. In each subsequent case, more features will be added to resemble the real life situation of a vortex generator on an airfoil.

Afterwards the conclusions from the comparisons between numerical and experiments will be gathered to make an assessment of the model. This should then lead to an advise regarding the use of the model as chosen from the trade-off table whilst highlighting shortcomings and recommendations for improvements.

1.5 Document Outline

In Part I the theory that is used will be summarised and discussed. Chapter 1 briefly describes the flow domain in which the vortex generators are commonly applied and why that is a useful application. In Chapter 2 the main purpose of vortex generators, boundary layer control, is discussed in depth. It high lights the ways vortex generators function as well as ways to identify the vortices created by different type of generators. Chapter 3 looks at the methods of modeling fluid dynamics and the complications that come with numerical modeling, such as turbulence modeling and numerical instability. Chapter 4 highlights the methods that will be used to inspect the quality of the results and briefly explains the choice of experiments in context of validation theory.

Part II discusses the three cases in which a vortex generator model will be modeled. Chapter 1 concerns the flow in a wind tunnel with a zero pressure gradient and focuses on initial validation as well as the capability of the model to distinguish between different geometries. In Chapter 2 a flow with an adverse pressure gradient is examined while also validating the ability of the model to represent the results of a parameter study, varying such things as device angle, height, and spacing. A DU-97-W-300 and a DU-93-W-210 are considered in Chapter 3, providing a second opportunity to test the model in an adverse pressure gradient. Furthermore, whether or not the model can exhibit phenomena such as stall-delay is tested.

In Part III the results and discussions from Part II are gathered and the overall performance of the model chosen in Part I will be evaluated. Based on those evaluations recommendations will be made that can further the research of this thesis.

Part I

Theory

Chapter 1

Flow Analysis of the Root Section of Wind Turbine Blades

As the Introduction has shown, the wind turbine industry has is determined to reduce the cost of energy (CoE). In the offshore market this has led to a race to build the largest wind turbine. For the onshore market the industry is looking to upgrade existing wind turbines and increase the efficiency with which the blades extract energy from the wind. One way to accomplish these goals for the onshore market is to apply upgrades to the blades, such as vortex generators, gurney flaps, or simply regular flaps. These upgrades improve the performance of the blade by increasing the amount of lift the airfoil produces.

Upgrades for a blade are typically applied in specific zones of the blade, such as the tip and root area, because of the difference in velocity. The root area can be defined as either the region where three dimensional flow occurs or the first third of the blade. This area of the wind turbine can provide solutions for both goals set by the onshore market. Previously, the root area has been neglected when developing a wind turbine because it does not contribute significantly to the production of energy. Additionally, structural demands for the blades constrain the aerodynamic possibilities at the root. For structural purposes, it is desirable to have a cylindrical shape which is not the most aerodynamic efficient shape. Lastly, the theory behind designing a blade shows an optimal chord length and angle of attack that are typically not implemented for the root section. This is mainly because of the aforementioned structural demands, though production limitations are also a factor here. The impact of these limitations on the chord and twist distributions is shown in Figure 1.2 for an arbitrary blade.

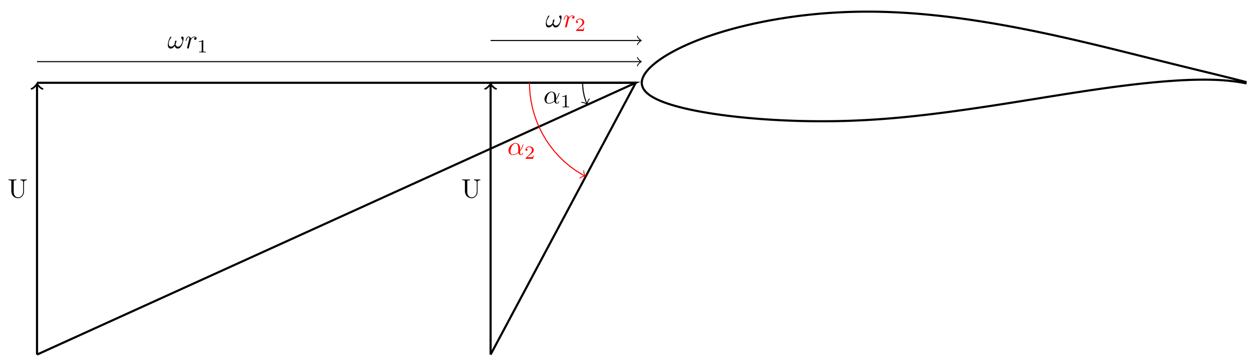

Figure 1.1: Illustration of the effect of rotational sampling on a wind turbine blade

In Figure 1.1 the incoming velocity on a blade without twist is shown. In this figure U resembles the incoming flow, assumed to have no shear or turbulence, and ω is the rotational velocity of the blades. This shows that if there is no twist at the root, denoted by r_2, the the angle of attack, denoted by α_2, will be significantly larger than at the tip. This means the airfoil at the root is much more likely to stall or be close to stalling, which reduces performance and can cause instabilities. Therefore the blade is twisted, in order to reduce the angle of attack as the blade reaches the hub of the wind turbine. Considering the amount of twist is limited due to production and structural requirements, the root regions still suffer occasionally from stall.

This previously highlighted limitations show that the root area has a lot of room for optimisation and research. In recent years the industry has made progress by developing the root area more, as shown by the comparison of a Vestas V66-1.75 with a Siemens SWT-3.2-113 in Figure 1.3.

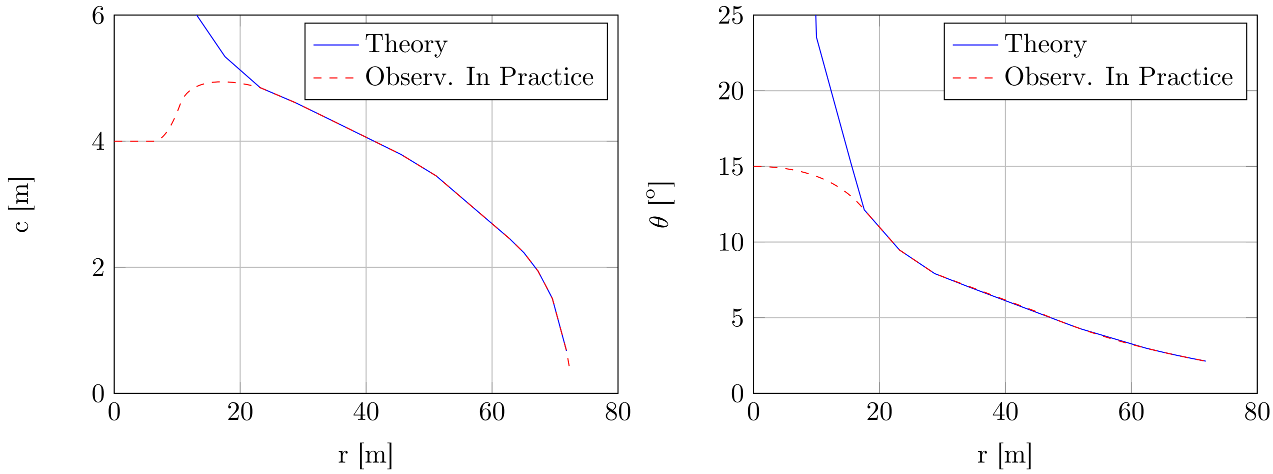

(a) Chord Distribution

(b) Twist Distribution

Figure 1.2: Illustration of the impact of constraints on blade design theory

(a) Vestas V66 1.75 MW

(b) Siemens 3.2 MW 113

Figure 1.3: Progress in root design of wind turbines

1.1 The Occurrence of Stall on Airfoils

Depending on the airfoil, experiencing high angles of attack as described in the previous section can lead to detrimental effects. The most significant effect being stall, a boundary layer separation common to airfoils. As described by Mueller and Batill[16] in certain flow conditions, Reynolds numbers ranging between 40.000 and 400.000, the pressure gradient on a surface becomes high enough to cause separation of the boundary layer. Mueller and Batill[16] continue by describing how complex this phenomenon can be as it also exhibits reattachment of the flow under certain conditions, formally described as a stall bubble shown by Figure 1.5. The energy introduced by the transition of a laminar boundary layer into a turbulent boundary layer reattaches the flow to the airfoil downstream of the surface, trapping stall in a bubble. Ashill et al.[17] shows through analysis of the wall vorticity, ω_w, that certain types of stall can be found analytically:

$$\frac{1}{2}\omega_w y^2 h_s = \dot{V} \tag{1.1}$$

With $\dot{V}$ representing the volumetric flow rate and h_s the distance between limiting streamlines, those that are close to the surface. If the wall vorticity tends to zero, the equation either has a saddle point or a singular as a solution. According to Ashill et al.[17] these solutions describes a stall bubble where the "separation surface encloses fluid that is not of the main stream". When the variable h tends to zero the flow will start to separate at the leading edge.

Pauley et al.[18] showed how an increase in the adverse pressure gradient can cause this stall bubble to become unsteady, shedding vortices with a certain frequency. Such unsteadiness can also be accomplished when the airfoil a change in angle of attack leads to a temporary increase in lift, known as dynamic stall and illustrated by Figure 1.4. In the work of Larsen et al.[19] a distinction is made between low and high frequency changes in angle of attack resulting in either trailing edge separation or leading edge separation respectively.

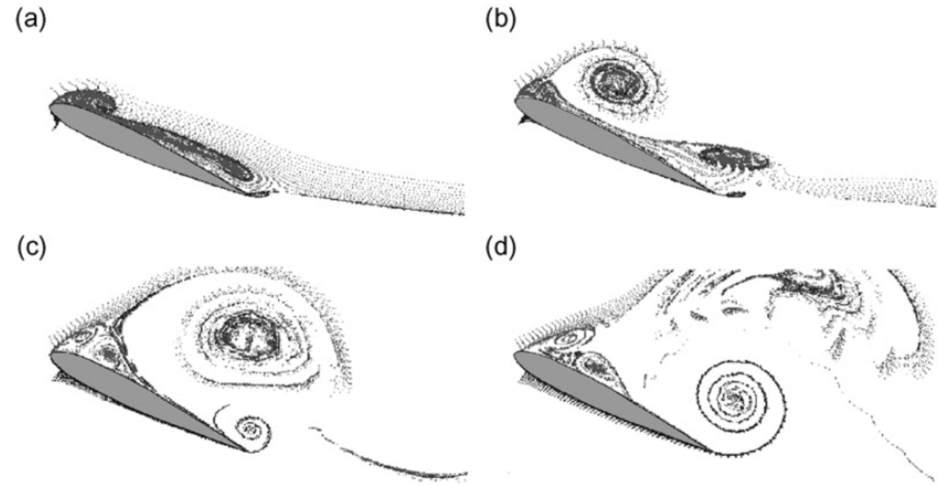

Figure 1.4: Schematic of dynamic stall where a leading edge vortex sheds over the airfoil, leading to a temporary increase of lift[19]

Seetharam et al.[21] have thoroughly investigated stall on NACA 2412 airfoil identifying additional parameters to quantify stall. Their research shows how separation starts at the trailing edge and moves upstream as the angle of attack is increased. Furthermore, as the angle of attack increases even more and the region of stall inhibits more of the span the flow effects become 3-D.

1.2 The Effect of the Coriolis Force and Centrifugal Force on Root Flow

In the root region of a wind turbine effects such as 3-D stall and unsteady stall bubbles are further complicated by rotational and gravitational effects. This combination has been examined for rotorcraft and propellers, but also specifically for wind turbines. Research by Schreck and Robinson[22] describes an experiment that was done in the NASA Ames wind tunnel with a horizontal axis wind turbine, showing that the onset of stall is actually delayed because of the rotational effects. Herraez et al.[23] state that the delay of stall, also known as the Himmelskamp effect, is due to a combination of rotational effects and gravitational forces. Furthermore,

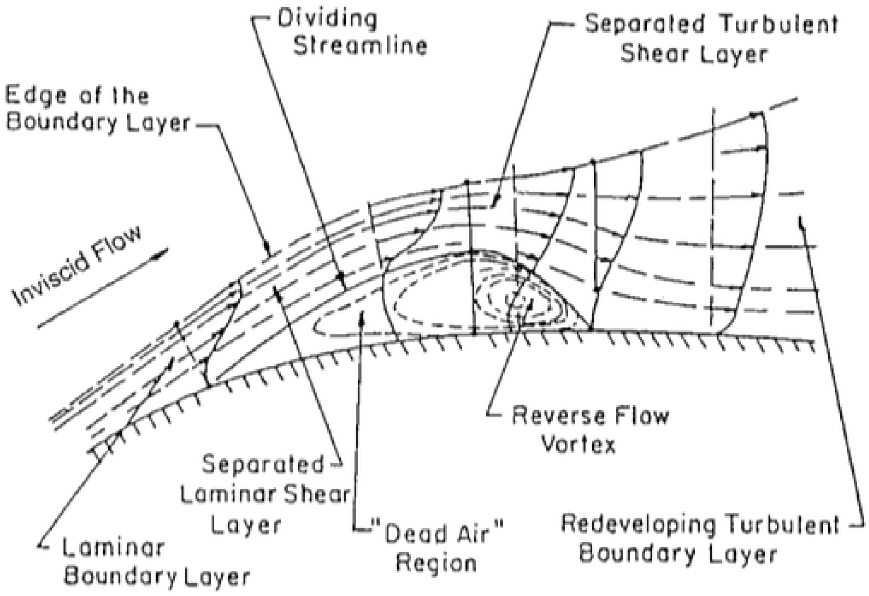

Figure 1.5: Characteristics of a separation bubble[20]

Herraez et al.[23] have shown that this effect has a larger impact on the pressure distribution than it does on the loads. This is because the Himmelskamp effect both reduces the suction peak and also delays the onset of stall. Akay et al.[24] further analysed the flow in and near the root region, using PIV to capture the flow at different azimuthal angles of a HAWT in the Open Jet facility of Technical University of Delft. Those experiments have shown that separation in the wake of the wind turbine can be seen in the negative radial vorticity and the flow reversal in the root region. Further complexities in the flow are found when observing the vortices shed by the root region, the transition from cylindrical sections to the maximum chords does not result in a single root vortex, at the maximum chord a vortex is also shed. Herraez et al.[23] have concluded that the centrifugal force, or Coriolis force, is the main source for spanwise flow.

Dumitrescu et al.[25] and Du et al.[26] have also made models for the inboard flow. Du et al.[26] use their model to calculate the location of the separation point and the momentum thickness. Whereas the model proposed by Dumitrescu et al.[25] can be used to modify blade element momentum codes to account for the aforementioned 3-D flow effects. Herraez et al.[23], note that the loss effects in the root occur more gradually than they do at the tip.

Chapter 2

Boundary Layer Control

Boundary layer control describes the mitigation of the onset of stall. This means that energy is transported into the lower regions of the boundary layer, either actively or passively, that allows the boundary layer to reattach to the surface. Studies such as the ones performed by Pearcey et al.[3], Anders and Watson[27], and Griffin[28] have proposed and demonstrated methods to accomplish this. Particularly the latter one is interesting as it one of the first published attempt to apply them to wind turbines. Although it accomplishes increasing the power output at moderate wind speeds, at lower wind speeds the output decreases. Such results highlight the sensitivity of boundary layer control that can be seen in other research as well.

2.1 Vortices as Structures in Fluids

Research into the structures of turbulence has been ongoing, with innovations such as particle image velocimetry offering new tools of analysis. Combined with wind tunnels developed for boundary layer research they can offer a glimpse into the dynamics of turbulence. Such an experiment has been conducted, though not only, by Carlier and Stanislas[29] where they discuss how different types of vortices are an integral part of turbulence. Structures such as horse shoe vortices and streamwise vortices are believed to be part of generation and conservation of wall turbulence. Carlier and Stanislas[29] further explain how the presence of streamwise vortices can cause streaks to occur, which transport low velocity fluid away from the wall.

Research by Velte et al.[31][30] into the vortices developed by vortex generators have shown that they exhibit self-similarity that can be expressed with linear equations. These equations are based on the assumption the vortices can be modeled with the Batchelor vortex model. This model can express the axial,u_ζ and azimuthal, u_θ, velocity based on size of the vortex core ϵ, helical pitch l, and vortex advection velocity, u_0:

$$u_\zeta = u_0 - \frac{\Gamma}{2\pi l}[1 - exp(-\frac{r^2}{\epsilon^2})] \tag{2.1}$$

$$u_\theta = \frac{\Gamma}{2\pi r}[1 - exp(-\frac{r^2}{\epsilon^2})] \tag{2.2}$$

The four input parameters are described by linear equations that are derived from statistical analysis of experimental data, these are shown in Figure 2.1. This analysis makes it possible to replicate the effects of the vortex generator, however, no accounts are made for the wall effects. In Figure 2.2b the streamwise development of the velocity magnitude is shown and in Figure 2.2a the streamwise development of the azimuthal velocity is shown. This shows how the vortex is both expanding and getting weaker. The model is applicable between 1-2 vane heights and 13 vane heights away from the vortex generator and device angles between 20 and 40 degrees. Outside this range the model does not track the stronger non linear effects.

The core of the vortex can be located using either the Q criterion or λ_2 criterion. The vortex core is also the location at which the convection velocity can be found. The location of the core allows a transformation of the Z and Y axis from which the azimuthal velocity can be calculated. The distance between the vortex core and the point at which the maximum azimuthal velocity occurs can be defined as the vortex core radius. With those parameters the helical pitch can be found using the following relation:

$$u_\zeta = u_0 - ru_\theta/l \tag{2.3}$$

Where for r the vortex core radius will be considered.

Alekseenko et al.[32] have further shown that the helical symmetry in the vortices can be expressed in two types, either left handed- or right handed symmetry as shown by Figure 2.3. These distinguish themselves in their direction of flow induced by the vortex. Right handed has the most effect on the velocity along the

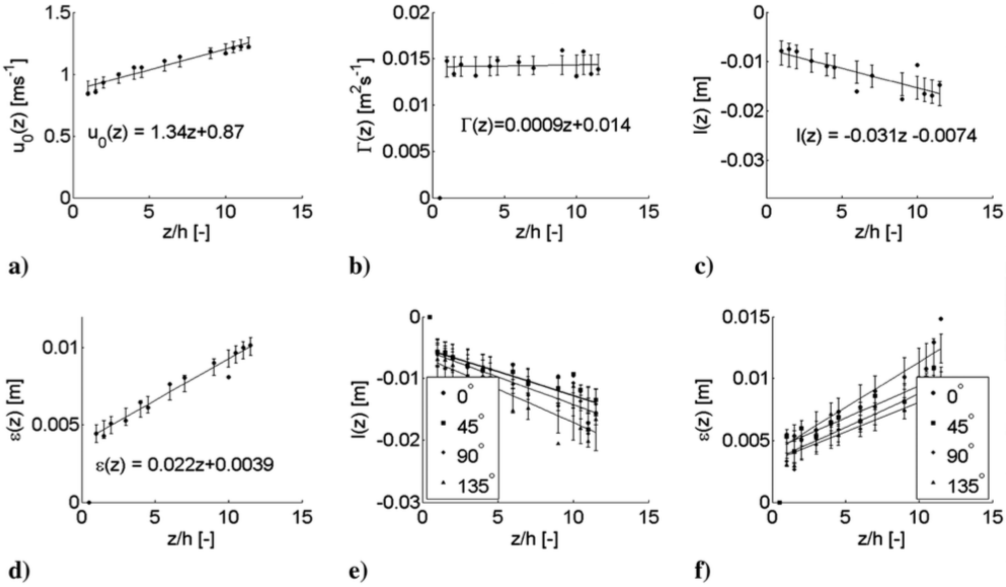

Figure 2.1: Helical symmetry and linearity for vortex flow parameters in a zero pressure gradient flow[31]

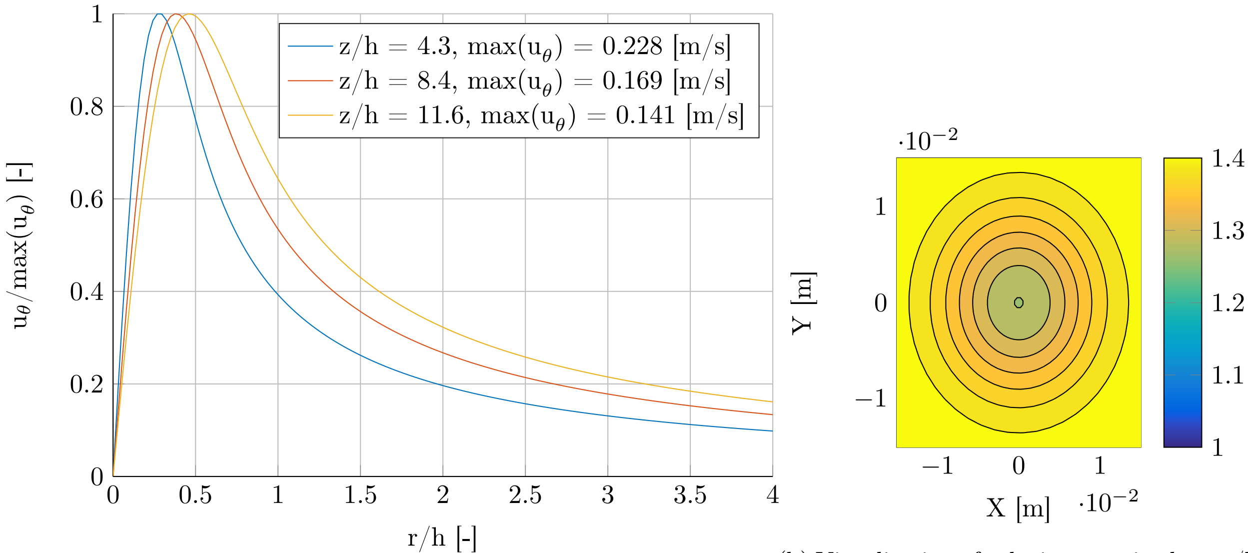

(a) Streamwise development of azimuthal Velocity

(b) Visualisation of velocity magnitude at z/h = 11.6

Figure 2.2: Demonstration of the self-similarity model of a vortex in a zero pressure gradient

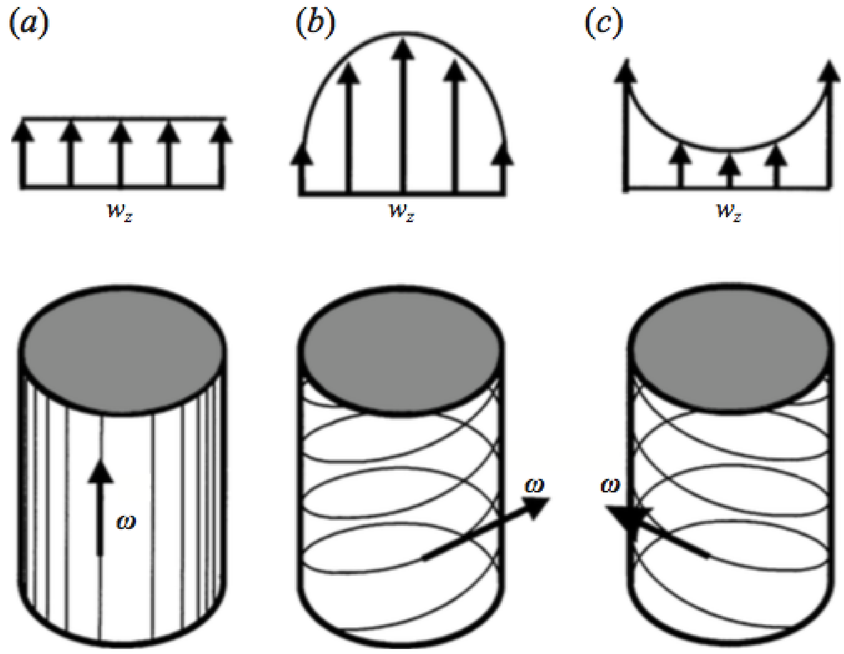

Figure 2.3: Models of a (a) Rankine vortex, (b) right handed helical vortex, and (c) left handed helical vortex[32]

geometrical axis whereas left handed symmetry has the most dominant effect along the same axis but on the periphery. Martemianov and Okulov[33] have investigated the practical implications of this distinction and have found that for heat transfer applications the left handed vortices are the most effective. They further state that the type of vortex generator device can further change the efficiency of such a left handed vortex and that it is possible for the vortex to transition from one type to the other.

2.1.1 Identification of a Vortex

Identifying a vortex is not a trivial matter, due to the variety in which vortices occur as well as their dynamic nature. Jeong and Hussain[34] discuss how previous definitions of vortex do not cover all occurrences of vortices, sometimes even including instances where no vortex is present. One of the discussed methods is the Q-criterion, which defines a vortex as the area where the second invariant of ∇u, Q, is positive and the pressure is lower than the ambient value. A second invariant contains the coefficients to the characteristic polynomial of ∇u:

$$\begin{aligned} Q &= \nabla u_{ij} \nabla u_{ji} \\ &= \cancelto{0}{\frac{\partial u}{\partial x} \cdot \frac{\partial v}{\partial y}} + \frac{\partial v}{\partial y} \cdot \frac{\partial w}{\partial z} + \cancelto{0}{\frac{\partial w}{\partial z} \cdot \frac{\partial u}{\partial x}} - \cancelto{0}{\frac{\partial v}{\partial x} \cdot \frac{\partial u}{\partial y}} - \frac{\partial w}{\partial y} \cdot \frac{\partial v}{\partial z} - \cancelto{0}{\frac{\partial w}{\partial x} \cdot \frac{\partial u}{\partial z}} \\ &= \frac{\partial v}{\partial y} \cdot \frac{\partial w}{\partial z} - \frac{\partial w}{\partial y} \cdot \frac{\partial v}{\partial z} \end{aligned} \tag{2.4}$$

Because this analysis is applied on a two dimensional plane XY certain elements in this equation can be considered zero. Continuity,equation (3.2), must be applied to obtain accurate results, therefore it is squared and expanded to obtain the following:

$$\begin{gathered} \left(\cancelto{0}{\frac{\partial u}{\partial x}} + \frac{\partial v}{\partial y} + \frac{\partial w}{\partial z} \right)^2 = 0 \\ \frac{\partial v}{\partial y}^2 + \frac{\partial w}{\partial z}^2 + 2 \frac{\partial w}{\partial z} \frac{\partial v}{\partial y} = 0 \end{gathered} \tag{2.5}$$

Implementing this into equation (2.4) leads to:

$$Q = -\frac{1}{2}\left(\frac{\partial v}{\partial y}^2 + \frac{\partial w}{\partial z}^2\right) - \frac{\partial w}{\partial z}\cdot\frac{\partial v}{\partial z} \tag{2.6}$$

This can be implemented in post processing tools or Matlab scripts to find the value for Q and thus identify the vortex. However, Jeong and Hussain[34] have found that the Q criterion lacking with respect to some flows. Therefore Jeong and Hussain[34] propose to to use the second eigenvalue of the following equation as a criterion:

$$\mathbf{S^2} + \mathbf{\Omega^2} = \left(\frac{1}{2}(\nabla u + \nabla u^T) + \frac{1}{2}(\nabla u - \nabla u^T)\right)^2 \tag{2.7}$$

With $\mathbf{S}$ and $\mathbf{\Omega^2}$ being the symmetric and anti-symmetric parts of the gradient of the velocity. Once again, due to the analysis being done on a two dimensional plane some elements can be neglected

$$\nabla u = \begin{bmatrix} 0 & 0 & 0 \\ 0 & \frac{\partial v}{\partial y} & \frac{\partial w}{\partial y} \\ 0 & \frac{\partial v}{\partial z} & \frac{\partial w}{\partial z} \end{bmatrix}$$

As Jeong and Hussain[34] show both criteria are in a essence related to each other, as shown below:

$$Q = \frac{1}{2}(\lambda_1 + \lambda_\mathbf{2} + \lambda_3) \tag{2.8}$$

The difference between the two is that the λ_2 criteria can distinguish between local pressure minima created by either unsteady straining or viscous effects[34], both effects are considered vortices by the Q criterion. In Figure 2.4 an example of both techniques applied a two dimensional velocity field is shown.

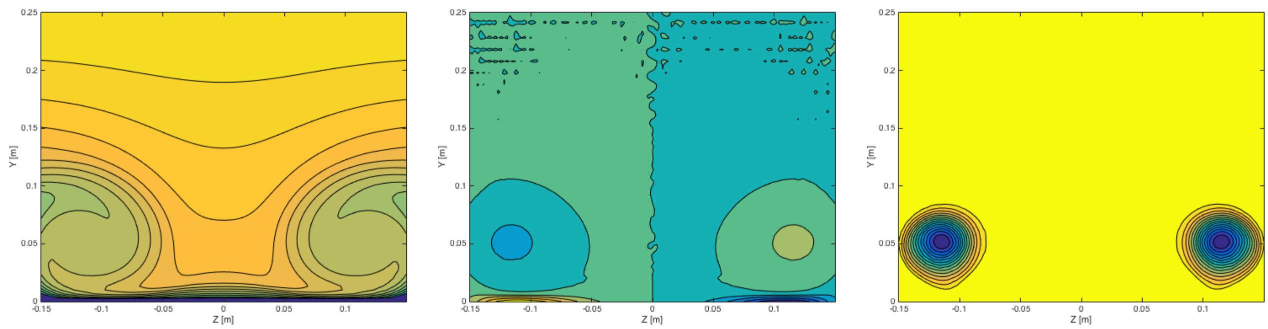

(a) Downstream Velocity Field (b) Vorticity (c) λ_2 Criterion

Figure 2.4: Demonstration of post processing a 2-D ZY plane obtained from a zero pressure gradient flow with a pair of counter rotating vortices

Further theory can provide additional criteria to test if the flow contains vortices. In 'Vortex Dynamics' by P.G. Saffman[35] the theorem proposed by Helmholtz is briefly discussed. This theorem can be summarised by three laws that describe flow with vortices:

- Fluid particles originally free of vorticity remain free of vorticity.
- Fluid particles with vorticity must either form a closed path or end in the boundaries of the fluid.
- The strength of a vortex tube, its circulation, does not vary with time during the motion of the fluid.

These laws are derived under the assumption that the fluid conforms to ideal barotropic characteristics and is influenced by conservative external body forces[35]. One of the parameters that will be investigated is the circulation of the vortices shed by the vortex generator. In order to calculate this the definition of Kevin's circulation theory is used:

$$\Gamma = \oint_{C(t)} \mathbf{u}\cdot d\mathbf{s} \tag{2.9}$$

With $C(t)$ representing a continuous closed curve, along which the velocity vector will be integrated. The continuous curve will be represented by a circle or ellipse, depending on what fits the vortex best.This leads to the following definition for $C(t)$:

$$C(t) = (r_{cz}\ \cos(t), r_{cy}, \sin(t)) \tag{2.10}$$

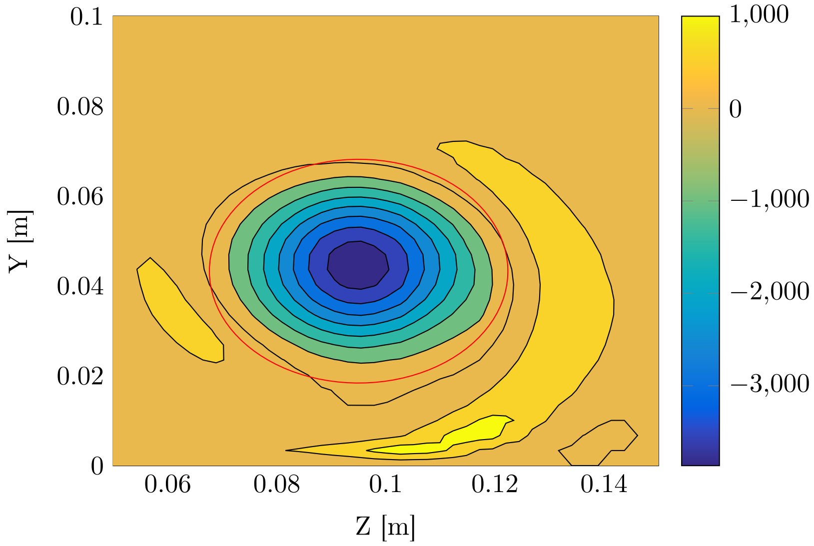

Figure 2.5: Contour for Circulation Line Integral Superimposed on Lambda 2 Criterion

Here r_{cz} and r_{cy} represent the radius of the circle or ellipse in their respective axes. This will be then be applied to the definition of circulation:

$$\Gamma = \oint_{C(t)} \mathbf{u}(C(t)) \cdot C'(t) d\mathbf{s} \tag{2.11}$$

The radii and location of the contour will be determined based on the λ_2 criterion, with the contour enclosing one object continuous object containing negative values of λ_2. This method is illustrated in Figure 2.5. However, in some cases the ellipse or circle cannot completely cover the vortex. Especially in the case of some PIV data, where the vortex seems to extend past the captured plane. This means that in terms of validation, especially with respect to Helmholtz theorems, some mismatch is to be expected especially as the plane is further downstream from the vortex generator. In those planes the vortex has grown sufficiently large that analyses such as the $lambda_2$ criterion become rather sensitive, for instance with the signal to noise ratio of PIV data. Furthermore, there will be some numerical round of errors in the sizing of the contour and the numerical integration along the curve. The influence of the amount of interpolation and integration points was evaluated for several planes and setups and found to be negligible.

With respect to Helmholtz third law of vortices, some discrepancies have been found. Yao et al.[36] have conducted experiments of varying device angles for vortex generators. For all angles they have found a decaying trend in the circulation which became stronger as the angle decreased. Yao et al.[36] also posit that CFD could be more capable of accurately predicted circulation compared to peak vorticity, due to the former's invisicid process characteristic.

2.2 Interaction Between Boundary Layer and Vortex Generator

Vortices are one of the most common structures to transport energy and can be used for boundary layer control. Cutler and Bradshaw[37][38] have researched the effectiveness of a vortex in a zero pressure gradient flow, placing vortex generators 0.3 and 0.7 span widths from the surface. Two vortices are created by a delta wing and their rotation is mirrored, leading to downward direction for the common flow. Such a vortex pair is shown to diverge from each other and move away from the boundary layer. Furthermore, Cutler and Bradshaw[37][38] show that, for the purpose of energy transfer, it is better to have the origin of the vortex closer to the boundary layer.

The origin of the vortex itself depends on the device that generates it. For the common vane type vortex generator the pressure difference across the span of the vane leads to a tip vortex. At the tip edge of the vane the pressure difference causes the flow to accelerate over the tip edge from the pressure side to the suction side, curling the flow in the process. However, there are other ways for vortices to appear in the flow. One such phenomenon has been found by Görtler[39] where it was found that certain parameters, such as concave surfaces, can trigger instabilities in the laminar boundary layer which can lead to creation of streamwise vortices. The occurrence of these vortices can be estimated with the following equation for the Görtler number G:

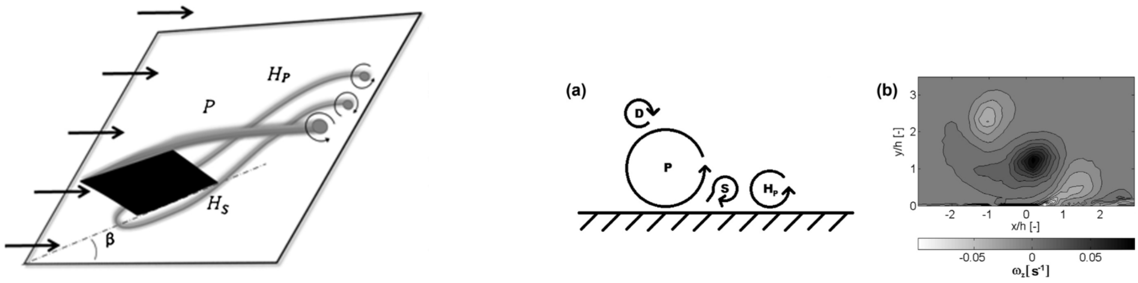

(a) Isometric view

(b) Illustrative and experimental spanwise view

Figure 2.6: Topology of the main structures created by a vortex generator[42]

$$G = \frac{U_e \delta_\tau}{\nu} \left(\frac{\delta_\tau}{R_c} \right)^{1/2} \tag{2.12}$$

With R_c as the curvature radius and δ_τ as follows:

$$\delta_\tau = \left(\frac{\nu \overline{x}}{U_e} \right)^{1/2} \tag{2.13}$$

Where $\overline{x}$ denotes the distance from the leading edge. As summarised by Floryan[40] literature defines the threshold of stability at $G = 0.4638$, but it is possible that the instability may not be detected till later. Floryan[40] notes how the flow seems to have a delayed response to perturbations that lead to Görtler vortices. The mechanism behind the Görtler vortices is not yet fully comprehended and the validity of the threshold Görtler number is still questioned. As Floryan[40] observes, multiple independent experiments have been unable to clearly identify the critical wave number for the instabilities. Floryan[40] even highlights experiments that suggest the onset of these vortices might not necessarily be a stability issue, but "the flow merely selectively amplifies disturbances already present in the oncoming stream".

Ashill et al.[17] identify vortex generators as being a viscous control method, due to the fact the main impact of vortex generators occurs within the boundary layer and effects on the free stream are negligible.

Further research by Velte et al.[41][42] into the vortices in the wake of the vortex generator revealed that the type of flow structures seen behind the vortex generator can be mapped for a combination of device height, with a constant aspect ratio, and device angle. These combinations originate from interaction between two mechanisms. Velte et al.[42] make a distinction between the basic vortex system and the secondary system. The first is displayed in Figure 2.6a with P representing the main vortex originating from the tip and H_S and H_P representing the sleeves of the horseshoe vortex on the suction and pressure side respectively.

The secondary represents the collection of vortices where H_S has been swept to the pressure side by P creating the system shown in Figure 2.6b. Here H_S has been absorbed by a vortex S that is created by the interaction of P with the boundary layer. Lastly, the vortex D can be created due to similar circumstances if the vortex S is intense enough. By varying height but keeping the aspect ratio the same whilst also varying the device angle it can be seen that these systems can exhibit variations, as shown by Figure 2.7. It can be seen that for small vanes no horseshoe vortex can be observed, Velte et al.[42] suggest this could be due to the vane height being smaller than the roll up vortex that creates the horseshoe vortex. Furthermore, the parameter study has shown that the circulation of the vortex does not always vary linearly with either the vane height or device angle. An assumption that is often made by vortex generator models that are based on lifting line theory.

Lögdberg et al.[43] have researched how much can be expected from the performance of vortex generators, by increasing the pressure gradient. Lögdberg et al.[43] note, among other things, that designing for optimal efficiency (of the vortex generator) might not be the most robust design. To categorise the sensitivity of vortex generators, Lögdberg[43] identifies several parameters to measure its performance. The shape factor H_{12}, for instance, can be used to quantify the boundary layer development.

$$H_{12} = \frac{\delta_*}{\theta} \tag{2.14}$$

In which δ_* is the displacement thickness, defined as the distance normal from the wall for which the rectangle area is equal to the velocity deficit due to boundary layer effects, such as shear stress. This can be expressed with the following equation, as discussed by Schlichting[44]:

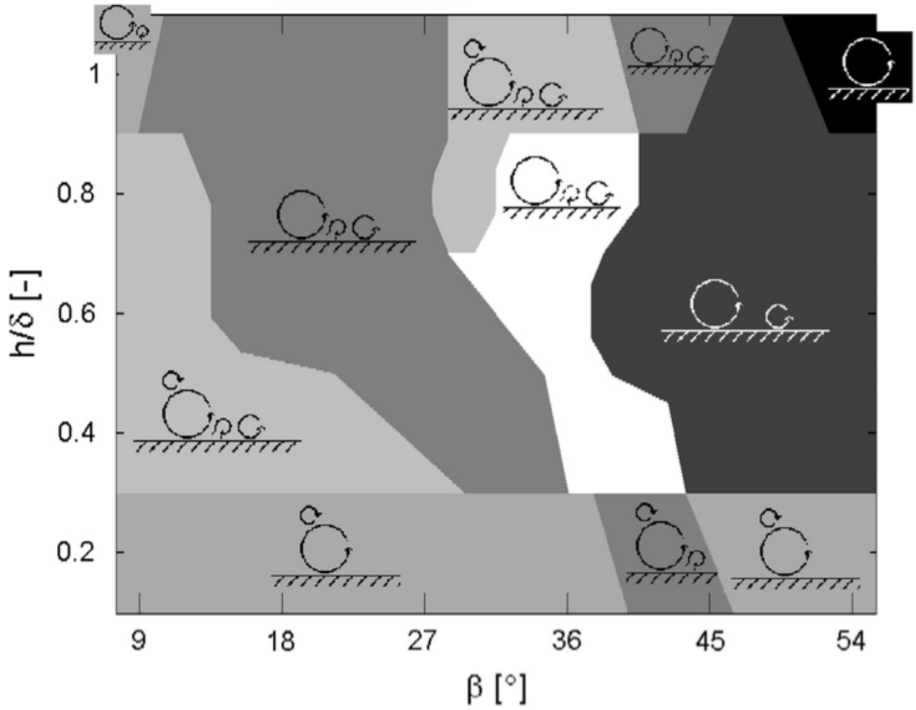

Figure 2.7: Composition of vortex structures for various device angles and boundary layer immersion ratio[42]

$$\delta_* = \frac{1}{U}\int_0^\infty (U-u)\,dz \tag{2.15}$$

And θ as the momentum thickness, similar to the displacement thickness it is the distance normal to the wall which compensates for the loss in momentum due to boundary layer effects and can be computed with the following equation:

$$\theta = \frac{1}{U^2}\int_{-\infty}^\infty (U-u)u\,dz \tag{2.16}$$

Combined with the backflow coefficient χ_w, the ratio between upstream and reverse stream direction[45], Lögdberg et al.[43] tracks the influence of vortex generators in adverse pressure gradient flows. They find these two metrics, H_{12} and χ_w, are proportionally related, but state that the shape factor is easier to calculate in the relevant areas. Lastly, they also note that backflow coefficient is correlated, non-linearly, to the circulation produced by the vortex generator.

In the work of Godard and Stanislas[46], shape factors are also used to quantify the performance of the vortex generators. Two additional shape factors are introduced in this paper, H_{23} and H, with the former expressed by the following equation:

$$H_{23} = \frac{\theta}{\delta_{**}} \tag{2.17}$$

Here δ_{**} represents the energy thickness, along the same analogy of the other two thickness definitions[44].

$$\delta_{**} = \frac{1}{U^3}\int_0^\infty (U^2-u^2)u\,dz \tag{2.18}$$

It is also possible to combine the previous mentioned shape factors in a new shape factor:

$$H = 0.5442H_{23}\sqrt{\frac{H_{23}}{H_{23}-0.5049}} \tag{2.19}$$

Which assumes that there is a relationship between H_{12} and the inverse of H_{23} which can be applied to a modified shape factor expression. A correlation with experimental data has shown that for a range, $0.723 < H < 0.761$, between where velocity profiles are tending towards separation[44]. For $H < 0.723$ the chance is high that separation has occurred.

Furthermore, their work also highlights skin friction coefficient as a parameter to track the degree of separation in both span- and stream-wise direction.

$$C_f = \frac{\tau_p}{\frac{1}{2}\rho U^2} \tag{2.20}$$

By modeling the flow over a bump and varying the vortex generators, Godard and Stanislas[46] have found that changes in the angle of the vortex generator can be tracked with the skin friction coefficient, confirming the optimal angle found in earlier research.

2.3 Types of Vortex Generators

In order to create the vortices that will transport energy to the surface a device needs to be placed on the airfoil. Many devices have been designed in the past 50 years, a selection of past designs are shown in Figure 2.8. Figure 2.8a are the "vane type" vortex generators, apart from the dowel which is of the second type, as defined by Ashill et al.[17]. Vortex generators of this type function by introducing vorticity into the flow that is linked to the bound vorticity of the object. The other type is the "obstacle type", shown in Figure 2.8b, and functions by converting the "boundary layer vorticity, which is normal to the axis of the main flow, into streamwise vorticity" as noted by Ashill et al.[17]. Ashill et al.[17] continue by distinguishing vortex generators further by the ratio of the device height and the boundary layer thickness. Conventional vortex generators are generally as high as the boundary layer if not more. Ashill et al.[17] define vortex generators that are less than half the boundary layer height as Sub Boundary-layer VG's (SBVG), also know as micro vortex generators, which is a more recent development. Their lack of height compared to the conventional vortex generator means they do not produce vortices that are as strong. However, Ashill et al.[17] note that the SBVG have the advantage of less drag. Due to the SBVG being less than half of the boundary layer the SBVG only perturbs the flow in the area that is most important for flow control without disturbing the free stream region.

In Lin et al.[47] there is a review of several of these and their specific applications. There have been some recent attempts to investigate new designs with the use of modern technology. Florin et al.l[48] for instance use a synthetic jet to provide active contro. Muller et al.[49] feed air through slots in the airfoil to control deep stall. Post and Corke[50] have shown that plasma actuators can be used to delay the onset of stall as well. Nonetheless, these techniques add a significant amount of complexity and dependencies, which for a system such as wind turbine can make things too expensive. Therefore, as far as application boundary layer control, industry tends to use vane type vortex generators. Although some research, such as proposed by Post and Corke[50], does provide minimal alternatives to the vane type.

The vane type vortex generators have been around for a long period of time and as a result of that different setups have been investigated. Recent research by Velte et al.[51] has started looking into the benefits of optimising the shape of the actual vane. They found that applying a dedicated airfoil for the vane can lead to drag reduction and lift increase compared to the regular flat delta wings applied in the industry. Furthermore the orientation of vanes in an array can be done in several ways. The main two variants are co-rotating pairs, resulting in common flow up, and counter rotating, forcing the common flow down. Research by Godard and Stanislas[46] has shown that the latter is the most effective in terms of boundary layer control, despite the fact that the vortices diverge and move away from the surface as mentioned prior. This has been confirmed by research from Manolesos et al.[52]. Though Lin et al.[47] have found that there are some cases where co-rotating is the more effective setup. For instance, on a swept wing such a setup proved to be more efficient.

2.4 Modeling of Vane Type Vortex Generators

Some research has been done to reduce the complexity of numerically modeling vortex generators. The Bender-Anderson-Yagle[1] (BAY) model was one of the first vortex generator models and is still widely used. The basic principle of this model is to model the vortex generator as a lift force which will be added to the source terms of the CFD solver.

A number of papers have focused on applying the BAY model to specific purposes such as turbo machinery while also adding drag effects[4]. Others have simply focused on verifying the model with their experimental data and highlighting their own additions or changes to the BAY model[5][6][7]. Though these papers do not mention if their model is capable of distinguishing between different vortex generator geometries. This might become particularly interesting as the vortex generator shapes become more intricate, as highlighted in a recent paper[8].

There have been attempts to approach the modeling in different ways. Methods such as immersed boundary layer[9], statistical descriptions[10], or the modeling of the generated vortex instead of the vortex generator itself[11][12]. Once again though, the variation of geometry is not highlighted specifically. Some different types

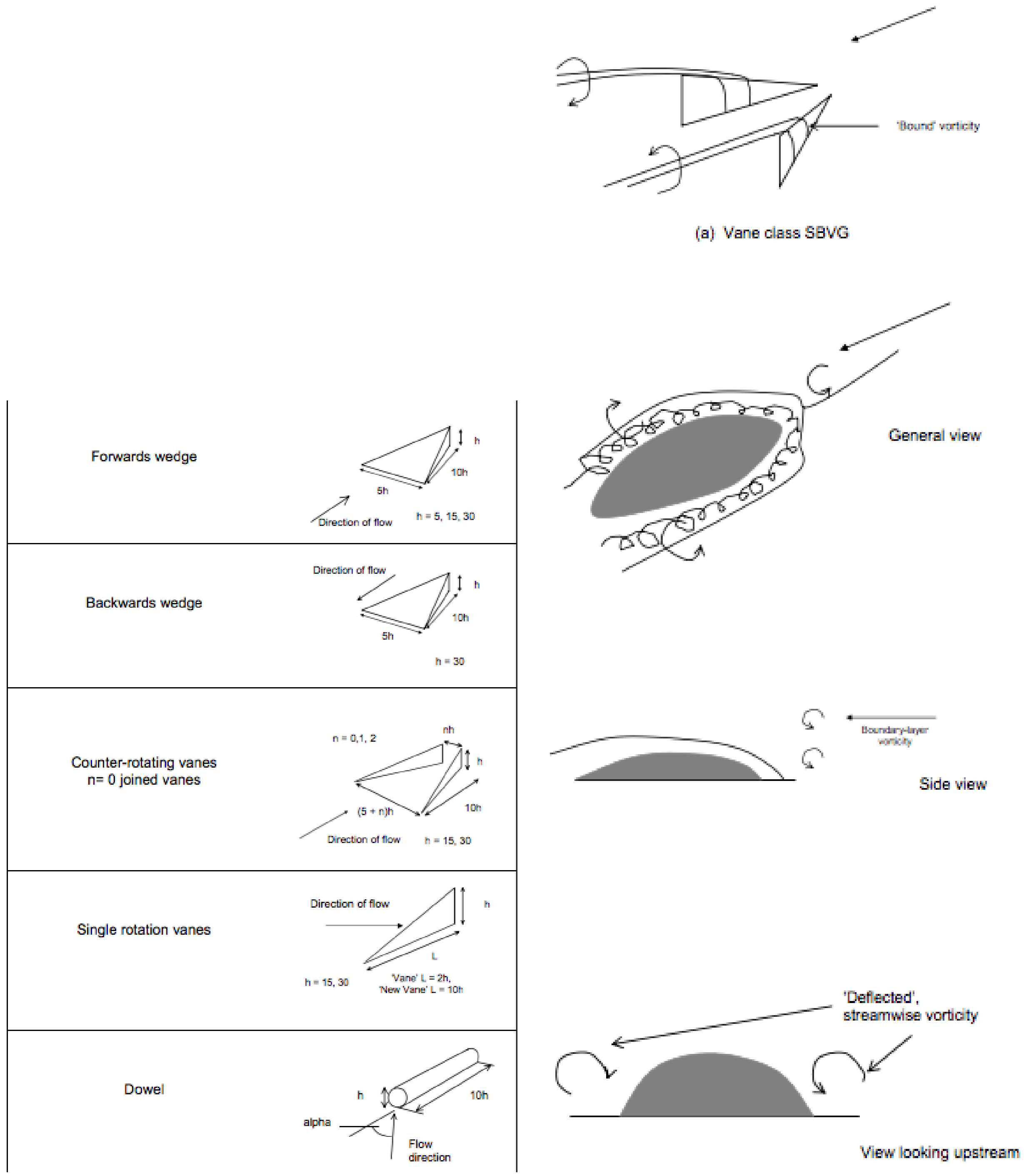

(a) Vane Type (b) Obstacle Type

Figure 2.8: An example of different types of vortex generators that have been examined in the recent decades[17]

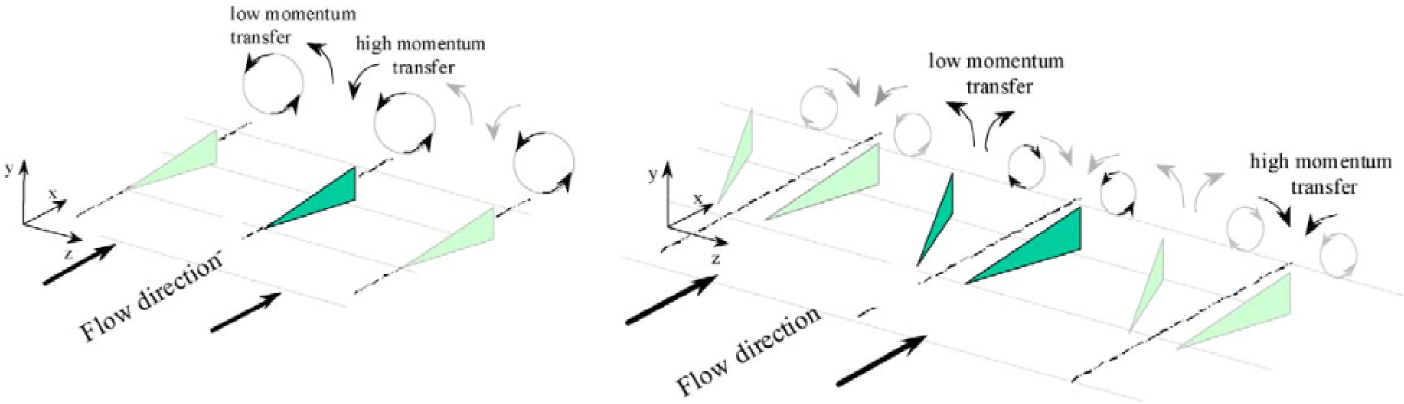

Figure 2.9: Illustration of the difference between co-rotating and counter-rotating vortex generator pairs[46]

of vortex generators are investigated, for instance Zhang[12] looks specifically into the delta wing type vortex generator. However, this led to a significant adaptation of previous models similar to those from Wendt[11].

In Table 2.1 all the aforementioned papers have been gathered and compared to the paper of Manolesos et al.[52], in which the capability of RANS to model the effects is researched. Among other things they also tested whether or not it is justifiable to use symmetry to simulate the entire span with vortex generators. They find that this is only accurate until a stall cell is created, such a situation would require a larger portion of the span for accurate results.

All papers of vortex generator models gathered in this thesis will be qualitatively judged compared to the paper by Manolesos et al.[52]. This will be done based on five characters. They are judged based on how accurate they represent the effects of a vortex generator, how much differentiation they can make between different vortex generator geometries, how much additional computational time they add, how complicated it is to implement them and lastly how much effort is required to calibrate them. Based on those results a model will be chosen to continue the work. Not all papers have judged their model on the criteria chosen for this table, therefore there is certain level of uncertainty. This will be highlighted by a question mark in the judgment.

For example, the model proposed by Bender et al.[1] is judged as being as capable as fully resolved CFD in terms of representing the effects of vortex generator. However, in terms of representing different geometries no mention is made and the implementation of the model suggest that this is limited as opposed to the almost unlimited capabilities, in this aspect, of fully resolved CFD. Nonetheless, the model is expected to be significantly faster due to comparisons made in Bender et al.[1]. Implementation should be easier due to the lack of complicated mesh geometries and minimal additional equations. It does require additional calibration efforts compared to fully resolved CFD, but they are minimal.

As can be seen in Table 2.1 all the models based on BAY model proposed by Bender et al.[1] are very close to each other. This is to be expected as they are all an iteration of the same model. The model proposed by Wallin is the most interesting of these as it promises to be free of tuning coefficients[7]. However, in the paper it has only been applied to S-ducts and further validation of this model was not found. Some of the mentioned interpretations, such as the one by Jirasek[6], and others have been compared in Florentie et al.[57]. These differentiate on how they implement the force from BAY on the mesh, some of these strategies are shown in Figure 2.10. Additionally, the combination of different turbulence models and BAY have been examined. Florentie et al.[57] conclude the Spalart-Almaras model is inadequate for representing the flow of a vortex generator in high Reynolds numbers. Reynolds Stress Transport models prove to be the most accurate, with the Shear Stress Transport model also providing similar results with less accuracy and at a lower computational cost. Considering the amount of research that is available on the BAY model and the results from the trade off table the BAY model is chosen as the model that will be implemented in this thesis.

Table 2.1: Qualitative trade-off table of various vortex generator models

	Type	Representation	Differentiation	Computation	Implementation	Calibration
Manolesos et al.[52]	**Fully resolved RANS**	**0**	**0**	**0**	**0**	**0**
Bender et al.[1]	Force source term	0	?/−	++	+	−
Booker et al.[14]	Vortex modeling	−	?/−	?/+	0	− −
Chima et al.[4]	Force source term	0	?/−	?/++	?/+	−
Wendt & Dudek [53]	Vortex modeling	−	?/−	?/+	0	−
Dudek [5]	Force source term	0	?/−	?/++	+	−
Fernandez et al.[54]	Vortex modeling	0	?/−	++	+	−
Fernandez et al.[54]	Experimental model	?/+	?/0	++	0	−
Ghosh et al.[9]	Immersed boundary	0	?/0	++	0	−
Hansen [55]	Phenomenological	−	?/−	?/++	+	−
Jirasek [6]	Force source term	0	?/−	?/++	+	−
Stillfried et al.[10]	Statistical model	0	?/−	++	−	−
Zhang et al.[12]	Vortex modeling	0	−	++	−	−
Wallin [7]	Force source term	0	?/−	++	+	0
Brunet [56]	Force source term	0	?/−	++	+	−

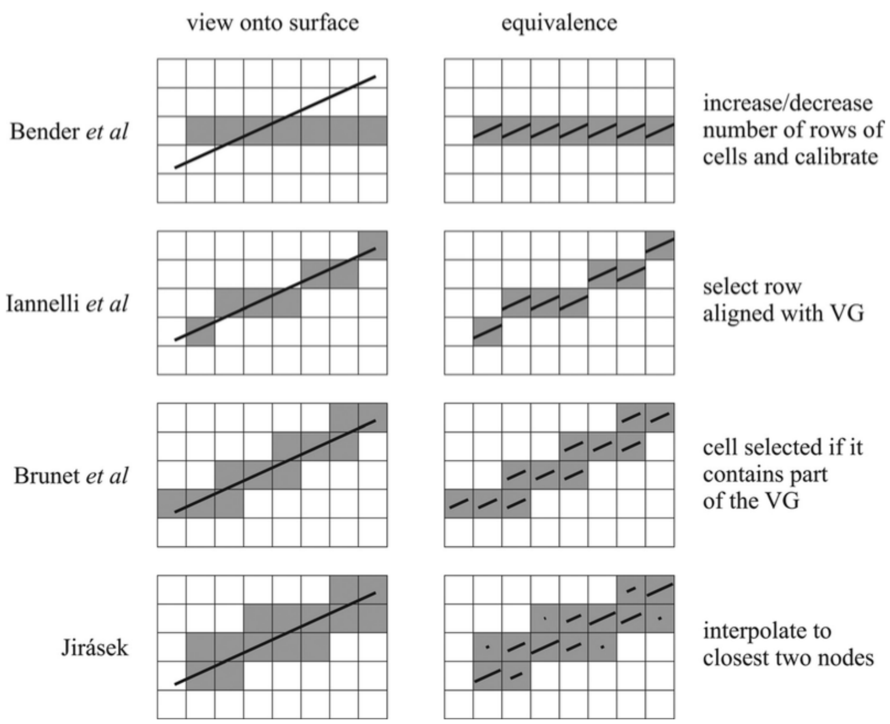

Figure 2.10: An example of different methods to distribute the body force of a vortex generator model across a mesh[14]

Chapter 3

Modeling of Fluid Dynamics

Previous sections have shown how sensitive boundary layer control can be and that the placement of vanes needs to be researched properly to ensure that the performance does not decrease. For some applications, such as wind turbines, this cannot be done experimentally due to the scale and finances of such a setup. Therefore the research and industry tends to use numerical analysis to optimise the use of vanes for wind turbines as shown by the work of Gaunaa et al[58] and Troldborg et al.[59]. However, even for numerical codes the scale can still be a challenge. Additionally the demand for high fidelity results and a fast simulation time are at odds with each other, leading to compromises in choice of numerical model and assumptions. It is therefore prudent to document these choices in order to put the final results in perspective in terms of the limitations imposed by the chosen models.

Numerical modeling can be subdivided in three categories. The first, Direct Numerical Simulation, solves the Navier Stokes equations for all finite scales. The second are labeled as scale-resolving simulations, described by Menter[60] as codes that resolve turbulence up until a certain scale. As opposed to the final third category which averages all scales, such as Reynolds Averaged Navier Stokes (RANS). The latter has been used the most used in the industry and research due to its capability to resolve the flow within a reasonable amount of time up to a certain accuracy. Recent studies have tried to move towards more accurate solvers, using for instance a hydrid system that applies RANS to the boundary layer and Large-Eddy Simulation to the rest[61]. Even though such efforts do result in a more accurate flow, the added computational time is still too significant for the industry.

3.1 Reynolds Averaged Navier Stokes

The common method to describe fluid flow analytically is to use the Navier Stokes equation, described below:

$$\rho(\frac{\partial u_i}{\partial t} + u_j \frac{\partial u_i}{\partial x_j}) = \rho g_i + \frac{\partial}{\partial x_j}(-p\delta_{ij} + \mu(\frac{\partial u_i}{\partial x_j} + \frac{\partial u_j}{\partial x_i})) \tag{3.1}$$

and the continuity equation:

$$\frac{\partial u_i}{\partial x_i} = 0 \tag{3.2}$$

Exact solutions can only be obtained for very specific cases and therefore it is quite often to make a number of assumptions to enable the possibility of fluid dynamics. One such popular method leads to the Reynolds Averaged Navier Stokes equation. It based on the idea that the velocity can be expressed in a mean and fluctuating component, otherwise known as the Reynolds decomposition:

$$u_i = \bar{u}_i + u_i' \tag{3.3}$$

This equation is then substituted into equation (3.1) and (3.2). The next step is to average the equations in time which leads to the Reynolds Averaged Navier Stokes equation:

$$\rho(\frac{\partial \bar{u}_i}{\partial t} + \bar{u}_j \frac{\partial \bar{u}_i}{\partial x_j}) = \rho g_i + \frac{\partial}{\partial x_j}(-\bar{p}\delta_{ij} + \mu(\frac{\partial \bar{u}_i}{\partial x_j} + \frac{\partial \bar{u}_j}{\partial x_i}) - \rho\overline{u_i' u_j'}) \tag{3.4}$$

with the latter term, $\rho\overline{u_i' u_j'}$, representing the Reynolds Stresses. A symmetrical three by three matrix of fluid stresses. This introduces six unknowns, which means there are four equations to solve a total of ten unknown parameters also known as the closure problem.

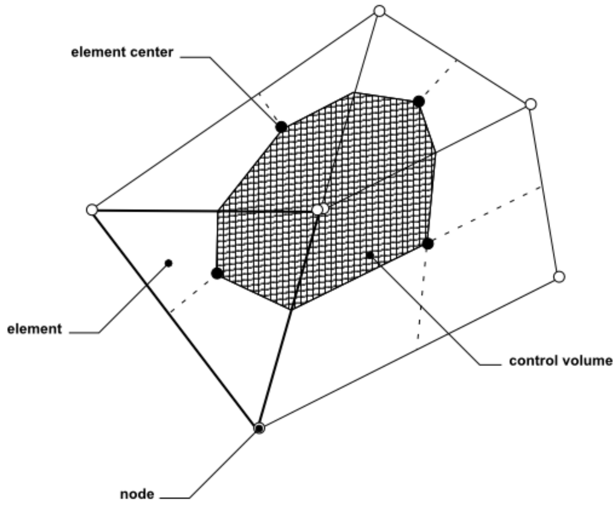

(a) Vertex centered control volume

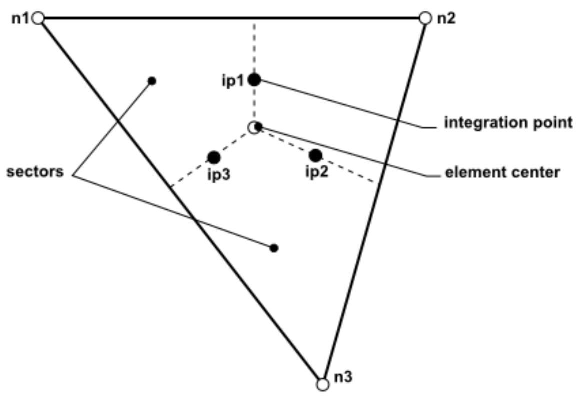

(b) Integration point definitions

Figure 3.1: Vertex centered control volume method[62]

3.1.1 Vertex Centered Control Volume Method on a Co-Located Grid

In this thesis the solver that will be applied uses the control volume method that are centered at the vertex, also known as the element nodes. This is as opposed to a centered control volume method. The vertex method is illustrated in Figure 3.1. The principle behind storing variables at the vertex as opposed to the central node of a volume is that a vertex method should be able to reproduce equally accurate results on a coarser grid. However, this does restrict the types of volumes used by the mesh to tetrahedral, hexahedral, wedge, pyramid and combinations thereof[62]. Co-located grid refers to the fact that all variables are stored at the same node, whereas a located or staggered grid has different grids for different variables. A co-located grid is simpler but can cause a decoupling to occur between the pressure and velocity, this will be discussed further in Section 3.4.

3.2 Turbulence models

To solve the closure problem several turbulence models have been suggested and tested in the past decades. Such models are often a balance between accuracy and computational cost, nor are the dynamics of turbulence fully understood yet. In this section a couple of models that will be used in this thesis will be discussed briefly. This section owes a great debt to the book written by David C. Wilcox[63], which is a very informative and well written book on development of turbulence modeling for computational fluid dynamics.

3.2.1 Wall Functions

Some turbulence models can opt to use to the law of the wall to model flow near the wall, which is an empirical relation for the flow in the viscous sub-layer, buff layer and the log law region. However, if the flow separates than the application of such functions tend to break down due to the inability to account for phenomena such as separation. Though Wilcox[63] does mention models such as the Nichols-Nelson wall function that have been applied successfully in separated flows. They do, however, enable the use of much coarser grids due to the fact the aforementioned regions no longer need to be resolved with nodes. Typically, in order to accurately compute the flow throughout the flow domain, the first cell height must follow $y+ \leq 1$, with $y+$ being: s

$$y+ = \frac{u_\tau y}{\nu} \tag{3.5}$$

With u_τ being the friction velocity, y the vertical coordinate and ν the kinematic viscosity. In Figure 3.2 the difference in both mesh domain and flow characteristics are demonstrated.

3.2.2 $k - \epsilon$ Model

The $k - \epsilon$ model is a two equation model, modeling both turbulent kinetic energy, k, and the dissipation, ϵ. As defined by Wilcox[63], this is a complete model capable of calculating a turbulent flow without prior knowledge such as mixing length models. Standard models of $k - \epsilon$ are so called "high Reynolds number models", meaning

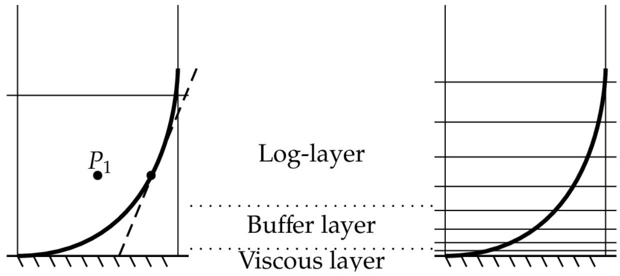

Figure 3.2: An illustration of the difference between wall functions(left) and full modeling(Right)[64]

that wall functions are used to model the flow near the wall. Adaptations for the "low Reynolds number models" do exist however. The turbulent kinetic energy is derived for $k-\epsilon$ by computing the partial derivative of k to time, the advection term, the turbulent transport, the dissipation and the production term.

$$\frac{\partial k}{\partial t} + \bar{u}\frac{\partial k}{\partial x_j} = \tau_{ij}\frac{\partial \bar{u}_i'}{\partial x_j} - \epsilon + \frac{\partial}{\partial x_j}\left[(\nu + \nu_\tau/\sigma_k)\frac{\partial k}{\partial x_j}\right] \tag{3.6}$$

Here $\bar{u}_j$ and x_j are the velocities and locations according to Einstein notation. Furthermore, $\tau_i j$ refers to an entry of the Reynolds Stress matrix, σ_k is a closure coefficient, and ν is the kinematic viscosity. And the rate of dissipation provides the value for ϵ:

$$\frac{\partial \epsilon}{\partial t} + \bar{u}_j\frac{\partial \epsilon}{\partial x_j} = C_{\epsilon 1}\frac{\epsilon}{k}\tau_{ij}\frac{\partial \bar{u}_i'}{\partial x_j} - C_{\epsilon 2}\frac{\epsilon^2}{k} + \frac{\partial}{\partial x_j}\left[(\nu + \nu_\tau/\sigma_\epsilon)\frac{\partial \epsilon}{\partial x_j}\right] \tag{3.7}$$

With σ_ϵ, $C_{\epsilon 1}$, and $C_{\epsilon 2}$ referring to more closure coefficients, used to tune the model. Both equations use the kinematic eddy viscosity, ν_τ, which comes from the Bousinessq Eddy Viscosity Approximation. For the $k-\epsilon$ model it is expressed as follows:

$$\nu_\tau = C_\mu k^2/\epsilon \tag{3.8}$$

Here C_μ represents a model constant. The Bousinessq Approximation assumes that macroscopic fluctuations in the velocity are equal to those on a molecular level. It comes from the assumption that the anisotropic stress tensor, $\mathbf{R}$ linearly relates to the mean strain tensor,$\mathbf{S}$, as explained by Schmitt[65]:

$$\mathbf{R} = -2\nu_\tau\mathbf{S} \tag{3.9}$$

For this to be valid the Knudsen number, the ratio between molecular mean free path and turbulence length scale, must be small[63]. Schmitt[65] has shown that for simple cases, such as flow past a rectangle at low Reynolds numbers, this does not hold up for the majority of the flow. Schmitt[65] points out that it is the mean velocity that is adequately estimated in most situations but that 2nd order statistics are often lacking in accuracy.

Wilcox[63] notes that the $k-\epsilon$ model is not well suited for flows with adverse pressure gradients. In several test cases for increasingly stronger pressure gradients Wilcox[63] has found that the $k-\epsilon$ model severely over predicts the skin friction coefficient and significant differences in the velocity profile. Though, the $k-\epsilon$ model has been the most widely used for a long period of time and is still being improved upon. Therefore, for some specific cases even those with separated flows, the $k-\epsilon$ can be used with accurate results.

3.2.3 $k-\omega$ Model

The $k-\omega$ model replaces the equation for dissipation with one for specific dissipation rate ω, also expressed as ϵ/k. The $k-\omega$ is also a closed model like the $k-\epsilon$ model but unlike the $k-\epsilon$ model it is inherently a "low Reynolds number" model, meaning that integration of every equation in the RANS model is carried out in every domain of the flow, including those near the wall. Though once again, "high Reynolds number" adaptations do exist. The expression for turbulent kinetic energy is slightly adapted, with closure coefficients β^* and σ^*:

$$\frac{\partial k}{\partial t} + \bar{u}_j\frac{\partial k}{\partial x_j} = \tau_{ij}\frac{\partial \bar{u}_i'}{\partial x_j} - \beta^* k\omega + \frac{\partial}{\partial x_j}\left[(\nu + \sigma^*\frac{k}{\omega})\frac{\partial k}{\partial x_j}\right] \tag{3.10}$$

The expression for the specific dissipation rate is as follows:

$$\frac{\partial \omega}{\partial t} + \bar{u}_j\frac{\partial \omega}{\partial x_j} = \alpha\frac{\omega}{k}\tau_{ij}\frac{\partial \bar{u}_i'}{\partial x_j} - \beta\omega^2 + \frac{\sigma_d}{\omega}\frac{\partial k}{\partial x_j}\frac{\partial \omega}{\partial x_j} + \frac{\partial}{\partial x_j}\left[(\nu + \sigma\frac{k}{\omega})\frac{\partial \omega}{\partial x_j}\right] \tag{3.11}$$

With β,σ_d,σ, and α representing the closure coefficients. For the $k-\omega$ model the kinematic eddy viscosity is expressed as follows:

$$\nu_\tau = \frac{k}{\tilde{\omega}}, \qquad \tilde{\omega} = max\left\{\omega, \quad \frac{7}{8}\sqrt{\frac{2S_{ij}S_{ij}}{\beta^*}}\right\} \tag{3.12}$$

Here S_{ij} represents the mean strain rate tensor. For the same cases that the $k-\epsilon$ model was compared to, as mentioned in the previous section, Wilcox[63] finds that the $k-\omega$ is capable of modeling flows that feature either separation or strong adverse pressure gradients well within range for aspects such as skin friction and velocity profiles. However, Wilcox[63] does note that the peak turbulent kinetic energy can be severely underestimated for channel and pipe flows. Furthermore, Wilcox[63] notes that the $k-\omega$ model has issues dealing with curvature and transition from laminar to turbulent.

3.2.4 $k-\omega$ Shear Stress Transport Model

Of particular interest for this thesis is the $k-\omega$ Shear Stress Transport (SST) model. In a recent review by Menter[66], who is also one of the main authors of this model, the development of the SST model is summarised as follows:

> The principle idea behind the SST models was to combine the best elements of the k-ϵ, the k-ω and the JK [Johnson-King] models. This was achieved by introducing functions which gradually blended the different elements of these models into a single formulation. Obviously, this is a pragmatic engineering approach, justified only by an improved model performance. It is to be explicitly stressed that the SST model owes much of its success to the robust and accurate near wall formulation of the 1988 Wilcox k-ω model.

Specifically, the combination means that $k-\omega$ is used close to the wall and $k-\epsilon$ for the free stream flow, with the exact ratio being controlled by so-called blending factors and functions. By combining these models the SST model manages to handle flows that feature strong pressure gradients without some of the downsides that plague $k-\omega$. One of those is the sensitivity to farfield or freestream boundary conditions, which Wilcox[63] notes has a more significant negative impact on $k-\omega$ than it does for $k-\epsilon$.

The Shear Stress Transport part of the model refers to the fact that this model includes the transport term for the turbulent shear stress[67]. This feature is only applied to the boundary layer of the flow. Its implementation delays the response of shear stress to the strain rate, but this can expression can explode numerically in the free stream[67].

Furthermore, SST was developed as part of research into adverse pressure gradients on airfoils. Such conditions define many of the domains boundary layer control is applied to, making SST therefore a logical choice in terms of numerically modeling the flow. However, examining boundary layer control in less aggressive conditions can also be of worth. This involves cases where there may be a transition in the boundary layer from laminar to turbulence, which as Menter[66] highlights as one of the more complex issues with fluid modeling. Research by Sørensen[68] summarises the implementation and validation of the γ-Re_θ model developed by Menter[66]. Sørensen[68] showed how the addition of a transition model improves the prediction of the onset of stall and an overall increased accuracy in drag predictions. However, it did come at the cost of increased grid sensitivity.

Due to the fact that SST is both computationally efficient and relatively accurate, much work has gone into upgrading the model to solve original issues. One of those is the inability of SST and general two equation models to accurately model the flow when it features strong curvatures or rotation. In Smirnov and Menter[69] the implementation of a curvature correction to the SST model is discussed. It adds a term to the production terms with upper and lower limits. This is due to the fact that SST has a tendency to overestimate the turbulence production and also for numerical stability. The lower limit represents a 'strong convex curvature(stabilized flow, no turbulence production)' whereas the upper limit represents 'strong concave curvature, enhanced turbulence production'[69]. Smirnov and Menter[69] have shown that for negligible to minimal addition of computational time the curvature correction manages to produce more accurate results for several curved or rotated flows, including a U-turn channel and a rounded tip on an airfoil. The latter case, for instance, with the curvature correction exhibits a suppression of turbulence in the vortex core shed at the tip, something that does not occur in the unmodified SST. Smirnov and Menter[69] mention that the lack of curvature correction leads to an overly fast decay of the core axial velocity.

An overproduction of turbulent kinetic energy by SST has also been observed at stagnation points, leading to a delay in stall when simulating the flow over an airfoil. To compensate for this there are two main methods, known as the clip factor and the Kato-Launder method. The clip factor method was introduced by Menter[67] and is expressed as follows:

$$P_k = min\left(P_k, C_{lim}\rho\epsilon\right) \tag{3.13}$$

With P_k representing the production turbulent energy and C_{lim} the clip factor, a dimensionless constant set to ten, which is multiplied with the density and turbulent eddy dissipation. The Kato-Launder method, proposed by Kato and Launder[70], which uses a similar expression but relates it to vorticity, due to the fact that the overproduction by turbulence models generally occurs in flow regimes of large strain and low vorticity.

3.2.5 Baseline Explicit Algebraic Reynolds Stress Model

All the previously discussed models have been build up upon the Bousinessq Approximation. However, as Wilcox[63] notes this assumption does not account for the fact that the kinematic eddy viscosity is also dependent on the flow history for example. This can cause issues for flows over curved surfaces, three dimensional flow or flows that exhibit secondary motion. One solution to this problem is to replace the Bousinessq Approximation by modeling the Reynolds Stressesr[71]:

$$\bar{u_i'u_j'} = k\left(a_{ij} + \frac{2}{3}\delta_{ij}\right) \tag{3.14}$$

Here a_{ij} represents the anisotropy tensor, enabling the modeling of anisotropic normal stress. This method of turbulence modeling is referred to as Reynolds Stress Modeling, with this specific case being Explicit Algebraic due to the algebraic derivation of the Reynolds Stress where the implicit functions have been rewritten into closure functions. Whereas 'Baseline' refers to the fact that the two equation model does not have the modification of the eddy viscosity formulation, accounting for transport effects of the principal turbulent shear stress[67]. This can lead to underprediction of separation effects.

The model is significantly more complicated than the previously mentioned models and can exhibit nonlinear behavior if not numerical instability. Nonetheless it has been proven to perform successfully for flows over curved geometry, flows that feature secondary motion and others[71][63] where the previous models have under performed.

3.3 Limitations of Turbulence Modeling

Research has been done to verify whether or not RANS is capable of analysing vortex generators[52]. It has shown that fully resolved geometry cannot represent the effects accurately. The principle behind RANS is to time average the flow which leads to the closure problem, requiring additional turbulence models to close the momentum equations of RANS. However, these equations assume that the cascade of energy transfer can be described a power law of $-\frac{5}{3}$. However, the flow in the boundary layer and around the vortex generator is much lower than the general flow around an airfoil. In the former these assumptions are no longer as valid anymore, leading to a physical error in the results[72]. This problem is not limited to RANS and cannot be solved by applying scale resolving simulations as shown by George and Tutkun[73].

RANS is always used in conjunction with a turbulence model and these can add additional computational time and errors depending on the type of flow. Research from Catalono and Amato has shown that the Shear Stress Transport (SST) Menter $\kappa-\omega$ model is the best compromise for transonic and high lift flows[74]. Kalitzin et al. have looked at the boundary layer performance of several turbulence models and propose implementations for the Spalart-Allmaras model to improve its viscous sublayer and logarithmic layer[75]. Furthermore, they state that the $\kappa-\omega$ model lacks significantly in the viscous sublayer, which is one of the models in the aforementioned SST model.

3.4 Numerical Instability

The implementation of a vortex generator model will most likely be introducing a high force and pressure gradient into the fluid domain. This could lead to numerical instability such as pressure or velocity oscillations. This issue has been discussed by Rhie and Chow[76] in 1983 in an effort to numerically model the occurrence of separation over an airfoil. To model this phenomenon Rhie and Chow[76] employ a solver based on SIMPLE, known as the Semi-Implicit Method for Pressure Linked Equations, with a $k-\epsilon$ turbulence model. The implementation, however, leads to oscillations in pressure, something which others have previously experienced as well as noted by Rhie and Chow [76].

In a paper by Réthoré and Sørensen[77] how this occurs is eloquently explained. When deriving the Navier Stokes equation in one dimension with a central differencing scheme the following expression for pressure at the central node is found, with the notations of the scheme displayed in Figure 3.3a:

$$P_P = \frac{1}{2}(P_{WW} + P_{EE}) \tag{3.15}$$

This means that the pressure at the center point, P_P, is not influenced by the the pressure of its neighbours, P_W and P_E. This can lead to an oscillation because [2 0 2 0 2] would be an acceptable solution to a grid as shown by Figure 3.3a. This is caused by interpolation of the convective term at the boundary of the central node. If the convective term is instead obtained by central differencing that takes into account the neighbour cells a different expression for pressure can be found.

$$P_P = \frac{1}{2}(P_W + P_E) \tag{3.16}$$

This will prevent oscillations in the pressure distribution and allow for non linear pressure distributions, as shown by figure 3.3b. However, Réthoré and Sørensen[77] note that this expression is valid when it is assumed that no force is applied on the domain. If that is the case then the expression for pressure is once again susceptible for oscillations. Applying a force to the central node P in the scheme from Figure 3.3a leads to the following expression between the force and pressure:

$$P_E - P_W = 2F_P \partial x \tag{3.17}$$

Which for the east and west cells, where there is no force $F_W = 0$ and $F_E = 0$, leads to:

$$P_P - P_{WW} = 0, \text{ and } P_{EE} - P_P = 0 \tag{3.18}$$

Therefore, when for instance a vortex generator is modeled, introducing force and a non linear pressure distribution, there is a chance that oscillations might occur in the pressure as shown by Figure 3.3a. Réthoré and Sørensen[77] propose to split the pressure jump on both faces of the central node, the pressure jump over the west face P_w^j and east face P_e^j. Then the same routine is applied, a central difference of the pressure values to compute the convection term and advection velocity. This method avoids pressure oscillations as shown by Figure 3.3b. In the solver used in this thesis oscillations caused by additional force are solved in a different manner. The pressure is still handled in a similar fashion, with a derivative of the pressure:

$$\left(\frac{\partial p}{\partial x_i}\Big|_{ip} - \frac{\bar{\partial p}}{\partial x_i}\Big|_{ip} \right) \tag{3.19}$$

The body force will then be distributed into this term:

$$\left((\frac{\partial p}{\partial x_i} - S_i)_i p - (\frac{\bar{\partial p}}{x_i} - \bar{S}_i)_i p \right) \tag{3.20}$$

Here the subscript 'ip' denotes an integration point as highlighted by Figure 3.1b and the overbar denotes the averaging of vertex values at the integration point[62]. This means that if a neighbouring point has no force attributed to it, it will experience some level of the force due to the high order derivative. This high order derivative is obtained when the expression for the advection velocity is implemented into the continuity equation.

The issue with pressure oscillation can be prevented entirely by using a staggered grid, but considering that is not an option within this thesis this option will not be investigated further.

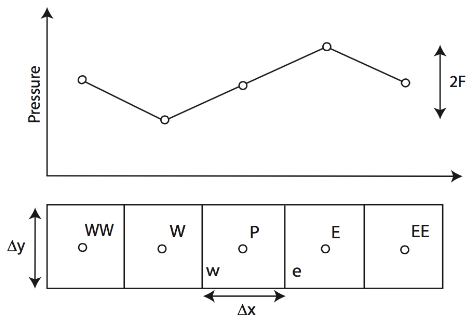

(a) numerical pressure wiggles in the solution

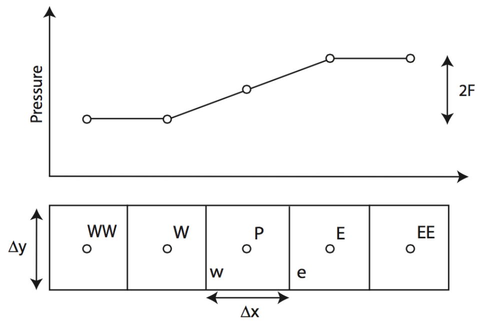

(b) solution with Rhie-Chow redistribution

Figure 3.3: Numerical instability and the effect of Rhie-Chow redistribution[78]

3.5 Mesh Quality

In order to produce accurate results with CFD one of the requirements is that the mesh of the fluid domain meets a certain quality standard. This standard can vary depending on the flow conditions, turbulence model and the type of solver that is applied. It is also not a single quantity but generally consists of checking various parameters of the mesh that has been generated and will depend on its type. Typically, two general methods of meshing can be found which can then be adapted for specific purposes. The first method is the so called unstructured mesh, which consists of tetrahedral elements that are spaced in a non uniform manner. This allows for simple and fast generation of a mesh, especially in a domain with complicated geometry. The other method is the structured mesh, build out of hexahedral volumes, and is ... . Though structured meshes can be more time consuming and complicated to generate, they are typically faster in solving due to the way the mesh is stored and handled by the solver. Figure **??** shows examples of both mesh strategies. They can also be combined when the boundary layer grows in a structured manner but the remainder of the flow domain is unstructured, which enables control over boundary layer modeling.

Within structured meshes it is possible to define different strategies when it comes to meshing certain objects. For example, when meshing airfoils there are two popular strategies in the industry, such as O-grids[79] and C-grids[80]. The O-grid is especially useful when a multitude of angles of attack are evaluated, whereas the C-grid can offer more control over refining the wake.

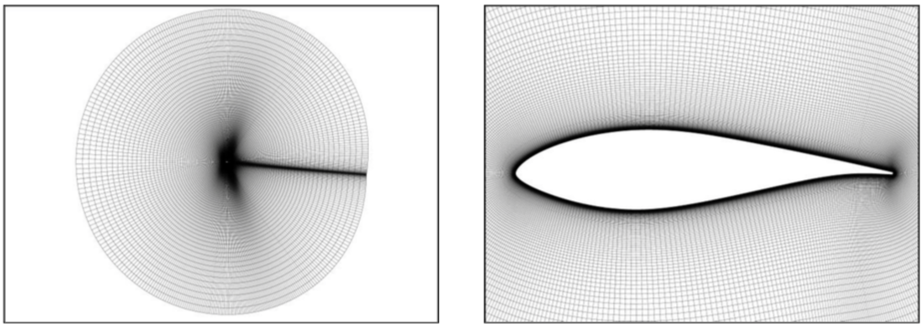

Figure 3.4: An example of an O-grid for meshing an airfoil[81]

Another facet of meshing that can be very powerful is refinement, making it possible to keep the element count down while still being able to resolve small scale flow phenomenon. This can be accomplished by a multi-body strategy or local adaptive meshing. The first method is a static method, where the fluid domain is divided in a number or bodies which will have varying sizes of elements. The second strategy is dynamic as it refines the mesh while the solution is being calculated. This refinement is based on the gradient of a pre-defined variable, constraints on the refinement, and criteria for when the refinement can take place. An example of these refinement methods is shown in Figure ..... .

Below several key mesh characteristics that indicate the quality of the mesh will be discussed, additionally the range within a 'good' mesh must be in will be denoted for future reference. This range is a mix of industry standards, solver manuals and academia standards and should therefore not be regarded as absolute.

- **Aspect Ratio:** This is typically the ratio between the width and height of a cell. For critical flow areas, except for near the wall, it is usually best if this does not exceed 100[62] and if the flow is aligned with the cell faces.
- **Volume Change:** The ratio between the volumes of two cells who have a common face, also known as smoothness. This ratio should stay between 1 and 2 ideally.
- **Jacobian Determinant:** A Jacobian Determinant is the determinant of a matrix of partial derivatives. In the context of a mesh this means the determinant of a matrix containing the partial derivatives of normal vectors of faces. An optimal element, such as a cube, will have a Jacobian Determinant of 1. Values below 0.5 are usually a sign of bad elements, this means that the normal vectors of two faces could be crossing each other.
- **Skewness:** Skewness is an indication how optimal the shape is with regards to corner angles. The Ansys user manual[62] regards those within 0 and 0.25 to be excellent and those elements with larger values to be increasingly inferior until they are degenerate with a value of 1.
- **Orthogonality Angle:** A measure of the angle between an edge and the normal vector of the integration points associated with that edge. From degenerate to ideal the range is 0 to 1.

- **Maximum/Minimum Face Angle:** Or the angle between two edges, should be between 20 and 110 degrees.

The parameters listed above are all of geometric nature and can therefore say nothing about the mesh quality with respect to the flow that is being solved on it. They should be combined with a grid independence study and comparisons to experimental data in order to make informed judgments about mesh and simulation results.

Chapter 4

Validation

Throughout the process of developing models for vortex generators several methods have been used for verification. In the papers previously mentioned either fully resolved Reynolds averaged Navier Stokes (RANS) solver are used or experimental data from similar setups, or even a combination of both. However, the parameters that are then used to verify often vary. In some studies, the peak vorticity is the parameter in the validation process[5], other studies look at axial velocity[13], or at the tangential velocity[14]. These studies all can see that the model lacks in some parameters at certain phases of the flow, but none are able to establish a complete picture of its performance. Therefore, this thesis will try to combine all the parameters discussed in Section 2.2. As stated by Oberkampf et al.[82], "validation, the relationship between computation and the real world, ie, experimental data, is the issue". They go on to state the common approach, the building block approach, to validate CFD results as follows:

> This approach divides the complex engineering system of interest into at least three progressively simpler tiers: subsystem cases, benchmark cases, and unit problems. The strategy in the tiered approach is to assess how accurately the computational results compare with the experimental data (with quantified uncertainty estimates) at multiple degrees of physics coupling and geometric complexity.

To follow this approach in this thesis the vortex generator model will therefore be applied in cases that increase in complexity. Some of these will be based on published journals which will provide additional analysis into the experiments as well as validation of the data.

4.1 Experimental comparison

The first three case are based on an experiments in the turbulent boundary layer wind tunnel in Lille, France. This tunnel is one of a kind due to its size, which allows the flow to develop a boundary layer thickness of 30 cm at high Reynolds numbers. Carlier and Stanislas have documented the structures inside the turbulent boundary layer of the wind tunnel, providing velocity and turbulent kinetic energy profiles for several Reynolds numbers[29]. Before validating the model the flow without the vortex generator will be analysed to ensure that the boundary layer develops appropriately. After which a paper by Velte et al.[83] will be used to validate the implementation of a vortex generator model. This paper features vortex generators of different shapes, such as rectangles, triangles and cambered rectangles, on the floor of the wind tunnel. These experiments have been conducted at a Reynolds momentum thickness number of 20000. There will be no adverse pressure gradient, constraining this case to the turbulent mixing caused by the vortex generator. Stereoscopic particle image velocimetry is used to measure velocity profile at various downstream planes. This case will make it possible to both validate the capability of the chosen model to simulate a vortex generator as well as the ability to differentiate between shapes.

The second case is based on a paper by Godard and Stanislas[46] and a paper by Bernard et al[84]. The latter describes the flow in the same wind tunnel of the first case when the floor features a bump. The paper provides coordinates of this bump making it possible to use this case to validate the model when the model has to operate in an adverse pressure gradient environment. Once again the flow characteristics, such as velocity and boundary layer characteristics, are thoroughly documented across several streamwise locations. Bernard et al[84] have done documented the flow over the bump at a Reynolds momentum thickness number of 28000, which is very close to the Reynolds Momentum thickness number of the experiments conducted by Godard and Stanislas[46].

Therefore, the flow over a bump in this wind tunnel can also be validated without the vortex generators. This is particularly of interest in this case, because as mentioned by Cuvier et al[85]. such a case tests the limits of RANS and associated turbulence models. After such a validation has been made the paper by Godard and Stanislas[46] will be used to validate the model for two aspects. The first is its capability to operate in flows with an adverse pressure gradient. Secondly, Godard and Stanilas[46] have also documented a parameter study, varying such parameters as aspect ratio and device angle for instance, which will make it possible to test the model for its sensitivity to those parameters.

The final third case will examine the flow over an airfoil, comparing the model to internal data that has documented the lift and drag as well as pressure distribution over a DU airfoil for various angles of attack. This will test two phenomenon, one being the ability to suppress the onset of stall and the other the additional drag induced by the vortex generators.

4.2 Grid Independence Study

Before validation between experimental data and the simulation results can be compared it needs to be established that the results are mesh independent, ruling out the influence of the meshed fluid domain on the results. This can be accomplished the following methods that will be discussed briefly.

4.2.1 Richardson's Extrapolation

In order to quantify the effects of the mesh on the results two methods will be used. These are the Richardson's Extrapolation and the Grid Convergence Index (GCI), a thorough explanation can be found in Roy[86], Roy[87], Roache[88], and Oberkampf et al.[82]. From Roy[86] an equation for the generalised Richardson's Extrapolation is obtained, which can be used for any arbitrary pth order scheme with any arbitrary refinement factor r. Considering the multi-body mesh that has been used the refinement ratio is defined as follows:

$$r_{12} = (\frac{N1}{N2})^{(1/D)} \tag{4.1}$$

With N1 being the amount of elements in the fine mesh and N2 the elements in the rough mesh respectively. The variable D denotes the dimension of the mesh. Richardson's extrapolation can give an estimation of what the exact solution would be, if the grid size spacing would go to zero. This is expressed by the following equation:

$$f_{exact} = f_1 - g_p \tag{4.2}$$

Here f_1 represents the solution variable on the fine mesh and g_p the error coefficient, as shown in the next equation:

$$g_p = \epsilon_{12}/(r_{12}^p - 1) \tag{4.3}$$

With ϵ_{21} being the error between the rough, f_2, and fine, f_1, solution variable:

$$\epsilon_{12} = f_2 - f_1 \tag{4.4}$$

The solution estimations and intermediate variables for the obtained solutions can be found in Table 2.4. The estimation from the Fine to Rough case could be considered the most accurate, due to the larger refinement ratio. Nonetheless, all these values are within one percent of each other. It must be noted that Richardson's Extrapolation is based on a couple of assumptions, that must be valid in order for the method to be valid. In Roy[87] a discussion can be found on these, a brief summary will be presented here. The assumptions are as follows:

1. Solutions are obtained in the 'Asymptotic range', e.g. the range where the discretisation error adheres to the order of accuracy of the numerical scheme.
2. Uniform mesh sizing.
3. Uniform and consistent mesh refinement.
4. No discontinuities in the solution.
5. Round-off error, iterative error, and statistical sampling error remain small compared to discretisation error.

In terms of assumption 2 and 3, the generalised Richardson's Extrapolation is used to handle the non uniform refinement. Furthermore, considering the low Mach number of the solution assumption 4 should not be an issue. It also assumed that an RMS of 1e-6 and minimal imbalances in the domain prevent assumption 5 from being a problem. Assumption 1 can be checked by plotting the numerical solution as a function of the mesh sizing, providing an observed order of accuracy. However, in this case there is no uniform sizing nor uniform refinement of said sizing. As a solution to this Roache[88] proposes a method to calculate the observed order of accuracy, denoted by $\hat{p}$, so that the comparison to the formal order of the scheme can be made. This is done by iterating the following equation with the underrelaxation factor ω:

$$\hat{p}^{k+1} = \omega \hat{p}^k + (1-\omega)\frac{ln(\beta)}{ln(r_{12})} \tag{4.5}$$

With β defines as:

$$\beta = \frac{\epsilon_{23}(r_{12}^{\hat{p}^k} - 1)}{\epsilon_{12}(r_{23}^{\hat{p}^k} - 1)} \tag{4.6}$$

4.2.2 Grid Convergence Index

The second method to quantify the quality of the results is the Grid Convergence Index (GCI), which as discussed by Roache[88] can be described as a method "to uniformly report grid convergence tests". The GCI is expressed for both a fine, denoted with one, and a course grid, denoted with two:

$$GCI_n = F_s|E_n|, \text{ for } n = 1, 2 \tag{4.7}$$

Here F_s represents the safety factor, Roache[88] a value of three for F_s. This transforms the GCI into an error band instead of an error estimator, enabling the general application of GCI (for any r and p). Additionally, E_n denotes the error estimator which can be calculated as follows for a fine grid:

$$E_1 = \frac{\epsilon_{12}}{1 - r_{12}^p} \tag{4.8}$$

And for a course grid:

$$E_2 = \frac{r_{12}^p \epsilon_{12}}{1 - r_{12}^p} \tag{4.9}$$

With p being the formal order of the scheme. These can be calculated for both the Rough to Medium and Medium to Fine meshes. If the following holds:

$$r^{\hat{p}} \approx \frac{GCI12_{fine}}{GCI23_{fine}} \tag{4.10}$$

Then, according to Roache[88], it can be said the solution is the in the asymptotic range with an error band to the solution defined by the GCI.

Part II

Validation

Chapter 1

Model Implementation

This chapter documents the implementation of a body force model in Ansys CFX. This model will be based on the work of Bender, Anderson, and Yagle[1]. It will be discussed briefly and afterwards the implementation will be demonstrated and validated.

1.1 Bender, Anderson & Yagle Vortex Generator Model

With the distribution of momentum across the mesh sorted it is now time to connect this to a physical relation to the force that would be applied by a vortex generator. As a reference the paper by Bender, Anderson, and Yagle[1] is used, henceforth referred to as BAY-model. As stated by Jirasek[6] this model is derived from the lifting line theorem and finds a lift force equation for the body force, expressed as follows:

$$\mathbf{L_i} = C_{vg} S_{vg} (\Delta V_i / V_m) \alpha \rho u^2 \hat{l} \tag{1.1}$$

C_{vg} is the model constant, related to the amount of cells the vortex generator occupies. The vortex generator is represented by the plan area S_{vg}, V_m as the total volume of mesh cells representing the vortex generator, α for the device angle. Furthermore, u represents the local velocity, V_i the local cell volume, ρ stands for the flow density, and $\hat{l}$ the unit vector for the direction of the force. However, instead of using the device angle and the unit direction vector the vortex generator can also be expressed by three unit vectors; the normal, tangential, the cross product of the previous two. These are displayed in Figure 1.1.

Introducing these unit vectors to equation 1.1 leads to the following:

$$\mathbf{L_i} = C_{vg} S_{vg} (\Delta V_i / V_m) \rho |\mathbf{u}^2| (\hat{u} \bullet \hat{n})(\hat{u} \times \hat{b})(\hat{u} \bullet \hat{t}) \tag{1.2}$$

The first vector dot product replaces the device angle based on the assumption that $\alpha \approx \sin\alpha$. Along the same assumption the direction unit vector $\hat{l}$ is expressed by the cross product of the unit velocity vector $\hat{u}$ and the unit vector $\hat{b}$. The last vector dot product is an approximation for the loss of lift force due to high devices angles.

This model was first published in 1999 by Bender, Anderson, and Yagle[1] and has been replicated by several others since then, such as Dudek[5] in 2011. Jirasek[6] has proposed a slight modification to the application of the lift force to the model. The vortex generator is regarded as a device with zero thickness. The momentum is then distributed amongst the elements of which the edges cross the zero thickness line that describes the vortex generator. Jirasek[6] poses that this should make the model independent of the model constant C_{vg}. Furthermore, the definition of the zero thickness line should allow for more freedom in defining a vortex generator array. The latter feature might not be necessary for this algorithm. Currently it is capable of defining a single pair and an array of multiples of such a pair should not introduce significant hurdles. Furthermore, although Jirasek[6] notes that the zero mean thickness should make the model independent of the constant C_{vg} it is not dropped from the equation. Slight variances for different values are still observed by Jirasek[6] and as such it does not seem to be a significant improvement. Furthermore, implementing the zero thickness line assumption in CFX is not trivial due to the need to evaluate crossing of element edges. However, if calling an edge was not an expensive CPU task in CFX then a zero mean line definition can lead to lower element requirements compared to a volume based search algorithm, such as currently implemented.

The BAY-model implementation follows equation 1.2 and is implemented into CFX with the use of CEL expressions, FORTRAN, and MATLAB. CEL refers to CFX Expression Language, which is the solver's internal code. They are used to define variables and link the FORTRAN script to the solver. The FORTRAN script executes the algorithm that identifies the vortex generator in the mesh. Lastly, MATLAB is used to translate a vortex generator geometry and setup into inputs necessary for the BAY model equation.

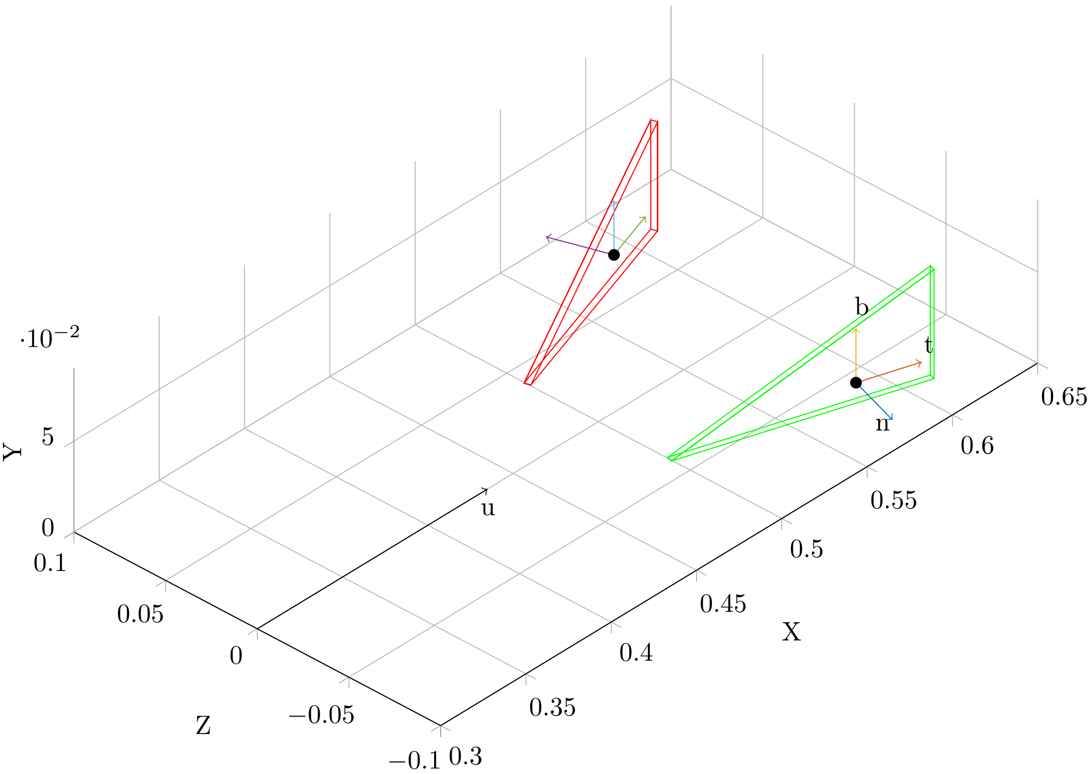

Figure 1.1: A counter rotating vortex generator pair with the corresponding vectors as used by the BAY model

The implementation does require additional signs in order to distinguish between negative and positive device angles. If the flow only has a streamwise component, i.e $u = [1,0,0]$, and our vortex generators are positioned such as in Figure 1.1 then the direction of the force on the flow is the same for both vortex generators. This is highlighted when the right hand side of the equation 1.2 is expanded below:

$$\mathbf{u}^2|(\hat{u} \bullet \hat{n})(\hat{u} \times \hat{b})(\hat{u} \bullet \hat{t}) = (u \cdot n_1 + v \cdot n_2 + w \cdot n_3) \cdot (u \cdot t_1 + v \cdot t_2 + w \cdot t_3) \cdot \hat{u} \times \hat{b} \tag{1.3}$$

Considering $\hat{b}$ only has a component in the Y direction and that $u = [1,0,0]$ this can be simplified to:

$$(u \cdot n_1 + v \cdot n_2 + w \cdot n_3) \cdot (u \cdot t_1 + v \cdot t_2 + w \cdot t_3) \cdot \hat{u} \times \hat{b} = u \cdot n_1 \cdot u \cdot t_1 \cdot u \cdot b_2 \tag{1.4}$$

This shows that the sign of the angle is not taken into account. The same applies for a flow with an incoming angle. In the example the sign of the force is negative, due a negative normal component and positive tangential and vertical components. Because the force generated by the vortex generator labeled 'B' in Figure 2.3, highlighted with the colour red, the forces for this generator will be multipled with -1 one.

The parameter V_m represents the numerical volume that represents the vortex generator. This must be known before the simulation is started, however the algorithm that identifies the cells that represent the vortex generator only runs during simulations. This means that an initial setup run for a couple of iterations is used to tune the setup and find the value for the numerical volume. A second parameter that may need to be tuned is the linearisation coefficient. This is used by the solver to ensure that any source term introduced does not cause the simulation to become unstable.

Lastly, there is the matter of the model constant C_{vg}. Bender et al.[1] identify two modes of operation for this constant, which they refer to as c. In this paper the behavior of the constant is plotted against the integrated cross flow kinetic energy κ as seen in Figure 1.2. The first mode happens for values of C_{vg} smaller than one and varies linearly with κ as shown by Figure 1.2. For values of C_{vg} larger than 5 the constant is in the asymptotic mode, where as Bender et al.[1] state:

> "(the) model source terms starts to dominate the other terms in the discrete finite volume equations.When this happens the flow tends to align itself with the orientation of the vortex generator, such that the local angle of attack approaches zero, i.e. $U \cdot \hat{n} \approx 0$, thus allowing the discrete momentum equations to maintain equilibrium."

In the evaluation of the BAY-model of Dudek[5] and Jirasek[6] this constant is set to ten to ensure that it is in this asymptotic mode. It is found that this is typically the best setup for the use of the BAY-model. Booker et al.[14] note that it is only the best setup if the volume of cells that represent the vortex generator is close to the physical volume of the vortex generator. Otherwise, the model constant is in the aforementioned linear region. Once a proper mesh has been established for a valid case a study with varying model constants will be done to verify that the implementation of the BAY-model acts as reported.

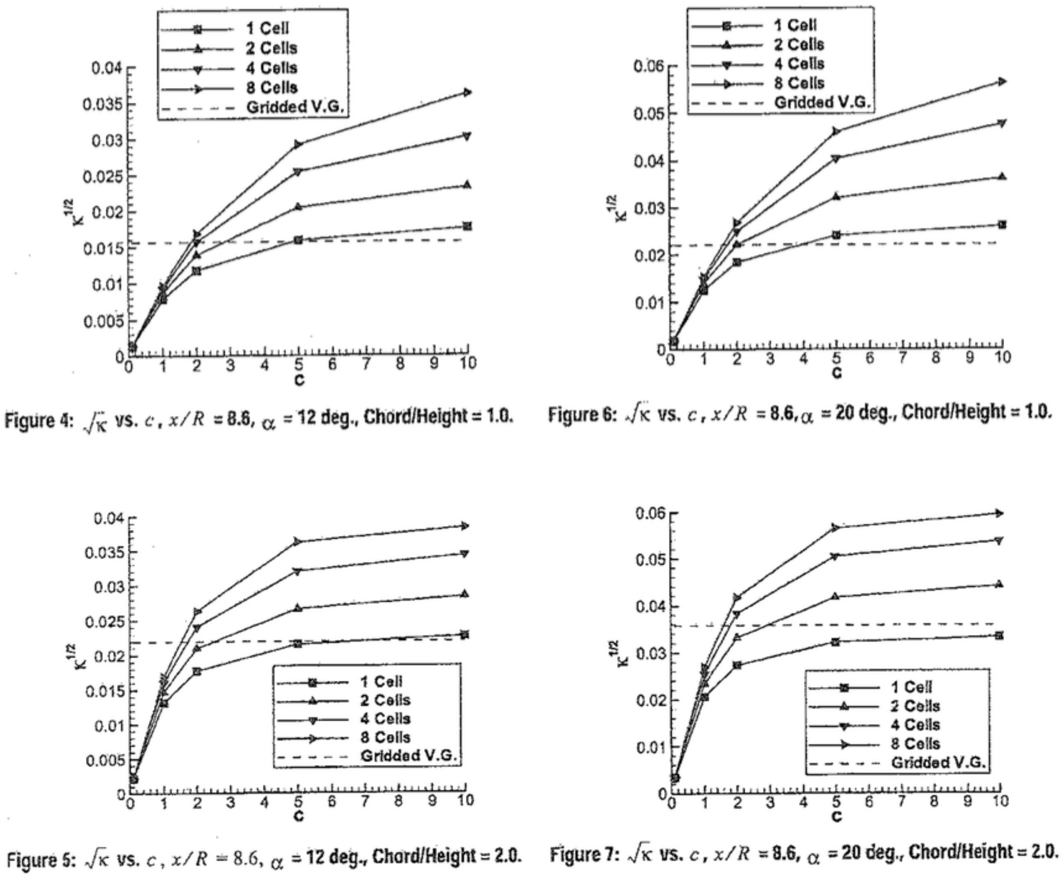

Figure 1.2: Behavior of integrated cross flow kinetic energy versus the BAY model constant C_{vg}[1]

The implementation of the BAY model is structured as follows

- Generation of input file
- Input handling
- Location flagging
- Source attribution

In the first step an input file is generated with the vortex generator coordinates and required inputs such as device angle and height. This data is read by CFX through a Junction Box Routine, enabling the data to be read by the solver. Locations are flagged 1 if they are inside the coordinates provided by the input data and 0 when they are not. The flag value is multiplied with equation(1.1) in the CFD solver, enabling it to model the effects of a vortex generator.

1.2 Input Data

The implementation of the code is designed to facilitate a large variety of vortex generator geometries and vortex generator arrays. This is done with a Matlab script which handles inputs such as the vortex generator height, length and angle. A file is generated with all the coordinates in the coordinate frame used by Ansys CFX. As shown by Figure 1.3 the Y and Z axis are swapped between Matlab and Ansys CFX. The generated file can be described as follows:

(a) Ansys CFX (b) Matlab

Figure 1.3: Default coordinate frame comparison

```
X coordinates Object A
Z coordinates Object A
X coordinates Object B
Z coordinates Object B
Device angle, Device height, Minimal Y value, Z location of mirror plane
```

Text 1: Input file generated by Matlab

1.3 Location Flagging Algorithm

One advantage of a body force model is the ability to interpolate onto an existing fluid domain. Instead of creating the solid object in the fluid domain, the body forces are interpolated onto the fluid domain. This requires a function that can determine whether or not a node is inside the object or not.

This can be accomplished with a conditional statements illustrated by the following pseudo code for a one dimensional situation:

if $X > minimum\ boundary\ and\ X < maximum\ boundary$ **then**
  source = 1;
else
  source = 0;
end

Algorithm 1: If condition to check whether input X is inside boundaries in one dimension

In this algorithm X represents the location on the X axis of a node element. The minimal and maximum boundary represent the respective minimum and maximum values along the X axis of an object. This algorithm can be expanded to three dimensions but it does require some additional statements. If the previous algorithm is simply expanded with two additional similar statements for Y and Z then the algorithm can only handle cubes and rectangles. However, it would also need to represent triangles as they are commonly used as vortex generators. Additionally, vortex generators are typically at an angle with the flow. As illustrated by Figure 1.4 this causes an issue if the algorithm is applied as proposed so far. Because a minimum and maximum boundary value can only describe a rectangle it will not be able to represent any object at an angle.

Two additional steps are incorporated in order to accommodate for geometries such as triangles and account for the device angle. The first is to rotate the coordinates on the XZ plane, this will prevent the issue shown in Figure 1.4. Secondly, in order to describe an object such as a triangle the boundary values for the XY plane will be described by a polynomial. For the triangle this can be done with the following equation:

$$\begin{aligned} Y &= a * X + b \\ a &= \frac{max(Y_{obj}) - min(Y_{obj})}{max(X_{obj}) - min(X_{obj})} \\ b &= min(Y_{obj}) - a * min(X_{obj}) \end{aligned} \tag{1.5}$$

Adding these two components to the previous pseudo code leads to the following:
The rotation matrix for this script is defined as follows:

$$\begin{bmatrix} \cos(\beta) & \sin(\beta) \\ -\sin(\beta) & \cos(\beta) \end{bmatrix}$$

This matrix will rotate any $[X, Y]$ coordinate in clock wise direction with input β. If a vortex generator has a streamwise angle of five degrees than β will be negative five. This will make the horizontal and vertical edges of the vortex generator parallel with the coordinate frame axis, thus preventing the issue from Figure 1.4.

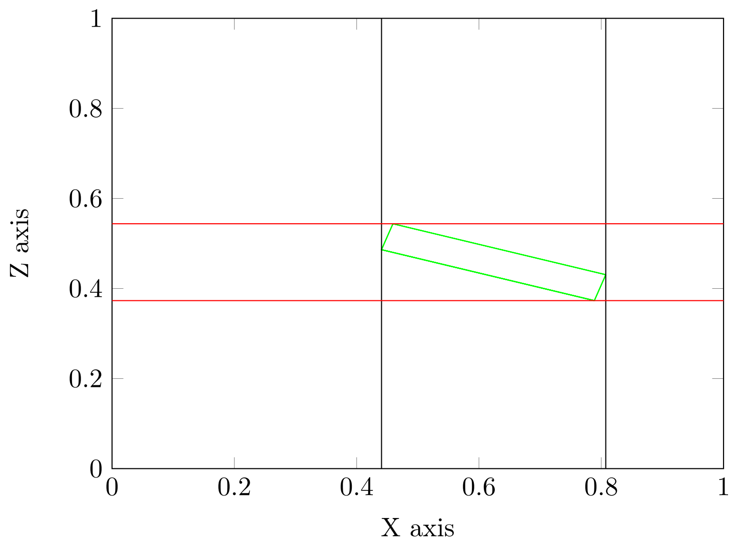

Figure 1.4: Illustration of the problem with rotated objects defined by maximum and minimum boundary values

input : Location(X,Y,Z), Object Coordinates
output: Source

set source to zero to initialise the values;
rotate both location and object with a rotation matrix and device angle;
compute polynomial coefficients;
evaluate Object Coordinates with max() and min() functions to setup boundary values;
if *X > minimum boundary X and X < maximum boundary and Z > minimum boundary and Z < maximum boundary* **then**
  compute maximum boundary Y at X with polynomial coefficients;
  if *Y > minimum boundary Y and Y < computed maximum boundary Y* **then**
    source = 1.0;
  end
else
  source = 0.0;
end

Algorithm 2: Pseudo code that checks whether X,Y,Z is inside the boundaries of an object in three dimensions

With these additions a single vortex generator can be replicated for any input angle and shape, as long as the shape on the XZ plane conforms to a rectangle or cube. When another conditional statement is added the code will also be able to replicate a vortex generator pair. This pseudo code splits the XZ plane at the mirror line between the two vortex generators. After which the points above the line will be evaluated for the vortex generator above the mirror line and vice versa. Because the body force of the vortex generator below the mirror line will have a force in the opposite direction of the Z axis the source value will be negative instead of positive. To illustrate this a mesh is made with an object inside and shown in Figure 1.5. The algorithm is applied to Matlab and has highlighted all the nodes it has found to be inside the object with black.

```
input  : Location(X,Y,Z), Object Coordinates
output: Source
set source to zero to initialise the values;
rotate both object A and B with a rotation matrix and their device angle;
compute polynomial coefficients;
evaluate Object Coordinates with max() and min() functions to setup boundary values;
if Z > mirror line Z coordinate then
    rotate location with A rotation matrix;
    if X > minimum boundary of A and X < maximum boundary and Z > minimum boundary and Z <
    maximum boundary then
        compute maximum boundary Y at X with polynomial coefficients;
        if Y > minimum boundary Y and Y < computed maximum boundary Y then
            source = 1.0;
        end
    end
else
    rotate location with B rotation matrix;
    if X > minimum boundary of A and X < maximum boundary and Z > minimum boundary and Z <
    maximum boundary then
        compute maximum boundary Y at X with polynomial coefficients;
        if Y > minimum boundary Y and Y < computed maximum boundary Y then
            source = -1.0;
        end
    end
end
```

Algorithm 3: Pseudo code that checks whether or not a point is either of two vortex generator vanes

The implementation in CFX is handled by Fortran code. The CFX manual contains an example of a Fortran routine with the purpose of applying momentum forces to a specific region in a two dimensional mesh. Therefore the implementation of the code will use this example as a guideline. The routine will require an additional program to function because of the user input data file. The user routine cannot simply read from a data file due to the way CFX manages its memory. It requires the use of a junction box routine which makes the user input data file available in the memory management system of CFX. This routine is provided by CFX and only requires minimal adaptation in the user subroutine.

Alternatives to the proposed method have been researched briefly. In mathematics and computational science this problem is known as the point in a polygon problem. Hormann and Agathos have written a review of techniques used to solve this problem and have highlighted two main methods to do so. They discuss the even-odd rule and the winding number algorithm. These methods are more robust than the proposed algorithm because they do not have a limitation on the shape of the object. However, their implementation is more complicated and could require additional computational time. Especially because their implementation in a three dimensional setup might not be trivial. However, the proposed algorithm is capable of describing a wide range of vortex generators and is very simple. For the purpose of this project it seems to be the most qualified algorithm.

Geometrical Shape Differentiation

Part of the research into the modeling capabilities of the BAY model is the extent of which it can replicate different shapes of vortex generators. In the discussion on the implementation of the model a method was shown that of handling shapes which have a rectangle shape on the XZ plane. The shape on the YX plane must be described by a first order polynomial. This means that it can handle both triangles and rectangles. However, the experiments conducted by Velte et al.[83] also include a cambered rectangle. This means that the

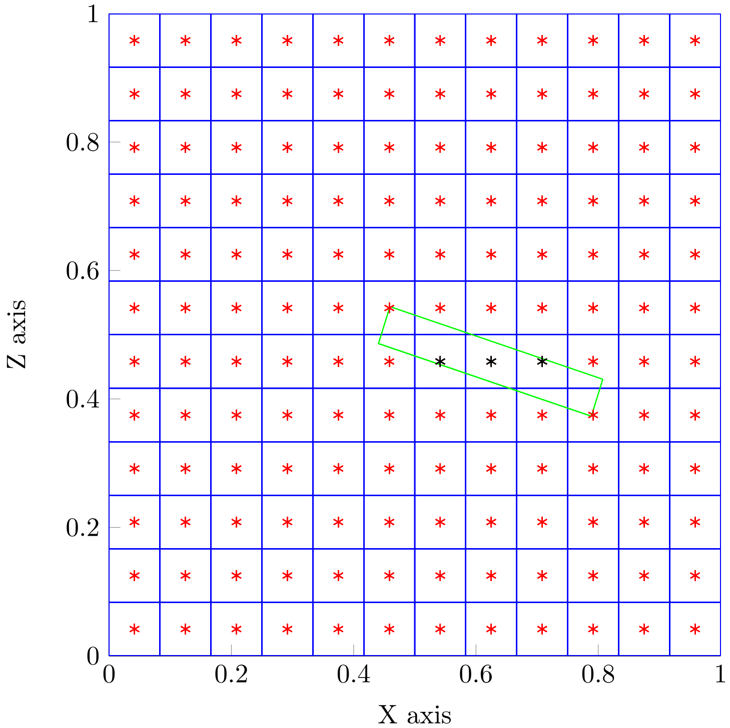

Figure 1.5: A 2-D demonstration of the boundary checking algorithm as implemented in Matlab

code has to be slightly adapted with respect to geometry and force allocation. The latter concerns the vector that is used to direct the force inhibited by the vortex generator. So far, this has only required a single vector due to a geometries being described by a singular plane, such a rectangle. However, for a cambered rectangle this is no longer the case and the normal vector would change along the length of the vortex generator. An assumption will be made here that considering the cambered rectangle is symmetric the average normal vector is similar to that of a normal rectangle. Obviously, this is quite a gross assumption but anything less would require significant adaptation of the current implementation of the BAY model. Since the cambered rectangle is not widely used in industry or research, with respect to vortex generators, it should not drive the structure of the code. It is better to optimise it for the more simpler common geometries such as the triangle and rectangle vortex generator. Nonetheless, it would worthwhile to investigate whether or not this assumption will enable the representation of such a shape.

This leaves the geometrical representation of the the vortex generator. Similar to the current implementation, the interrogated point location and the vortex generator coordinates are rotated. In addition, they are also translated and only the absolute values are considered. This reduces the cambered rectangle to a curved rectangle in a quadrant, as shown by Figure 1.6. This is possible because the camber is defined by a radius of curvature and a device length, in other words merely a section of a circle. In Figure 1.7 the result of the object allocation algorithm is visualised. It is clearly visible that the algorithm is capable of representing these three different shapes.

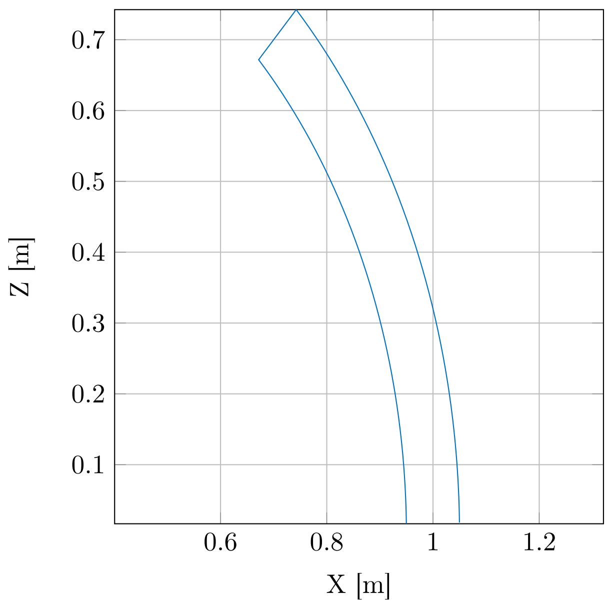

Figure 1.6: Example of cambered rectangle vortex generator object domain

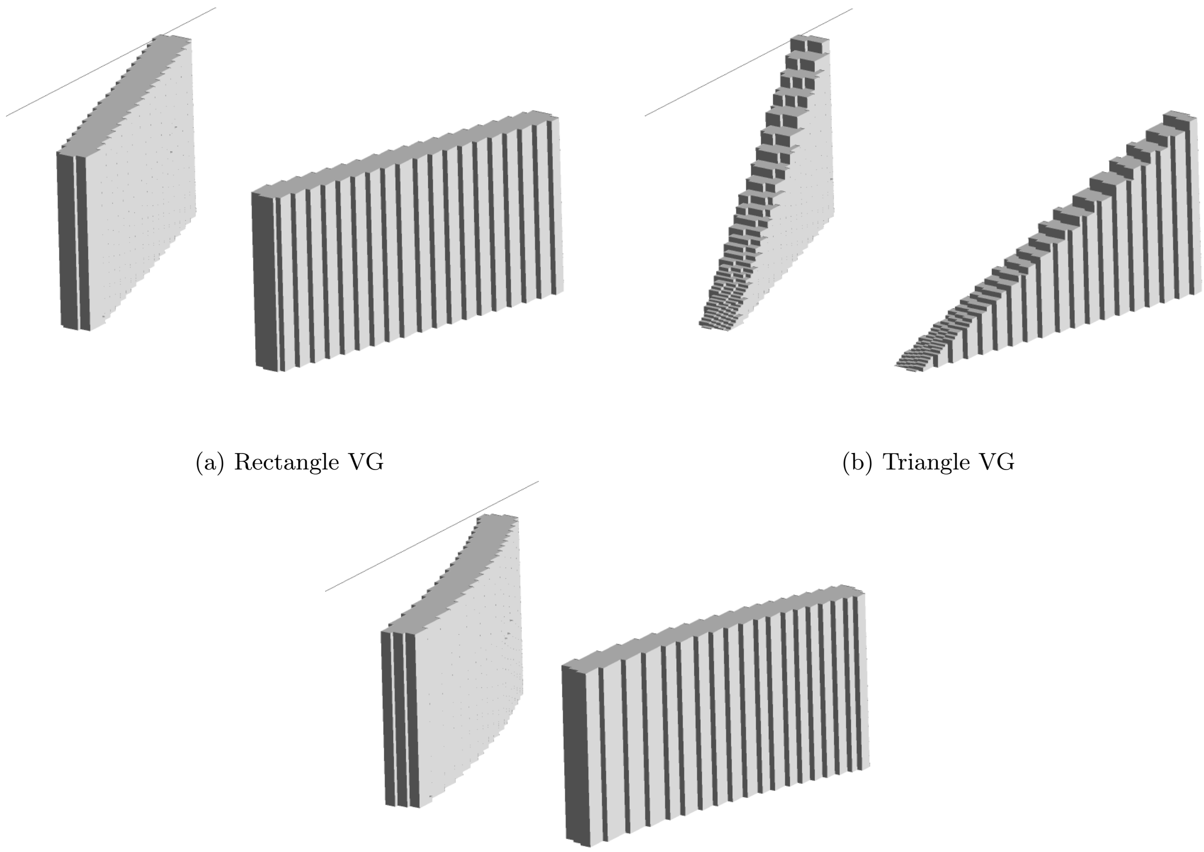

(a) Rectangle VG

(b) Triangle VG

(c) Camber VG

Figure 1.7: A visualisation of the vortex generators as created by the BAY-model algorithm and implemented in Ansys CFX 15

1.4 Validation

A simple case will be used to validate that the implementation is done correctly and that it can be used to attribute source momentum. This case will mimic flow through a wind tunnel. Only a section will be modeled, applying symmetry to the right, left and top faces. Because the main focus is to validate the algorithm and not the physical model, the mesh quality and flow characteristics will be neglected unless they appear to affect the implementation.

The CFX manual recommends the use of Rhie-Chow distribution and corresponding coefficient of the source momentum to ensure stability and convergence of the solver. The Rhie-Chow redistribution according to the Ansys manual prevents "velocity wiggles" when the body force is discontinuous. Furthermore, there is also a linearisation coefficient but this is only applicable when the source terms are related to flow velocity. This will be of interest later when the BAY model is applied.

The inlet condition is a 4 m/s flow normal to the plane and at the outlet the static pressure is 0 Pa. For turbulence modeling the Shear Stress Transport model is chosen and the transition model is set to fully turbulent. The converge criteria were kept default for a root mean square error of $1E-4$. The introduction of the body force did not introduce instabilities to the computation or did it significantly increase the amount of iterations required for convergence.

Some results are presented to show that the implementation has been done successfully. In Figure 1.8a the the body force applied to the mesh is shown. The vortex generator geometry is highlighted with lines. As the figure shows, the force is not distributed in the boolean method applied by the algorithm. This is due to the Rhie-Chow distribution of the body force. This leads to the force to extend past the vortex geometry.

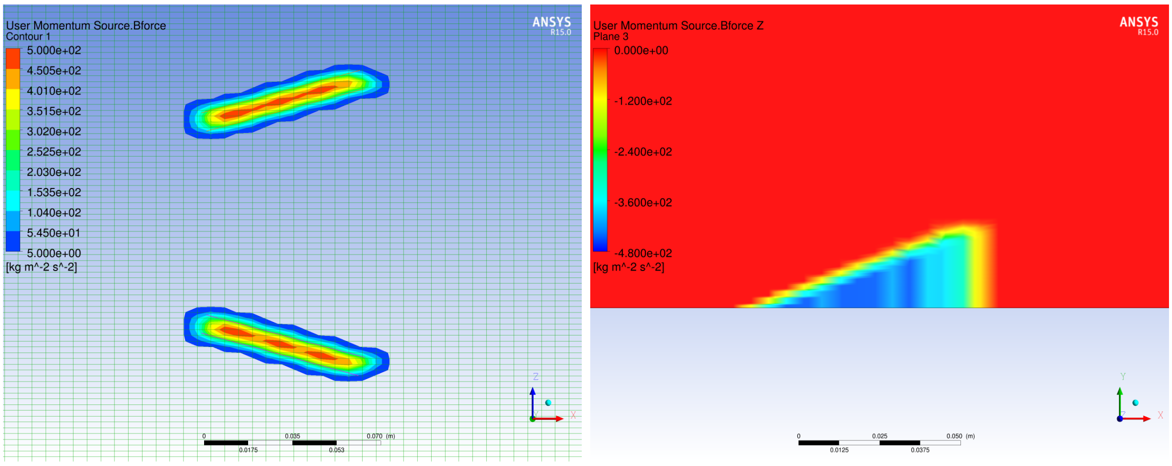

(a) Mesh overlay on top down view on XZ plane with VG coordinates and body force

(b) Body force Z component slice through vortex generator

Figure 1.8: Implementation of constant body force

1.4.1 BAY Model Constant C_{vg}

The first validation step is to compare the behaviour of the BAY algorithm in CFX to the original paper published by Bender et. al[1]. Among other things, the influence of the model constant C_{vg} is discussed and shown to exhibit asymptotic behavior past a certain value. This is shown in Figure 1.2. A variation of the model constant values has been implemented in CFX and is shown in Figure 1.9. In this simulation the triangle geometry has been used with a vortex generator thickness definition of 10 mm. This leads to a numerical vortex generator volume of $4.78 \times 1e^{-5}$ compared to the physical volume of $7.20 \times 1e^{-6}$.

Figure 1.2 shows, atleast in this case, the implemented model behaves as discussed by Bender et al.[1]. Futhermore, it also confirms that choosing to set $C_{vg} = 10$ is a valid decision in terms of accuracy. What is not discussed explicitly in Bender et al [1] is that increasing the C_{vg} might improve accuracy it does come at a computational cost. The difference in computational time between $C_{vg} = 1$ and $C_{vg} = 15$ is a factor of four.

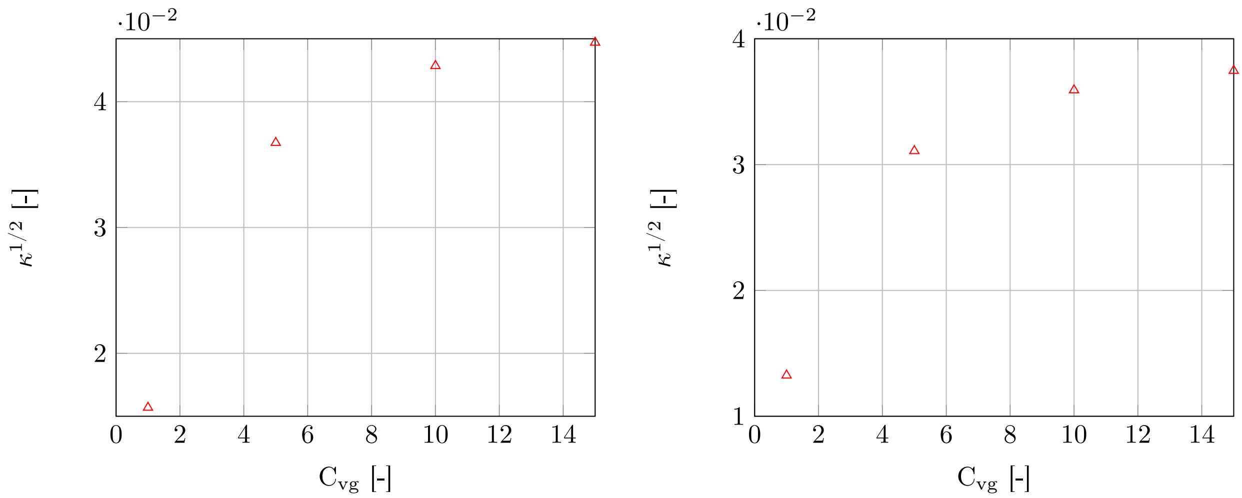

(a) Downstream position from VG $x/h = 3$

(b) Downstream position from VG $x/h = 12$

Figure 1.9: Variation of the BAY model constant C_{vg} at various downstream positions in a zero pressure gradient flow with a single counter rotating vortex generator pair

Chapter 2

Zero Pressure Gradient In A Turbulent Boundary Layer Wind Tunnel

In this Chapter the BAY model implementation will be compared to experimental results from a measurement campaign of turbulent flow in a wind tunnel, with a tripped boundary layer at the inlet. It also featured three different shapes of vortex generators and has PIV data from multiple planes downstream. The data will also be used to evaluate the influence of various CFD setup parameters on the accuracy of the generated flow.

2.1 Experimental Description

The experimental campaign that will be used to evaluate the BAY model has been conducted in the Turbulent Boundary Layer wind tunnel in Lille, France, shown in Figure 2.1. It can handle inlet velocities up to 10 ms^{-1} leading to a momentum thickness Reynolds number of 28000. Though the experiment conducted in this tunnel is referred to as a zero pressure gradient case, there is an actual negligible pressure gradient. The term zero pressure gradient is used to conform with standards found in published papers. A description of the vortex generator geometry can be seen in Figure 2.2. The device height is $h = 60[mm]$ and the length is $2h$. In the paper by Velte et al.[83] a flow is analysed at a Reynolds number of 17000 based on the momentum thickness. This can be calculated with the following equation:

$$Re_\theta = \frac{U\theta}{\nu} \tag{2.1}$$

In which U is the external velocity, generally taken as the free stream velocity and u the local velocity. The momentum thickness, θ, is based on equation (2.16). For the Reynolds number the kinematic viscosity, ν, is also used. Furthermore, Velte et al.[83] measure at planes 3h, 12h, 25h, and 40h away from the vortex generators. Several vortex generator pairs were spread spanwise across the wind tunnel test section to create a cascade of vortices, generating a periodic flow in the spanwise direction. It also helps to avoid effects of the wall in the measurement area. The results were obtained with a stereo PIV setup as described in Velte et al.[83].

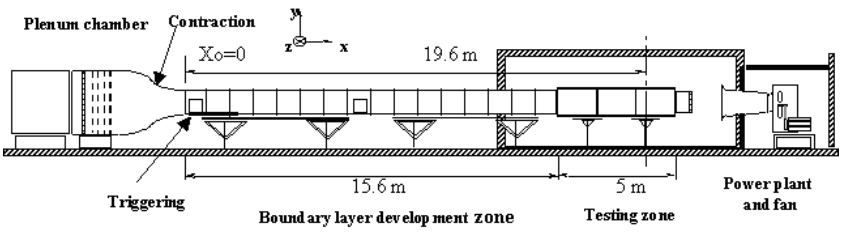

Figure 2.1: General dimensions of the turbulent boundary layer wind tunnel in Lille, France

2.2 Mesh Strategy

Modeling the vortex generator means that the complexity of the mesh is reduced, due to the lack of resolving vortex generator geometry. For the current case, flow with a zero pressure gradient in a wind tunnel, that means the mesh can a very straight forward hexagonal mesh. However, the combination of the dimensions of the wind tunnel and the flow conditions can result in a large mesh, especially if the first cell height conforms to $y+ \leq 1$.

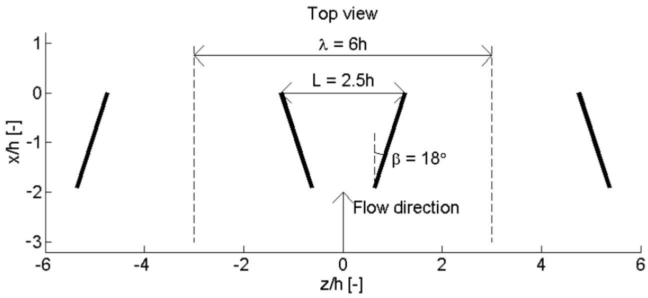

Figure 2.2: Vortex generator geometry and location for the zero pressure gradient experiment campaign as described in Velte et al.[83]

Table 2.1: List of boundary conditions for fluid domain of the zero pressure gradient case

Location	Boundary Condition
Inlet	Opening with Prescribed Streamwise Velocity Profile & Turbulence Intensity
Outlet	Averaged Pressure Over Outlet with Relative Pressure at 0 Pa
Floor	No Slip Wall
Sides	Symmetry
Top	Symmetry

Therefore, it is decided to split the fluid domain with the use of symmetry, making it possible to implement local refinement. Additionally, the domain is split in multiple bodies, allowing local refinement in the wake and the area of the vortex generator. It also enables the possibilities to limit the implementation of the BAY model to a body smaller than entire fluid domain, reducing its effect on the computational time.

In order to capture all the necessary information to compare to these measurement planes the mesh needs to be sized accordingly. In Figure 2.3 the chosen dimensions are shown and Figure 2.4 shows the final results for the medium mesh. The streamwise length is set at 3.5 meters, giving 0.5 meters for the inlet flow to settle whilst covering the 2.4 meters after the vortex generator for the measurement planes. An additional 0.5 meter is added in order to prevent the outlet influencing the measurement plane significantly, the remaining 0.1 meter covers the vortex generator. The width of the domain is according to the size shown in Figure 2.2, 0.36 meter. The height is based on the wind tunnel dimensions, 1 meter, and the symmetry condition applied to the top boundary. The mesh represents a quarter section of the test section.

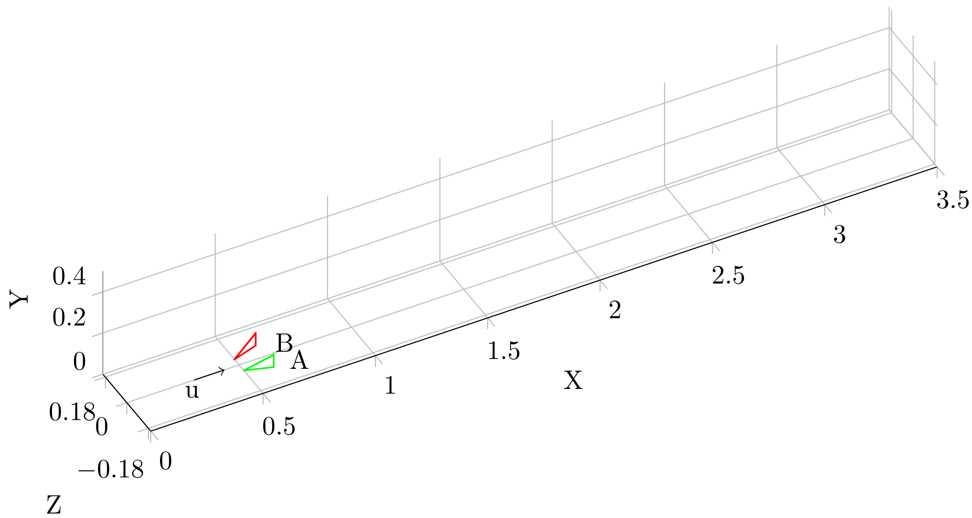

Figure 2.3: Dimensions of the fluid domain for the zero pressure gradient case

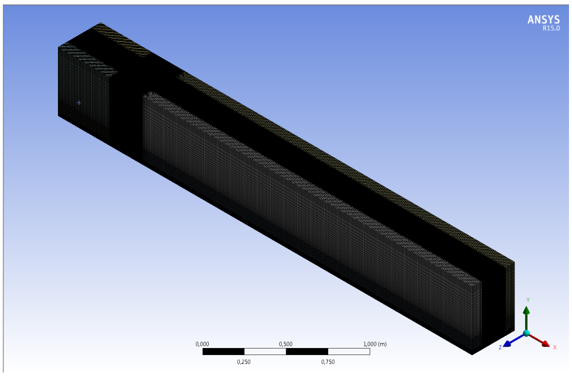

(a) Isometric view

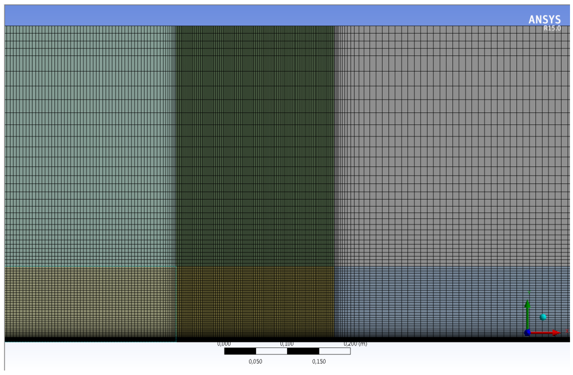

(b) Side view

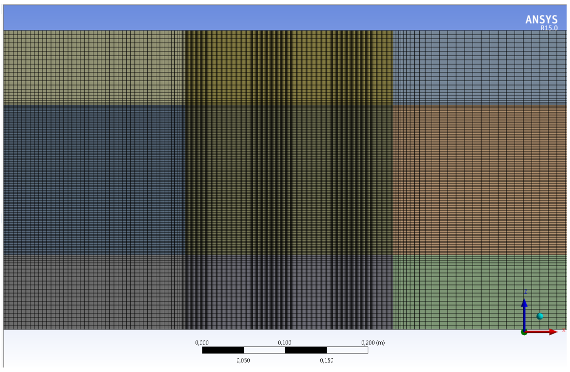

(c) Top view

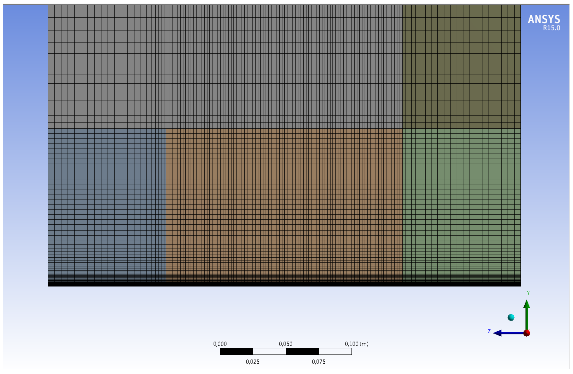

(d) Front view

Figure 2.4: Medium mesh with local refinement bodies

2.2.1 Grid Independence Study

In order to perform a grid independence study a rough and fine mesh were made based on the initial mesh that was created with this strategy. Their respective sizing and a few key criteria can be found in Table 2.2.

For validation efforts it is important to know the influence of the mesh on the results, thus a grid independence study has been conducted. This involved calculating the flow over the three meshes described in the previous section. In order to compare them they were resolved for the same convergence criteria. These were determined by observing the pressure drop over the flow domain, the difference between the inlet and outlet pressure. It was observed that this value had converged for a root mean square (RMS) error of 1e-6 with minimal imbalances in the solution, this can be seen in Figure 2.5. Furthermore, for all three meshes it was observed that the $y+$ value for the first cells was below one. The solutions are shown in Table 2.3. In Table 2.4 the values for the Richardson's Extrapolation for the three meshes are presented according to the theory laid out in Section 4.2.1.

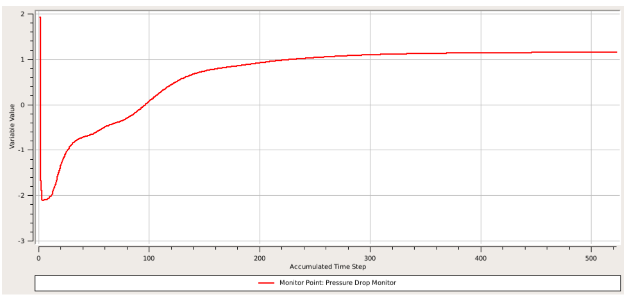

(a) Pressure drop over the inlet and outlet

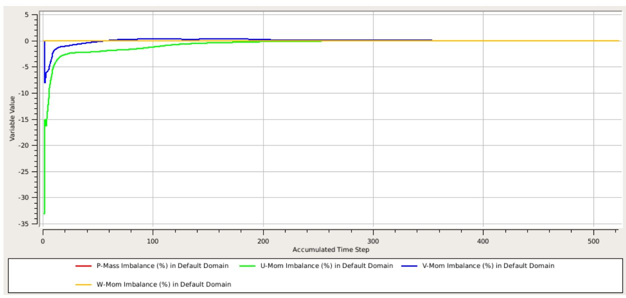

(b) Imbalances of the fluid domain

Figure 2.5: Convergence behavior for simulating the BAY model in a zero pressure gradient flow in Ansys CFX

For this case a $GCI12_{fine} = 2.4\%$ and a $GCI23_{fine} = 1.5\%$ was found. The ratio from equation (4.10) was found to be within 35 % which means that the solution is not entirely in the asymptotic range. Considering this fact, the medium mesh would be best for validation in terms of speed and accuracy. The solutions obtained from this mesh should be within 1.5 % with a 97 % confidence level, due to the safety factor. Furthermore, the observed order of accuracy $\hat{p} = 0.61$, which is considerably lower than the formal order of two.

The discrepancies between the observed order of accuracy and as consequence the GCI can probably be

Table 2.2: Size table for grid independence study for the zero pressure gradient case

	Rough Mesh	Medium Mesh	Fine Mesh
First cell height [m]	4.25e-5	2.5e-5	2e-5
Boundary layer growth rate [-]	1.1	1.1	1.1
Inflation layers [-]	52	55	58
Global growth rate [-]	1.2	1.2	1.2
Streamwise wake [m]	1.75e-2	1e-2	5e-3
Streamwise vortex generator [m]	2.5e-3	1.5e-3	1.5e-3
Normal to stream wise vortex generator [m]	2.25e-3	2e-3	1.75e-3
Vertical vortex generator [m]	2.5e-1	9e-2	5e-2
Inlet streamwise [m]	1.25e-2	5e-3	2.5e-3
Vertical flow region [m]	2e-2	1.25e-2	1e-2
Amount of elements [-]	2.61e6	7.53e6	18.44e6
Maximum Determinant value	1.0	1.0	1.0
Maximum Aspect Ratio	420	453	335
Maximum Volume Change	1.35	2.1	1.64
Maximum Skewness	1.0	1.0	1.0
Orthogonality	6.7	0.028	1.99

Table 2.3: Simulation results for grid independence study in the zero pressure gradient case

	Rough Mesh	Medium Mesh	Fine Mesh
Vortex generator numerical volume [m^3]	5.175e-5	4.774e-5	4.678e-5
Pressure drop Inlet – Outlet [Pa]	1.151	1.153	1.157
Reynolds Momentum Thickness [-]	16990	16990	17040
Iterations to convergence [-]	523	489	465
CPU time [hours:minutes:secs / CPU cores]	00:40:06 / 64	3:05:30 / 32	03:54:21 /64

Table 2.4: Richardson's Extrapolation for a p=2 order solution scheme for the grid independence study in the zero pressure gradient case

	Rough to Medium mesh	Medium to Fine mesh
Refinement ratio	1.42	1.39
2nd order error coefficient g_p	-0.0060	-0.0044
Exact solution f_{exact}	1.1592	1.1611

explained by the mesh strategy and subsequent mesh refinement. Though the fine mesh is refined in some areas and is significantly larger than the medium mesh, it might actually not be as refined when it comes to the solution. This is difficult to check, considering the amount of refinements possible and the required time to simulate all the options. Therefore, it is assumed the results have converged and that those obtained from the medium mesh are within single digit error bounds, considering the fact that the solution for all three meshes is within a single percentage and that the grid independence study shows some measure of accuracy. For the next cases increased effort will be made to ensure that the refinement is more consistent.

2.3 Flow Without Vortex Generators

Assessing the difference in accuracy between the simulation results of the BAY model and the experiments cannot be done without first assessing how different the simulated flow without the vortex generator is from the unperturbed flow measured during the experiment campaign. Ideally this would be done by simulating the flow over the entire wind tunnel and capturing the boundary layer development. A preliminary attempt was made, as can be seen in Appendix, but it could not capture the boundary layer development successfully. This attempt was, however, severely constrained by both time and resources. Considering the fact that the wind tunnel itself is 20 meters long, the mesh setup for modeling the flow with vortex generators would consume a considerable amount of computational time. Therefore, the decision was made to use the velocity profile obtained from experiments as an inlet conditions, thereby ensuring that the boundary layer thickness would have the appropriate thickness.

A simulation with this setup was computed to check that the assigned velocity profile would not change considerably over the fluid domain, thus invalidating any comparison with experimental data. In Figure 2.6 these results can be seen. There is a slight speedup in the free-stream region and the flow near the wall is less steep than in the experimental data. This is probably due to the fact that RANS has problems modeling the turbulent kinetic energy accurately.

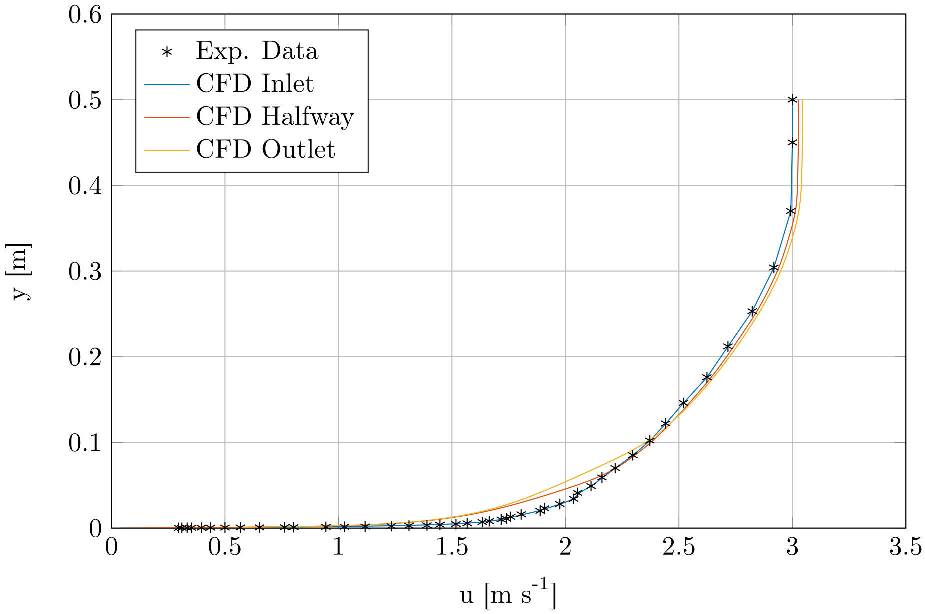

Figure 2.6: Development of streamwise velocity profile of CFD in the zero pressure gradient flow

2.4 Results

In this section the results obtained from CFD simulations will be compared to experimental data as described in Section 2.1. The results will show the influence of different vortex generator shapes, such as a triangular, rectangular, and a cambered rectangular vortex generator. Furthermore meshing strategies such as local adaptive refinement, tip refinement, and local coarsening of the mesh will be evaluated. Lastly, the influence of turbulence intensity and translational periodicity will be shown. Both the CFD and the experimental results shown have been post processed with the same scripts, based on the theory laid out in Section 2.1.

Table 2.5: Simulation results for different vortex generator shapes in a zero pressure gradient with a $Re_\theta = 17000$ at the inlet

	Rectangle	Triangle	Cambered
Pressure drop Inlet – Outlet [Pa]	1.332	1.153	1.364
Reynolds θ [-]	16990	16990	16990
Iterations to convergence [-]	676	488	724
CPU time [hh:mm / cores]	02:19 / 64	01:40 / 64	02:30 /64
Mesh elements [-]	7.53e6	7.53e6	7.53e6

2.4.1 Vortex Generator Shapes

Part of the research into the modeling capabilities of the BAY model is the extent of which it can replicate different shapes of vortex generators. As previously shown, in Section 1.3, the BAY model is capable of replicating at least three different geometries. Though, the camber geometry does not feature the variation of the vectors along its chord. Research by Velte et al.[83] features these three geometries in the Turbulent Boundary Layer Wind Tunnel. Those results will be used to validate the capability of the the BAY model to distinguish between different geometries.

Discussion of Results

In Figure 2.7 the streamwise development of the previously mentioned vortex parameters are shown, for both the experimental data and the CFD simulations. In terms of circulation, in Figure 2.7a, it can be seen that for all the data points that circulation remains constant, as expected, up until 30 device heights downstream. After which there is significant decay in the experimental data. This is due to the mentioned problems with contour definition and the fact that for the plane at 50 device heights some of the vortex seems to be outside of the PIV window. With that in mind, the values for the triangle vortex generator seem to agree quite well whereas there is some overestimation for the rectangular. This could potentially be due to the thickness of the rectangular vortex generator as defined in the BAY model implementation.

As far as peak vorticity, Figure 2.7b, goes all CFD simulations capture the trend quite well but do overpredict the values across all downstream positions slightly. For the core radius, core velocity and helical pitch, it should be reiterated that according to Velte et al.[31] this model is valid between 3 and 13 device heights, after which the non linear effects reduce the validity. Furthermore, it does not account for the presence of the wall. This means the model does not account for geometrical limitations and disturbances of the velocity. Nonetheless, the initial downstream positions for the vortex core radius and helical pitch, Figures 2.7c and 2.7e, match the slope of the experimental data. The rectangle slope of the helical pitch of the CFD simulation does seem to suggest a slower twisting vortex than the experimental data suggest. The core velocity at the first station is quite overpredicted by the rectangular and camber CFD simulations, nor does the slope match the trend shown by the experimental data.

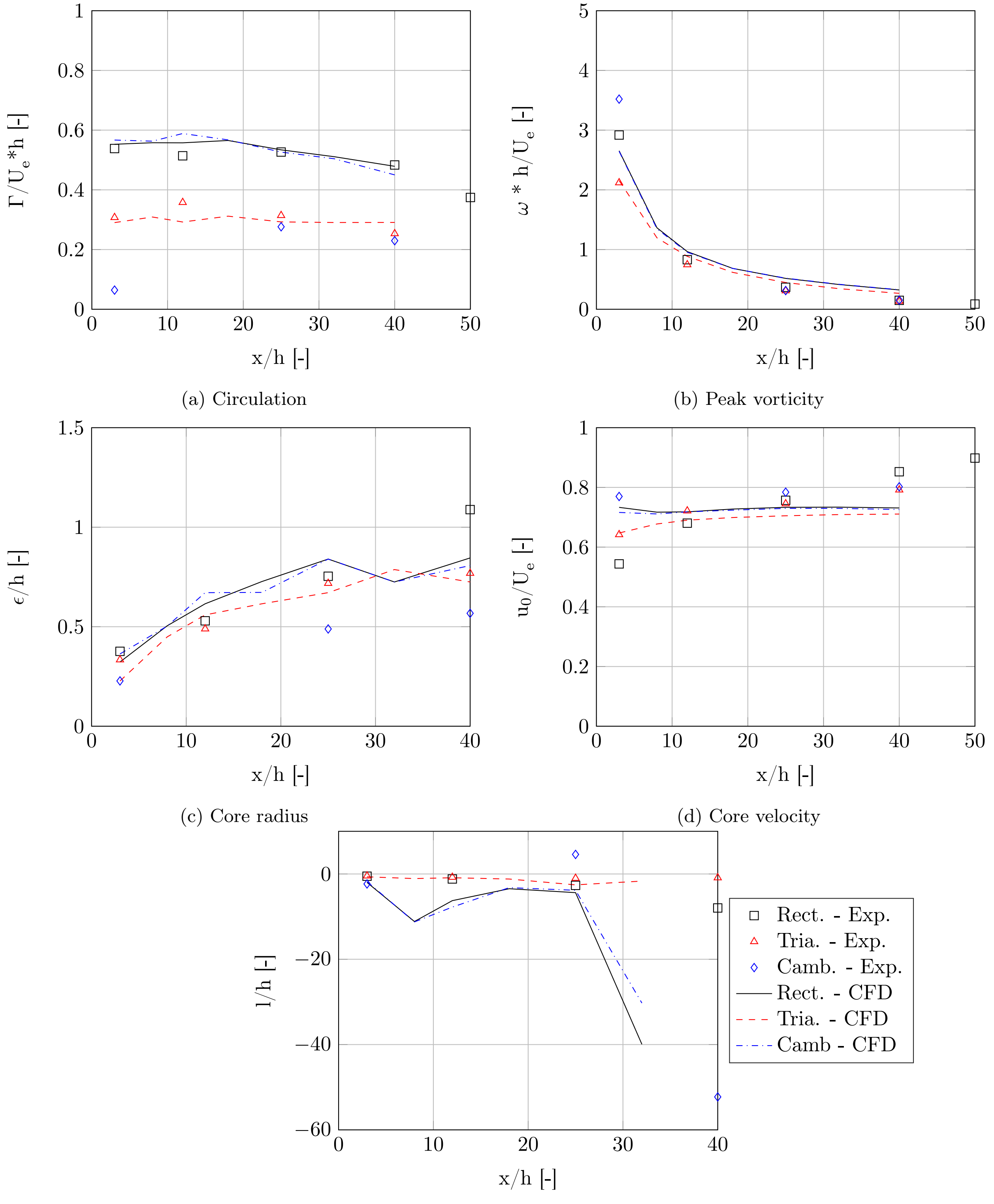

(a) Circulation

(b) Peak vorticity

(c) Core radius

(d) Core velocity

(e) Helical pitch

Figure 2.7: Streamwise development of various parameters for both triangle and rectangle vortex generator vanes, $Re_\theta = 16990$ at the inlet

2.4.2 Effects of Vortex Generator Thickness

One of the user inputs for the implementation is the thickness of vortex generator. This controls the volume, together with the vortex generator length and height, that will be used to flag mesh elements. As mentioned in previous reports, it is believed that there is no direct relationship between the definition of this volume and the actual thickness represented in the fluid domain. Therefore several thickness have been evaluated and will be compared to experimental data. Three cases have been run for a thickness of 10 mm, 7.5 mm, and 2.5 mm.

Table 2.6: Simulation results for different values for the BAY model vortex generator vane thickness in a zero pressure gradient with $Re_\theta = 16990$ at the inlet

	10 mm	7.5 mm	2.5 mm
Pressure drop Inlet – Outlet [Pa]	1.153	1.158	1.142
Reynolds θ [-]	16990	16990	16990
Iterations to convergence [-]	488	607	1128
CPU time [hh:mm / cores]	01:40 / 64	3:50 / 32	07:07 /32
Mesh elements [-]	7.53e6	7.53e6	7.53e6

Discussion of Results

Figure 2.8 shows the streamwise development for various thickness of the triangular vortex generator. Although there is some difference to be seen in the circulation, Figure 2.8a, this could be due to the numerical errors based on shifting the contour and the amount of the vortex that is covered. The thinnest vortex generator, with a thickness of 2.5 mm, does show some improvement with respect to vorticity, shown in Figure 2.8b, core velocity, Figure 2.8d, and helical pitch, Figure 2.8e, overall the three configurations seem to produce more or less the same results. Differences in the vortex core radius, shown in Figure 2.8c, can most likely be attributed due to the variation inherent in the post processing method. Especially given the fact that the other stations match almost exactly. Overall, the thinnest vortex generator seems to produce a weaker vortex as evidenced by the lower circulation, lower core velocity and lower peak vorticity. Though the differences could be considered negligible.

It is also important to note that, with respect to the use of the BAY model constant C_{vg}, the fact that a thickness definition of $10\,mm$, which leads to a numerical vortex generator volume seven times as big as the physical vortex generator, does not significantly impact the accuracy. The thinnest definition here, which is 1.5 times as big with respect to the volume, is not significantly more accurate.

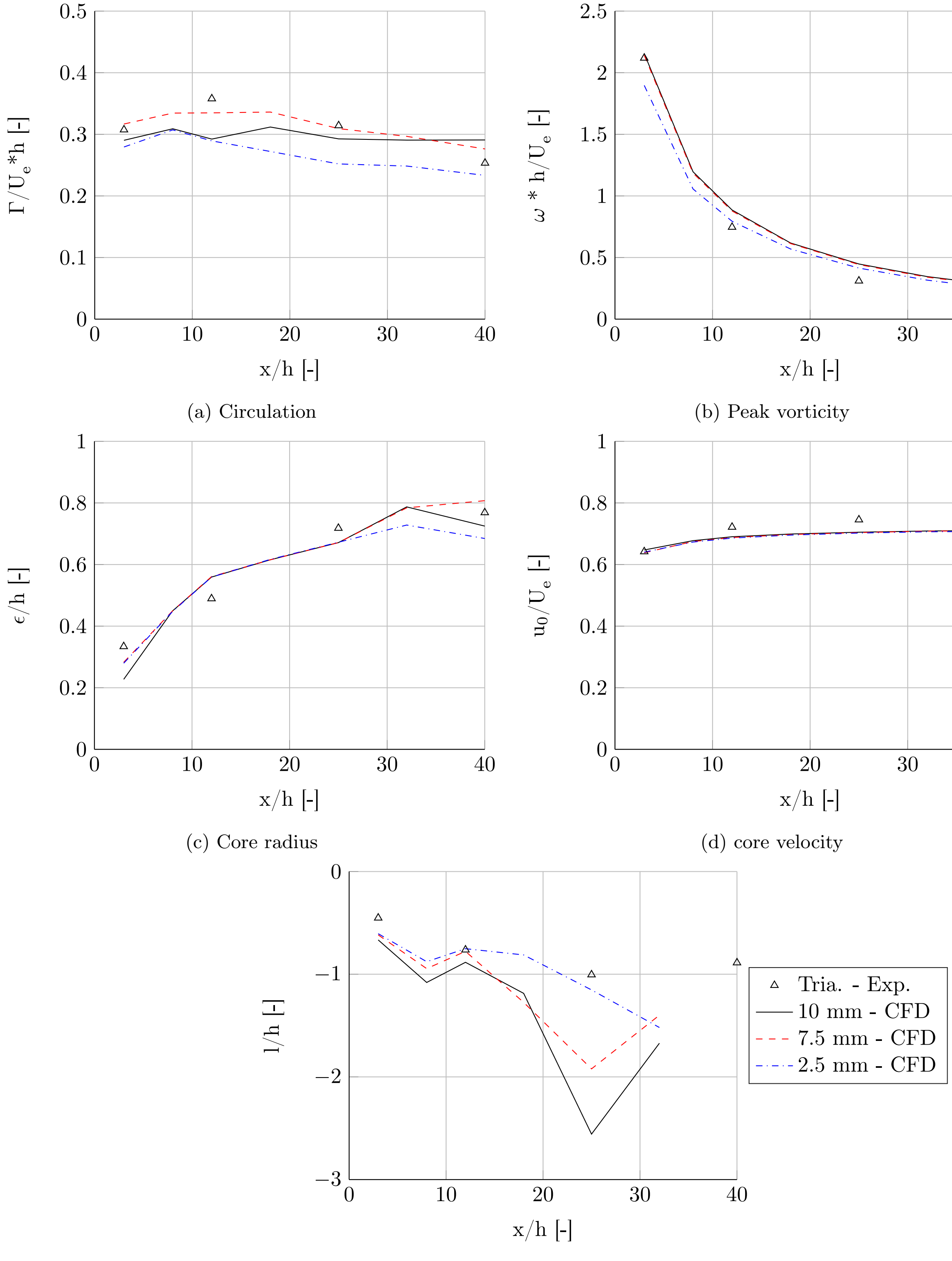

(a) Circulation

(b) Peak vorticity

(c) Core radius

(d) core velocity

(e) Helical pitch

Figure 2.8: Streamwise development of various parameters for different values for the BAY model vortex generator vane thickness in a zero pressure gradient with $Re_\theta = 16990$ at the inlet

2.4.3 Influence of Different Mesh Strategies

In this section some methods that can be applied to meshing a fluid domain are examined and their influence on the accuracy of the results is discussed. This is not exhaustive study of all mesh strategies that could be applied in conjunction with the BAY model. Some have been tried previously, such as a body fitted mesh by Florentie et al.[57]. However, this did not show a significant improvement in the results shown by Florentie et al.[57].

Table 2.7: Simulation results for various meshing strategies for the BAY model in a zero pressure gradient case with $Re_\theta = 16990$ at the inlet

	Base	R = 1.1	R = 1.2	Tip Ref.	Coarse = 2	Coarse = 4
Pressure drop Inlet – Outlet [Pa]	1.153	1.159	1.160	1.155	1.139	1.142
Reynolds θ[-]	16990	16990	16990	17000	17010	17010
Iterations to convergence [-]	488	583	588	642	407	304
CPU time [hh:mm / cores]	01:40 / 64	01:57 / 64	01:56 /64	05:51 /64	00:43 /64	00:20 /64
Mesh elements [-]	7.53e6	9.43e6	11.11e6	19.39e6	3.84e6	2.47e6

Adaptive Meshing

The first case employs a method that locally refines the mesh based on certain parameters. In CFX this is done based on "h-refining", hierarchical refinement, which splits each node that fits the refinement criteria. This refinement criterion can be any flow parameter and will be evaluated based on its gradient. For this study the flag variable, used to determine whether or not a point is inside the vortex generator, is used. This does mean that the vortex generator will be refined on its "surfaces" and not its core.

The local refinement typically done in stages, specified by the user. To investigate the effect on accuracy of this method two adaptive strategies have been employed. The first uses a refinement ratio of 1.1 and the second case refines with a ratio of 1.2. The convergence criteria for the local refinement method is setup in such a way that the errors introduced by interpolating to the new nodes are reduced in order to prevent a blow up of errors.

Discussion of Results

Overall, as shown by Figure 2.10, the effect of locally refining the mesh at the vortex generator does not seem to have any significant effect on the accuracy of the results. The peak voriticty and core velocity, Figures 2.10b and 2.10d, show minimal differentiation and only at the initial and final measurement position. Once again, the more substantial differences in circulation, Figure 2.10a, could be explained by the method by which it is obtained. However, it is curious to see that this offset is more or less the same for both refined meshes, which may suggest that the circulation has in fact increased slightly.

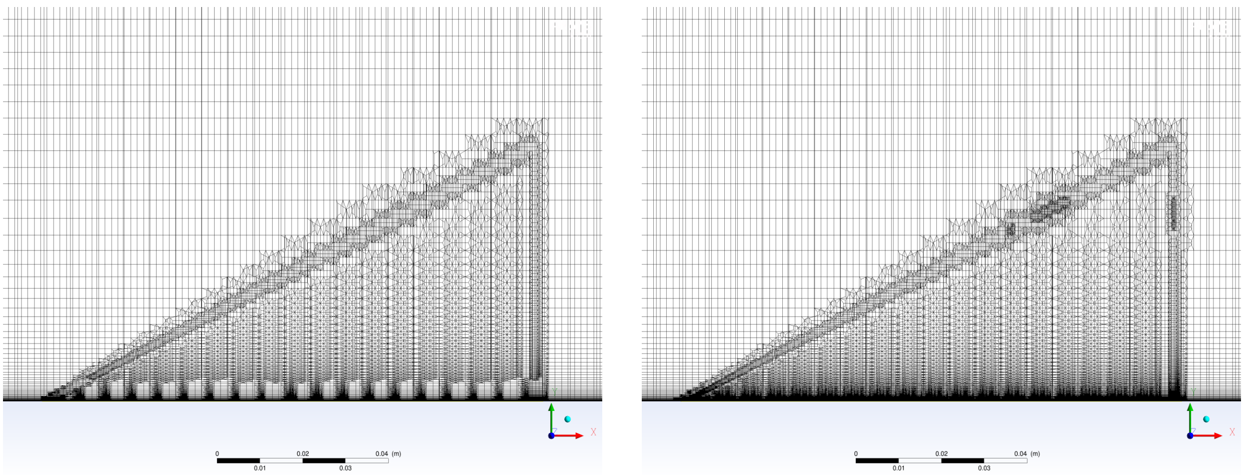

(a) Refinement factor 1.1

(b) Refinement factor 1.2

Figure 2.9: Adapted Mesh After Local Refinement Based On Vortex Generator Location

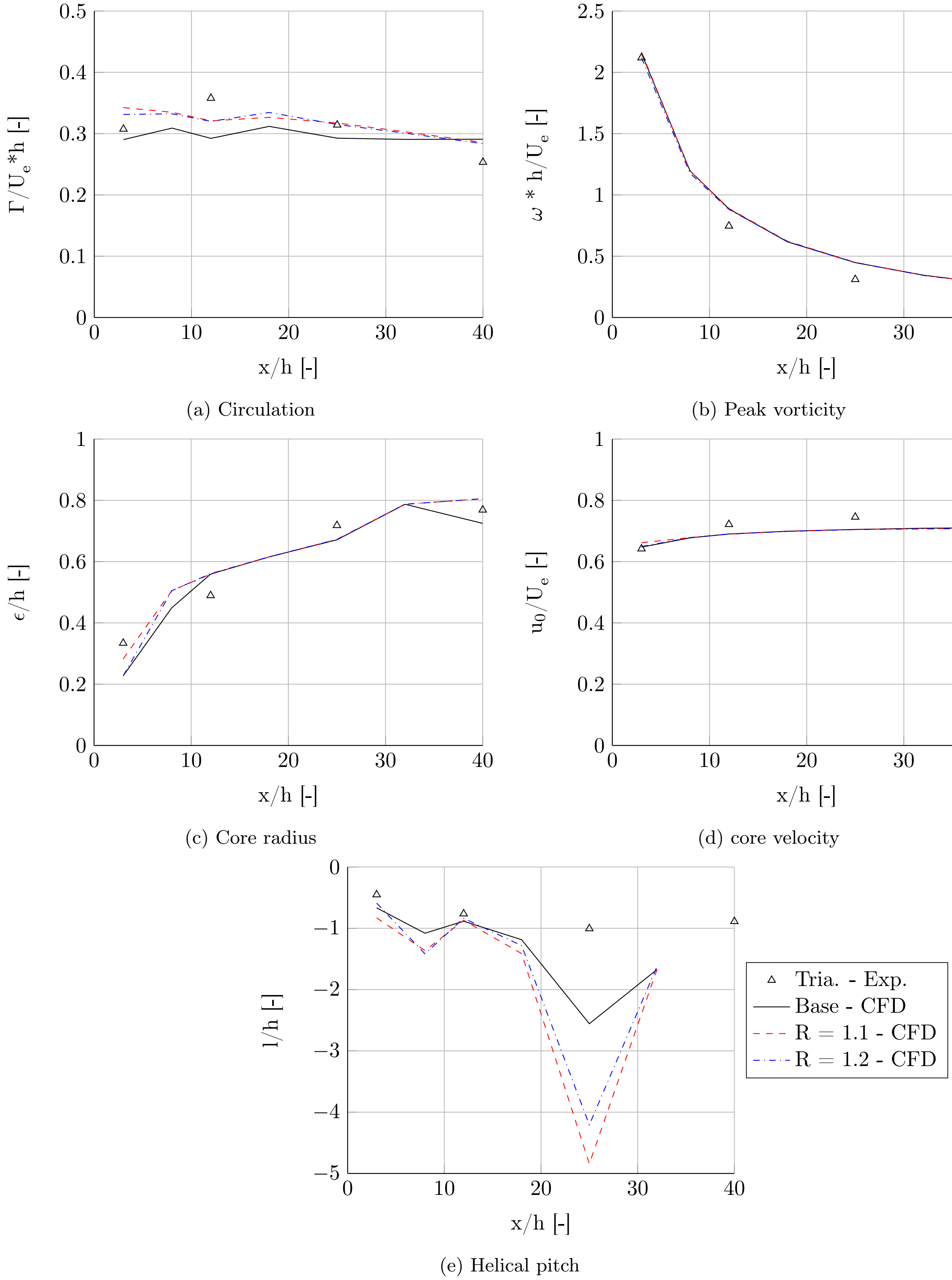

Figure 2.10: Streamwise development of various parameters for locally refined meshes, based on the presence of the vortex generator vane, with refinement factors R = [1, 1.1, 1.2], $Re_\theta = 16990$ at the inlet

Tip Refinement & Translational Periodicity

One mesh strategy is to refine the mesh along the horizontal axis at the height of tip of the vortex generator. This was proposed by Dudek[5] and showed considerable improvement in the peak vorticity compared to experimental results, however it did not improve the rate of decay. An attempt was made to refine the base mesh in a similar method as described by Dudek[5]. The result can be seen in Figure 2.11. The mesh size grows with a rate of 1.1 from a vertical size of 0.1 mm at the tip height of the vortex generator. The remaining dimensions have been kept the same as much as possible. The size of the mesh can be found in Table 2.7.

Further more the validity of the symmetry boundary conditions are tested by modeling the base flow with translational periodicity instead. This allows the motion of flow through one side into the other. This could potentially influence the movement of the vortex as it travels downstream.

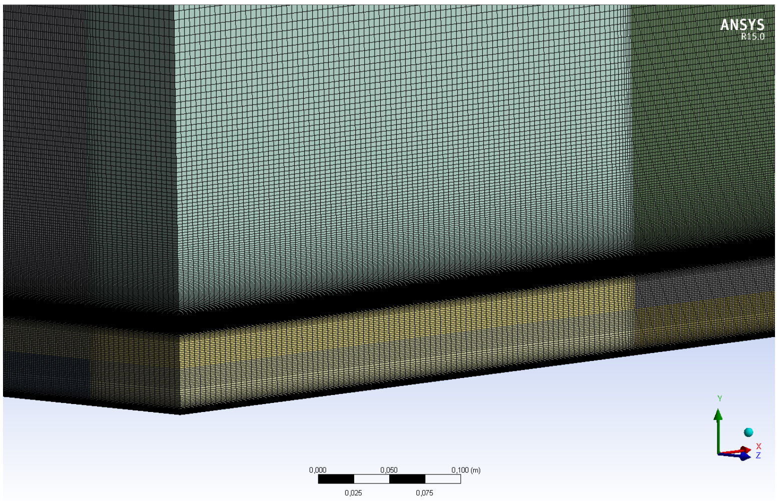

Figure 2.11: Screenshot of the mesh with tip refinement along the streamwise axis

Discussion of Results

Figure 2.12 shows that the tip refinement does not significantly improve the results obtained by the base settings. A slight increase in peak vorticity at the initial downstream can be seen but it is not as significant as obtained by Dudek [5]. However, she finds the most marked improvement at positions closer than 3 device heights downstream, which are not shown here. As far as the other parameters go the changes are minimal, with respect to vortex core radius and circulation, Figures 2.12c and 2.12a. The differences in the helical pitch, Figure 2.12e, happen in the area at which the validity of the model is questionable. Only the offset in the core velocity, Figure 2.12d, seems to be an actual improvement. However, it comes at the cost of increasing the mesh size almost three times.

With regards to translational periodicity it can be seen that it has no significant impact on any of the vortex parameters discussed in this section. The slight variation seen in the circulation, Figure 2.12a, is most likely attributed to the variation in the line integral. The movement of the core location is shown in Figure 2.12f and shows that with regards to the variations tested here they do not influence the motion of the vortex core. However, translational periodicity might be more effective when the spacing of the vanes with respect to the boundaries diminishes. For all variations it can be seen that the vortex simulated by BAY does not move spanwise as rapidly as was observed in the experiments. Despite this difference, both CFD and the observed vortices seem to approach to the same spanwise position.

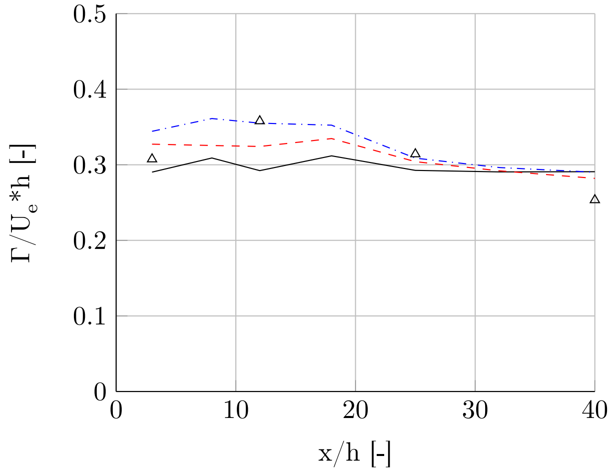

(a) Circulation

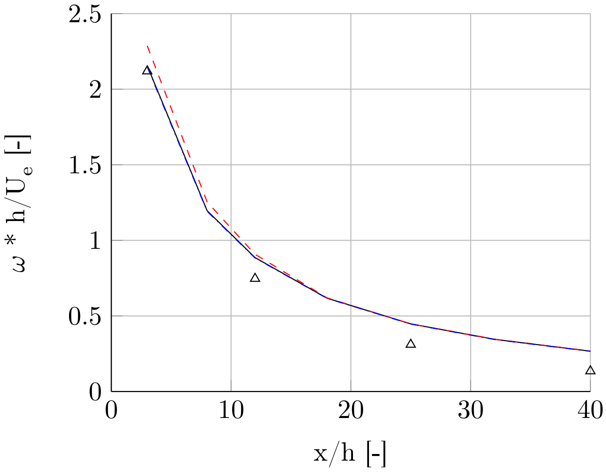

(b) Peak vorticity

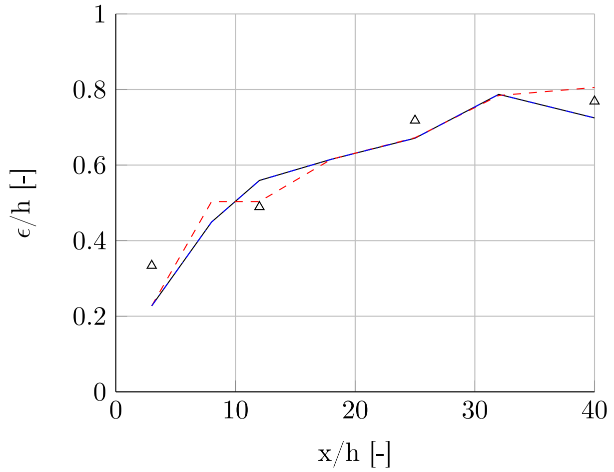

(c) Core radius

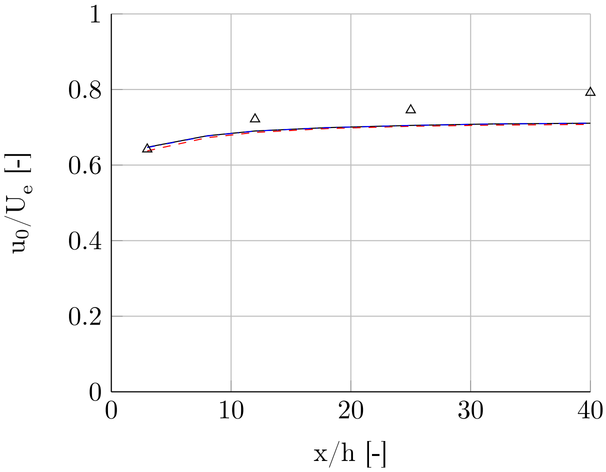

(d) core velocity

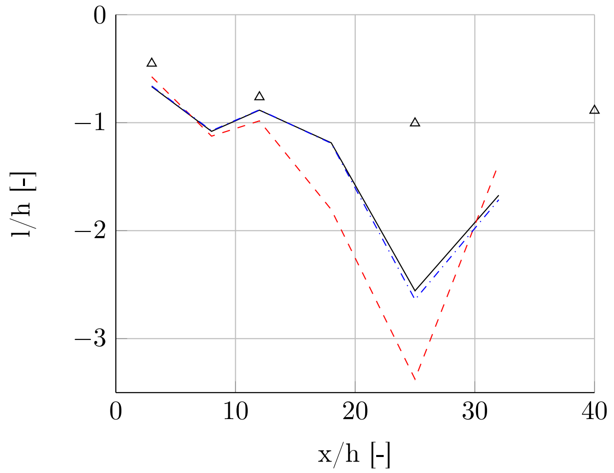

(e) Helical pitch

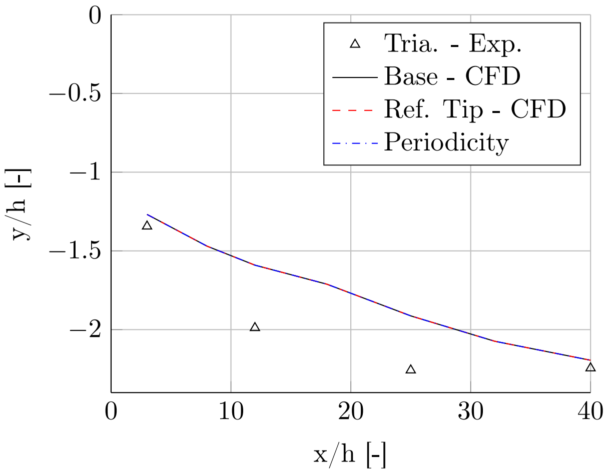

(f) Core Location

Figure 2.12: Streamwise development of various parameters for vortex generator tip refinement of the mesh, $Re_\theta = 16990$ at the inlet

Vortex Generator Area Coarsening

The final examined method is a coarsening of the body where the vortex generators are placed. However, it must be noted that this is technically a coarsening of the majority of the mesh. Horizontal and spanwise sizing in the vortex generator area determine the sizes in those dimensions for the inlet and wake as well. This could be mitigated by applying local refinement on other areas where higher resolution is required. Nonetheless, a documentation of this variation can be useful. 1.5 to 3 to 6 and 2 to 4 to 8

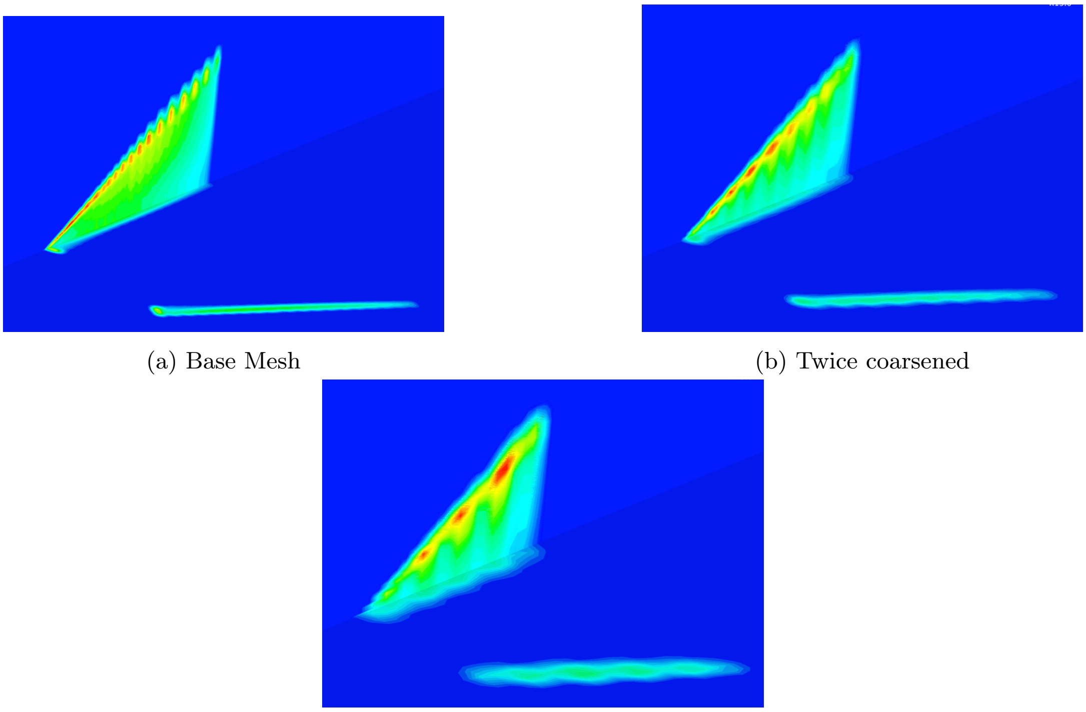

(a) Base Mesh

(b) Twice coarsened

(c) Four times coarsened

Figure 2.13: Distribution of momentum force of the BAY model for various mesh resolutions

Discussion of Results

The effects of coarsing the entire body used as the vortex generator domain are shown in Figure 2.14. When the mesh is coarsened by a factor of two the circulation, shown in Figure 2.14a, seems to match quite well still. However, when the mesh is coarsened further the circulation seems to start to decay, which would be a violation of the Helmholtz criterion. The vorticity, Figure 2.14b, is also significantly lower, which would be closer to the experimental data but the trend in the initial positions does not have a strong of a descent as shown by the experimental data. The vortex core radius and helical pitch, Figures 2.14c and 2.14e, seem to match quite well for the base and first coarsened mesh. The coarsest mesh seems to match closer to the experimental data, if the offset in the first downstream position can be attributed to the post process method. As the core velocity is concerned, Figure 2.14d, coarsening the mesh seems to decrease the accuracy but only slightly so.

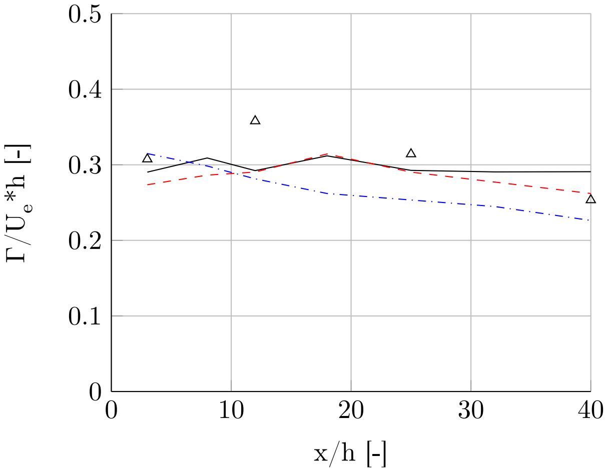

(a) Circulation

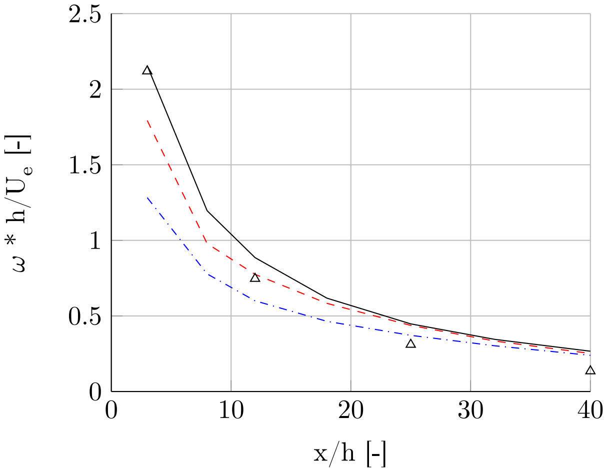

(b) Peak vorticity

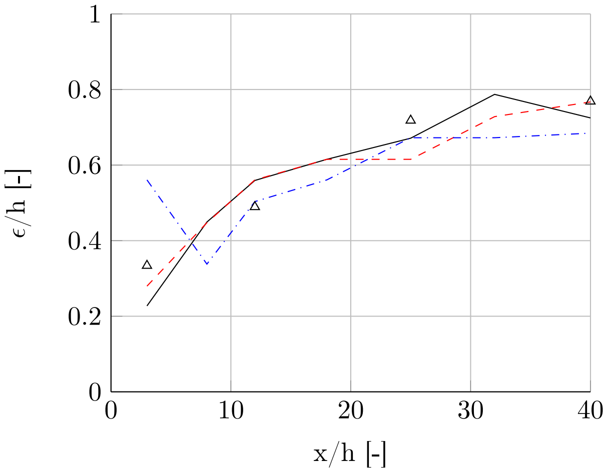

(c) Core radius

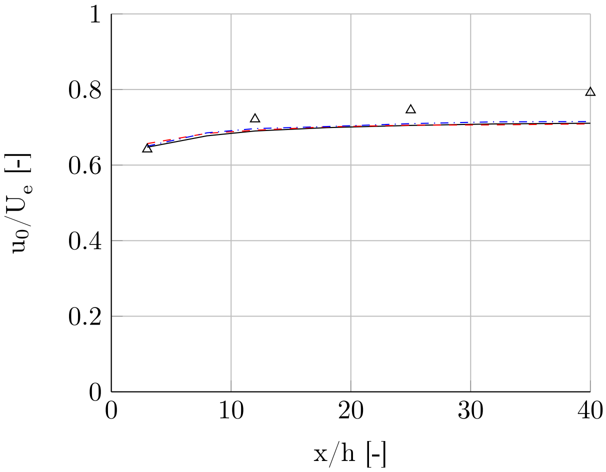

(d) core velocity

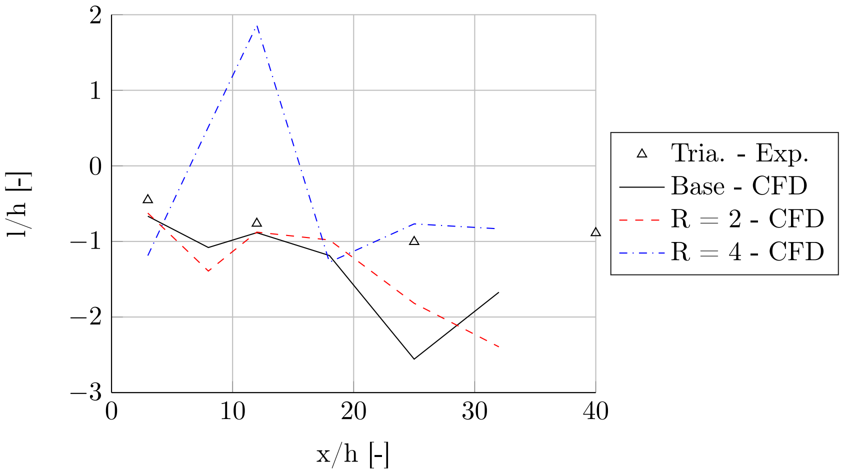

(e) Helical pitch

Figure 2.14: Streamwise development of various parameters for locally coarsened meshes with refinement factors R = [1, 2, 4], $Re_\theta = 16990$ at the inlet

2.4.4 Turbulence Intensity

In this section the effect of different values for the turbulence intensity will be investigated. This will be done on the base mesh and an edit of the turbulence intensity parameter on the inlet boundary conditions. The overall information is shown in Table 2.8.

Table 2.8: Simulation results for increasing turbulence intensity at the inlet for a zero pressure gradient with $Re_\theta = 16990$

	TI = 5%	TI = 1%	TI = 10%
Pressure drop [Pa]	1.153	1.134	1.200
Reynolds θ [-]	16990	16980	17000
Iterations to convergence [-]	488	889	428
CPU time [hh:mm / cores]	01:40 / 64	3:00 / 64	01:30 /64
Mesh elements [-]	7.53e6	7.53e6	7.53e6

Discussion of Results

Figure 2.15 shows the effect of varying the turbulence intensity with respect to BAY model and a zero pressure gradient. The highest turbulence intensity seems to suppress the vortex, while the lowest intensity does the opposite. There is a clear hierarchy in the circulation, Figure 2.15a and the peak vorticity, Figure 2.15b. In terms of the development of the vortex core radius, Figure 2.15c, the variation in turbulence intensity does not seem to affect the vortex significantly. For a turbulence intensity of 5% the initial peak vorticity seems to match better, though it might be that with an intensity of 1% the wake is more accurately captured. The dip in the helical pitch, Figure 2.15e for an intensity of 10% is most likely an outlier instead of an actual trend. Turbulence intensity is a flow parameter, unlike the other parameters varied in this study, therefore the differences observed in these results are to be expected.

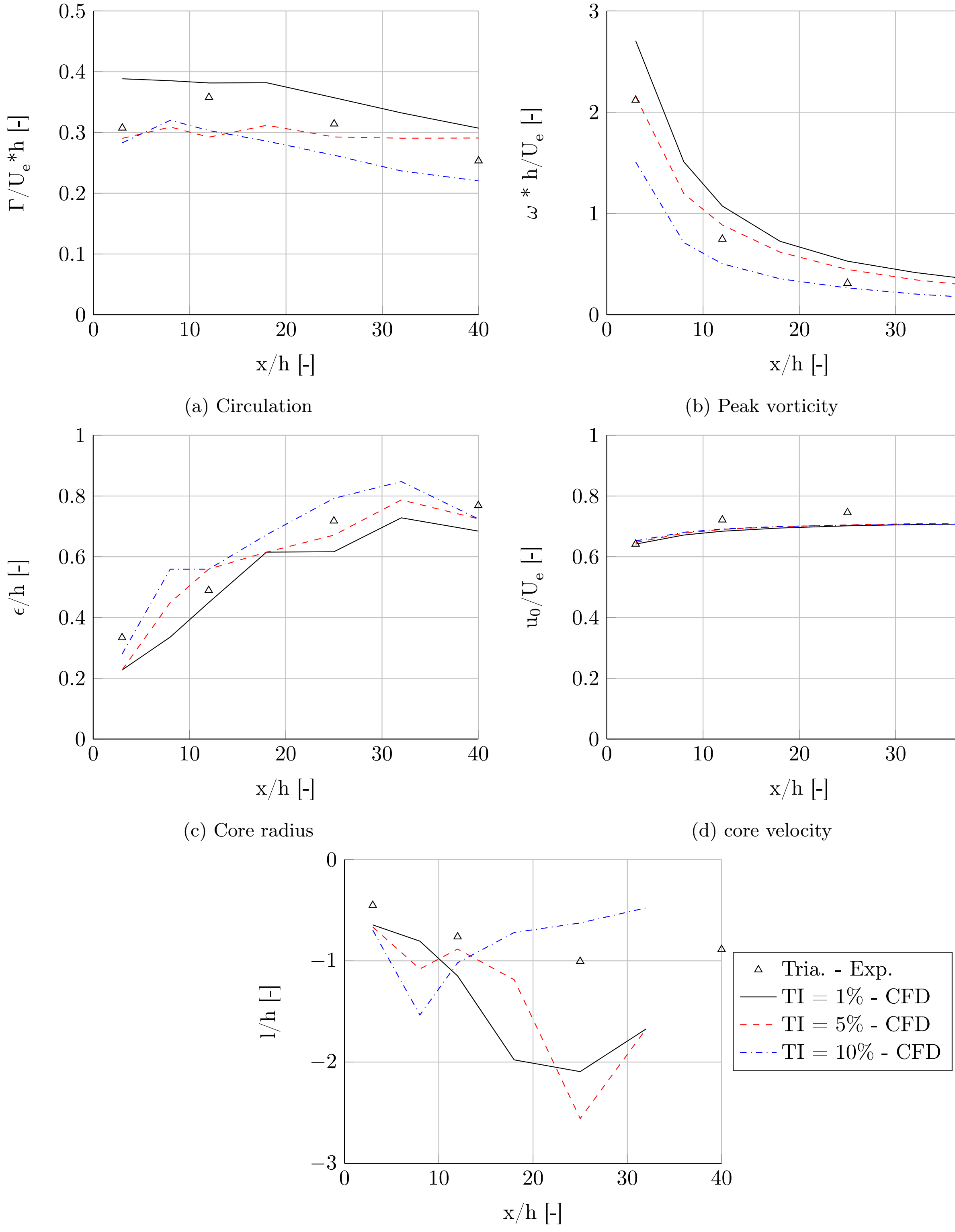

(a) Circulation

(b) Peak vorticity

(c) Core radius

(d) core velocity

(e) Helical pitch

Figure 2.15: Streamwise development of various parameters for Turbulence Intensity at the inlet, TI = [5%, 10%, 15%], $Re_\theta = 16990$

2.4.5 Plane Analysis

The general trend from the results shown in the previous sections suggests that the BAY model is quite capable of reproducing most aspects of the flow behind a vortex generator, such as circulation and peak vorticity. However, literature suggests that at initial planes downstream of the vortex generator the discrepancy is typically larger. Though many papers have conducted similar validations comparisons, the Reynolds number is rarely mentioned in these cases, such as Yao[36] whose experiments were also used by Dudek [5]. The same can also be said for Florentie et al.[57] whose comparison refers to the work of Waithe who also obtained his data from Yao[36], much like Allan et al.[89]. However, the setup described in those papers suggests a lower Reynolds number than the experiment used in this comparison.

To validate this behavior a comparison with another zero pressure gradient experiment was conducted, described in Appendix B, at a Reynolds Momentum Thickness number of 3124. The flow setup and vortex generator geometry in this experiment resembles those of the aforementioned authors. The BAY model performed according to the trends shown by those authors. Additionally, a fully resolved CFD analysis was performed independently and shows a similar degree of underprediction of the peak vorticity.

In this section several downstream planes from the simulations and experimental campaign of the rectangular vortex generator are shown in Figures 2.16 and 2.17 to analyse this increased accuracy of the BAY model. In Figure 2.16 the XZ planes with λ_2 criterion, vorticity and stream wise velocity are shown at a downstream position of the vortex generator of three device heights. The streamwise velocity, Figure 2.16f, shows that there is a significant lack of roll up for the flow simulated with the BAY model. However, as evidenced by the plot of the vorticity and λ_2 there is a vortex present in the flow. All figures of the experimental data, such as Figure 2.16a, show some degree of spanwise asymmetry, but this is most likely due to plane alignment instead of actual flow asymmetry. The plot for vorticity, Figures 2.16c and 2.16d, show that the vortex modeled by the BAY model seems to be slightly spread out. Analysing this with λ_2, Figures 2.16a and 2.16b, confirms the slight expansion and also highlights the difference in intensity of the experimentally observed vortex and numerically generated vortex.

In Figure 2.17 shows the same three parameters again but further downstream, at 25 device heights downstream of the vortex generator. The noise in the measurements is slightly more visible in the experimental planes, due to the fact that the difference between levels has gotten smaller making analysis more sensitive to signal to noise ratio.

A similar trend, underprediction initially that transforms into slight overprediction, was observed in Appendix B. However, the extent is much less pronounced in this case. This is most likely due to the higher Reynolds numbers which aids the assumptions that made by turbulence models, as discussed in Section 3.3.

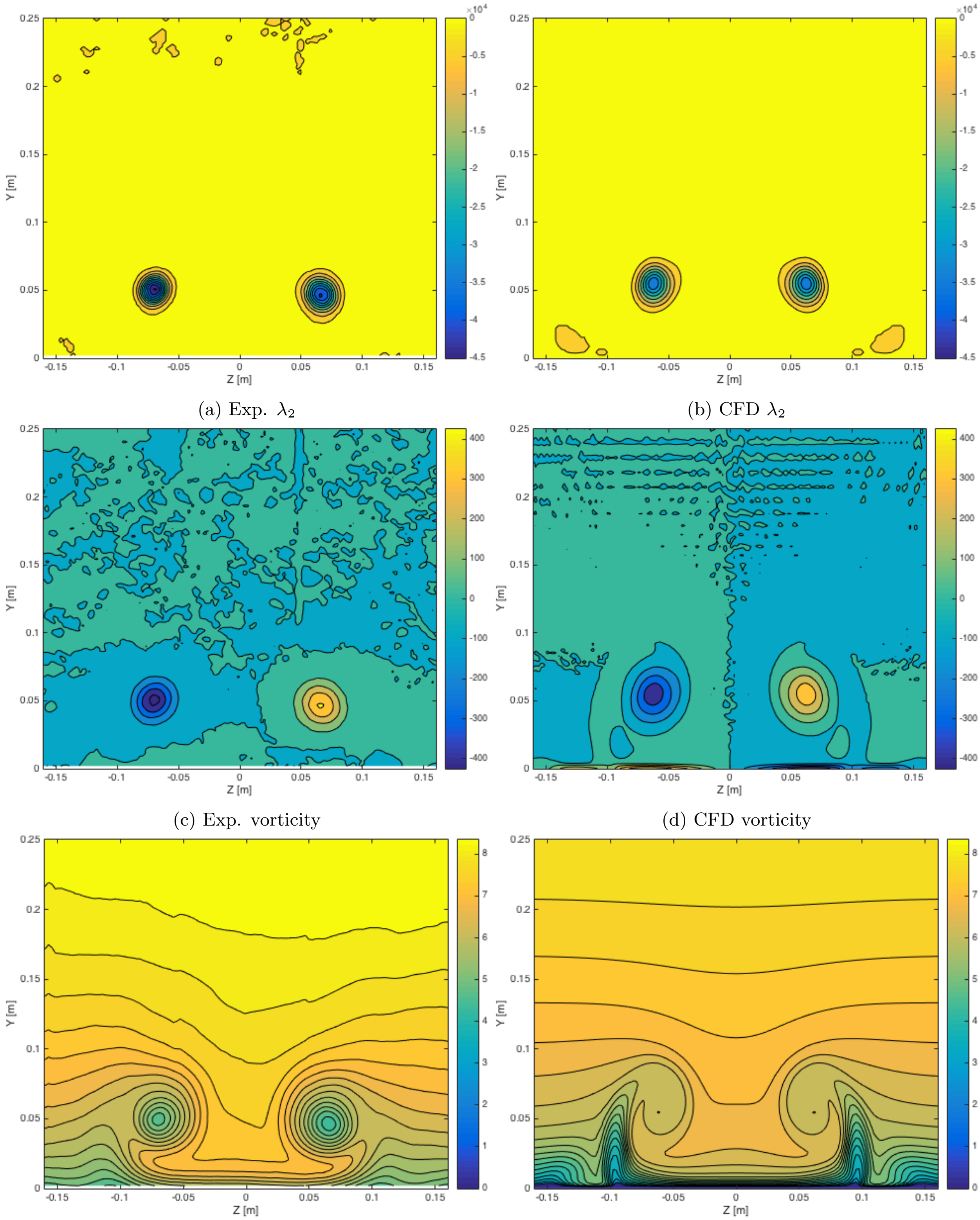

(a) Exp. λ_2 (b) CFD λ_2

(c) Exp. vorticity (d) CFD vorticity

(e) Exp. Streamwise Velocity (f) CFD Streamwise Velocity

Figure 2.16: Plane comparison between CFD and experimental data for streamwise Velocity, λ_2, and vorticity for the rectangular vortex generator at $x/h = 3$, $Re_\theta = 16990$ at the inlet

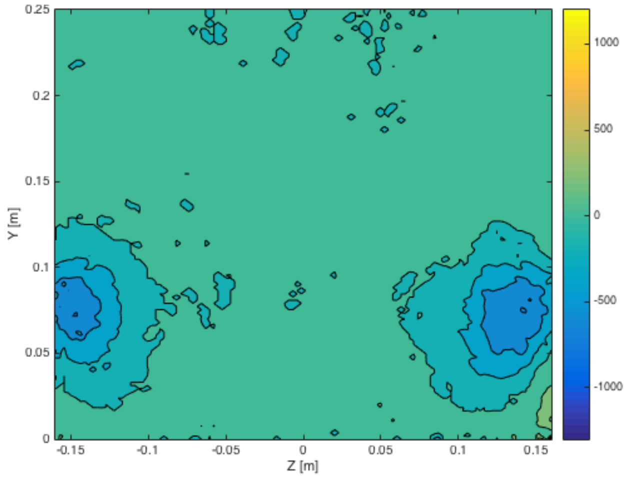

(a) Exp. λ_2

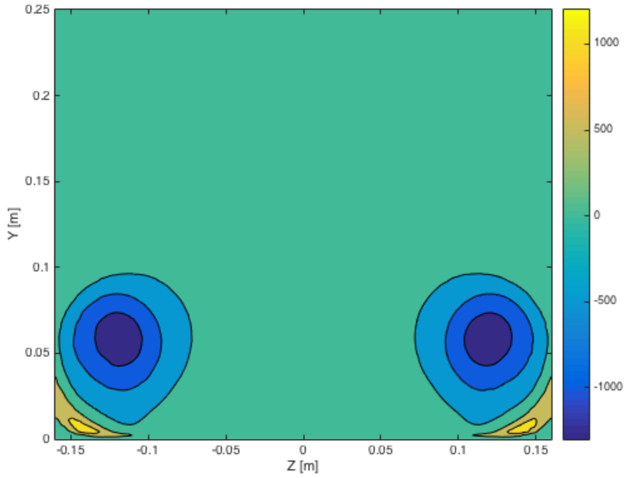

(b) CFD λ_2

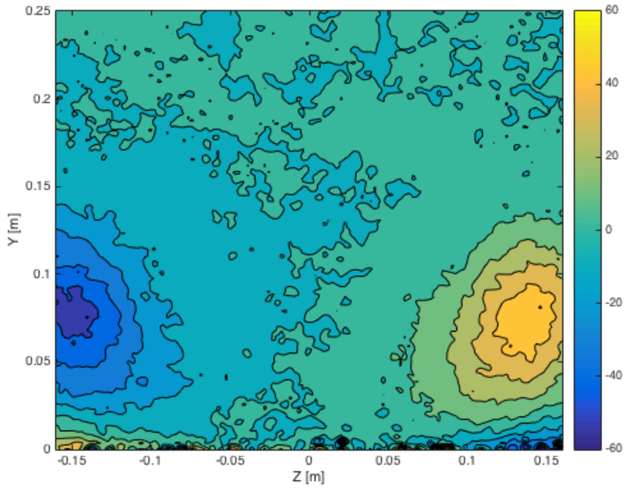

(c) Exp. vorticity

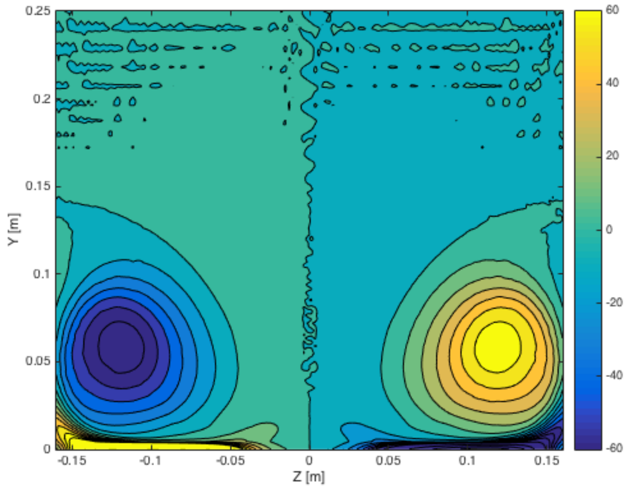

(d) CFD vorticity

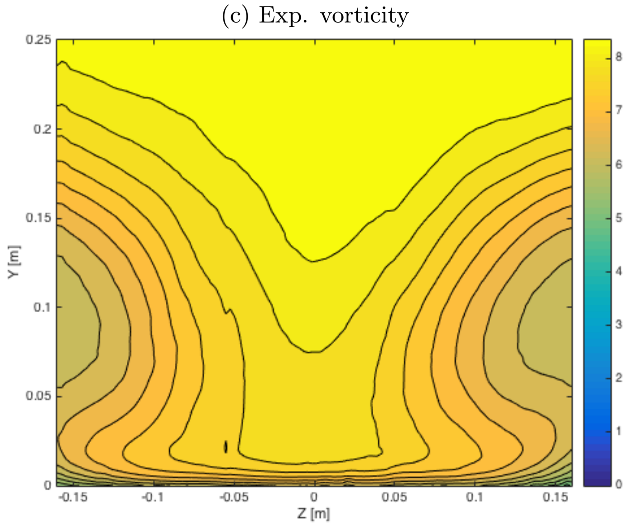

(e) Exp. Streamwise Velocity

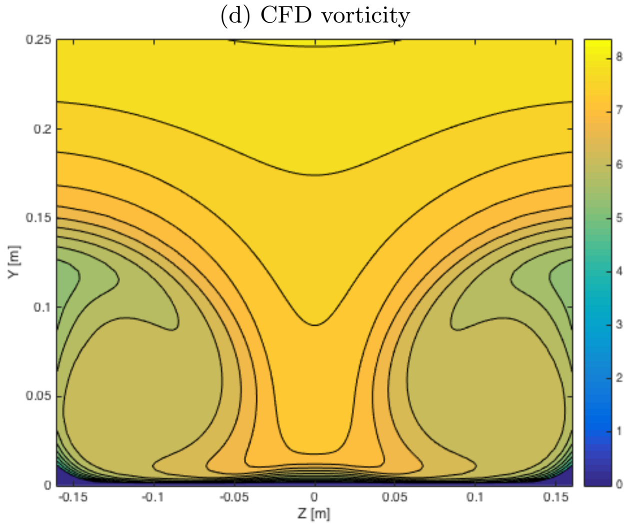

(f) CFD Streamwise Velocity

Figure 2.17: Plane comparison between CFD and experimental data for streamwise velocity, λ_2, and vorticity for the rectangular vortex generator at $x/h = 25$, $Re_\theta = 16990$

Chapter 3

Adverse Pressure Gradient In A Turbulent Boundary Layer Wind Tunnel

In this chapter the BAY model implementation will be compared to a parameter study conducted in the Turbulent Boundary Layer tunnel from Lille, France introduced in the previous chapter. A carefully designed bump has been placed in the test section causing an adverse pressure gradient to appear. The flow over this bump without vortex generators has been extensively documented, making it possible to explain the differences with the experimental observations in greater depth.

3.1 Additional Features for the BAY Model Implementation

In order to account for the curvature of the bump the location flagging algorithm needs a modification. When defining the vortex generator in the XY plane the minimal boundary is no longer static, but a function of the streamwise position. To reflect this, the boundary values will now be obtained from three linearly interpolated lines, shown in Figure 3.1. The coefficients of these lines will be passed to the user routine in a similar fashion as described in Section 1.2. Based on the sign of the first coefficient of the first line, the black dashed line in Figure 3.1, the algorithm will determine the minimum boundary on the XY plane based on the first and second line, black and red, or the first and third line, black and blue. The maximum boundary on the XY plane is determined by the remaining line. This way the algorithm can account for both directions of rotation for the vortex generator.

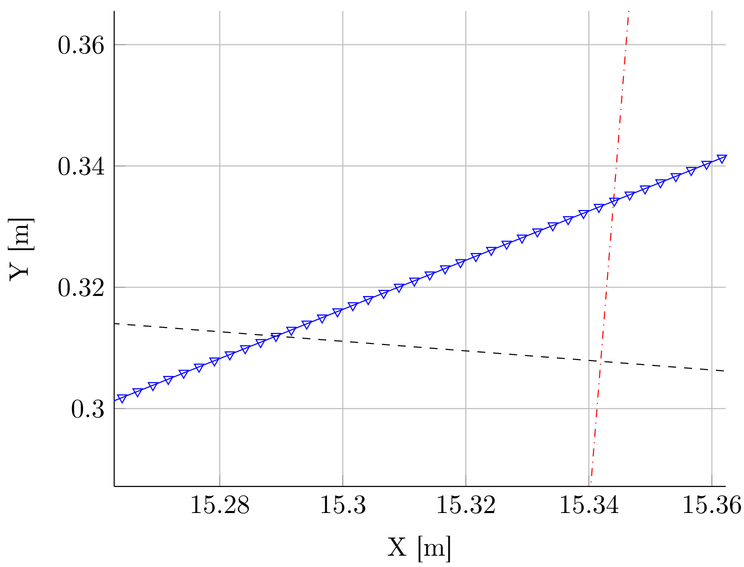

Figure 3.1: Example of boundary lines, for rotated vortex generator, describing the maximum and minimum values used by the BAY algorithm to determine if a mesh point represents the vortex generator

In the previous cases the rotation of the vortex generator with respect to the coordinate frame was not taken into account in the BAY equation. This means the local flow velocities must be rotated according to the local angle of rotation, denoted in Figure 3.2 with θ. Afterwards the forces are rotated again to match the global coordinate frame. The three vectors used by the BAY equation are computed in the local coordinate frame of the vortex generator on a flat plate.

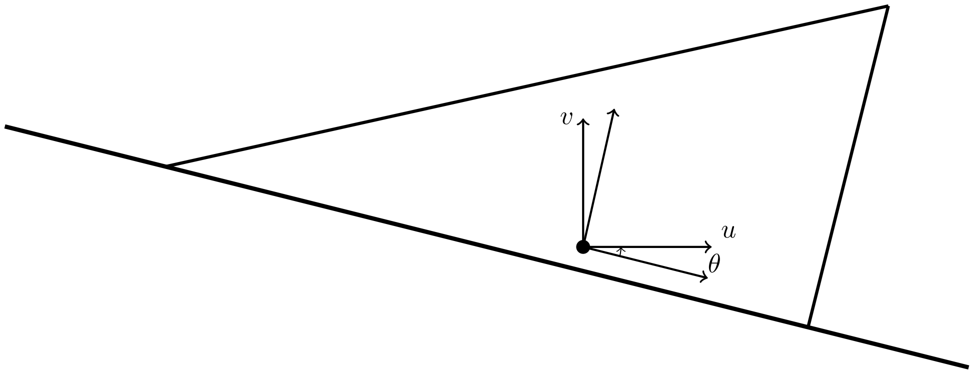

Figure 3.2: Illustration of the effect of rotating the vortex generator and the local velocity components

3.2 Flow Without Vortex Generators

In this case the performance and accuracy of the BAY model implementation will be examined in an adverse pressure gradient flow. This case is based off the experiment and results discussed in the paper of Bernard et al.[84] and the paper of Godard and Stanislas[46]. Both papers concern experiments in the same wind tunnel from the previous case, at a high Reynolds Momentum Thickness number of 22000. In order to obtain the adverse pressure gradient a bump is placed on the floor of the tunnel, as shown in Fig 3.3. Bernard et al.[84] have documented the flow over this bump with several parameters of the flow along various locations, measured with a combination of hot wire anemometry and pressure measurements. In Godard and Stanislas[46] this is repeated but now vortex generators are introduced on the bump. Additionally, Godard and Stanislas[46] focus more on the skin friction development and also have some PIV analysis of the flow.

Initially the flow without the vortex generators will be recreated and documented in terms of the parameters used by Bernard et al.[84]. This is especially necessary because as noted by Cuvier et al.[85], where a similar experiment with respect to Bernard et al.[84] is discussed, the simulation of adverse pressure gradient flow is difficult to model accurately by methods such as RANS. By thoroughly documenting the flow aspects without vortex generators the influence of the BAY model can be isolated to a higher degree.

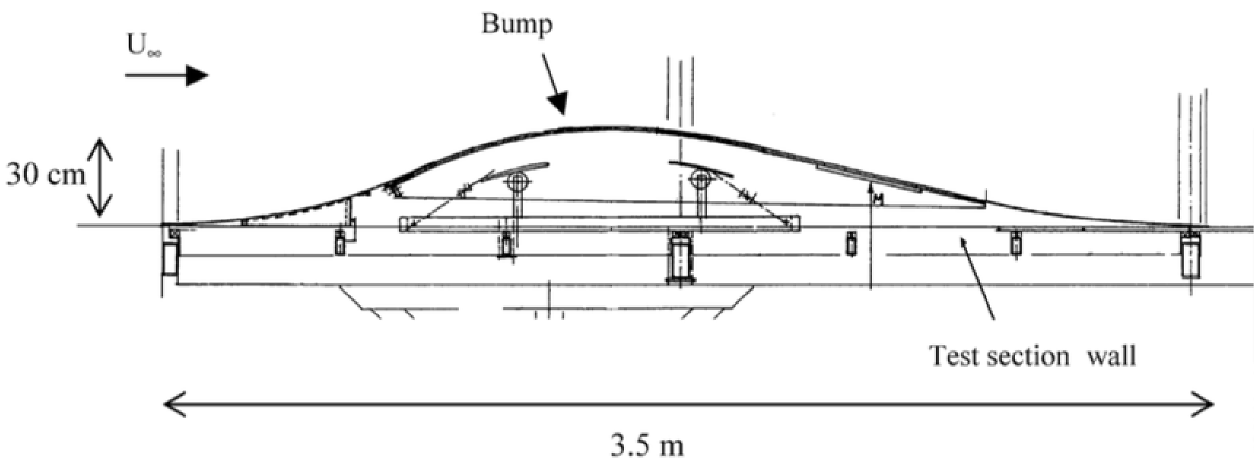

Figure 3.3: Model depiction of the bump in the Turbulent Boundary Layer Tunnel[46]

Bernard et al.[84] mention that the bump was specifically designed for the purpose to enable the study of adverse pressure gradient flow. Separation must be prevented in order to keep the flow characteristics two dimensional. The bump is designed with this purpose in mind, using a two dimensional CFD code with a $k-\epsilon$ turbulence model. In order to match the results produced by this design procedure the setup includes the ability to pitch the bump three degrees in both directions.

3.2.1 Geometry And Mesh

The coordinates of the bump are published by Bernard et al.[84], however their resolution is not adequate for a high quality mesh. Furthermore, the clustering of points cannot be resolved into a smooth curve. Therefore the points must be interpolated, introducing a measurement error between the proposed CFD simulation and the published results. This interpolation must also have a smooth derivative in order to prevent parameters such as the pressure gradient from producing abnormal results. This has lead to the decision to use an eighth degree polynomial fit between the available points. A comparison can be seen in Figure 3.4 and its derivative is shown in Figure 3.5. This shows that there is some slight deviation from the published points, but a smooth derivative has been obtained. It is believed however, that these points do not accurately represent the geometry used in the experiments. The points at $X = 18.58$ introduce a bump in the surface that would prohibit a smooth first derivative.

Because Bernard et al.[84] mention the ability to tilt the bump to match the results obtained from CFD the geometry at the extremes is also investigated. In Figure 3.6 the original bump along with an estimation of what the bump might be at 3 degrees tilted in both directions. How this rotation is accomplished specifically is not mentioned by Bernard et al.[84] and the interpolation of the rotated data points proved to be more difficult to match than the original values. Therefore, even if the results generated from those geometries prove to be more accurate than the base mesh they should be treated with increased caution.

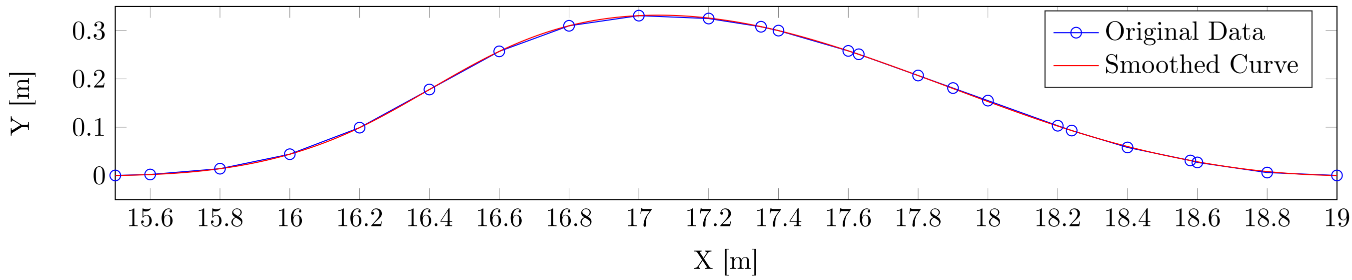

Figure 3.4: Illustration of the bump in Turbulent Boundary Layer Tunnel and an interpolation of the geometry

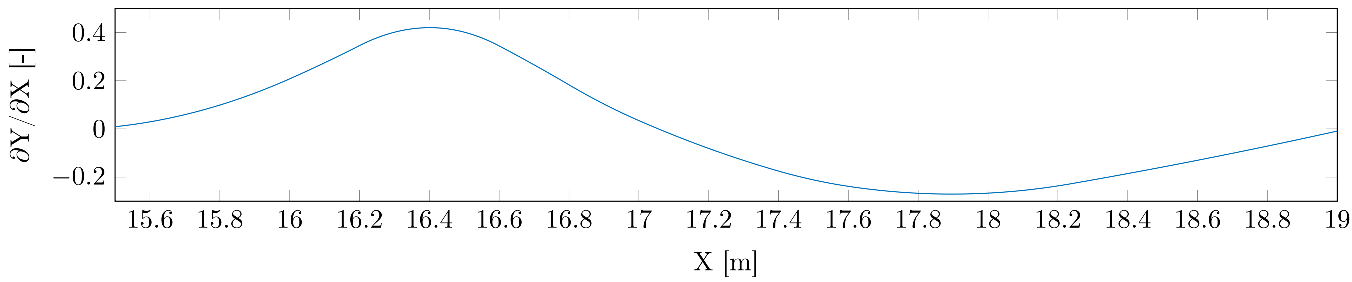

Figure 3.5: Derivative with respect to the Y Axis of the interpolated geometry

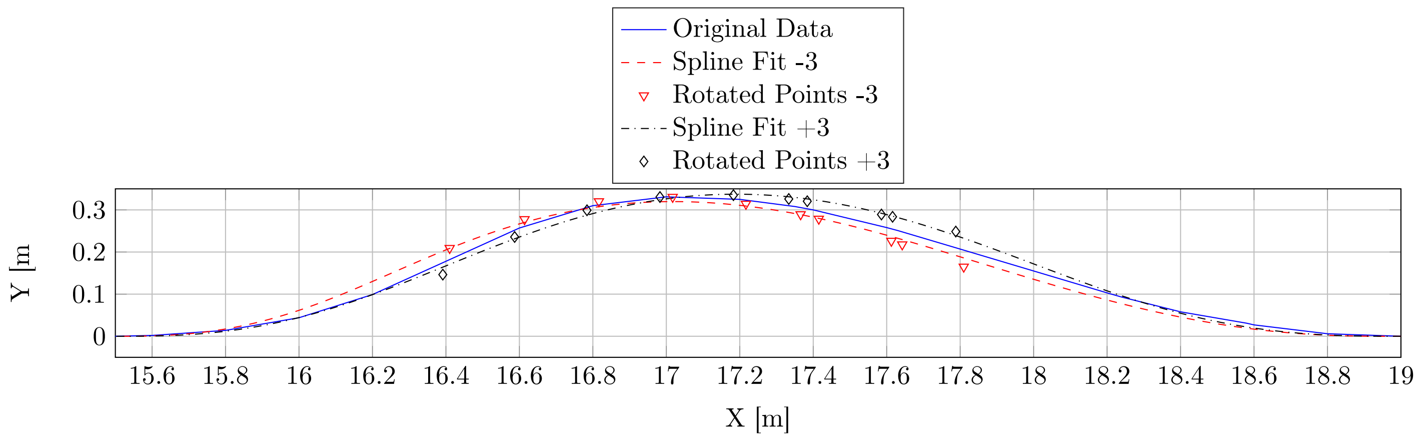

Figure 3.6: Rotated bump coordinates with respective spline fits

The fluid domain is meshed according to a structured method with inflation layers in the boundaries in order to satisfy the y^+ requirement for the turbulence models. This is done according the first cell height, which has been set to $2e-5\,m$ and inflated for 71 layers with a growth rate of 1.1. The final mesh contains $1.655e6$ elements, a maximum corner angle between 90 and 116 degrees, an aspect ratio between 1 and 130 in the main flow region, Skewness between 0 and 0.28, Orthogonality between 0.90 and 1, and a volume change between 0.93 and 1.6. A screenshot of this mesh can be seen in Figure 3.7. This mesh will be used to examine the flow characteristics and parameters with respect to the data provided by Bernard et al.[84].

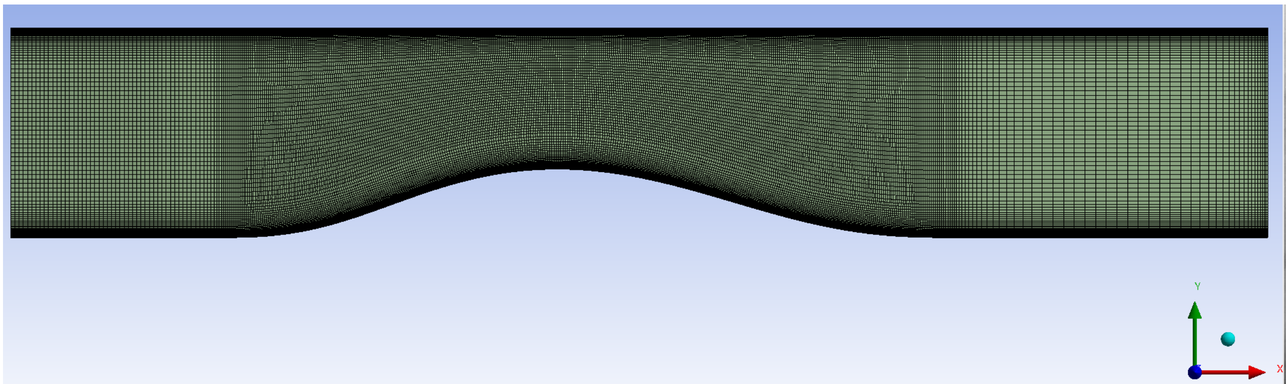

Figure 3.7: Screen capture of meshed fluid domain for the adverse pressure gradient case

3.2.2 Validation

In the paper of Bernard et al.[84] a large number of parameters are documented across several longitudinal location. Furthermore, some numbers from a CFD analysis are presented. The following parameters from Bernard et al.[84] will be used to analyse the results from the CFD simulations:

- Displacement, Momentum, Energy Thickness
- Shape factors; H, H_{12}, H_{23}
- Coefficient of Pressure
- Pressure distribution
- Pressure Longitudinal distribution
- Inlet Turbulent Kinetic Energy
- Skin Friction Coefficient
- Streamwise Reynolds Momentum Numbers

Some results will be plotted along the coordinate s which is a curvilinear abscissa along the surface of the bump.

In order to compare the effects of certain simulation variables a Base case will be defined. It will be modeled with a SST turbulence model, with 5 % turbulence intensity at the inlet combined with a $10.32ms^1$ normal inlet velocity. The geometry of this 'Base' case used all points given by the paper of Bernard et al.[84]. Furthermore, the inlet is positioned 0.5 m from the bump and the outlet 1 m. The boundary conditions are summarised in Table 3.1. A larger number of variables have been compared. For the sake of readability only those that are deemed most promising will be discussed here, others are shown in Appendix C.

On the basis of the variations tried in Appendix C it was decided to attempt a different method of interpolating the geometry and focus on the SST model with curvature correction and the BSL-EARSM model. For the SST model both a medium and high turbulence intensity were tested, denoted respectively by $U_\infty = 10ms^{-1}$ and $TI = 10\%$ in Figureẽffig:comp1sfc. Additionally, the velocity profiles are also shown in Figure 3.10.

3.2.3 Results & Discussion

Table 3.1: List of boundary conditions for fluid domain of the adverse pressure gradient case with $Re_\theta = 27328$ at the inlet

Location	Boundary Condition
Inlet	Opening with Prescribed Streamwise Velocity Profile & Turbulence Intensity
Outlet	Averaged Pressure Over Outlet with Relative Pressure at 0 Pa
Floor	No Slip Wall
Sides	Symmetry
Top	Symmetry

Table 3.2: Reynolds Momentum numbers and shape factors at various streamwise locations in the adverse pressure gradient case

Case	Re_θ, $x = 17.35$	Re_θ, $x = 17.63$	Re_θ, $x = 17.90$	Re_θ, $x = 18.24$	Re_θ, $x = 18.58$
Bernard et al.[84]	4887	10501	17131	26112	32384
Dassault NS[84]	4658	8822	14581	21298	25668
Base	-2860 (3552)	6824	16285	20241	23019
$U_\infty = 10$	4683	9520	16291	19848	23337
TI = 10%	4709	9491	16743	21116	24633
BSL-EARSM	4718	9475	16468	20873	24551
	H_{12}, $x = 17.35$	H_{12}, $x = 17.63$	H_{12}, $x = 17.90$	H_{12}, $x = 18.24$	H_{12}, $x = 18.58$
Bernard et al.[84]	1.24	1.319	1.471	1.703	1.693
Dassault NS [84]	1.246	1.303	1.433	1.688	1.876
Base	0.685 (1.268)	1.444	1.736	2.792	3.176
$U_\infty = 10$	1.280	1.465	1.891	2.787	3.024
TI = 10%	1.263	1.423	1.750	2.466	2.694
BSL-EARSM	1.278	1.459	1.832	2.576	2.791
	H, $x = 17.35$	H, $x = 17.63$	H, $x = 17.90$	H, $x = 18.24$	H, $x = 18.58$
Bernard et al.[84]	1.18	1.05	0.95	0.87	0.85
Dassault NS [84]	1.15	1.05	0.93	0.84	0.80
Base	0 + 0.730i (1.108)	0.923	0.878	0.825	0.789
$U_\infty = 10$	1.100	0.943	0.861	0.812	0.780
TI = 10%	1.123	0.961	0.8735	0.819	0.787
BSL-EARSM	1.098	0.940	0.856	0.797	0.768

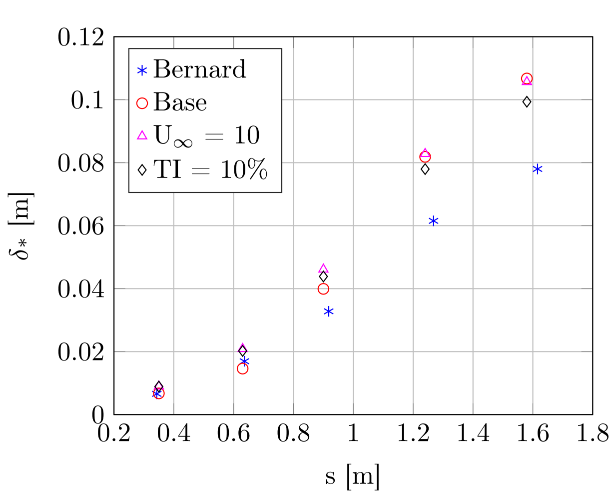

(a) Displacement Thickness

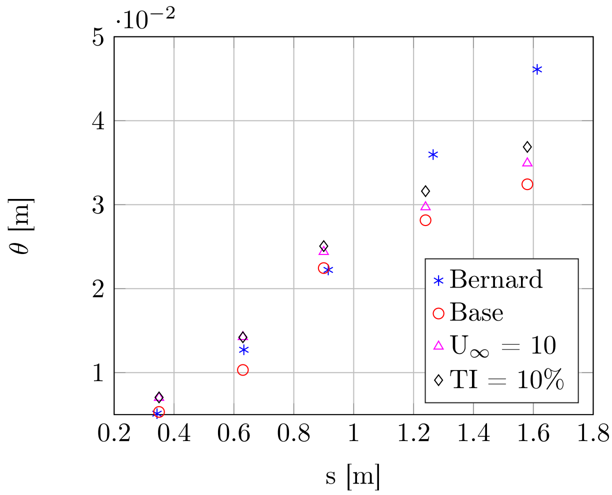

(b) Momentum Thickness

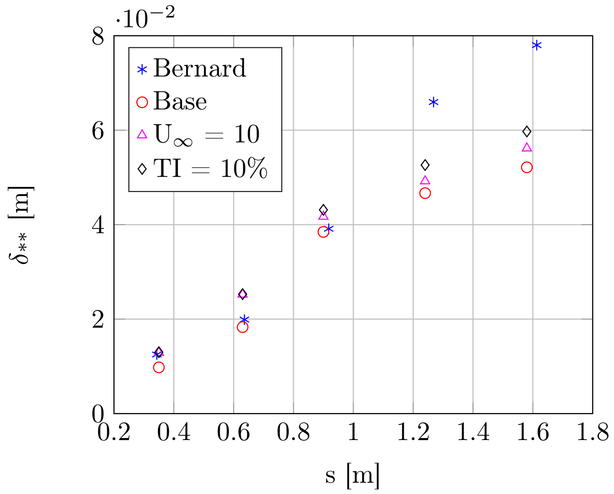

(c) Energy Thickness

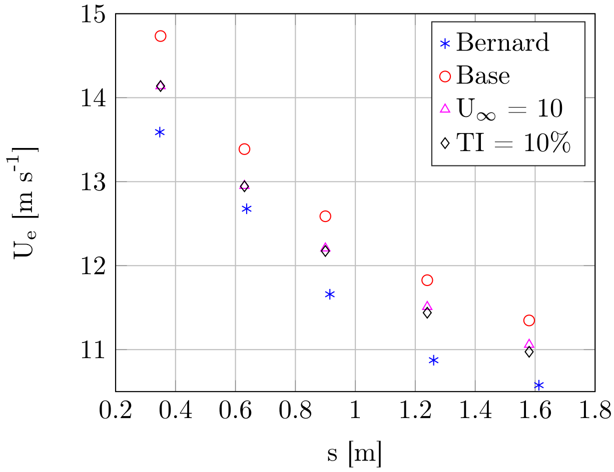

(d) Convection velocity

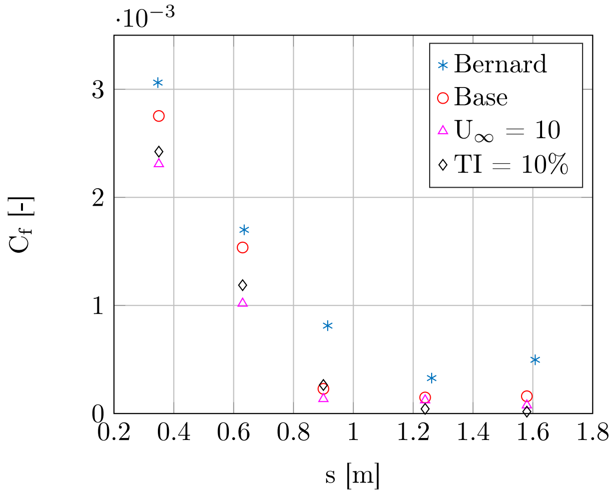

(e) Skin Friction Coefficient

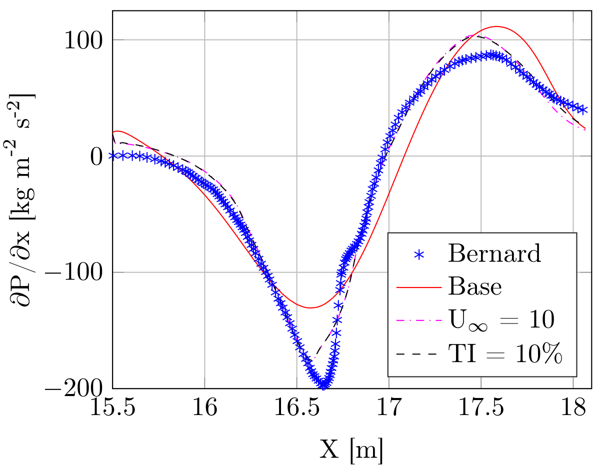

(f) Pressure Gradient

Figure 3.8: Comparison for various flow parameters in adverse pressure gradient flow, $Re_\theta = 27328$ at Inlet

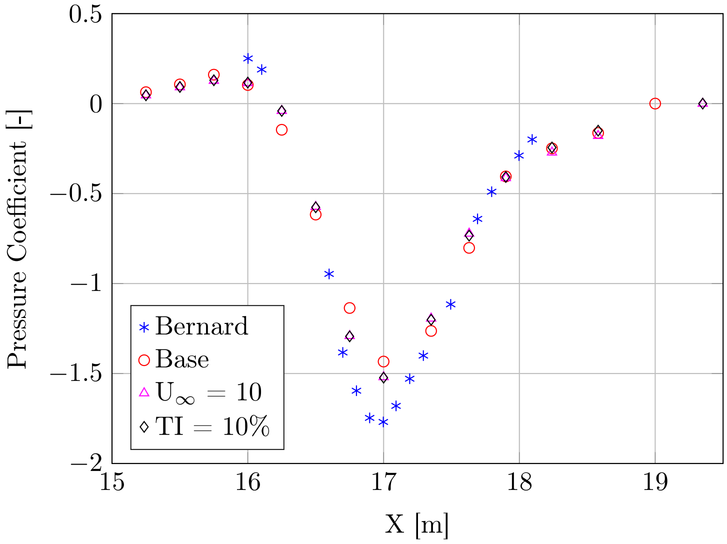

Figure 3.9: Coefficient of pressure comparison for different turbulence models, $Re_\theta = 27328$ at Inlet

One of the difficulties with validating the flow is the contraction that occurs in the windtunnel, which leads to a speed up of the flow. This makes traditional boundary layer analysis impossible, in the sense that it produces values that are non physical. However, in Bernard et al.[84] no mention is made of this nor has contact with the authors been successful. Therefore, for those stations where the flow does not contain a defined free stream region the maximum velocity is chosen as the free stream velocity. For a comparison both methods are shown for the 'Base' case, with the maximum velocity as free stream velocity method between parentheses. Although the method applied by Bernard et al.[84] could not be obtained, Table 3.2 does show very similar values for both CFD and the experimental values.

Regarding the first two stations, it can be seen that the Reynolds numbers for the updated geometry is much closer than the previous cases. However, as the flow develops the differences become negligible with respect to Reynolds numbers and shape factors. Only the H_{12} is significantly lower for an increase in turbulence intensity.

The thickness parameters shown in Figures 3.8a,3.8b, and 3.8c reveal that the boundary layer seems to match relatively closely in the initial stages but differs more further downstream. This is due to the separation that occurs in the simulation, but was not seen by Bernard et al.[84]. Increasing the turbulence intensity improves the situation slightly, but not enough to match the experimental data.

A similar trend can be seen for the convection velocity in Figure 3.8d, matching decent in the first three stages and diverging more in the latter two. For all values the improved geometry does lead to better predictions compared to the previous case.

The skin friction coefficient, shown in Figure 3.8e, is under predicted more significantly in the initial stages. It also seems better in the latter two stages, but these are actually less accurate due to the separation that has occurred.

A significant improvement can be seen in the pressure gradient, Figure 3.8f, and a smaller improvement in the peak of the pressure coefficient from Figure 3.9.

In Figure 3.10 the development of the velocity profile is shown and compared to the data from Bernard et al.[84]. However, the horizontal axis is poorly defined and therefore the similarity in magnitude should be considered certain. Bernard et al.[84] that their CFD result show a similar over prediction of momentum in the first velocity profile, shown in Figure 3.10a. For the next two velocity profiles, Figures 3.10b and 3.10c, the profiles seem to be very similar. Figures 3.10d and 3.10e show the biggest difference, due to the aforementioned separation in the simulation. Increase the turbulence reduces the effect, as expected, but cannot cover the gap to the experimental data.

Lastly, BSL-EARSM has also been briefly investigated and seems to be further predict much less separation than the tested cases, which leads to a minor improvement to the skin friction coefficient in the latter two stages. All other parameters remain the same, with pressure gradient being an exception. Just like in the previous report, BSL-EARSM leads to a more severe under prediction of the pressure gradient.

All possible parameters that have been tested have not been able to reach the Reynolds Momentum Thickness numbers, shown in Table 3.2, that were found by Bernard et al.[84]. As shown in the figures depicting the convection velocity U_e, such as Figure 3.8d and Figure C.5d for example, the convection velocity is actually overestimated. Considering the fact that both the displacement and momentum thickness are relatively close in most cases, apart from the initial longitudinal position, there could be another parameter that has a significant discrepancy.

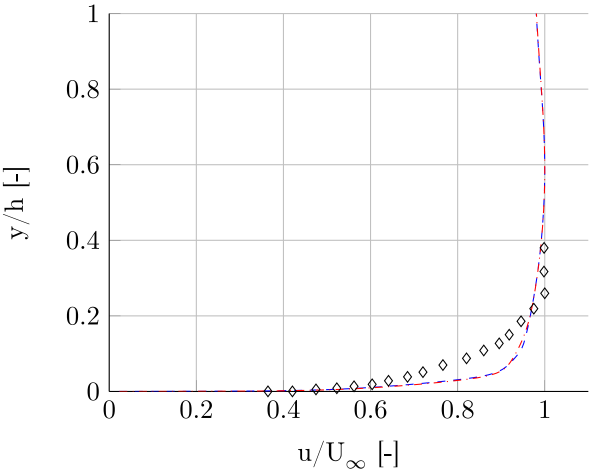

(a) X = 17.35 m

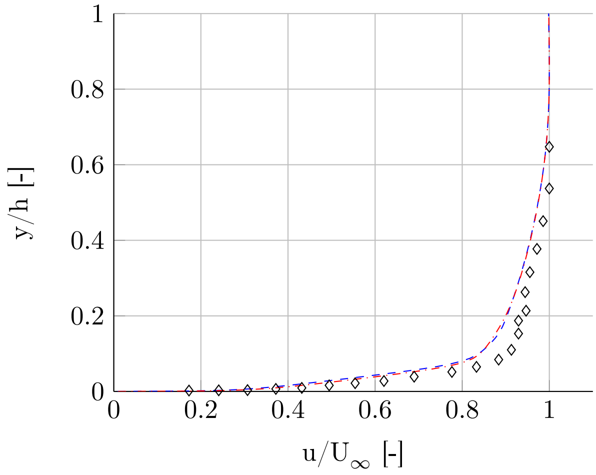

(b) X = 17.63 m

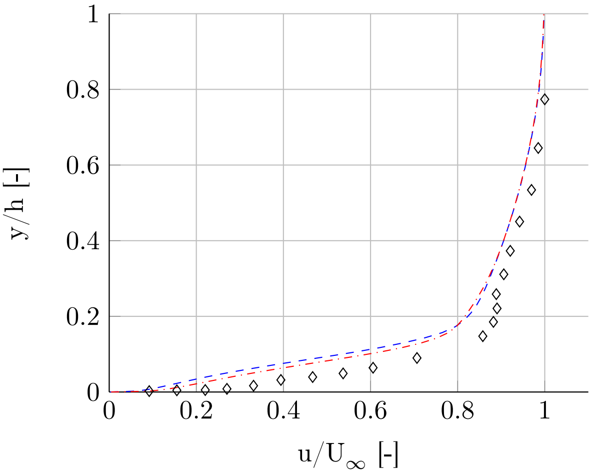

(c) X = 17.90 m

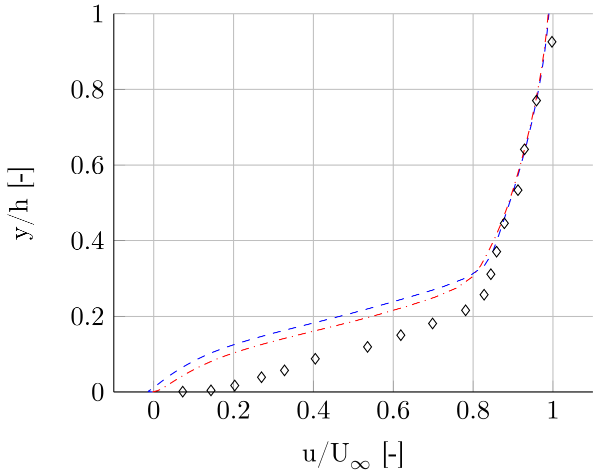

(d) X = 18.24 m

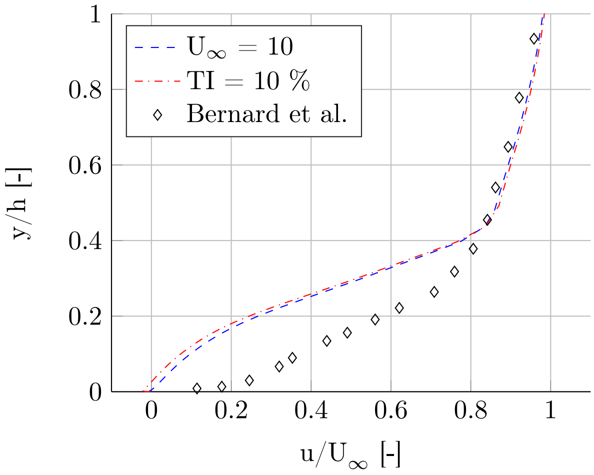

(e) X = 18.58 m

Figure 3.10: Development of streamwise velocity profiles in adverse pressure gradient, $Re_\theta = 27328$ at Inlet

Although a large amount of information of the flow is given, the dynamic viscosity is not explicitly declared, which is relevant for Reynolds numbers. However, with the measurements from Bernard et al.[84] an approximation of what the dynamic viscosity might have been can be found and compared to the value used by the numerical simulation. Bernard et al.[84] define a dimensionless pressure quantity, P^+, as follows, which uses the dynamic viscosity, ν:

$$P^+ = \frac{\partial P}{\partial X}\frac{\nu}{\rho u_\tau^3} \tag{3.1}$$

The longitudinal pressure gradient, $\frac{\partial P}{\partial X}$, and density, ρ, are known but the friction velocity, u_τ, is not. Nonetheless, it can be calculated with the following equation:

$$u_\tau = \sqrt{\frac{\tau_p}{\rho}} \tag{3.2}$$

The wall shear stress, τ_p, is also not directly available, but can be obtained from the skin friction coefficient, C_f.

$$C_f = \frac{\tau_p}{\frac{1}{2}\rho U_e^2} \tag{3.3}$$

Going through this routine for the longitudinal locations provided by Bernard et al.[84] reveals the following values for the kinematic and dynamic viscosity in Table 3.3

Table 3.3: Implied dynamic and kinematic viscosity along longitudinal locations in the adverse pressure gradient case

Parameter	$X = 17.35$	$X = 17.63$	$X = 17.90$	$X = 18.24$	$X = 18.58$
$\nu\,[m^2s^{-1}]$	$1.536e^{-5}$	$1.531e^{-5}$	$1.409e^{-5}$	$1.318e^{-5}$	$1.476e^{-5}$
$\mu\,[kgs^{-1}m^{-1}]$	$1.879e^{-5}$	$1.872e^{-5}$	$1.723e^{-5}$	$1.611e^{-5}$	$1.805e^{-5}$

This variation, along with the difficulty in obtaining the external velocity U_e, could explain why the Reynolds number is somewhat under predicted. Especially because in the solver the dynamic viscosity and pressure are constant throughout.

Though these results are not exhaustive, it does beg the question whether or not it is possible to match the flow conditions to a degree obtained by the simulations from Dassault that were published in Bernard et al.[84]. Considering the fact that Dassault has only simulated this case in a two dimensional domain with the $k - \epsilon$ model, raises some questions. Modeling the flow in such a way prohibits the occurence of any separation to begin with. If Bernard et al.[84] needed to pitch their model then the validity of the comparison could be at stake. Since publishing others have attempted to model the flow over this bump with numerical solvers. Specifically, several attempts have been done with Direct Numerical Solvers such as Marquillie et al.[90] and using a hybrid Large Eddy Simulation from Gungor and Suresh[91], but due to the nature of DNS these have been limited to Reynolds Momentum Thickness numbers below 1000. Both authors have also noted the occurrence of separation in their simulation, though in their cases it happens slightly more upstream. Finally, there the SST model has the tendency to overpredict the effect of separation. This is due to the underprediction of the turbulent stresses in regions where separation occurs as noted by Menter et al.[92].

3.3 Flow With Vortex Generators

3.3.1 Grid Independence Study

To ascertain the quality of the results produced by this parameter study a grid independence study was conducted. Three meshes have been made and have been evaluated according to Richardson's Extrapolation and the Grid Converge Index (GCI). Previous efforts in the zero pressure gradient case have suggested that the multi-body approach to meshing could negatively affect these studies. Therefore the sizing of the rough and fine mesh was done rigorously this time by using a constant spacing factor between each mesh and the base mesh. Nonetheless, full control over the spacing and the elements cannot be obtained due to the algorithm of the mesh software that can overwrite user input to accommodate the facilitation of a mesh. Furthermore, due to the nature of a parameter study the mesh will change slightly, either in dimension or the area of interest will be moved. However, conducting a grid independence study for all variations is outside the scope of this project. It will be assumed that if the same meshing rules are applied that a single grid independence study can be applied to all results, despite changes in the mesh. In order to support this assessment the mesh has been setup accordingly, the body for the vortex generator is sufficiently large and uniformly spaced that it should be able to accommodate multiple setups.

In Figure 3.11 the mesh strategy is shown for the base mesh. It features a refinement near the peak of the bump, the area where most of the vortex generators will be placed in the parameter study. This refinement expands moderately towards the inlet and even less so towards the outlet. The growth of the boundary layer and remaining mesh causes some skewness and squeezing of the elements near the contraction, this is unavoidable but the quality of all three meshes has been guarded and both the skewness, max value of 0.36, and orthogonality quality, minimal value of 0.84, are still well within acceptable ranges. An attempt was made to further increase the quality by applying a bias to cells that attach to the boundary layer, to facilitate a smooth transition, but this did not have a significant affect, mainly due to the meshing software. As a compromise the boundary layer is extended further, to prevent a large volume expansion and skewness between elements. This leads to a boundary layer between 68 and 70 layers, depending on the roughness of the mesh, all starting from a first cell height of $2.5e-05\,\mathrm{m}$ with a growth rate of 1.1. This satisfies $y+ < 1$ for the majority of the fluid domain except for the contraction at the peak of the bump, where $y+$ is found to be about 1.1. Lastly, the spacing in the body for the vortex generator has been set to 4 mm streamwise and 2 mm spanwise for the medium mesh. In Table 3.4 the total elements of each mesh and their respective spacing factor and refinement ratio are shown. Furthermore, the two rightmost columns show the amount of iterations and CPU time it took to reach the user defined convergence. It was found that at an RMS value of $1e^{-6}$ the pressure drop had reached a steady state. All these results were obtained on a 128 core cluster of CPU's.

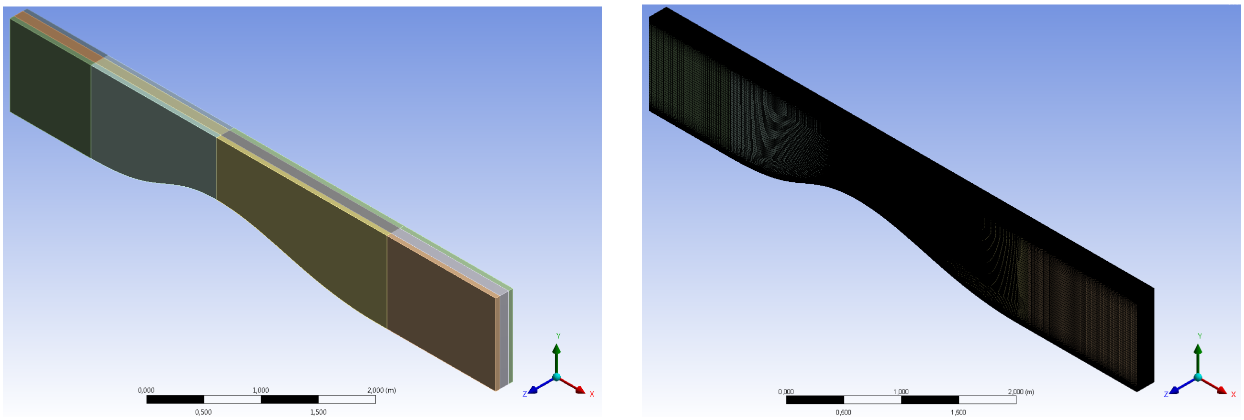

(a) Multi-Body Approach

(b) Meshed Multi-Body

Figure 3.11: Mesh strategy for the adverse pressure gradient case

Table 3.4: Grid Independence Study parameters for the adverse pressure gradient case

Mesh	Mesh Size $\times 1e^6$ [-]	Size Ratio [-]	Ref. Ratio [-]	Pressure Drop [Pa]	C_f [-]	Total Iter. [-]	CPU Time [hh:mm]
Rough	6.48	1.5	1.3052	5.974	3.532e-3	4502	08:53
Medium	14.42	1	–	5.877	3.748e-3	4922	18:28
Fine	32.69	0.675	1.3138	5.759	3.709e-3	5362	43:54

For the Richardson's Extrapolation and GCI the pressure drop over the inlet and outlet as well as the value of the wall shear stress at X = 18.58 m are observed, these values can be seen in Table 3.4. When the pressure drop is evaluated the observed order of accuracy, $\hat{p} = 1.17$. Furthermore, the ratio of GCI's is similar to the refinement ratio to the power of the observed order of accuracy. This means the solution is in the asymptotic range of convergence. However, the values for the GCI are rather high, 84% and 71% respectively, which suggests a rather large error band. These have been computed with a safety factor of $F_S = 3$, as suggested by Roache[88]. Though lower values have been used, which would bring the error band down below 30%. This is still a large error band, but considering the unsteadiness of the flow and the trouble RANS modeling has with an adverse pressure gradient in this setup the results are still decent. An analysis of the skin friction coefficient, C_f, could not be used in this case due to non linearity of the obtained values.

3.3.2 Parameter Study Results

The purpose of this validation is two-fold, first the accuracy of the BAY model in an adverse pressure gradient flow is tested. Secondly, the ability of the BAY model to perform a parameter study is tested. Both these aspects will be tested based on an experiment campaign documented by Godard and Stanislas[46]. In this report the effects of changing the immersion ratio, vortex generator spanwise spacing, aspect ratio, and vortex generator angle. One other main parameter introduced by Godard and Stanislas[46] is ΔX_{vg}, which is the streamwise distance from X = 18.58 m. This position reflects the point where Godard and Stanislas[46] have measured the minimum of the skin friction coefficient. These parameters are visualised in Figure 3.12.

In order to compare the results from Godard and Stanislas[46] to the CFD results the same non-dimensionalisation must be applied. This introduces an error the results, however, because the main parameter, the vortex generator height, is non-dimensionalised by the boundary layer height. As shown by the report from week 11 the flow over the bump without the vortex generators does not resemble the measurements completely accurately. Furthermore, due to the non-dimensionalisation by both the boundary layer height and the vortex generator height, matching the parameter ΔX_{vg} becomes an iterative loop due to the dependency of the boundary layer height on the streamwise position. These two facts lead to the situation that the parameters used in the CFD study do not exactly overlap with those from Godard and Stanislas[46], nonetheless they have been carefully chosen to be as close as possible. The setup for the cases are shown in Table 3.5. In the right hand row the computational time is shown it took for each case to reach the convergence criteria of $RMS = 1e^{-6}$, at which point the pressure drop has reached a steady state. All cases, except for 2 – 2 where 128 cores were used, have been computed on a 64 core system.

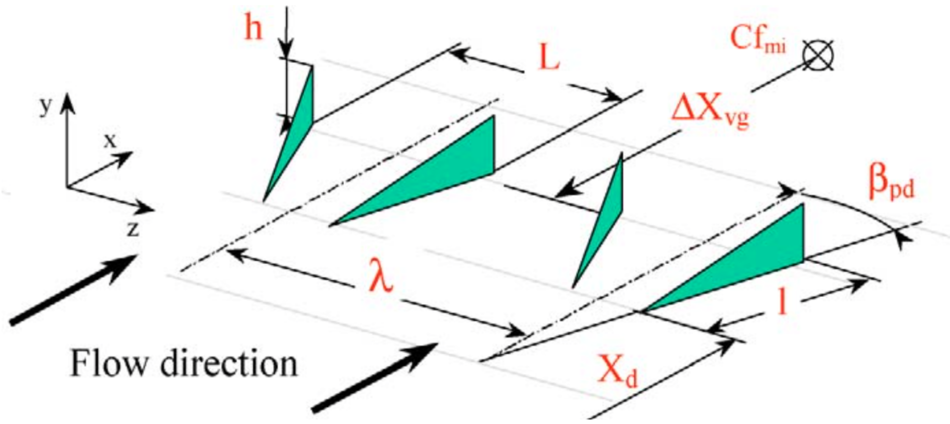

Figure 3.12: Vortex generator parameters as used by Godard and Stanislas[46]

Table 3.5: Parameter study for the adverse pressure gradient case, $Re_\theta = 27328$ at Inlet

Case	h/δ [−]	β [degree]	$\Delta X_{vg}/h$ [−]	l/h [−]	L/h [−]	λ/h [−]	CPU Time [hh:mm]
1 – 1	0.20	**13**	46	2	2	8	19:09
1 – 2	0.20	**18**	46	2	2	8	15:29
1 – 3	0.20	**23**	46	2	2	8	14:40
1 – 4	0.20	**28**	46	2	2	8	11:41
2 – 1	0.2	18	46	2	**1.400**	8	15:34
2 – 2	0.2	18	46	2	**2.267**	8	08:53
2 – 3	0.2	18	46	2	**3.133**	8	15:26
2 – 4	0.2	18	46	2	**4.000**	8	13:07
3 – 1	**0.200**	18	*46.4*	2	2	8	18:44
3 – 2	**0.252**	18	*45.2*	2	2	8	18:04
3 – 3	**0.304**	18	*47.4*	2	2	8	17:16
3 – 4	**0.356**	18	*48.1*	2	2	8	19:28
3 – 5	**0.408**	18	*45.1*	2	2	8	20:37
3 – 6	**0.460**	18	*45.1*	2	2	8	21:40
4 – 1	0.37	18	56	**1**	2.5	6	09:51
4 – 2	0.37	18	56	**2**	2.5	6	07:19
4 – 3	0.37	18	56	**3**	2.5	6	07:39

3.3.3 Results & Discussion

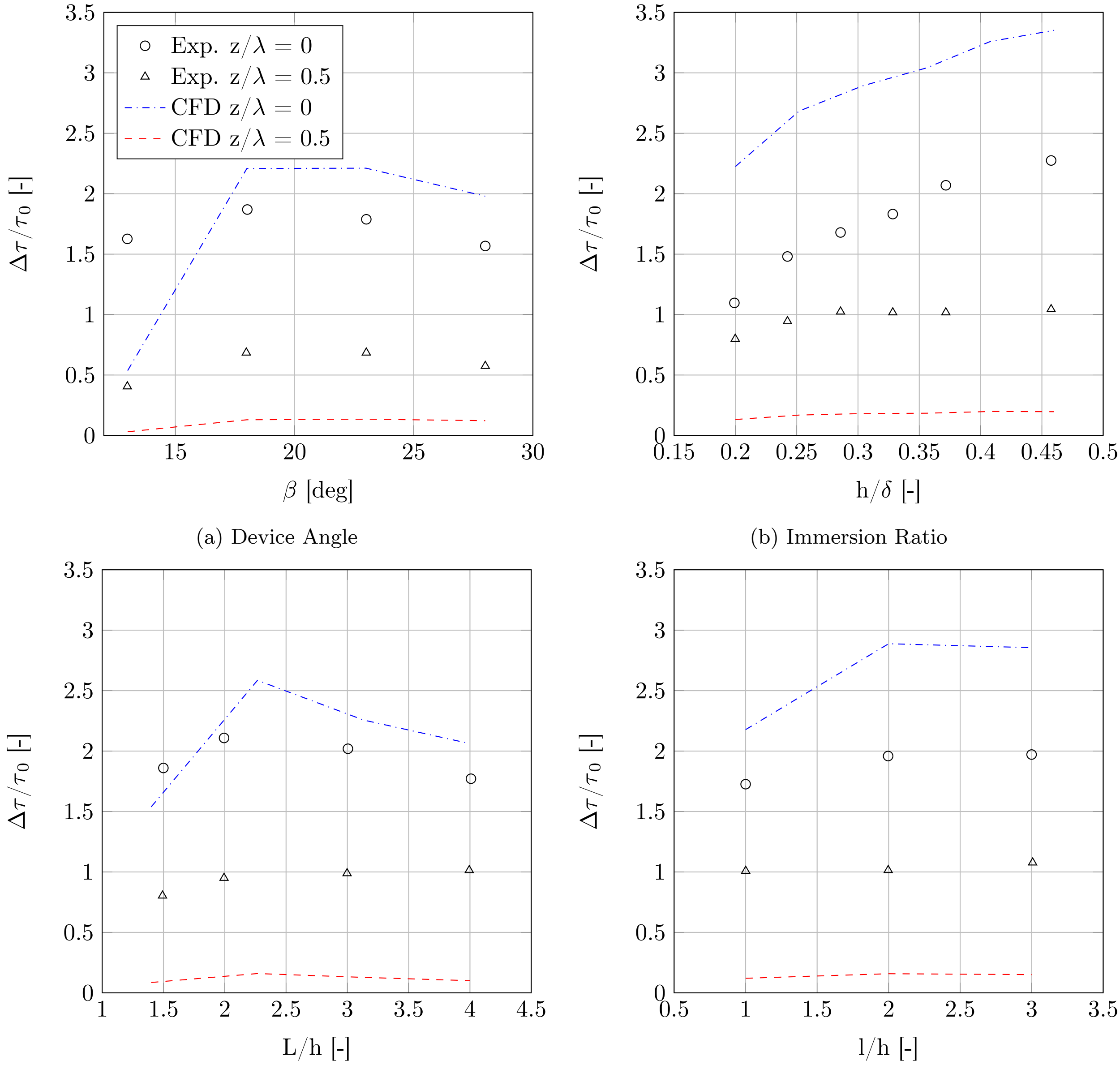

(a) Device Angle

(b) Immersion Ratio

(c) Trailing Edge Spacing

(d) Aspect Ratio

Figure 3.13: Parameter study comparison between BAY model and experimental data for adverse pressure gradient over a bump, $Re_\theta = 27328$ at Inlet

In Figure 3.13 the results of Table 3.5 are shown and compared to the experimental data from Godard and Stanislas[46]. In the results $z/\lambda = 0$ refers to a position between two vortex vanes, whereas $z/\lambda = 0.5$ is along the axis between the two vortex pairs. Taking into account the differences noted previously in Section C.3, it can still be said that the BAY model matches the overall trend with respect to parameter variation.

For all four parameters tested the BAY model exhibits similar trends and peaks around the values shown by the experimental data. However, there is a offset present in all parameters. Especially for the variation of the immersion ratio, a significant offset can be seen. This is explained by the different upstream position from the measurement position. Godard and Stanislas[46] have measured at $\delta X_{vg} = 56$ which is ten device heights further upstream, which means the effects would be less at the measuring point. Overall offset found in the results can be attributed to the fact that the flow without the vortex generators already has separation, changing the value of τ_0. For small device angles and trailing edge spacing, Figures 3.13a and 3.13c, the BAY model seems more sensitive than the experimental data. However, this could be due to the difference in the unperturbed flow.

An attempt to investigate the flow parameters in a similar fashion to Chapter 2 was made, however, it revealed secondary structures that influenced this analysis significantly. For the case $1-2$ these structures are highlighted with iso volumes based on the λ_2 criterion as shown in Figure 3.14. These structures have been found in all cases, though for last few runs in case 3 the vortex was seen to move more in a spanwise direction. Whereas for case 4–3 the structures are less distinguishable.

It is not entirely clear where these structures come from and how physically correct their presence is. In Godard and Stanislas[46] only a select few spanwise planes from the PIV planes are shown, which do not seem to exhibit similar structures nor do the authors mention having observed them at all.

One possible explanation for these structures might be the Görtler vortices as summarised in Section 2.2. Papers such as the work of Craft et al.[93] have shown that RANS models are capable of capturing the dynamic and unstable event of Görtler vortices. Considering the criteria described by equation (2.12) the flow over this bump should trigger the Görtler vortices, though as mentioned in Section 2.2 this criteria is subject to research and the flow can have a delayed response to the perturbations. Nonetheless, the values in the region of the secondary structures are well above the threshold for instability.

Marquillie et al.[94] have performed a DNS at a low Reynolds number based on inlet height of roughly 600 on geometry that resembles the bump that was modeled in this chapter. In their results Marquillie et al.[94] have observed coherent structures that transform into counter rotating vortices due to instability. In addition Marquillie et al.[94] have also noted the presence of horse shoe vortices.

Considering these arguments, it is very likely that the vortices from the vortex generator could perturb the flow in such a way that it becomes unstable in the boundary layer and produces coherent vortex structures as shown by Figure 3.14. However, the structures that appear alongside the vortices produced by the vortex generator are turning in the same direction, they are not counter rotating with respect to the vortex they appear alongside of. Considering this is often the case when Görtler vortices appear it may suggest that something else is happening.

Nonetheless, the results from Figure 3.13 does show a similarity between the experimental results and the CFD simulations. Given the fact that capturing the base flow is not a trivial matter, as discussed in Section 3.2.3, and that a flow of this nature is prone to instabilities it is not so surprising to see secondary structures appear in the simulations.

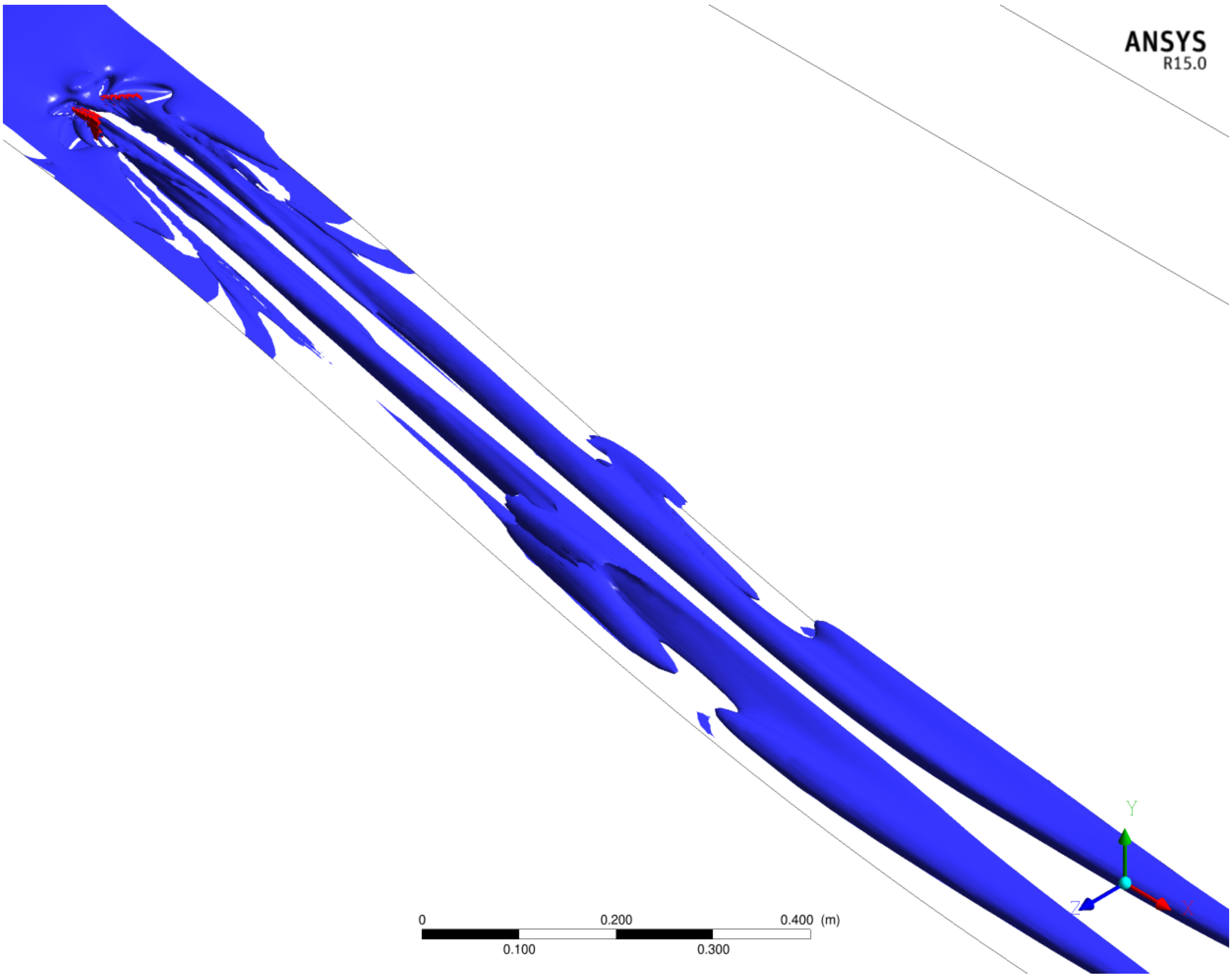

Figure 3.14: Iso volume of λ_2 showing the vortex structures created along the tail end of the bump for case 1 – 2

Chapter 4

Polar Comparison For Thin and Thick Airfoils

4.1 DU-97-W-300

In this section the effects of adding a vortex generator pair on the DU-97-W-300 will be presented. The Reynolds number based on the chord length has been observed to be 3e6 in the experiment. The flow over the clean airfoil is tripped and will also be compared. The DU-97-W-300 is known as a thick airfoil with a thick trailing edge, typical for airfoils in the root area of a wind turbine blade.

4.1.1 Experimental Description

Experimental data obtained from a wind tunnel experiment on a DU-97-W-300 airfoil will be used to evaluate the performance of the BAY model on an airfoil. A description of the airfoil can be found in Timmer and Van Rooij[95] and the experimental data is obtained from Siemens Wind Power.The boundary layer is tripped with zigzag tape which is 0.5 mm high, 12 mm thick and at angles of 60 degrees. The zigzag tape is placed close to the leading edge. It will be a second attempt to investigate the performance in an adverse pressure gradient flow. Furthermore, the effect on the pressure distribution can be analysed by comparing the values for the lift and drag coefficient. For this purpose the aforementioned airfoil will be simulated for a range of angles of attack in order to obtain, among others, the polar data that will be used for comparison.

The experimental data has been obtained from a measurement campaign conducted in the Low Turbulence Tunnel at the facilities of Delft Technical University. This tunnel features a test section of 1.25 by 1.80 meter and 2.60 meter in length and has a turbulence level less than 0.1%. The values for lift and post-stall drag have been obtained from the pressure distribution and the pre-stall drag is averaged from the wake measurements.

The vortex generators are placed at $x/c = 0.55$ but the geometry of the delta vortex generators cannot be shared publicly.

4.1.2 Flow Without Vortex Generators

Modeling the flow over a thick airfoil with a significant trailing edge can be a difficult task for RANS solvers, no matter the turbulence model used. Therefore, the flow over the airfoil without the vortex generators is also modeled, provided a benchmark to compare the results with the vortex generator to. It will also be used to identify the region of stall, since this will most likely be over predicted by the RANS simulation.

The mesh for this simulation is based on a 1 meter chord with an area of influence shaped like a circle with a diameter of 6 chords. This circle can rotate inside the actual flow domain, which is a rectangle that has edges with 200 chords length. This ensures there will be no effect of the domain on the airfoil and the flow can develop without any restrictions. The rotation is accomplished with Ansys CFX's General Grid Interface (GGI), which facilitates the connection between two, potentially non-matching, faces. This connection is done through interpolating values across an interface between two domains. The GGI ensure conservation by balancing the flux on from both domains at the interface. This setup means there only needs to be one mesh with which all angles of attack can be computed. An example of such a setup is shown in Figure 4.1, where Far Field resembles the outer domain and Near Field the inner domain containing the airfoil.

The final mesh setup contains 10.8e6 elements. Along the surface 1200 elements are placed in a linear fashion in streamwise direction, and 30 elements were placed in a similar fashion along the span of the airfoil. Due to the domain size only covering a single vg pair, large three dimensional separation will most likely not be captured. The boundary conditions and details for the GGI are listed in Table 4.1.

Table 4.1: Overview of boundary conditions for simulating flow over an airfoil

Far Field	
Location	Boundary Condition
Inlet	Uniform Streamwise Velocity & Turbulence Intensity
Outlet	Averaged Static Pressure with Relative Pressure at 0 [Pa]
Top	No Slip Wall
Bottom	No Slip Wall
Sides	Symmetry
Near Field	
Location	Boundary Condition
Airfoil Surface	No Slip Wall
Sides	Symmetry
Interface	
Mass & Momentum	Turbulence
Conservative Interface Flux	Conservative Interface Flux

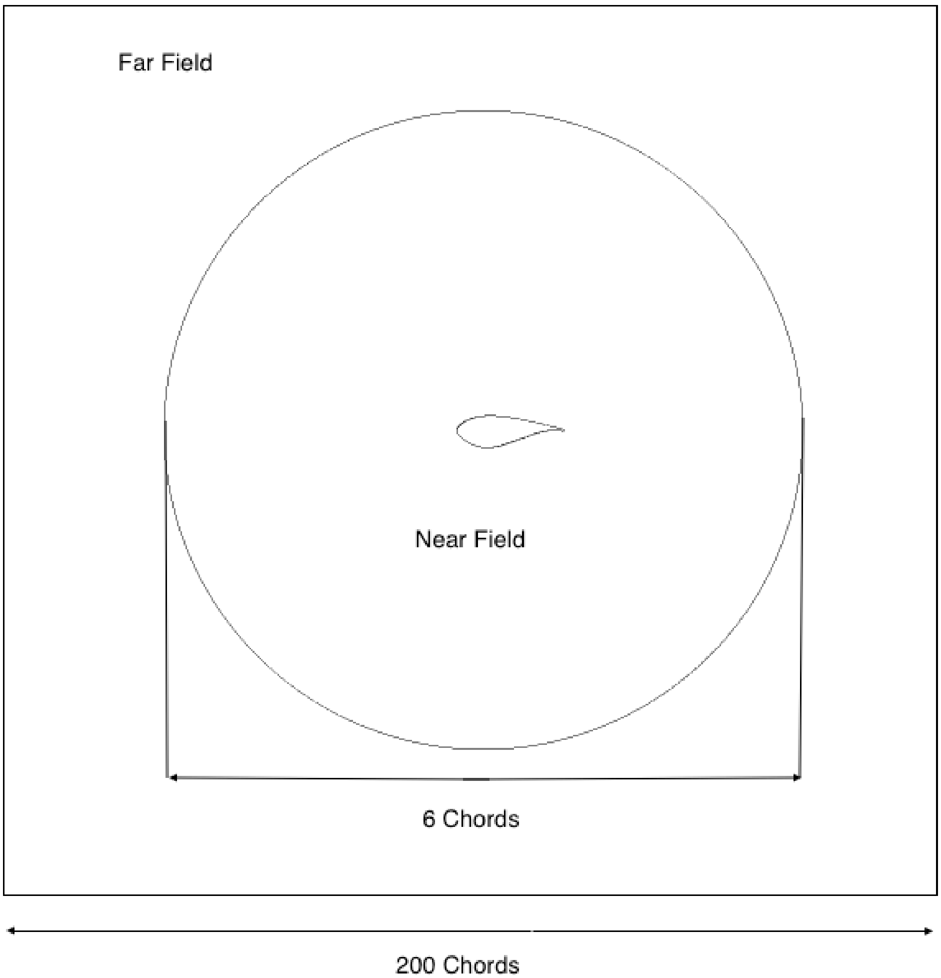

Figure 4.1: Illustration of the airfoil domain with GGI Far Field and Near Field domains and dimensions

A mesh grid independence study has not been conducted for this airfoil for several reasons. First, the mesh is based on a mesh that has been used previously and has been confirmed to produce accurate results. The previous efforts on grid independence study have not been successful, despite the second attempt resizing the mesh in a rigorous manner. However, the validation has shown up until this point that the results are nonetheless quite accurate with respect to experimental data. Considering simulating a polar on a large mesh will take a considerable amount of time the grid independence study is neglected.

For the simulation setup the Shear Stress Transport with the curvature correction is used with a turbulence intensity of 1% to capture the low turbulence intensity of the wind tunnel. Initial analysis of the flow over the airfoil without vortex generators revealed a significant overprediction of the stall angle, between 13 and 14 °. At these high angles it was found that the vortex generator setup modeled by BAY did not produce any significant delay in stall or increase the lift. To reduce the effect of overpredicting the stall angle the Kato-Launder and curvature correction production limiters are used. Ideally the numerical domain would be larger, in order to facilitate the modeling of three dimensional stall, but this would lead to an oversized mesh with a long computational time.

In order to facilitate a stable simulation of the flow over the 3-D domain of the airfoil a 2-D analysis with slip conditions on the surfaces is used. The airfoil is at an angle of attack of zero degrees and the resulting flow is interpolated onto the 3-D Domain. Afterwards, each subsequent angle is computed based on the previous results. Besides the residual and the imbalances, the lift and drag coefficient are also monitored to ensure convergence has been obtained. However, for angles below minus three and above fourteen degrees the airfoil starts to shed vortices, causing the solution to oscillate. Those results have been excluded from the analysis. Due to the modification of the turbulence model the flow at the pressure side of the airfoil started to exhibit separation at 1 ° and 0 °, this was not seen with the unmodified turbulence model.

In Figure 4.2 the results for these simulations are compared to experimental results. Figure 4.2a shows the polar for the lift coefficient. It can be seen that with CFD analysis, with the modifications mentioned previously, is capable of capturing the stall angle but it still features an overprediction of the lift value. Furthermore, past stall the lift coefficient does not recover as shown by the experimental values. This is most likely due to the reduced turbulence momentum as a result of the modifications. In the linear region the agreement with the experimental data is quite good. In Figure 4.2b it can also be seen that the values for drag are underpredicted by the CFD simulation, however for the separated flow the values for drag are more exaggerated. One explanation for the lack of accuracy in the drag prediction is that thickness of the boundary layer induced by the zigzag tape is not captured accurately. The velocity profiles are not available to check this assumption.

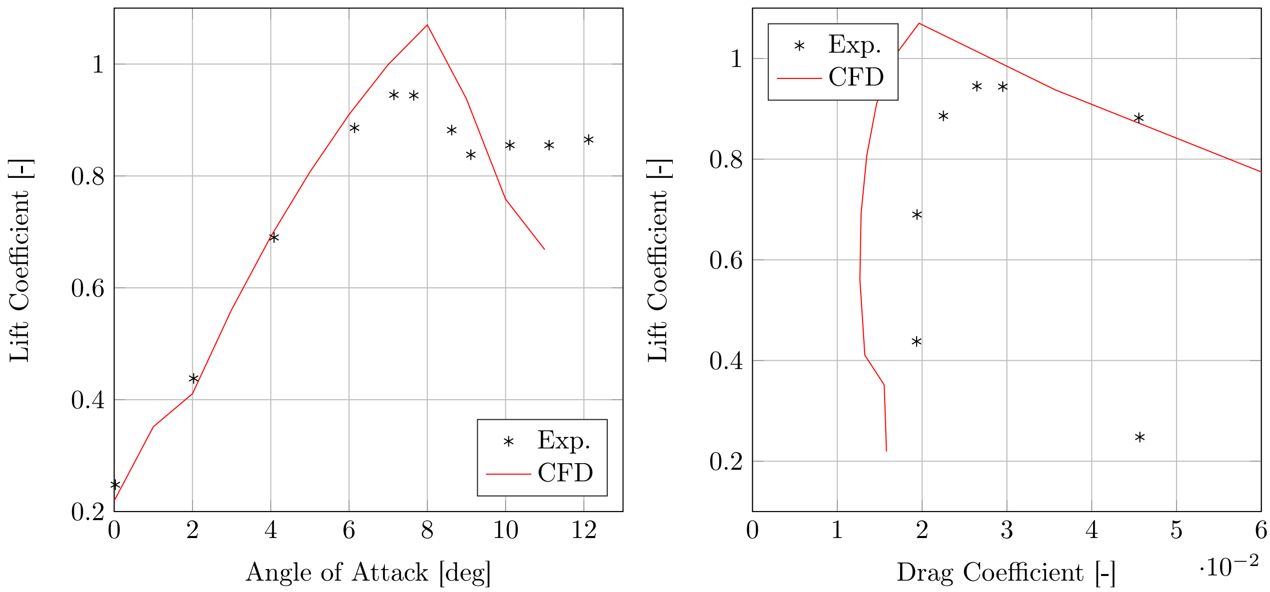

(a) Polar Comparison

(b) Lift and Drag Coefficient

Figure 4.2: Comparison between fully turbulent CFD simulations and zz tape tripped experiments for the DU-97-W-300 for Re = 3e6

4.1.3 Flow With Vortex Generators

To simulate the flow over the airfoil with vortex generators the same strategy, described in the previous section, is used. The addition of the vortex generator means the simulation needs to run longer in order to resolve the vortices. The simulation is further complicated by the interaction of these vortices by the vorticity structures at the trailing edge at some angles of attack. This interaction causes the trailing edge vortices to separate. This shedding of vortices means that solving the flow with a steady solver should be supported by an unsteady analysis, but there were no resources for this at the time. This phenomenon is displayed in Figure 4.3. This vortex shedding was only observed between angles of attack between zero and three.

This complexity is reflected in the computational time which averages to 14 hours on 128 cores for each angle in a polar computation. Convergence was determined based on the domain imbalances and lift and drag coefficients having settled.

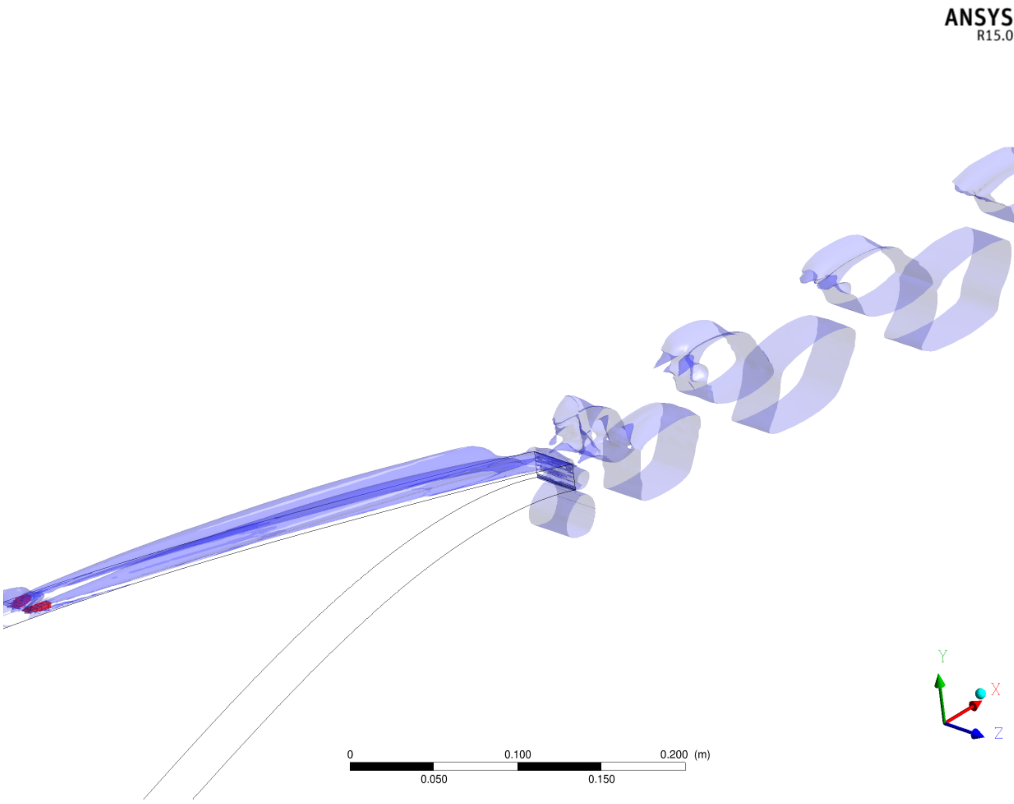

Figure 4.3: λ_2 Contours of vortex shedding on the DU-97-W-300 with Vortex Generators at $x/c = 0.55$ for Re $= 3e6$

4.1.4 Results & Discussion

Figure 4.4a shows the lift coefficient as a function of the angle of attack on the airfoil equipped with vortex generators. As can be seen the flow modeled by CFD is quite accurate for the linear region of the curve, similarly to the flow without the vortex generators. Additionally, it also features the overprediction in magnitude of the Lift as well as slight delay in the occurrence of stall. As shown by the residual of the lift magnitude between a setup with and without vortex generators, Figure 4.4b, the trend introduced by the vortex generators is captured by the BAY model but it is exaggerated. However, this is most likely due to the turbulence modeling setup.

Figures 4.4c and 4.4d show both airfoil setups for the experimental and numerical case, once again displaying that the effect of the vortex generators is captured by the BAY model apart from the increased magnitude and slight delay in stall angle. Figures 4.4e and 4.4f show the behavior of the lift coefficient as a function of the drag coefficient. As was previously established, CFD has a tendency to underpredict the effect of drag. Furthermore, the numerical setup does not include the base that is added along with the vortex generators on the actual airfoil. Nonetheless, it can be clearly seen that the influence of adding vortex generators to the airfoil is captured by the numerical simulation.

In Figure 4.5 the velocity profiles at specific spanwise locations for an angle of attack of 6° and 10° are shown. Due to the counter rotating setup of the vortex generator there will be an area of upwash from the vortices, typically at $z/\lambda = 0$ and $z/\lambda = 1$, and an area of downwash at $z/\lambda = 0.5$. This effect is shown by velocity profiles of the simulations with the vortex generator containing more momentum, seemingly fuller, as shown clearly in Figure 4.5a. Whereas for upwash the velocity profile tends to show a deficit compared to the

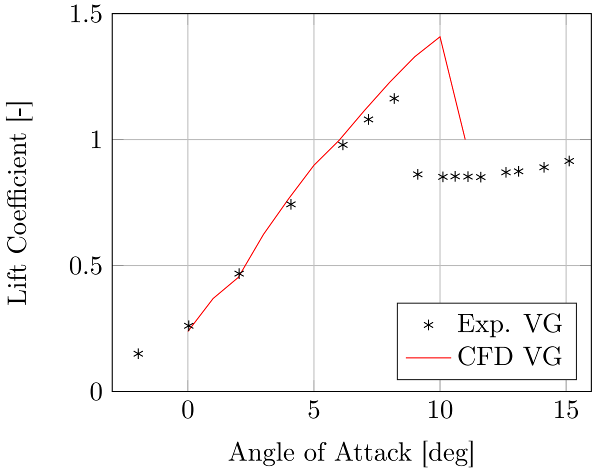

(a) Polar Plot

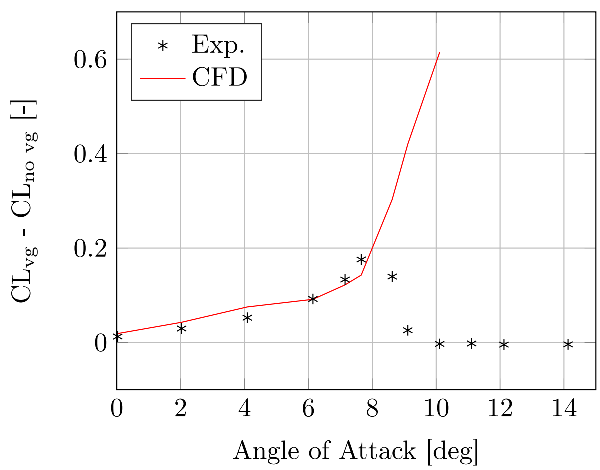

(b) Increase in CL

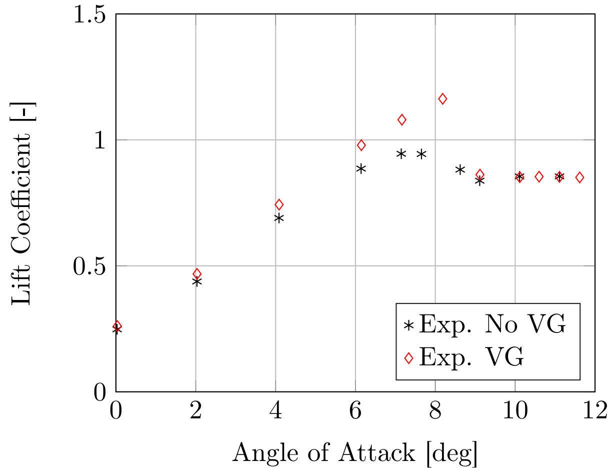

(c) Experimental Polar

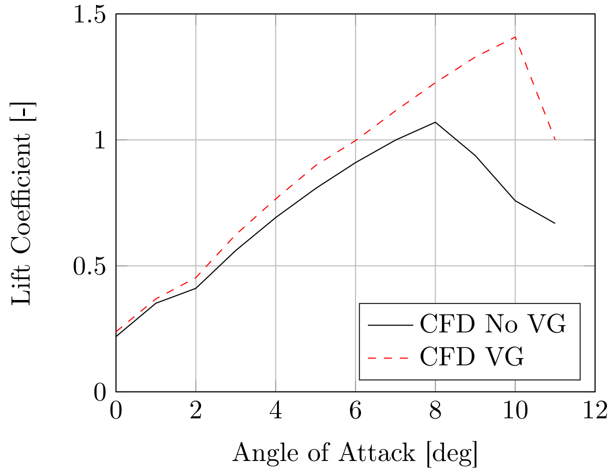

(d) CFD Polar

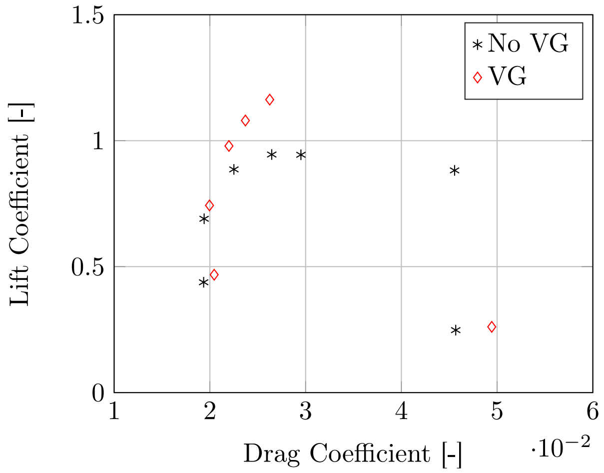

(e) Lift vs. Drag Exp

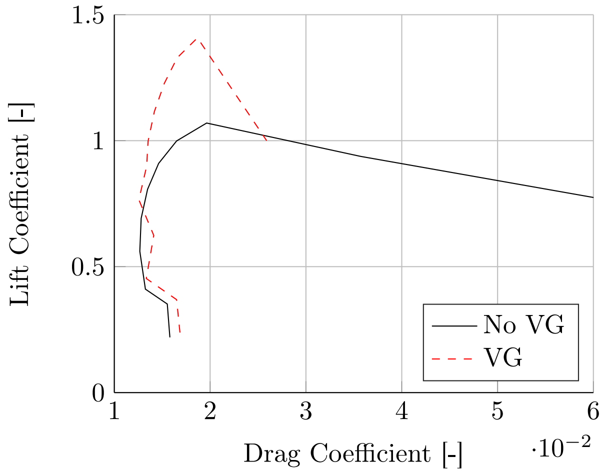

(f) Lift vs. Drag CFD

Figure 4.4: Polar Evaluation of fully turbulent CFD Simulations of vortex generators at $x/c = 0.55$ on the DU-97-W-300 for Re = 3e6

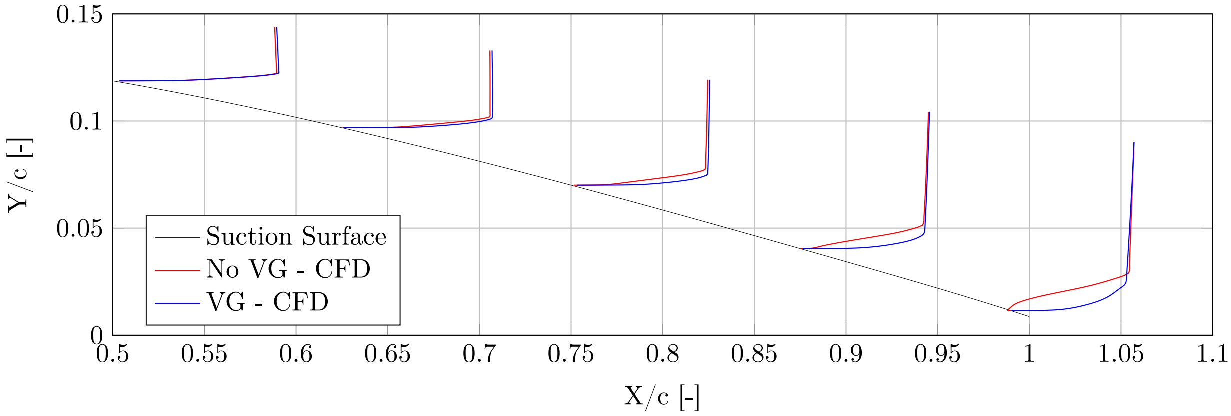

(a) Angle of attack = 6° at $z/\lambda = 0$

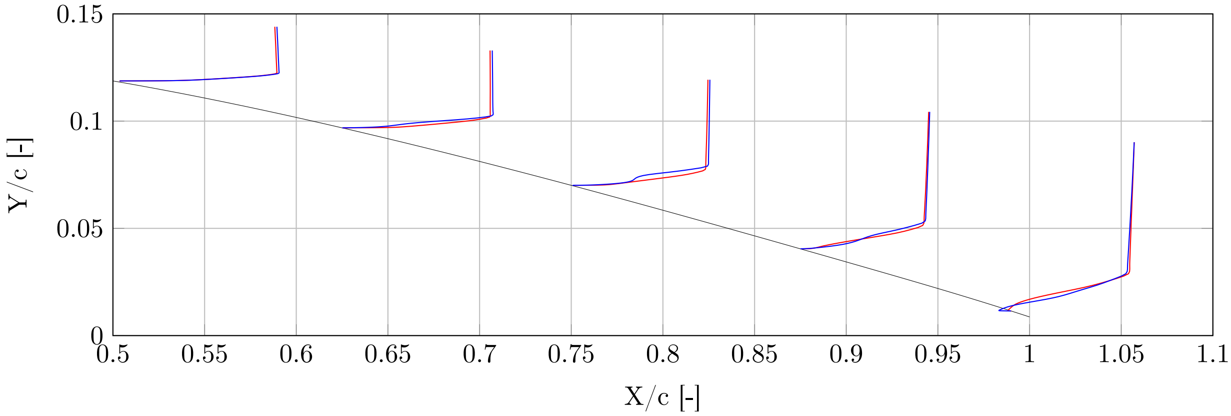

(b) Angle of attack = 6° at $z/\lambda = 0.5$

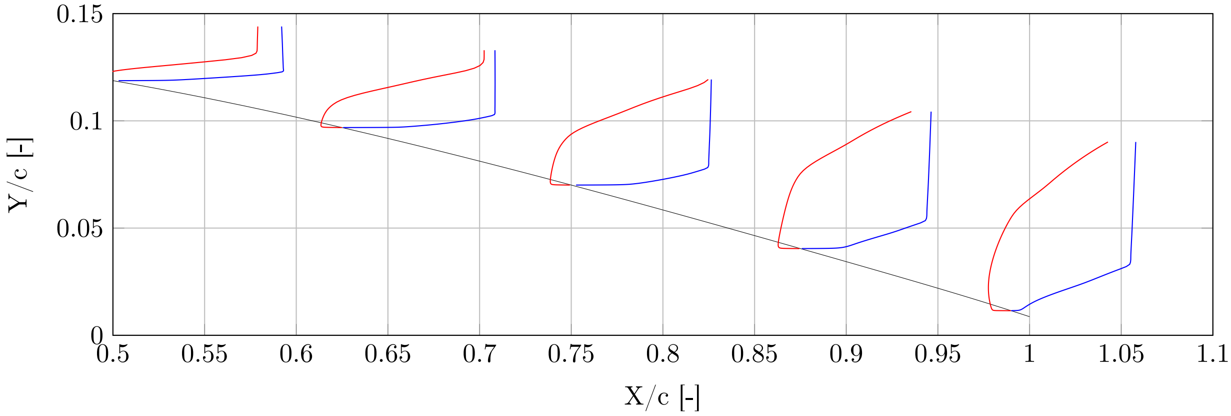

(c) Angle of attack = 10° at $z/\lambda = 0$

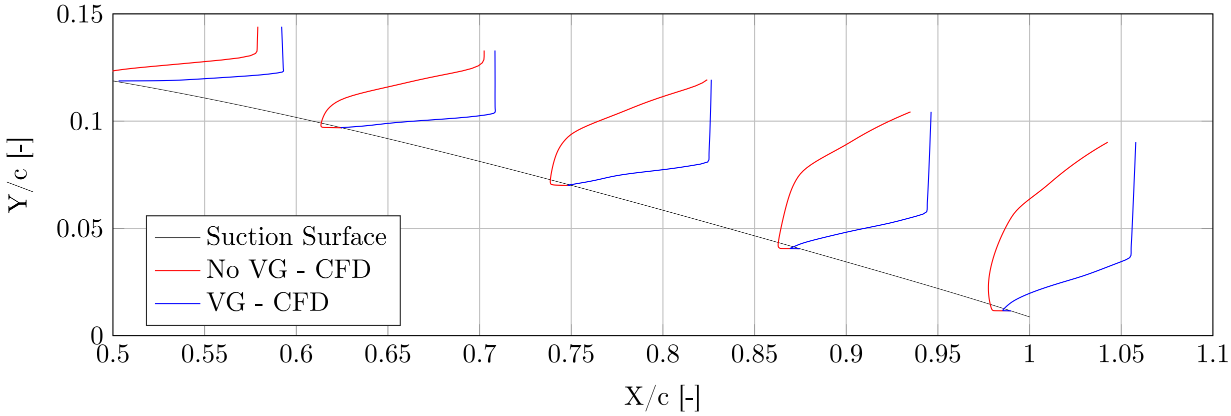

(d) Angle of attack = 10° at $z/\lambda = 0.5$

Figure 4.5: Streamwise velocity profile comparison for vortex generators at $x/c = 0.55$ on the DU-97-W-300 for Re = 3e6 at AoA of 6° and 10°

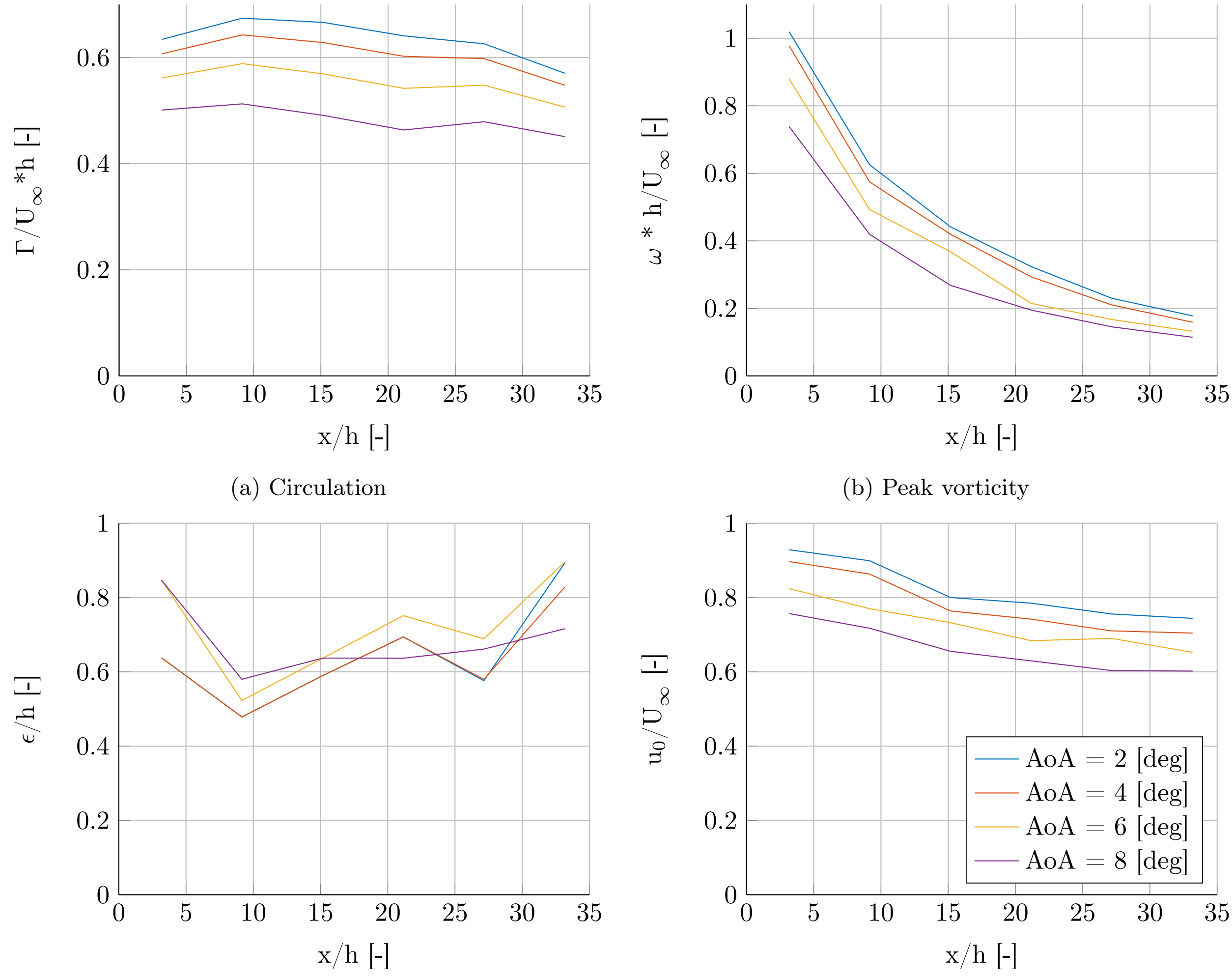

(a) Circulation

(b) Peak vorticity

(c) Core radius

(d) Core velocity

Figure 4.6: Streamwise development of various parameters with vortex Generators at $x/c = 0.55$ on the DU-97-W-300 for Re = 3e6, Angle of Attack = 2, 4, 6, 8 °

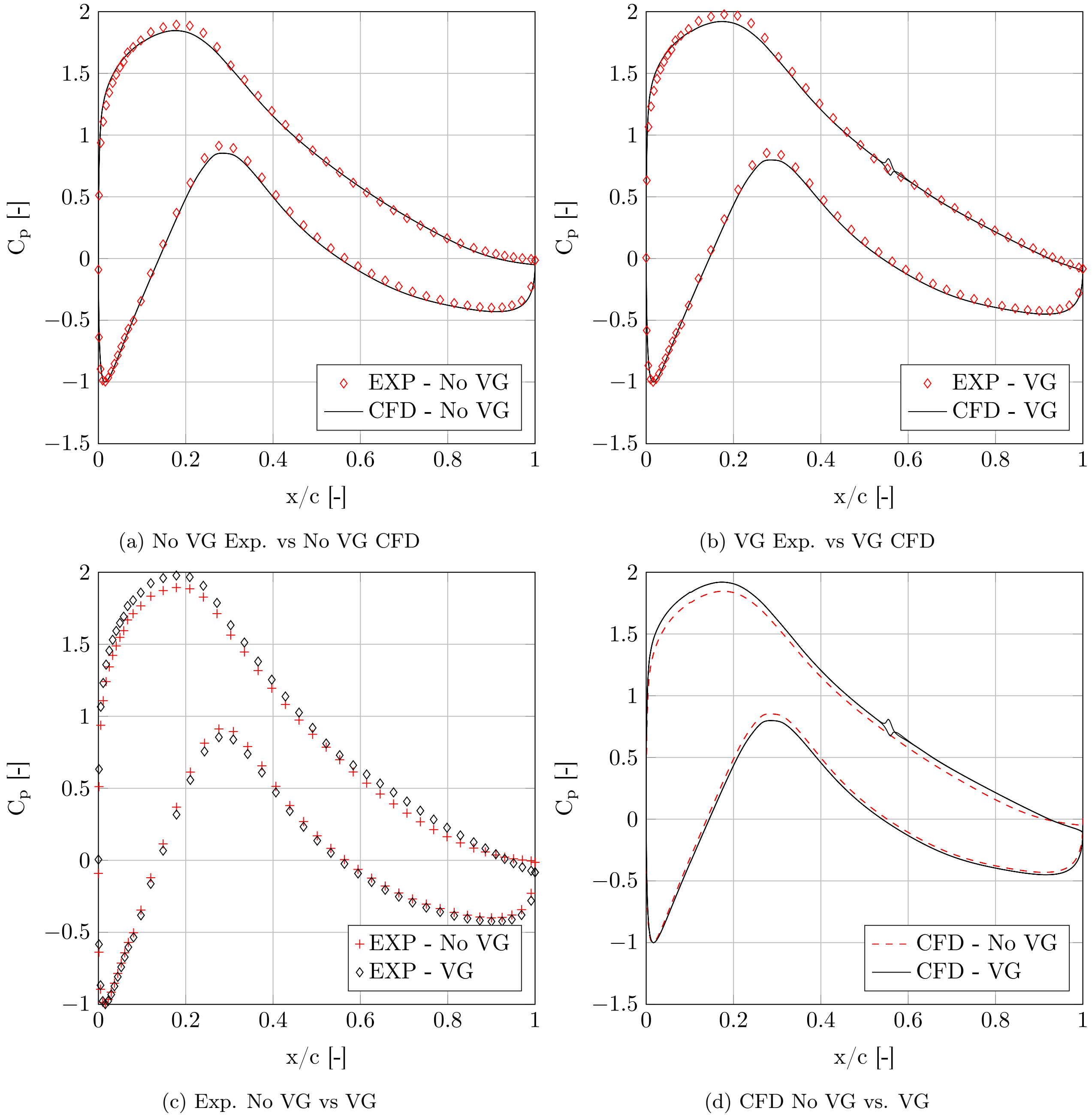

(a) No VG Exp. vs No VG CFD

(b) VG Exp. vs VG CFD

(c) Exp. No VG vs VG

(d) CFD No VG vs. VG

Figure 4.7: Pressure coefficient comparison for vortex generators at $x/c = 0.55$ on the DU-97-W-300 for Re = 3e6, Angle of Attack = 6 °

baseline, as shown by Figure 4.5b. As the flow travels downstream there can even be a slight separation at the trailing edge, as shown in Figure 4.5b.

Figures 4.5c and 4.5d show that stall is clearly prevented with the addition of the vortex generators. The previous mentioned regions of upwash and downwash can also still be observed at this angle of attack.

Figure 4.6 shows the streamwise development of vortex parameters, as shown in the previous chapters, for a range of angles of attack. Though there is no experimental data available to validate these tendencies, they are nonetheless valuable to gain insight into the flow parameters. For instance, Figure 4.6a shows that the circulation of the vortices can be considered constant with only a slight hint of dissipation towards the trailing edge. Furthermore, the magnitude of circulation decreases as the angle of attack increases. This is due to the boundary layer growing and becoming more turbulent, leading to a general drop in velocity across the vortex generator. This is further reflected by the tendency in peak vorticity, Figure 4.6b, where magnitude drops as the angle of attack increases.

For all angles of attack a slight growth of the vortex size can be observed in Figure 4.6c. The initial vortex core seems to be larger, but this may be overpredicted due to the presence of the wall having a strong effect on the velocity distribution. The tendency shown by core velocity, Figure 4.6d, shows opposite behavior compared to the results of the zero pressure gradient. This is most likely due to the general flow deceleration being stronger than the local flow of the vortices. The reduction in the velocity components towards the trailing edge is dominates the flow to such an extent that secondary flow analysis, such as convection velocity, is difficult to accomplish.

The distribution of the pressure coefficient is plotted in Figure 4.7 to provide a method to look for additional lift gained by adding vortex generators. Figure 4.7c shows that for the experimental observations there is a clear increase in pressure on the pressure surface around $x/c = 0.3$ and a decrease on the suction side, near the leading edge as well as near $x/c = 0.5$. These trends are matched by the results obtained from CFD as shown by Figure 4.7d. However, as shown by Figure 4.7b, the slope of pressure along the suction side at the leading edge is not matched entirely. Though this is most likely attributed to a lack in accuracy in the base flow, shown in Figure 4.7a, where a similar trend in the offset can be spotted.

At a chordwise position of $x/c = 0.55$ two bumps can be spotted in the pressure distribution for the CFD results in Figure 4.7b. These show the pressure decrease in the downwash region, along the center axis of a vortex generator pair, and the pressure increase along the upwash region, at the outskirt of a vortex generator pair. In the experimental results these effects are averaged along the span.

4.2 DU-93-W-210

The flow over the DU-97-W-300 is difficult to model due to the thickness of the airfoil and its thick trailing edge. Therefore a second attempt is made with the DU-93-W-210, which is a much thinner airfoil. The analysis on the DU-93-W-210 will cover a smaller number of angle of attacks because a majority of the flow features have already been investigated on the DU-97-W-300 with success. The Reynolds number based on the chord length has been observed to be 1e6 in the experiment.

4.2.1 Experimental Description

The measurement campaign of the DU-93-W-210 was carried out at a Reynolds number of one million on a clean airfoil surface. This data has been kindly shared by ir. W.A. Timmer and can also be found in Timmer and Van Rooij[95]. The values for lift and post-stall drag have been obtained from the pressure distribution and the pre-stall drag is averaged from the wake measurements. These measurements were carried out in the TU Delft Low Speed Wind Tunnel on an airfoil with a 0.6 meter long chord. The setup for the vortex generators is shown in Figure 4.8 and measurements have been obtained for three chordwise positions, $x/c = 0.2$, 0.4, 0.6.

4.2.2 Flow Without Vortex Generators

The mesh for the DU-93-W-210 is made in a fashion similar to that of the DU-97-W-300 described previously. It also features a 1 meter chord with an area of influence shaped like a circle with a diameter of 6 chords. For the purpose of obtaining results for various angles of attack the GGI method is once again applied. The final mesh setup contains 12.7e6 elements. Along the surface 1120 elements were place with a higher density in the spanwise region where vortex generators would be place. Along the span 30 elements have been placed, but for the outer domain only 15 elements were used. The GGI method is capable of interpolating between the domains, enabling a reduction in mesh size. The first boundary cell height was set accordingly to $y+ < 1$.

In Figures 4.9a and 4.9b the results are shown for the flow over the airfoil without the vortex generators. For the sake of comparison the results of Bertagnolio et al.[96] and experimental results at a higher Reynolds number with fixed transition have also been included. Bertagnolio et al.[96] have conducted a comparison

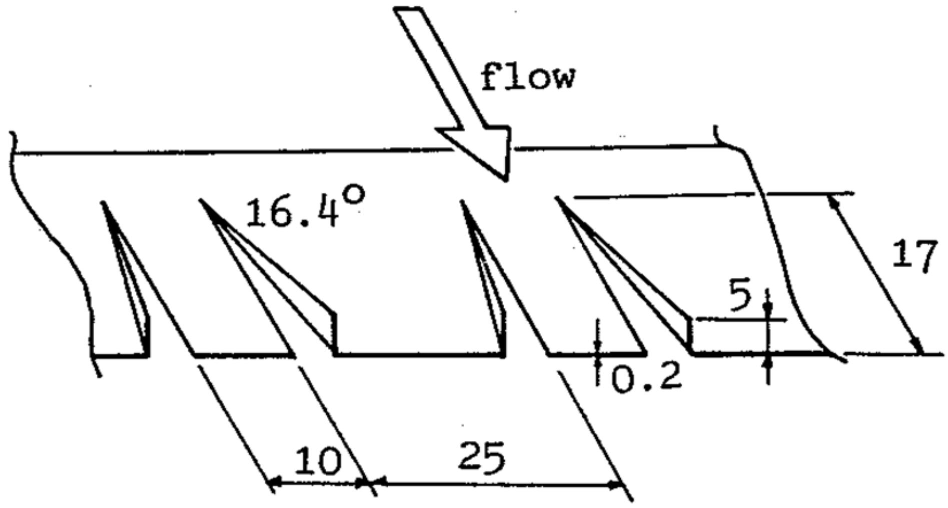

Figure 4.8: Illustration of the vortex generator setup on the DU-93-W-210 with 0.6 meter chord[95]

between experimental measurements and several setups for CFD, such as two dimensional RANS with fully turbulent and transitional modeling as well as three dimensional Detached Eddy Simulation (DES). As can be seen in Figure 4.9a both CFD analyses underestimate the magnitude of lift in the linear region and overestimate the stall angle. The difference in stall, Figure 4.9b, is less pronounced apart from the drag being slightly larger towards stall. The difference between the results from Bertagnolio et al.[96] and those obtained in this thesis could be attributed to the fact that in Bertagnolio et al.[96] it is a 2-D analysis compared to the 2.5-D analysis described in this thesis.

The second set of experimental data has been measured at a Reynolds number of 1.5e6 and features a zigzag tape of 0.38 mm height at a chordwise position of $x/c = 0.10$ on the suction side of the airfoil. This set does not feature vortex generators but is used to validate the fully turbulent behavior modeled by CFD. The comparison for lift, Figure 4.9a, shows that the magnitude for the linear region matches quite well in this case but the onset of stall and the stall angle are not matched. This is due to the overproduction of turbulent kinetic energy. A similar trend is shown for drag, Figure 4.9b, where for low angles of attack the drag is matched quite well but the values for stall do not match. Overall, the fully turbulent modeling of the DU93 can be considered accurate for the linear region with an overprediction of the stall behavior.

Bertagnolio et al.[96] have accomplished better results with a transition modeling for their turbulence modeling. A transition model has not been incorporated due to the added complexity and time. Furthermore, the transition location is not known which makes introduces uncertainty and additional setup time.The main purpose is to validate the flow with the vortex generators. The presence of the vortex generators trips the boundary layer. The closer the vortex generators are to the leading edge, the close the flow approaches a fully turbulent flow as modeled by CFD. This supports the decision to use fully turbulent modeling, which has been shown to be quite accurate in the linear region.

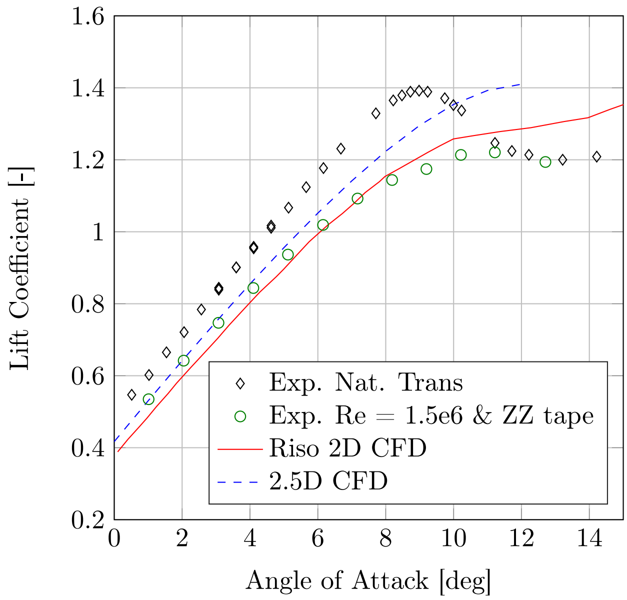

(a) Lift Coefficient

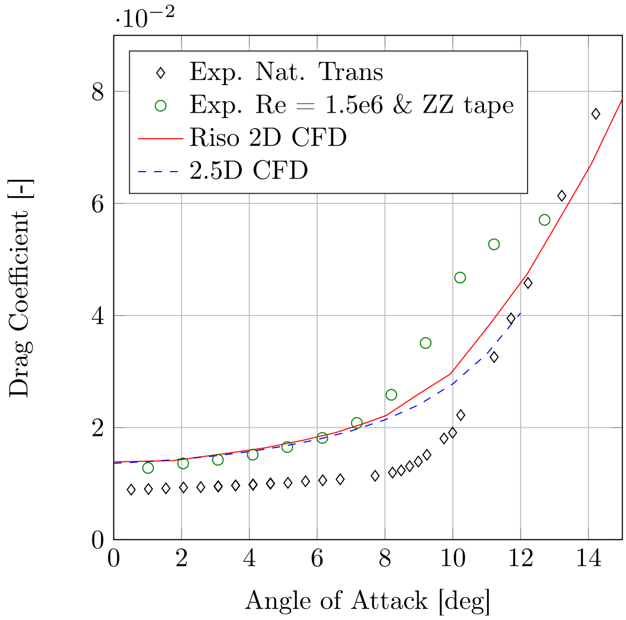

(b) Drag Coefficient

Figure 4.9: Comparison between fully turbulent CFD simulations and zz tape tripped experiments for the DU-93-W-210 at Re = 1e6

4.2.3 Flow With Vortex Generators

To compare with the measurements the flow for an angle of attack of 5, 9, 13, 15, 17° will be simulated for vortex generators at a chordwise position of $x/c = 0.4$. These angles are based on the results from the flow without the vortex generator. An additional run has been simulated for an angle of attack at 15° to better capture the onset of stall. The vortex generator geometry, depicted in Figure 4.8, is scaled to compensate for the larger chord in the CFD domain. A single angle of attack needed on average 20 hours on 256 cores to reach convergence. This was observed by monitoring the domain imbalances and the lift and drag coefficient values.

4.2.4 Results & Discussion

Figure 4.10a compares the lift polar for the flow with the vortex generators. It shows that the CFD simulations match the measurements quite well in the linear area. It is not clear whether or not the simulation with the vortex generators would have predicted the same stall angle. It was assumed that the overprediction observed in the stall angle in the flow without the vortex generators would have a similar effect on the flow with the vortex generators. CFD results would suggest the airfoil stalls around 16°, considering that the slope between 13° and 15° is showing a decrease with respect to the previous angles. This is an overprediction of 2° with respect to the simulation data. A similar trend can be seen for drag, Figure 4.10b, where the lower angles of attack are matched quite well by the BAY simulations whereas the trend in stall is not captured adequately, this is most likely due to the lack of large scale 3-D effects and steady state simulation.

Figures 4.10c and 4.10d highlight the difference that was foreshadowed in the discussion on the flow without the vortex generators. The vortex generators seem to make a more significant impact in the results obtained by CFD, shown in Figure 4.10d. However, as noted the results without the vortex generator is less accurate due to a choice in turbulence model. The presence of the vortex generators validates the fully turbulent turbulence model in this case. Additionally, the results from the DU-97-W-300 have shown it is possible to match the lift trends quite well with the vortex generators. Therefore, the gap shown in Figure 4.10d can be attributed mainly due to the choice in turbulence models and not an overestimation of the effect of vortex generators.

The pressure distribution at an angle of attack of 9°, shown in Figure 4.11, shows similar trends compared to pressure distribution shown for the DU-97-W-300. The pressure peak at the vortex generator is more pronounced in the experimental data, due to it being located closer to the accelerated flow. Once again, the pressure distribution from CFD shows the pressure along the center axis and the outskirts of a vortex generator pair, depicted by the bumps. The jump in pressure on the pressure side in the experimental data is caused by a laminar separation bubble. Though the CFD results do not contain this bubble or the pronounced acceleration, the results match quite well, as was previously shown in the polar comparison of Figure 4.10a.

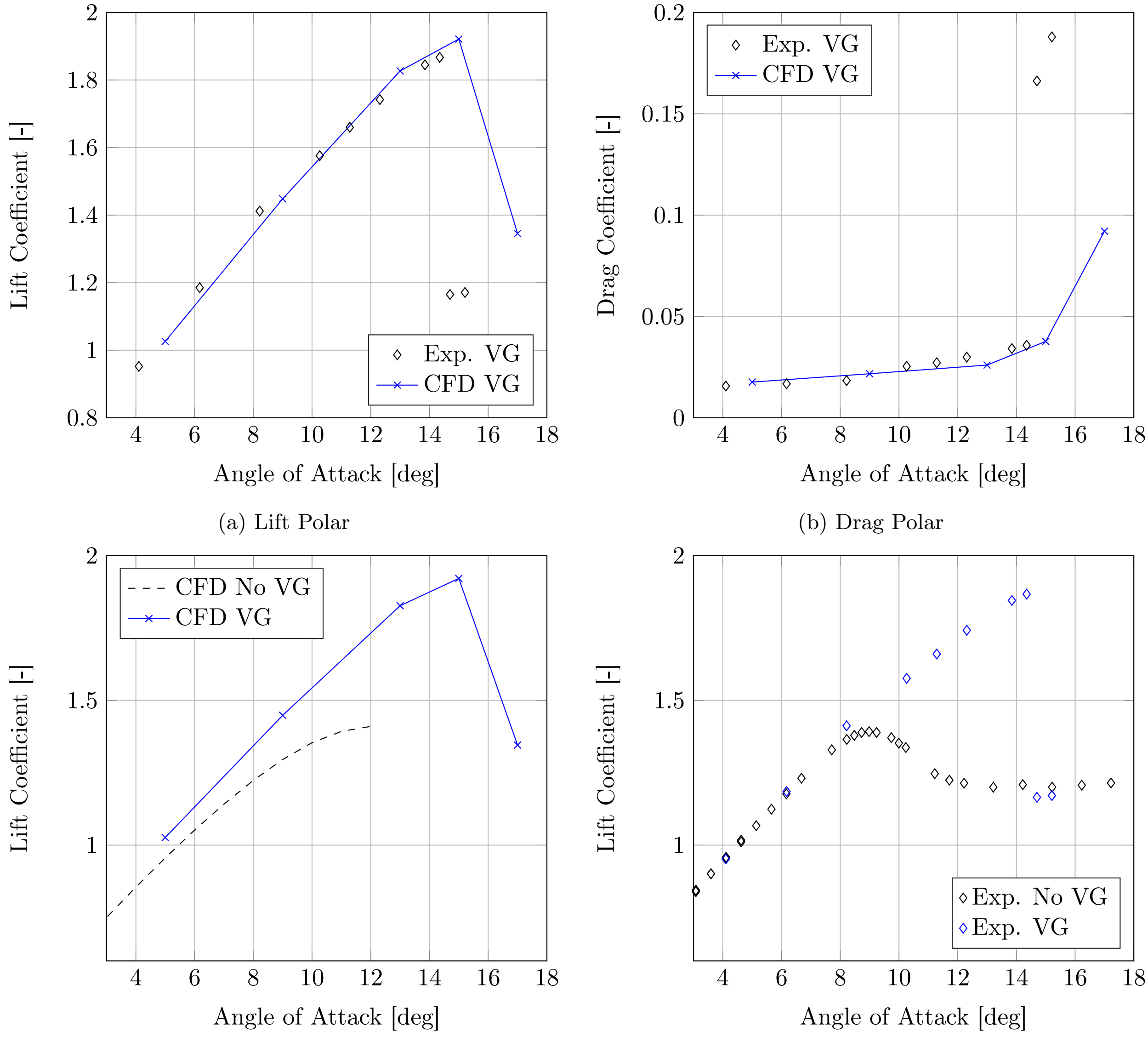

(a) Lift Polar

(b) Drag Polar

(c) CFD Polar

(d) Experimental Polar

Figure 4.10: Polar evaluation of CFD simulations of vortex generators at $x/c = 0.40$ on the DU-93-W-210 for Re = 1e6

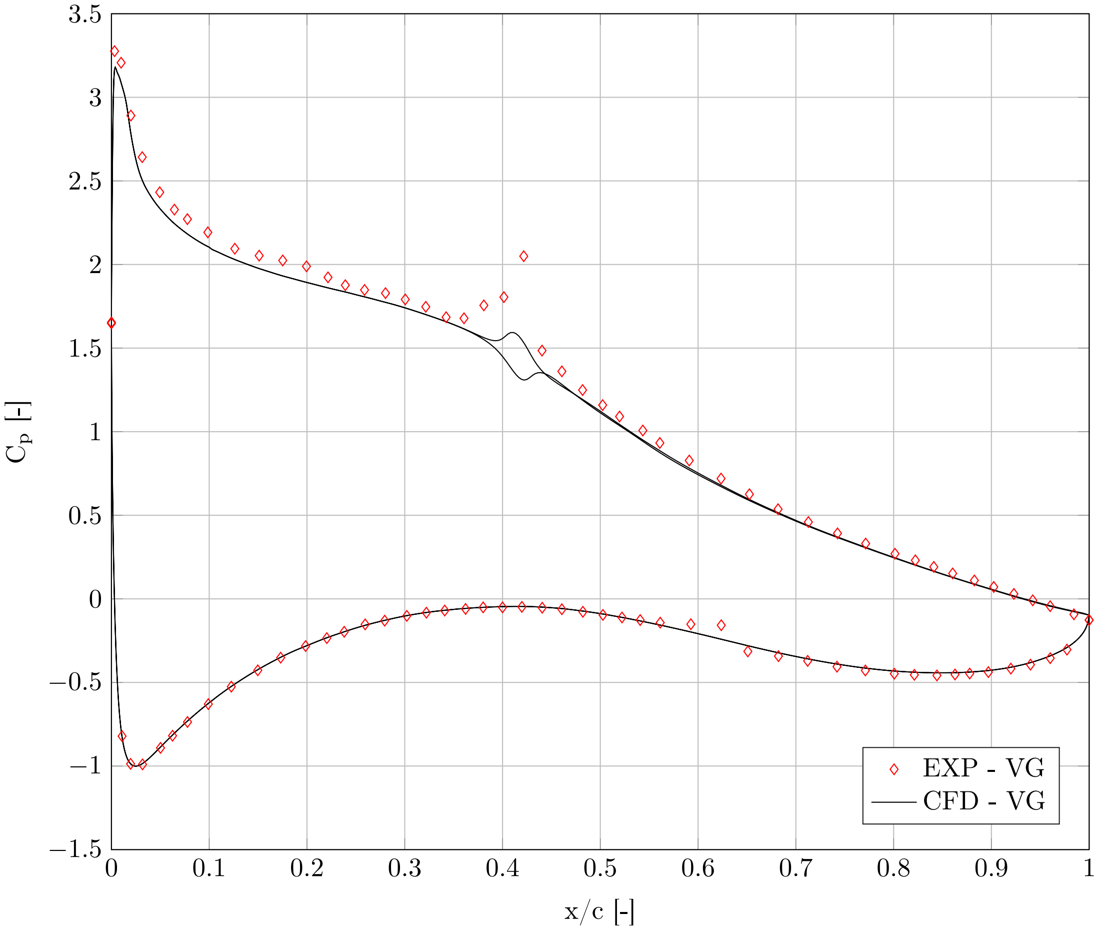

Figure 4.11: Pressure coefficient distribution for the DU-93-W-219 with vortex generators at $x/c = 0.40$ at Re = 1e6, Angle of Attack = 9°

Part III

Conclusion

Chapter 1

Conclusion

In this chapter the results and observations from Part II will be briefly summarised and discussed in the larger context of validating the BAY model implementation. Afterwards recommendations will be given that can build on the research described in this thesis.

1.1 Discussion

As laid out in the Introduction of this thesis, the purpose was to investigate the principle of boundary layer control through vortex generators and how it can be effectively modeled. Initial research of the published models revealed that the model proposed by Bender, Anderson, and Yagle[1] based on the lifting line theory could potentially be the most effective model. This model was implemented successfully, as evidenced by the validation in Section 1.4 of Part II, and subsequently validated with experimental data in a zero pressure gradient case. This revealed that the BAY model is capable of distinguishing between a rectangular and triangular vortex generator in a similar fashion as observed in experimental data. However, when it comes to a cambered vortex generator the BAY model may need modification. This is because the normal vector of a cambered vane changes along its chord, an effect that is currently not present in the BAY model.

Investigating flow parameters and BAY model setup has shown that the BAY model itself is not very sensitive to its inputs. Varying the volume the vortex generator is represented with and refining the mesh elements inside that volume do not significantly impact the accuracy of the BAY model. However, when the fluid body that encapsulates the vortex generator is coarsened, effects can be noticed. This is most likely due to the fact the initial downstream region is captured inside this fluid body, thus influencing the creation of the vortex.

A similar case has been simulated at a lower Reynolds Momentum Thickness number, see Appendix B, which showed a larger discrepancy between the simulation and the experimental values. This was also observed for fully resolved CFD analysis. The increased performance at higher Reynolds number can be explained based on the observations on turbulence modeling made by George and Tutkun[73]. A higher Reynolds number means that the assumption the turbulent energy cascades according to the $-5/3$ law is more valid.

When it comes to modeling the vortex generators in an adverse pressure gradient a two step approach was used. Experimental data from Godard and Stanislas[46] enabled the validation of the capability of the BAY model to perform a parameter study. Although validating the base flow proved to be difficult, due to missing crucial information and questionable assumptions, the results of the BAY model nonetheless matched the trends observed by Godard and Stanislas[46]. Modeling various setups for vortex generators shows similar optimal values for parameters such as the device angle, trailing edge spacing, and aspect ratio. Considering the uncertainties with the base flow it may be prudent to validate such a parameter study in an experiment that is easier to match.

The second step in validating the BAY model in an adverse pressure gradient involved replicating a polar for lift and drag on an airfoil. For this particular case a DU-97-W-300 and a DU-93-W-210 were considered, at a Reynolds number of 3e6 and 1e6 respectively. The former concerns a thick airfoil with a thick trailing edge, which can be challenging to solve. With the use of a curvature correction and the Kato-Launder production correction a decent match in the linear area of the lift polar is obtained. The stall angle is slightly over predicted and drag is significantly underpredicted. Nonetheless, the effect of adding the vortex generators is captured quite accurately. The amount of lift added per angle of attack matches the trend of the experimental data. Furthermore, effects such as additional drag and the up wash and down wash can be observed in the CFD results.

Matching the flow over the clean DU-93-W-210 airfoil did not match as well as with the DU-97-W-300, though this matches the trend of results published by others. Simulating this airfoil with RANS leads to an underprediction of the lift in the linear region and an over prediction of the stall angle. A different turbulence model might have improved the flow over the clean airfoil, but this was not the purpose. A fully turbulent flow can be a valid assumption for flow over an airfoil equipped with vortex generators. The agreement between the simulations and the measurements would suggest that this assumption was indeed valid. Furthermore, it confirms the results observed for the DU-97-W-300. Simulating vortex generators with the BAY model on an airfoil can capture the effects of stall delay and increase of drag according to trends observed by measurements.

In both the zero pressure gradient case and the first adverse pressure gradient case establishing grid independent results proved to be difficult. This is despite the fact the meshes were created according to principles of Richardson's Extrapolation and the Grid Convergence Index. A lack of grid independency indicates a larger uncertainty and the possibility of flow phenomena caused by the mesh geometry. However, these methods are based on simplistic meshes for general flow problems that generally do not contain dominant secondary flow phenomenon. Despite the lack of confirmation according to these theories, all simulations presented in this study have shown convergence and agreement with experimental data.

1.2 Recommendations

Based on the observations made in the previous section the following recommendations are made that can be used to follow up on the work shown in this thesis.

- **Confirm the trend of improved accuracy due to high Reynolds numbers.** The comparison of results on flat plates with a zero pressure gradient suggests that the model becomes more accurate with an increase in Reynolds number. Additional comparisons with other setups, such as on adverse pressure gradient, should be conducted in order to confirm this.

- **Investigate the flow development close the vortex generator.** As the flow analysis in chapter on the zero pressure gradient has shown, the downstream flow close the vortex generator shows the largest discrepancies. It might be more than a grid resolution issue due to the fact that even the fully resolved case still shows a significant gap with experimental data.

- **Investigate additional flow identification parameters.** Although the analysis in this thesis is not comprehensive, a large number of flow parameters were considered. Nonetheless, when some parameters seemed to match quite closely others were still quite off. The analysis of flow statistics and dynamics, for instance, could provide insight into these models that steady analysis cannot offer.

- **Investigate flow anomalies.** While validating the BAY model in the adverse pressure gradient the vortices generated by the vanes exhibited interaction with other flow structures. In the case of the flow over the bump secondary structures were observed, but could not be confirmed with experimental data. The results of the DU-97-W-300 polar showed a strong interaction between the thick trailing edge vortices and the vane vortices. However, all simulations carried out in this thesis have been steady and therefore these phenomenon could be a numerical artifact instead of physical flow phenomenon. Therefore, unsteady simulations and additional experimental data should be carried out to confirm these occurrences.

- **Improve the efficiency of the BAY model.** The purpose of this thesis was the validation of a model of vortex generators. However, the power of a model such as BAY is in a combination of both accuracy and a reduction in computational cost. Establishing the latter is not trivial, due to the fact that a good mesh depends on the users skill and has a large impact on solver time. Nonetheless, an attempt can be made to compare the solver efficiency. Furthermore, by adapting the BAY model constant and the linearisation coefficient significant gains in computational time can be made. Lastly, as a support measure, it would be valuable to investigate a proper method to determine grid independence outside of experimental validation.

- **Improve the setup of the BAY model.** Expanding the geometry representation capacity of the BAY model implementation. Allowing the modeling of airfoil like shaped vortex generators by facilitating a change in the model vectors along its chord. Adapting the algorithm to a three dimensional surface would also allow it to be applied on an entire blade of a wind turbine instead of a single section of it. Lastly, taking a closer look at the requirements for the wake mesh size will help in obtaining a certain level of accuracy from the BAY model.

- **Investigate the addition of drag to the BAY model.** The BAY model as it was published[1] and implemented in this thesis does not contain an expression for the drag induced by the vane. Chima[4] has suggested a method to accomplish this but does not validate or comment on the effects of adding this term. Adding this component could increase the accuracy of modeling the velocity deficit close to the vortex generator.

Part IV

Appendix

Appendix A

Zero Pressure Gradient Boundary Layer Development Simulation

A.1 Summary

During this thesis an effort was made to compute the flow through the wind tunnel from Lille. The primary reason for this was to familiarise with the CFD software. The secondary reason was to investigate how accurate the boundary layer development and other flow characteristics would be modeled by Reynolds Averaged Navier Stokes complemented by Shear Stress Transport turbulence modeling.

Two cases were analysed using numerical software, one being a 2-D flow and the other 3-D. Using papers published on experiments from the tunnel the boundary conditions were set. However, for the 3-D case computational limitations made it impossible to obtain grid independent results. When comparing the results to experimental data a significant difference could be seen between all three data sets. Further analysis of the turbulent kinetic energy suggests this may be partially due to the setup configuration.

A.2 Process

In two of the three validation cases the Turbulent Boundary Layer from Lille France has been used for the experimental data, which will be used to validate the vortex generator model. This meant that it would be valuable and necessary to document the numerical flow in these cases without the vortex generator, establishing a data set to compare the vortex generator model to. Considering the relative simplicity of modeling flow over a flat plate, it was also deemed to be a good method to familiarise with the software package.

Information about the wind tunnel has been obtained through the official website and an assortment of published papers. In Figure A.1 a schematic of the tunnel is shown. It should also be known that the test section is 1 meter in height and 2 meter in depth. As described by Carlier and Stanislas[29] the flow is tripped at the entrance of the tunnel, in order to increase the thickness of the boundary layer. A comparison between tripped and non-tripped flow shows that this does not significantly affect the turbulence statistics. Furthermore they mention that conditioning of the flow prior to entering the tunnel section leads to a turbulence level of 0.3 % of the external velocity at the entrance.

A manual with accompanying data, obtained from the experiments of Carlier and Stanislas[29], for the wind tunnel has also been provided. The data contains, among other things, the horizontal velocity along the height and turbulent kinetic energy for several Reynolds momentum thickness numbers. These will be used to compare the data from the numerical analysis.

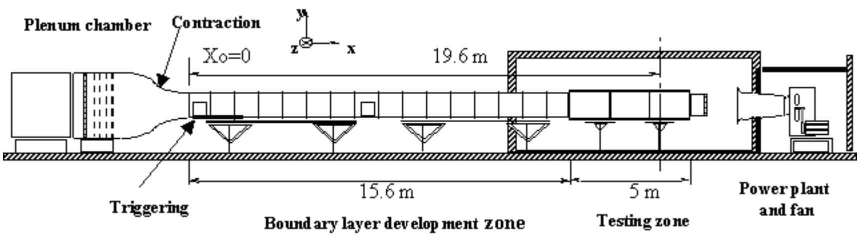

Figure A.1: Schematic of Large Wind tunnel for Boundary Layer[15]

The description from Carlier and Stanislas[29] will be used to determine the characteristics of the boundary

Table A.1: Boundary Conditions

Boundary	Type	Parameters
Front	Inlet	Hor. Velocity & Turb. Intensity
Back	Outlet	Static Pressure
Bottom	Wall	Roughness
Left	Symmetry	–
Right	Symmetry	–
Top	Symmetry	–

conditions. These are listed in Table A.1. It is assumed the floor can be modeled as a smooth wall, no mention is made of roughness in any of the papers about this wind tunnel. Furthermore, symmetry will be used to minimize the volume of the modeled domain.

At the front a uniform horizontal velocity will be ascribed that matches to the Reynolds momentum thickness number obtained in the experiments, $Re_\theta = 17000$. The turbulence will be modeled by the Shear Stress Transport, this should reflect the fully turbulent characteristic of the tripped boundary layer.

The mesh consists of hexagonal elements with a bias factor applied in the vertical direction. This is done to ensure the elements at the wall do not exceed a wall value of 1 without creating excessive elements. All other directions, horizontal and depthwise, are simply linearly spaced. For the latter direction two cases can be distinguished. The 2-D case has only a single element in the depthwise direction, assuming the flow can be 2-D. Whereas the 3-D case has several elements in the depthwise direction. The latter case, requires a significant increase in memory to compute the flow. The cases were run on a computer with sixteen GB of RAM which limited the amount of elements to twelve million. This causes a serious issue with results for the 3-D case because the results cannot be made grid independent. Trends can be spotted, but only with caution.

A.3 Results

For the 2-D case it was found that when using 800 vertical elements and 2000 horizontal elements the result is grid independent. The proof for this cannot be shown because data of the grid independence study was not saved. The wall height of the first cells is 0.1860, well below the suggested value of one. This was obtained by giving a high bias factor to the vertical elements, this could lead to extreme aspect ratios but it did not exceed any significant level. In Figure A.2a the results are shown at various streamwise positions, depicting the boundary layer development at an inlet velocity of 3.0 m/s. It can be seen that the development growth stabilises in the latter section, something which is also seen in the experiments.

In Figure A.2b the results are shown for the 3-D case. As mentioned, however, these are not grid independent because the equipment prevented any further increase of elements. The results shown were obtained with a mesh of 200 vertical elements by 2000 horizontal elements and 30 elements along the depth. The wall height of the first elements was below one again, 0.1436. It can be seen that the thickness of the boundary is much larger when compared to the 2-D case. Furthermore, the growth of the boundary layer does not seem to have stabilised as much as in the 2-D case.

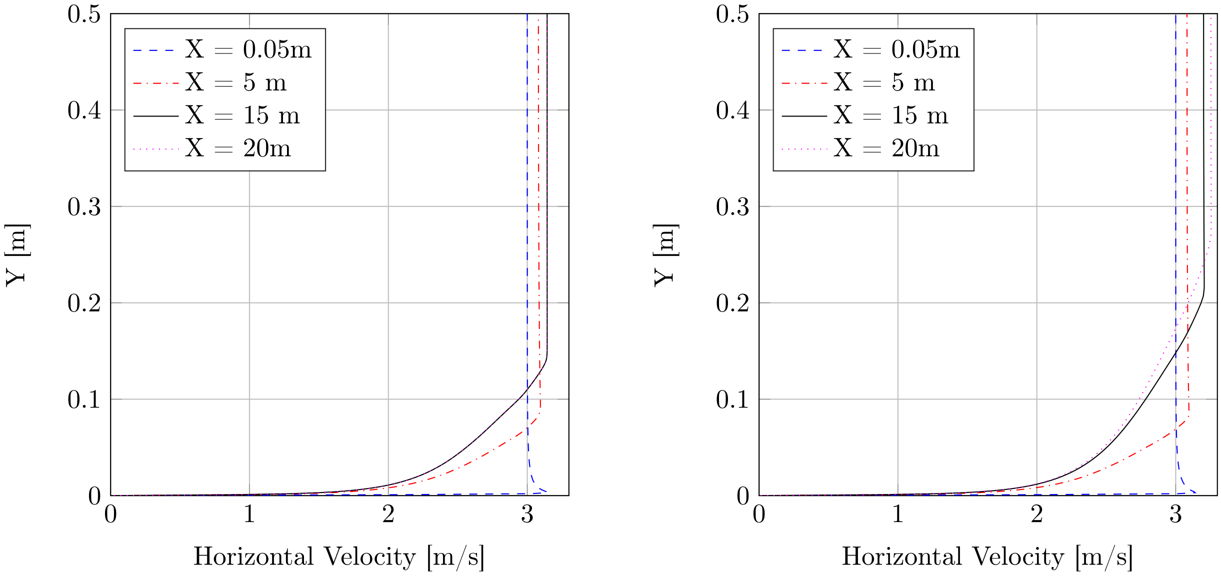

(a) 2-D Case

(b) 3-D Case

Figure A.2: Boundary layer development in numerical flow for $Re_\theta = 8200$

In Figure A.3a the velocity profiles at 20 meters from the entrance are taken and compared to the velocity profile gathered by hot-wire anemometry at 19.6 meters from the entrance. This figure shows that there is a significant difference between all three. To investigate the difference between these three results the turbulent kinetic energy at this location is also plotted, seen in Figure A.3b. This highlights that very close to the wall the 2-D and 3-D cases are actually quite similar but very different from the experimental values. This could point to a problem within the setup of the numerical solver, such as the roughness of the wall. The difference between 2-D and 3-D seems to be in the extent with which the turbulent kinetic energy grows.

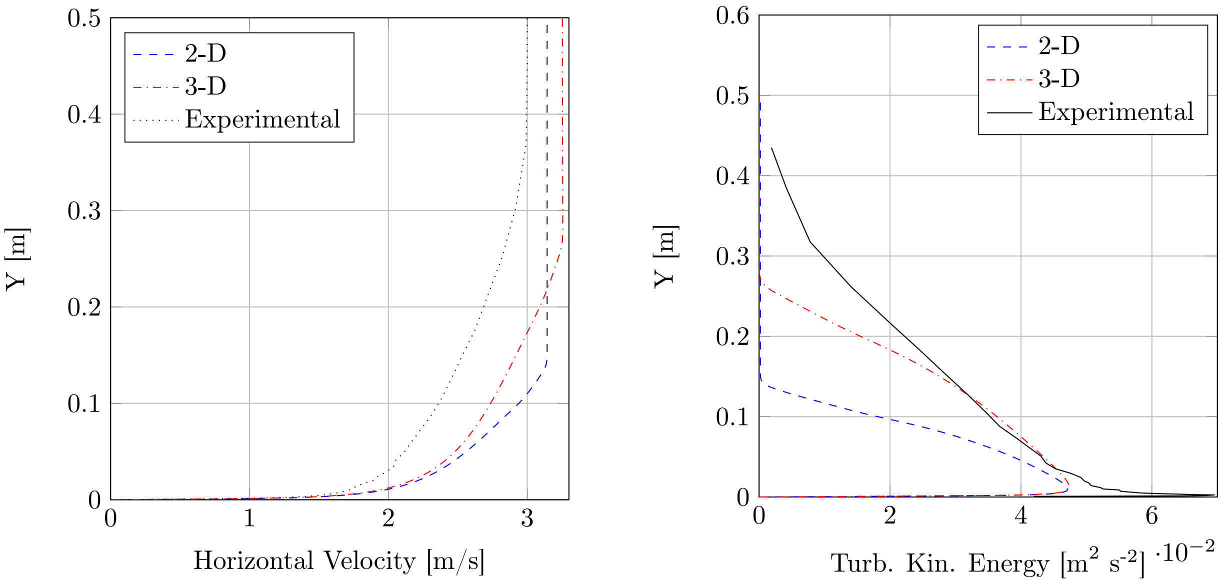

(a) Velocity profile comparison

(b) Turbulent kinetic energy comparison

Figure A.3: Comparison between numerical and experimental results for the velocity profile at $Re_\theta = 8200$

A.4 Recommendations

Due to the scope of the project this case will not be investigated much further. However, if it were it would be of interest to re-do the numerical cases to document and obtain grid independent results. This way the difference between the two cases, 2-D and 3-D, can be assessed with more confidence. Furthermore, the difference in turbulent kinetic energy peaks near the wall between numerical and experimental results needs to be investigated. One solution could be to verify whether or not the wall can indeed be modeled as a smooth wall.

For the sake of the project however, it would be of note to keep in mind the difficulty numerical solvers may have with such boundary layer development. In the validation cases the numerical domain will be smaller and the experimental velocity profiles will be used as inlet flow. It should be verified, before the model is validated, whether or not the numerical solver applies this inlet condition properly. In other words, if the test section of the tunnel is modeled, does the velocity profile remain stable as seen in experiments.

Appendix B

Zero Pressure Gradient Comparison Low Reynolds Number

In this report the BAY model discussed in this thesis will be compared to experimental results and simulation results of a fully resolved CFD run. The main purpose of this study was to compare the results of the BAY model with that of RANS simulation of a fully resolved grid, including the vortex generator geometry. Comparisons are made for rectangular and triangular vortex generators, though the experimental data only contains the rectangular data. It should be noted that at the inlet the Reynolds Momentum Thickness number is 3124, as opposed to 18000 for the case used in the main validation.

B.1 Overall Remarks

This report compares the results between a fully resolved CFD simulation of a counter-rotating vortex generator pair with the BAY model simulation of the same setup. This simulation is based on a measurement campaign conducted in the Boundary Layer Tunnel of TU Delft. Two of those contained a setup with a rectangular and triangular vortex generator, these will be replicated with the BAY model. In Table B.1 the parameters for the vortex generator are shown and in Figure B.1 they are illustrated. For the flow domain the same inlet conditions from the fully resolved case are used for the simulations with the BAY model. This includes using a velocity field containing the streamwise, spanwise and vertical velocity over the entire inlet. Those were obtained by simulating the boundary layer development and gathering data from the point where the boundary layer matched that of the wind tunnel.

Furthermore a turbulence intensity of 5% is used in conjunction with the Shear Stress Transport model, with no further alterations or models. This setup is similar to that of the fully resolved CFD simulation. The flow domain has a height of 425 mm and the width is chosen according to the VG pair separation, equal to 30 mm. The height of the domain is half of the wind tunnel height, 250 mm. To compensate a symmetry boundary condition has been used. Based on the domain length the Reynolds number is 4.49e5 whereas based on the boundary layer statistics the Reynolds momentum thickness is 3214. The free-stream inlet velocity is $15ms^{-1}$ and the boundary layer thickness is roughly $20mm$. It should also be noted that due to fully resolved the boundary layer at every surface, the mesh also features a refinement along throughout the domain along the edges of the vortex generator. This can be beneficial to resolving the peak vorticity and developing the vortex, as noted by Dudek[5].

Table B.1: Vortex Generator Parameters

VG Property	Symbol	Value [mm]	Nondimensionalised by VG height
Device Height	h	5	1
Trailing Edge Separation	d	12.5	2.5
Vane Chord Length	l	12.5	2.5
VG Pair Separation	D	30	6
Attack Angle	Φ	18 [deg]	–
Streamwise Position	X_{VG}	985	197

B.2 Results

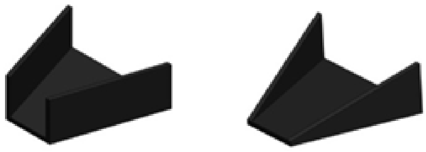

(a) Rectangular/triangular vortex generator models

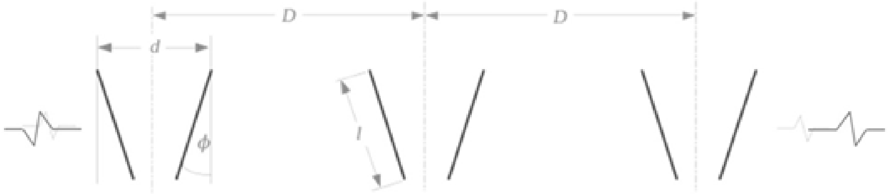

(b) Vortex generator array layout

Figure B.1: Illustration of the Vortex Generator Setup

Table B.2: Simulation Results for Fully Resolved and BAY-model Simulations

	F.R. Rectangle	BAY Rectangle	F.R. Triangle	BAY Triangle
Total Mesh Elements [-]	8.95e6	2.24e6	5.10e6	2.24e6
CPU Time [hh:mm / Cores]	00:33 / 96	00:20 / 64	00:19 / 64	00:25 / 64

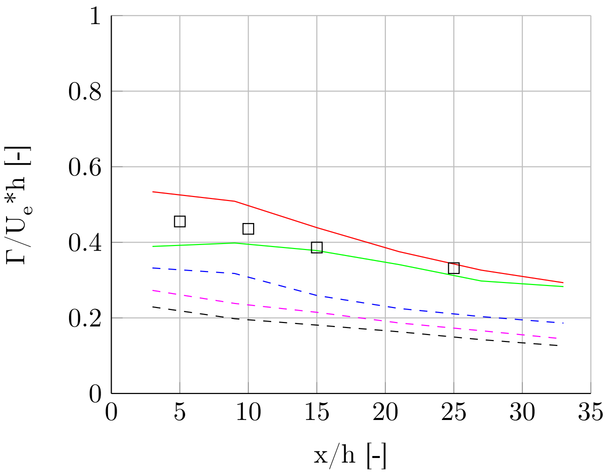

(a) Circulation

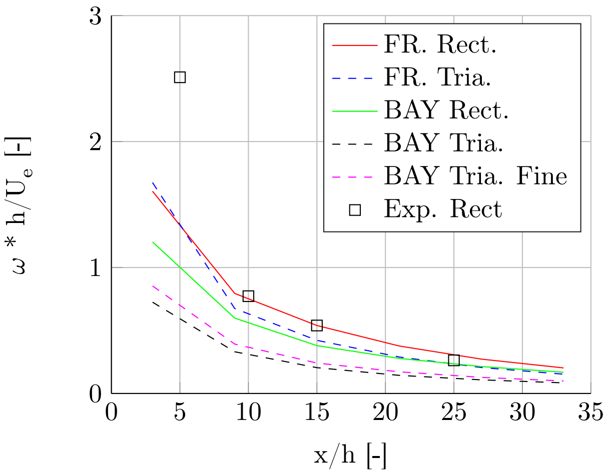

(b) Peak vorticity

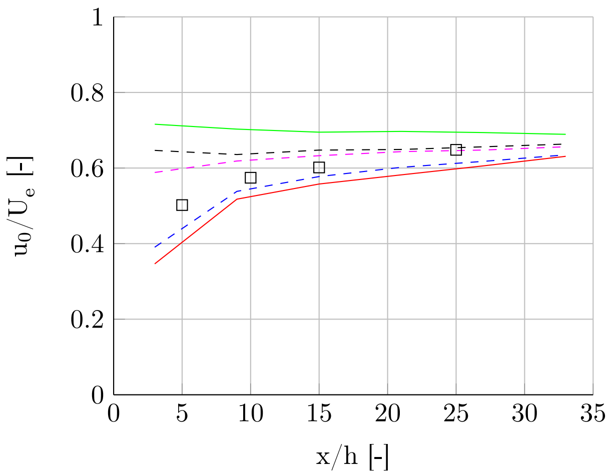

(c) Core velocity

Figure B.2: Streamwise development of various parameters for the BAY-model and a Fully Resolved CFD simulation

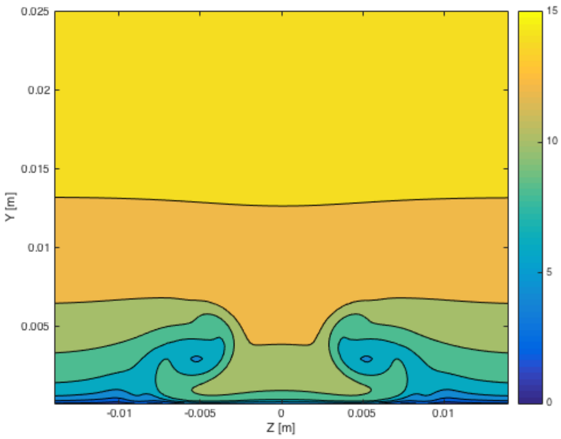

(a) F.R. x/h = 3

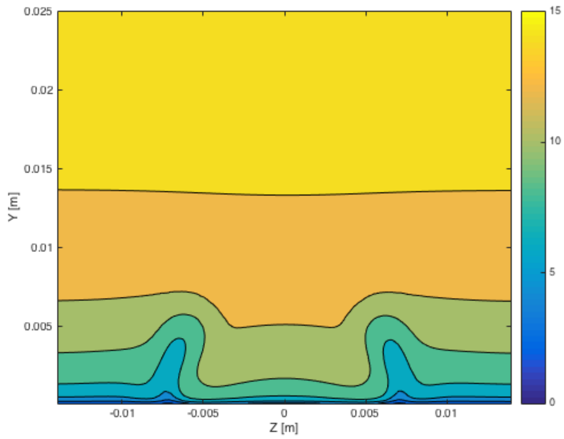

(b) BAY x/h = 3

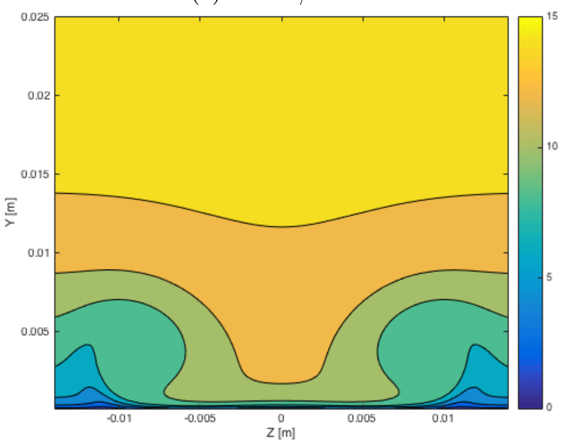

(c) F.R. x/h = 15

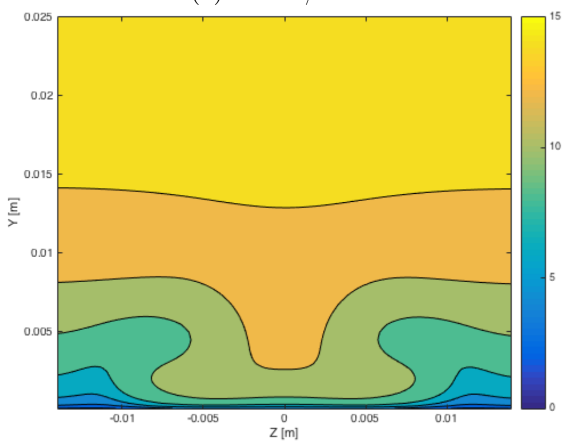

(d) BAY x/h = 15

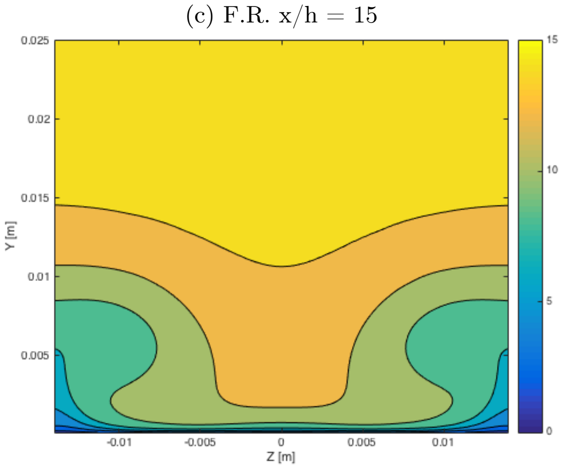

(e) F.R. x/h = 27

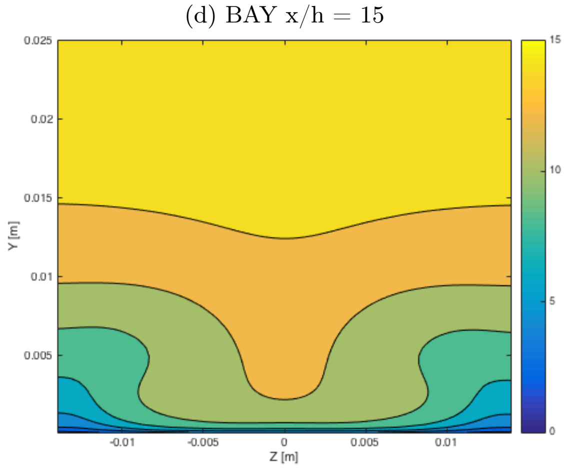

(f) BAY x/h = 27

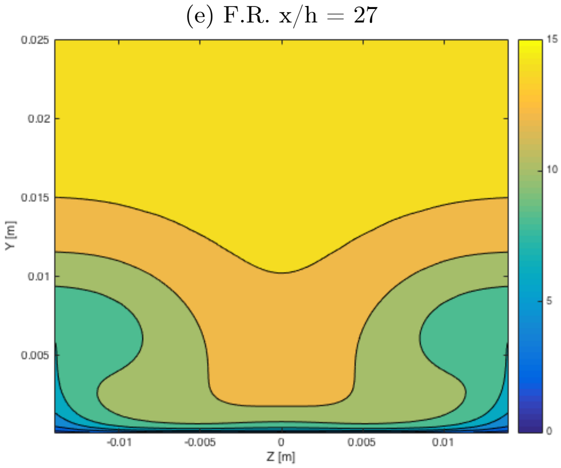

(g) F.R. x/h = 33

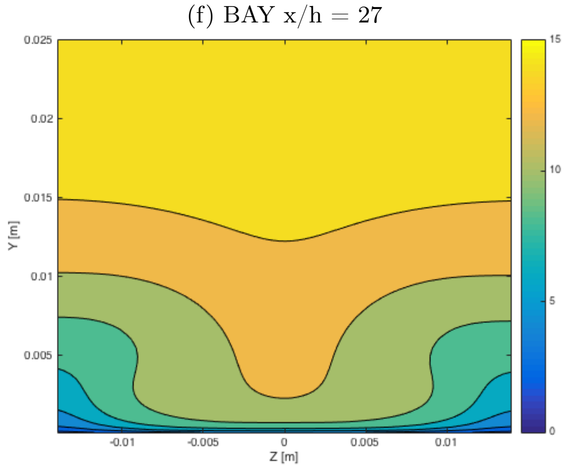

(h) BAY x/h = 33

Figure B.3: Velocity Plane Development between the BAY-model and a Fully Resolved CFD simulation

B.3 Discussion

The results from Figure B.2 shows that for both the rectangle and the triangle the BAY model has a tendency to underpredict the generated vortex, with this underprediction being more pronounced for the triangular vortex generator. The rectangular vortex generator seems to match the CFD simulation much better downstream, beyond 20 device heights. However, when comparing both BAY and the fully resolved CFD to experimental data, for the rectangular vortex generator, the gap between BAY and CFD seems to less significant.

It has to be noted that the PIV data used to obtain the experimental data showed asymmetry between the two vortices, therefore the values shown are the averaged values of those two vortices. In terms of circulation, Figure B.2a, the BAY has a slight underprediction whereas the CFD simulation overpredicts by more or less the same amount. For the peak vorticity, shown in Figure B.2b, both CFD and BAY fail to capture the peak vorticity near the VG. The CFD simulation matches the experimental data better in the mid region, between x/h 10 and 15, whereas the BAY model matches the further downstream positions better. With regards to convection velocity, it

To investigate the offset for the triangular vortex generator a more refined mesh was made, based on the average sizes used by the fully resolved mesh. This mesh ended up featuring 11.8 million elements, which is substantially more than the fully resolved case. However, the mesh for the BAY case did not feature the more aggressive growth ratios in some regions. It also did not contain the aforementioned tip refinement, which as stated can improve the initial development of the vortex. This has not been attempted in this case, due to the time required to develop such a mesh as documented in the previous case.

The refined mesh does capture the larger velocity deficit in the core at the initial downstream positions, as shown by Figure B.2c. This is most likely due to the smaller volumes being more capable of capturing the vortex. However, even at a more refined level the CFD simulation does have a significant underprediction of the core velocity.

In Figure B.3 the streamwise velocity is shown at downstream planes for both the fully resolved and BAY simulations. Especially at the initial downstream position, Figures B.3a and B.3b, highlight the difference between the BAY model and the fully resolved simulation. The BAY model does not seem to be able to model the entire structure of the vortex at that point. However, as the planes at $x/h = 27, 33$ show, Figures B.3f and B.3h, the downstream velocity matches much more. The only difference is that the effect of the vortex has not penetrated further towards the freestream region, due to the less stronger development in the initial region.

This discrepancy between the fully resolved geometry and the BAY model has been found in published articles such as Dudek[5] and Florentie et al.[57]. However, the first validation that compared the BAY model to experimental data from Velte[83] showed a much closer agreement. For both the experimental data used in this case and that of Velte[83] the vortex generator had a similar vortex generator parameters such as a h/δ of 0.2 and a device angle of 18 degrees. The only real difference is the Reynolds number in this case. Based on the boundary layer the Reynolds momentum thickness number for the experiments of Velte[83] is 17000 whereas the fully resolved simulation has been conducted for a Reynolds Momentum thickness of 3124.

Appendix C

Adverse Pressure Gradient Flow Validation

C.1 Summary

In this section results are presented from simulations on the mesh from the previous section. It was found that for all cases discussed below the $y^+ < 1$ condition was met and no problems occurred at any time during solving. This includes no extreme imbalances in the solution and a converged value for the pressure drop.

C.2 Variation of Parameter

To find the right setup for the simulation several parameters will be varied and compared to the results from Bernard et al.[84]. These parameters are shown below:

- Length of Inlet
- Length of Outlet
- Inlet Velocity/Reynolds Number
- Turbulence Intensity At Inlet and length scale
- Turbulence Model (k-ϵ | SST | BSL - EARSM)

In order to compare the effects of certain simulation variables a 'Base' case will be defined. It will be modeled with a SST turbulence model, with 5 % turbulence intensity at the inlet combined with a 10.32 $m\,s^{-1}$ normal inlet velocity. Furthermore, the inlet is positioned 0.5 m from the bump and the outlet 1 m. A lengthened inlet distance of 1 m and similarly 7.5 m will be tested and henceforth referred to as 'Extended Inlet' and 'Extended Outlet'.

Table C.1: Reynolds Momentum Numbers and Shape Factors at Various Streamwise Locations

Case	Re_θ, $x = 17.35$	Re_θ, $x = 17.63$	Re_θ, $x = 17.90$	Re_θ, $x = 18.24$	Re_θ, $x = 18.58$
Bernard et al.[84]	4887	10501	17131	26112	32384
Dassault NS[84]	4658	8822	14581	21298	25668
Base	-2860	6824	16285	20241	23019
$k-\epsilon$	-3283	5734	15585	24273	28562
BSL-EARSM	-827	8938	17996	22026	25451
SST-CR	-907	8790	18123	21627	24418
$U_\infty = 9.4$	-919	8838	18128	21535	24324
$U_\infty = 11$	-963	8698	18123	21767	24536
Extended Inlet	-975	8744	18131	21675	24443
Extended Outlet	-2815	6759	16293	20246	22980
TI = 10 %	-927	8553	18408	23650	26650
TI = 15 %	-909	8510	18453	24236	27345
Rot. -3 deg	1619	11305	19026	23025	26148
Rot. +3 deg	-3287	6717	17317	19630	21932
	H_{12}, $x = 17.35$	H_{12}, $x = 17.63$	H_{12}, $x = 17.90$	H_{12}, $x = 18.24$	H_{12}, $x = 18.58$
Bernard et al.[84]	1.24	1.319	1.471	1.703	1.693
Dassault NS [84]	1.246	1.303	1.433	1.688	1.876
Base	0.685	1.444	1.736	2.792	3.176
$k-\epsilon$	0.782	1.395	1.486	1.821	1.963
BSL-EARSM	-0.141	1.403	1.791	2.830	3.163
SST-CR	-0.009	1.386	1.737	2.834	3.260
$U_\infty = 9.4$	-0.017	1.392	1.753	2.871	3.297
$U_\infty = 11$	0.078	1.379	1.714	2.779	3.201
Extended Inlet	0.071	1.384	1.723	2.815	3.239
Extended Outlet	0.680	1.448	1.738	2.798	3.191
TI = 10 %	0.088	1.353	1.597	2.383	2.734
TI = 15 %	0.092	1.343	1.565	2.270	2.597
Rot. -3 deg	1.812	1.417	1.736	2.416	2.642
Rot. +3 deg	0.782	1.384	1.838	3.633	4.361
	H, $x = 17.35$	H, $x = 17.63$	H, $x = 17.90$	H, $x = 18.24$	H, $x = 18.58$
Bernard et al.[84]	1.18	1.05	0.95	0.87	0.85
Dassault NS [84]	1.15	1.05	0.93	0.84	0.80
Base	0 + 0.730i	0.923	0.878	0.825	0.789
$k-\epsilon$	0 + 0.826i	0.914	0.906	0.830	0.800
BSL-EARSM	0 + 0.335i	0.964	0.875	0.811	0.773
SST-CR	0+0.365i	0.973	0.883	0.831	0.796
$U_\infty = 9.4$	0 + 0.365i	0.970	0.882	0.831	0.795
$U_\infty = 11$	0 + 0.386i	0.976	0.886	0.832	0.797
Extended Inlet	0 + 0.386i	0.973	0.884	0.832	0.796
Extended Outlet	0 + 0.734i	0.919	0.878	0.826	0.789
TI = 10 %	0 + 0.389i	0.992	0.901	0.835	0.802
TI = 15 %	0 + 0.389i	1.000	0.907	0.847	0.804
Rot. -3 deg	0.741	0.959	0.876	0.823	0.793
Rot. +3 deg	0 + 0.887i	0.968	0.884	0.848	0.809

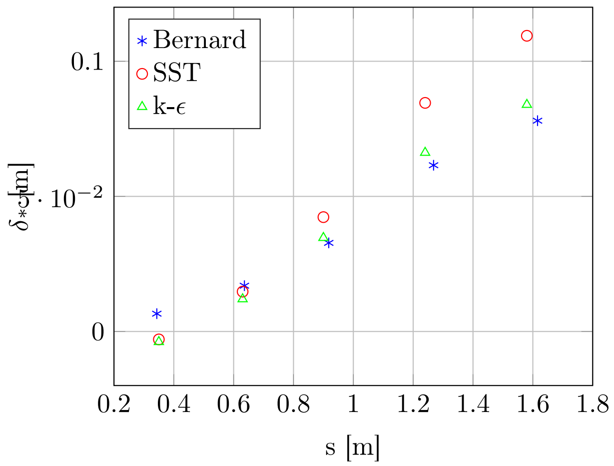

(a) Displacement Thickness

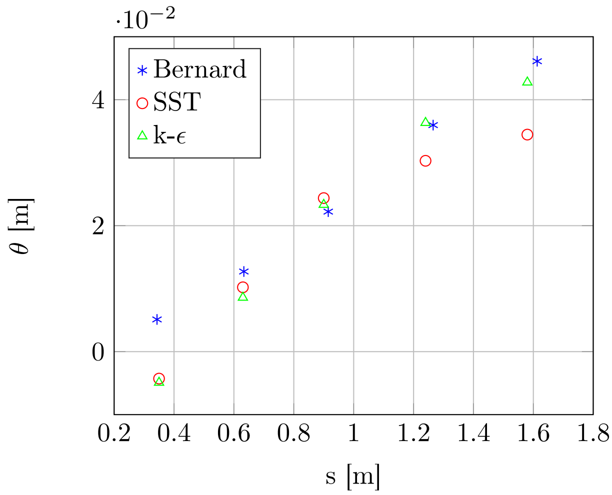

(b) Momentum Thickness

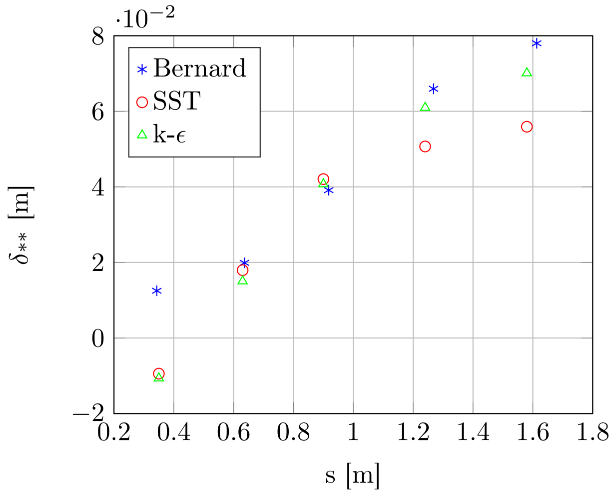

(c) Energy Thickness

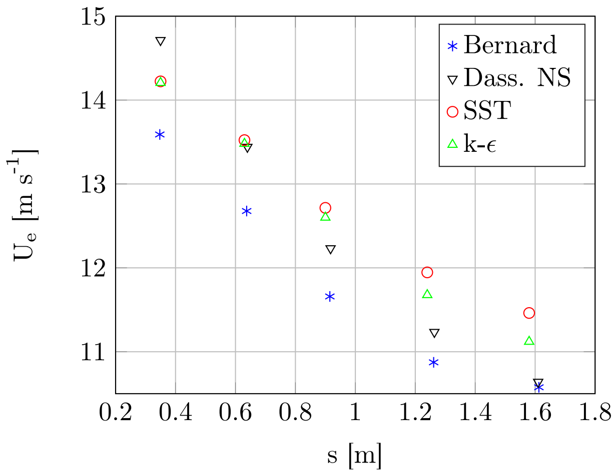

(d) Convection velocity

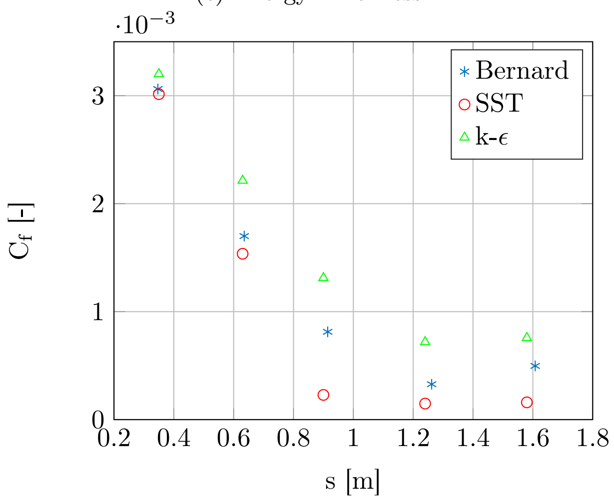

(e) Skin Friction Coefficient

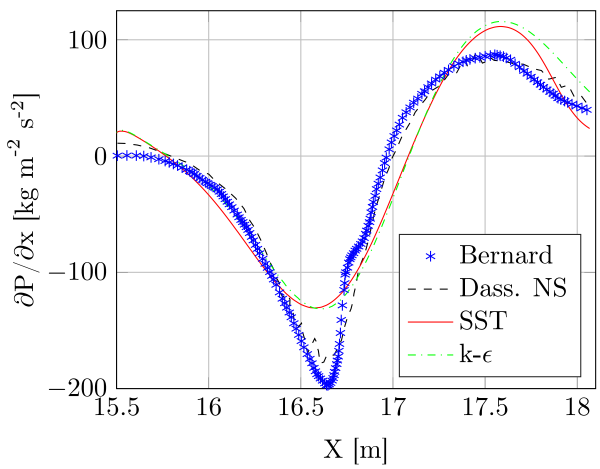

(f) Pressure Gradient

Figure C.1: Comparison for Various Flow Parameters in Adverse Pressure Gradient Flow for Turbulence Models

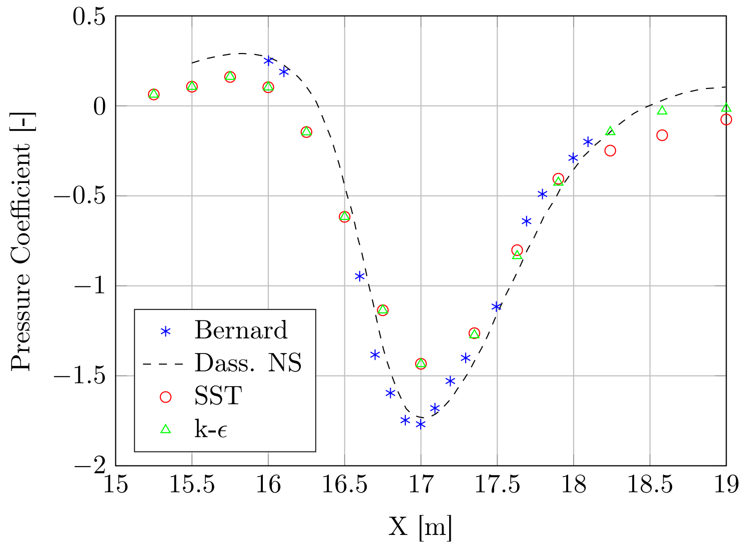

Figure C.2: Coefficient of Pressure Comparison for different Turbulence Models

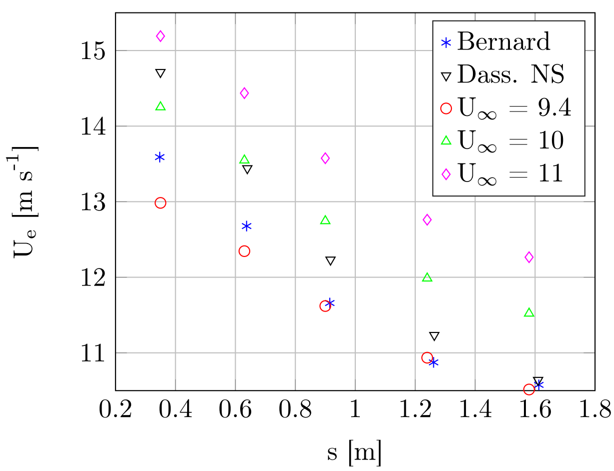

(a) Skin Friction Coefficient

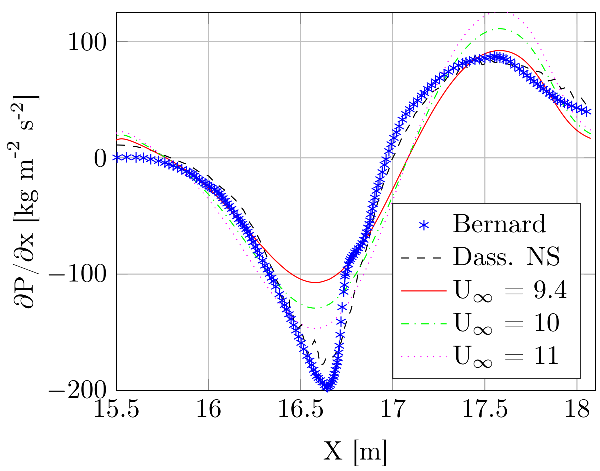

(b) Pressure Gradient

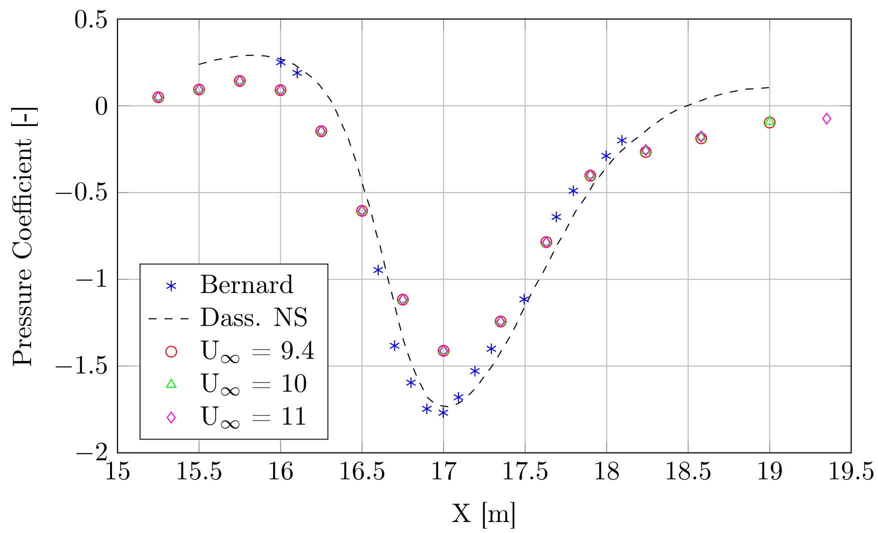

(c) Coefficient of Pressure

Figure C.3: Comparison for Various Flow Parameters in Adverse Pressure Gradient Flow for Different Inlet Flows

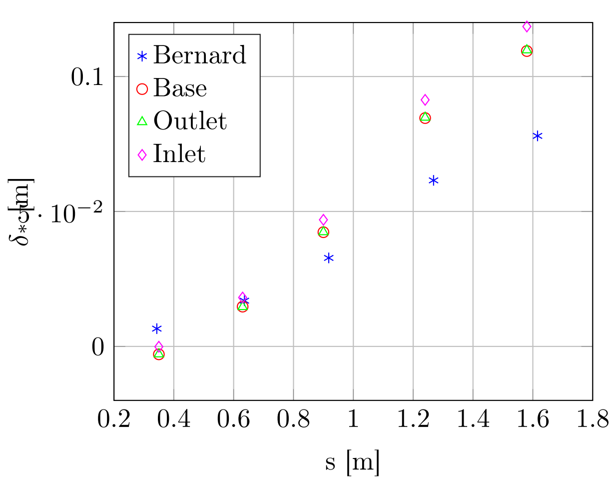

(a) Displacement Thickness

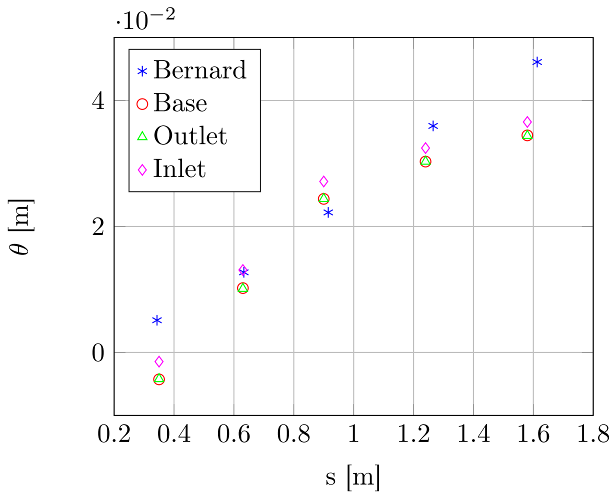

(b) Momentum Thickness

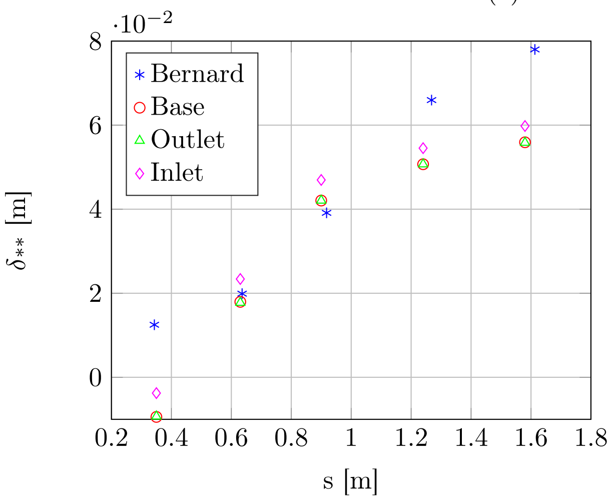

(c) Energy Thickness

Figure C.4: Comparison for Various Flow Parameters in Adverse Pressure Gradient Flow for Various Inlet/Outlet Sizes

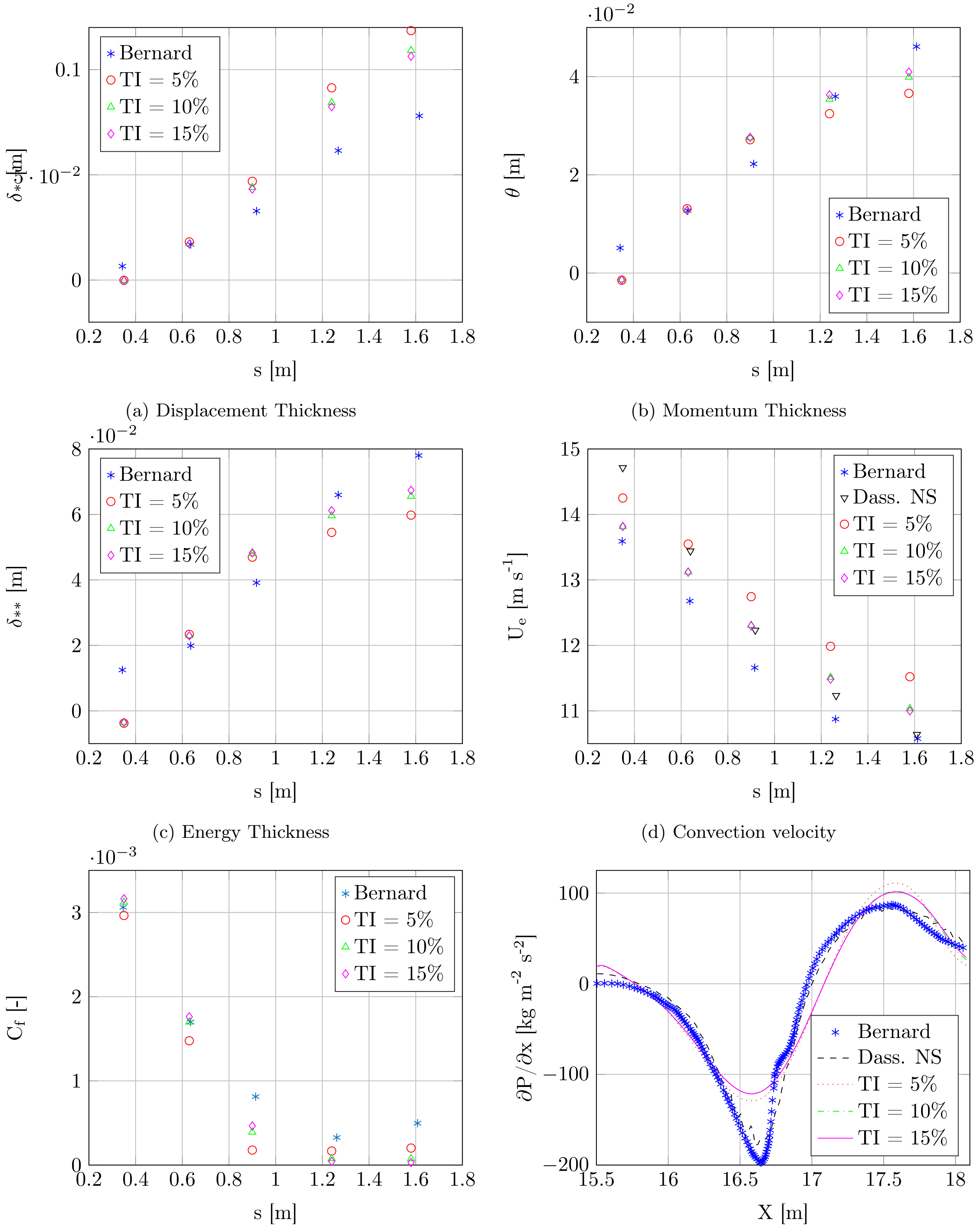

(a) Displacement Thickness

(b) Momentum Thickness

(c) Energy Thickness

(d) Convection velocity

(e) Skin Friction Coefficient

(f) Pressure Gradient

Figure C.5: Comparison for Various Flow Parameters in Adverse Pressure Gradient Flow for Different Inlet Conditions with respect to Turbulence

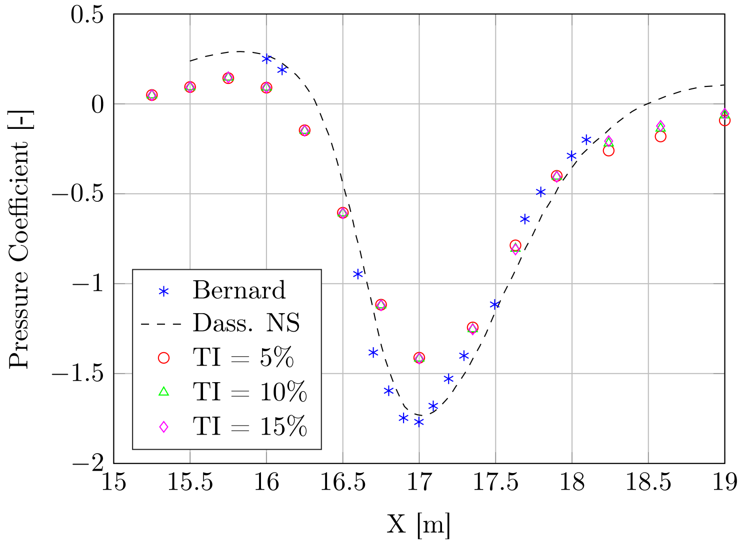

Figure C.6: Pressure Coefficient for different Turbulence Inlet Conditions

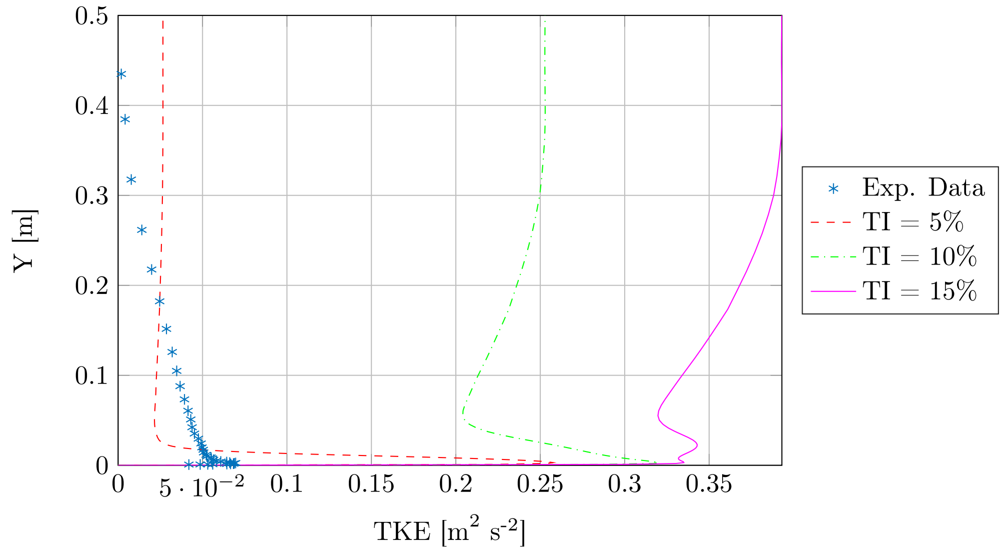

Figure C.7: Turbulent Kinetic Energy, at the inlet, for different Turbulence Inlet Conditions

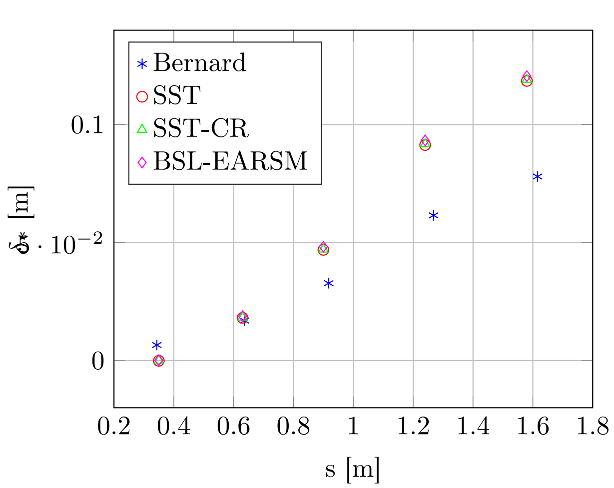

(a) Displacement Thickness

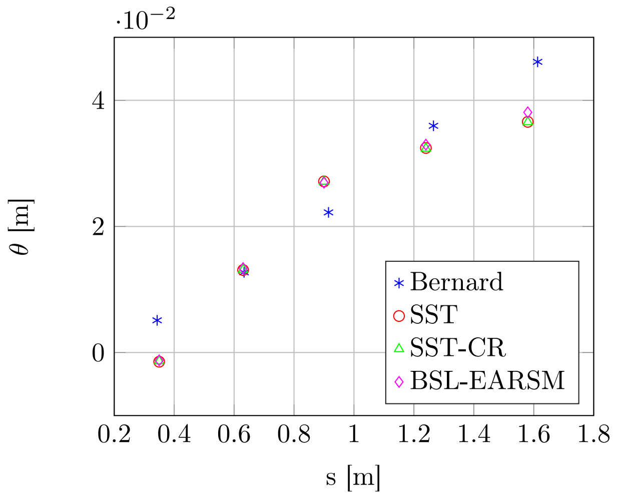

(b) Momentum Thickness

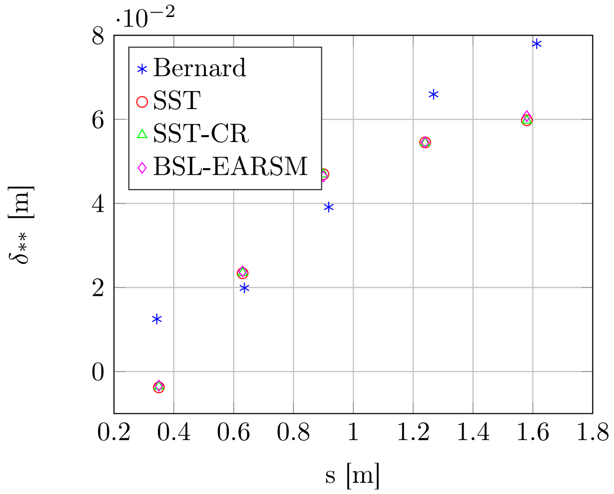

(c) Energy Thickness

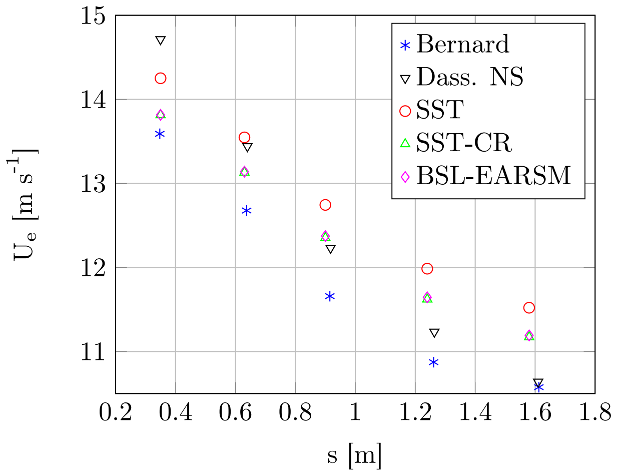

(d) Convection velocity

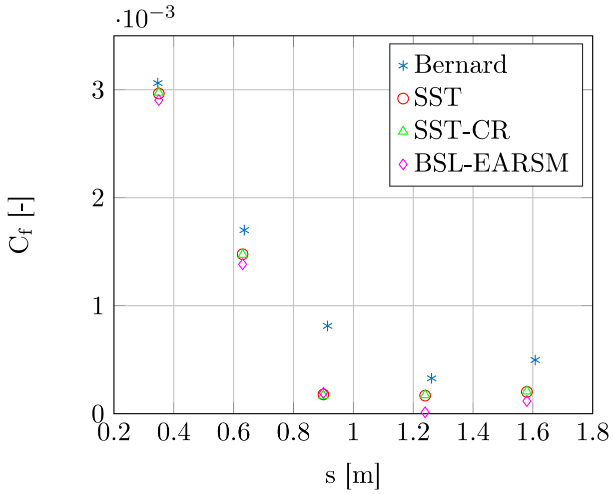

(e) Skin Friction Coefficient

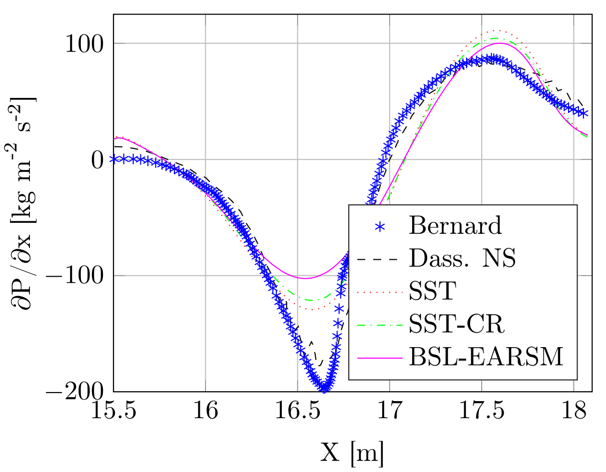

(f) Pressure Gradient

Figure C.8: Comparison for Various Flow Parameters in Adverse Pressure Gradient Flow for Different Turbulence Models

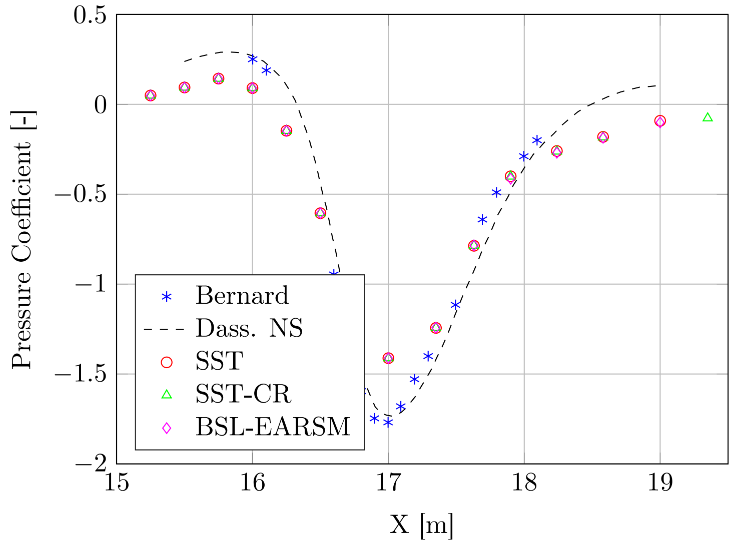

Figure C.9: Pressure Coefficient for Different Turbulence Models

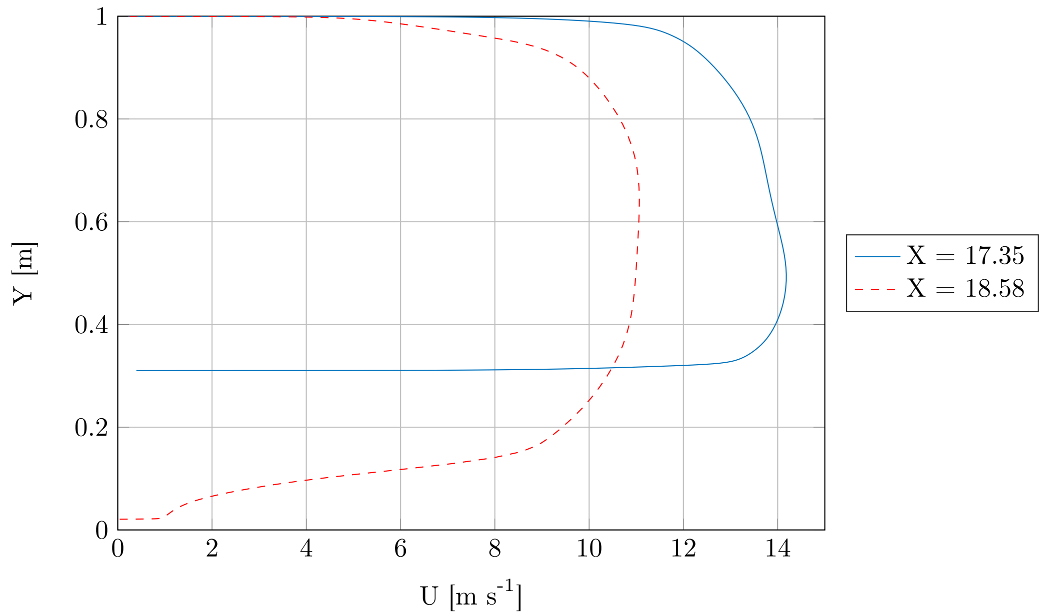

Figure C.10: Velocity profiles at different longitudinal positions, for BSL-EARSM

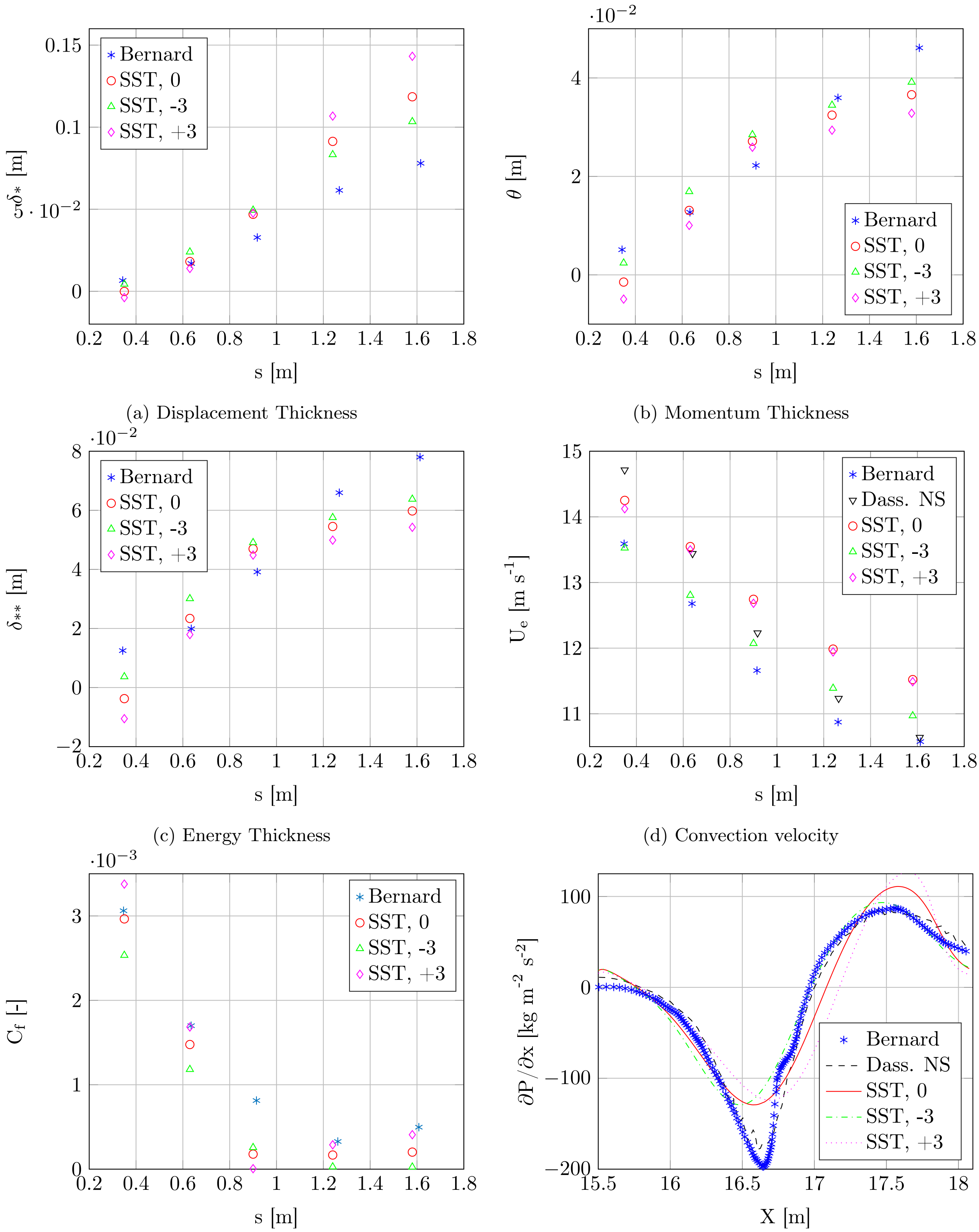

(a) Displacement Thickness

(b) Momentum Thickness

(c) Energy Thickness

(d) Convection velocity

(e) Skin Friction Coefficient

(f) Pressure Gradient

Figure C.11: Comparison for Various Flow Parameters in Adverse Pressure Gradient Flow with Rotated Bumps

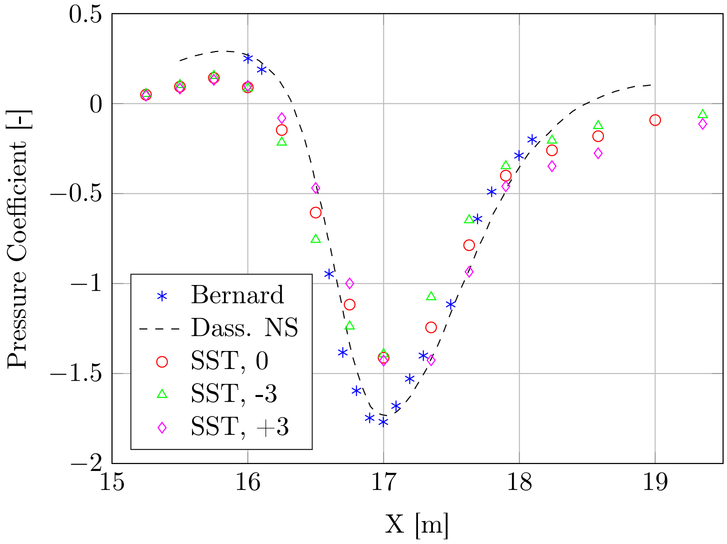

Figure C.12: Pressure Coefficient for Rotated Bump Configurations

C.2.1 Velocity Profile Development

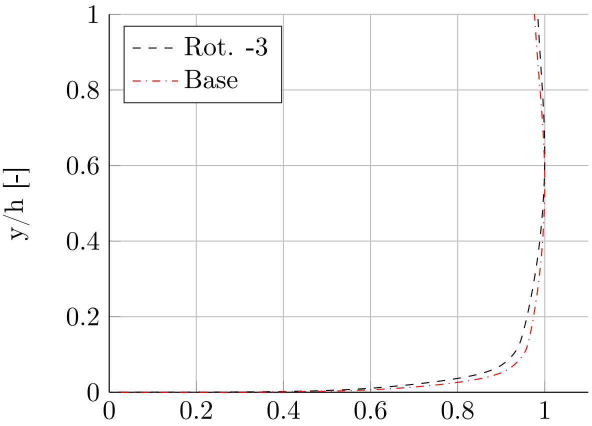

(a) X = 17.35 m

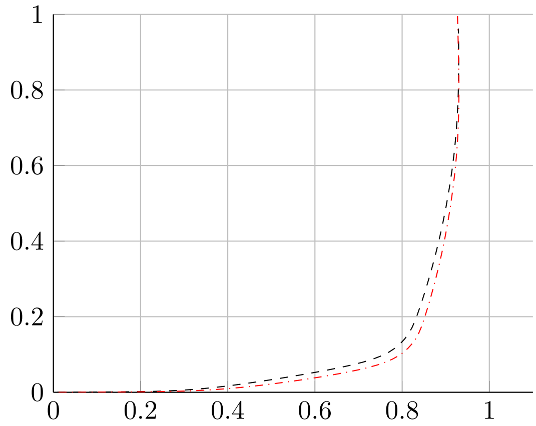

(b) X = 17.63 m

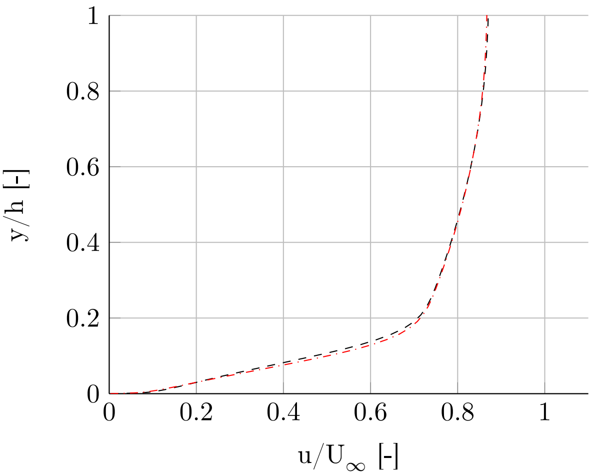

(c) X = 17.90 m

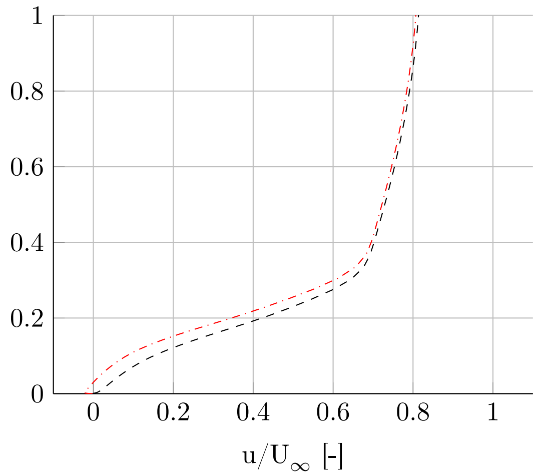

(d) X = 18.24 m

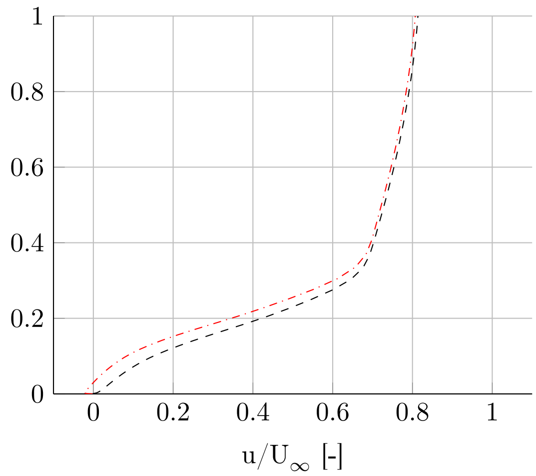

(e) X = 18.58 m

Figure C.13: Development of Velocity Profiles

C.3 Discussion

General Patterns

Three parameters shows a distinctive offset among all variations that have been presented. The distance between the pressure gradient peaks is substantially smaller compared to Bernard et al.[84], for example in Figure C.1f. However, this offset is less pronounced in the pressure coefficient, such as in Figure C.6. Furthermore, the convection velocity is overestimated in all simulations and the skin friction coefficient is lower in most cases, as evidenced by Figure C.8d and Figure C.5e. With respect to the difference in pressure distribution, it is expected that there would be some difference given the fact that the geometry does not match perfectly. Furthermore, the geometry in the actual experiment could have been pitched within the plus or minus three degrees as mentioned previously. This would significantly impact the distribution of pressure across the surface, however Bernard et al.[84] have not mentioned whether or not this functionality was used.

Regarding the convection velocity there is the issue of boundary layer development. The flow over the bump is not always fully developed at certain locations, as can be seen in Figure C.10. This makes it difficult to determine the value for the convection velocity, which additionally also affects parameters such as the displacement thickness and others. It also explains the negative values obtained for the shape factor H, as seen in Table C.1. From Figure C.10 it can be seen that at $X = 17.35$ the flow is accelerating near the bump surface and that the convection velocity for this case variation is lower than the maximum velocity, $U_e = 13.82 m\, s^{-1}$ compared to $14.18 m\, s^{-1}$. This results in small if not negative values for the displacement and momentum thickness and consequently negative shape factors. This issue becomes less pronounced further downstream as gets closer to being fully developed.

With that in mind, there is still a significant gap between the boundary layer definitions between the simulation and experimental results. This is most likely because the flow in the numerical simulation is in some cases very close to separation, but in most cases separation occurs. Schlichting[44] notes that flows with values of H between 0.723 and 0.761 will be prone to separation, with values below this range having separated. Though none of the values in Table C.1 are within that range, several are very close and do exhibit negative streamwise velocities at certain longitudinal positions.

Overall, those cases with higher turbulence intensities seem to be better at approaching those results recorded by Bernard et al.[84]. This is a logical consequence, the more energy the flow contains the more capable it is staying attached to any surface. However, when the velocity profiles and turbulent kinetic energy distributions for these cases show some questionable patterns. In Figure C.7 the turbulent kinetic energy is compared to data gathered from internal documents, documenting benchmarks for flow in the wind tunnel used by Bernard et al.[84]. This shows that although increased turbulence intensity may improve some aspects of the flow, the energy distribution is increasingly further off from what was measured. The velocity profiles also show a peculiar transition close to the wall, as shown in Figure C.10 for $X = 18.58$.

Specific Parameter Cases

In Figure C.1 the difference between $k - \epsilon$ and SST is shown, this was done in order to related to the simulation results from Dassault who used a two dimensional $k - \epsilon$ code. In all parameters but the skin friction coefficient and the pressure distribution it can be seen that $k - \epsilon$ does seem to perform better. Especially the over prediction of the skin friction coefficient is a trend that has been seen before. However, it remains nonetheless questionable how accurate the other results are considering the assumptions and limitations of $k - \epsilon$, which is not known for its accurate separation modeling[66].

The inlet velocity has been varied in order to find the value that would approach the Reynolds numbers from Bernard et al[84] while also satisfying the other parameters, these results are shown in Figure C.3. However, the increase in velocity barely affects the Reynolds numbers downstream of the peak of the bump. The convection velocity is a much closer match for the lower velocity, which is to be expected considering the lower flow velocity in general. Furthermore, the increase of the velocity profile is the only parameter that accomplishes a positive change in the pressure gradient towards the experimental data but the coefficient of pressure stays unchanged. Otherwise the differences between the variation of inlet velocity are negligible.

The domain size has been varied and studied with the results shown in Figure C.4. Not all parameters have been shown here as the differences are insignificant. Only the increased outlet has some effect on the results, showing improvements with respect to the momentum and energy thickness but an overestimation for the displacement thickness. It might be that the inlet profile has not fully settled in the 'base' case.

As mentioned in the discussion of general trends, an increase in turbulence intensity can prevent the onset of separation, these results are shown in Figure C.5. The reduction in convection velocity, as shown by Figure C.5d, is a result of the increased turbulence reducing the main flow while increasing the boundary layer flow. Nonetheless, overall the increase in turbulence intensity does not significantly reduce the gap between the simulation and the experimental data.

Another examined parameter is the use of the Baseline Explicit Algebraic Reynolds Stress Model (BSL-EARSM), that according to the Ansys manual "capture [...] secondary flows and flows with streamline curvature and system rotation"[62]. This is made possible by including "a nonlinear relation between the Reynolds stresses and the mean strain-rate and vorticity tensors". Furthermore, turbulent kinetic energy is no longer modeled as isotropic. The SST model also has the ability to account for curvature with a correction coefficient, this model has also been included. Figure C.8 shows that the boundary layer characteristics do not change significantly but both BSL-EARSM and the curvature corrected SST improve in their values for the convection velocity, something which is reflected by more accurate Reynolds numbers in table C.1. However, BSL-EARSM slightly under predicts the skin friction value and both have slightly diminished pressure gradients in Figure C.8e.

Considering that all variations tested here have under predicted both the coefficient of pressure and the pressure gradient an attempt was made to see if changing the angle of the bump, as mentioned by Bernard et al.[84], could be useful in this situation. In Figure C.11 the results are shown for the flow over the bump tilted zero and three degrees in both directions. In terms of pressure no significant improvement can be seen, other than the the longitudinal shift in the location of the peaks. The pressure gradient for minus three degrees seems to match overall more but still lacks in magnitude, as shown by Figure C.11f. However, when it comes to convection velocity and the overall boundary layer characteristics the flow over the bump when titled minus three degrees seem to match much closer to the experimental data. This is not the case for the skin friction coefficient, however, where it performs the worst out of the three configurations. It is also interesting to note that for the Reynolds numbers and Shape Factors from Table C.1 it comes closest to matching the experimental data.

Bibliography

[1] E. Bender, B. Anderson, and P. Yagle, "Vortex generator modeling for navier-stokes codes," in *Third ASME/JSME Joint Fluids Engineering Conference, Paper No. FEDSM99-6919*, 1999.

[2] H. H. Larsen and L. S. Petersen, "Dtu international energy report 2014," November 2014.

[3] H. Pearcey, *Shock-induced separation and its prevention by design and boundary layer control.* Pergamon, 1961.

[4] R. V. Chima, "Computational modeling of vortex generators for turbomachinery," *ASME Turbo Expo 2002: Power for Land, Sea, and Air*, 2002.

[5] J. C. Dudek, "Modeling vortex generators in a navier-stokes code," *AIAA journal*, vol. 49, no. 4, pp. 748–759, 2011.

[6] A. Jirasek, "Vortex-generator model and its application to flow control," *Journal of Aircraft*, vol. 42, no. 6, pp. 1486–1491, 2005.

[7] F. Wallin and L.-E. Eriksson, "A tuning-free body-force vortex generator model," *AIAA Paper*, no. 2006-0873, 2006.

[8] M. O. L. Hansen, C. M. Velte, S. Øye, R. Hansen, N. N. Sørensen, J. Madsen, and R. Mikkelsen, "Aerodynamically shaped vortex generators," *Wind Energy*, pp. n/a–n/a, 2015.

[9] S. Ghosh, J.-I. Choi, and J. R. Edwards, "Numerical simulations of effects of micro vortex generators using immersed-boundary methods," *AIAA journal*, vol. 48, no. 1, pp. 92–103, 2010.

[10] F. V. Stillfried, S. Wallin, and A. V. Johansson, "Vortex-generator models for zero-and adverse-pressure-gradient flows," *AIAA journal*, vol. 50, no. 4, pp. 855–866, 2012.

[11] B. J. Wendt, "Parametric study of vortices shed from airfoil vortex generators," *AIAA journal*, vol. 42, no. 11, pp. 2185–2195, 2004.

[12] L. Zhang, K. Yang, J. Xu, and M. Zhang, "Modeling of delta-wing type vortex generators," *Science China Technological Sciences*, vol. 54, no. 2, pp. 277–285, 2011.

[13] U. Fernandez, P.-E. Réthoré, N. Sørensen, C. Velte, F. Zahle, and E. Egusquiza, "Comparison of four different models of vortex generators," in *Proceedings of EWEA 2012 - European Wind Energy Conference & Exhibition*, 2012.

[14] C. D. Booker, X. Zhang, and S. I. Chernyshenko, "Large-scale vortex generation modeling," *Journal of Fluids Engineering*, vol. 133, no. 12, p. 121201, 2011.

[15] "Laboratoire mecanique lille." `http://lml.univ-lille1.fr/?page=144&menu_curr_set=144`. Accessed: 2015-10-01.

[16] T. J. Mueller and S. M. Batil, "Experimental studies of separation on a two-dimensional airfoil at low reynolds numbers," *AIAA Journal*, vol. 20, no. 4, pp. 457–463, 1982.

[17] P. Ashill, J. Fulker, and K. Hackett, "A review of recent developments in flow control," *Aeronautical Journal*, vol. 109, no. 1095, pp. 205–232, 2005.

[18] L. L. Pauley, P. Moin, and W. C. Reynolds, "The structure of two-dimensional separation," *Journal of Fluid Mechanics*, vol. 220, pp. 397–411, 1990.

[19] J. W. Larsen, S. R. Nielsen, and S. Krenk, "Dynamic stall model for wind turbine airfoils," *Journal of Fluids and Structures*, vol. 23, no. 7, pp. 959–982, 2007.

[20] J. M. Lin and L. L. Pauley, "Low-reynolds-number separation on an airfoil," *AIAA journal*, vol. 34, no. 8, pp. 1570–1577, 1996.

[21] H. Seetharam, E. Rodgers, and W. Wentz Jr, "Experimental studies of flow separation of the naca 2412 airfoil at low speeds," tech. rep., NASA, Washington United States, 1975.

[22] S. Schreck and M. Robinson, "Rotational augmentation of horizontal axis wind turbine blade aerodynamic response," *Wind Energy*, vol. 5, no. 2-3, pp. 133–150, 2002.

[23] I. Herráez, B. Akay, G. van Bussel, J. Peinke, and B. Stoevesandt, "Detailed analysis of the blade root flow of a horizontal axis wind turbine," *Wind Energy Science Discussion*, vol. 2016, pp. 1–33, 2016.

[24] B. Akay, D. Ragni, C. Simão Ferreira, and G. Bussel, "Experimental investigation of the root flow in a horizontal axis wind turbine," *Wind Energy*, vol. 17, no. 7, pp. 1093–1109, 2014.

[25] H. Dumitrescu, V. Cardoş, and A. Dumitrache, "Modelling of inboard stall delay due to rotation," in *Journal of Physics: Conference Series*, vol. 75, p. 012022, IOP Publishing, 2007.

[26] Z. Du and M. Selig, "The effect of rotation on the boundary layer of a wind turbine blade," *Renewable Energy*, vol. 20, pp. 167–181, 2000.

[27] J. Anders and R. Watson, "Airfoil large-eddy breakup devices for turbulent drag reduction," in *American Institute of Aeronautics and Astronautics, Shear Flow Control Conference, Boulder, CO*, 1985.

[28] D. A. Griffin, "Investigation of vortex generators for augmentation of wind turbine power performance," tech. rep., National Renewable Energy Lab., Golden, CO (United States); Lynette (R.) and Associates, Seattle, WA (United States), 1996.

[29] J. Carlier and M. Stanislas, "Experimental study of eddy structures in a turbulent boundary layer using particle image velocimetry," *Journal of Fluid Mechanics*, vol. 535, pp. 143–188, 2005.

[30] C. M. Velte, M. O. Hansen, and V. L. Okulov, "Helical structure of longitudinal vortices embedded in turbulent wall-bounded flow," *Journal of Fluid Mechanics*, vol. 619, pp. 167–177, 2009.

[31] C. M. Velte, "Vortex generator flow model based on self-similarity," *AIAA journal*, vol. 51, no. 2, pp. 526–529, 2012.

[32] S. Alekseenko, P. Kuibin, V. Okulov, and S. Shtork, "Helical vortices in swirl flow," *Journal of Fluid Mechanics*, vol. 382, pp. 195–243, 1999.

[33] S. Martemianov and V. L. Okulov, "On heat transfer enhancement in swirl pipe flows," *International Journal of Heat and Mass Transfer*, vol. 47, no. 10, pp. 2379–2393, 2004.

[34] J. Jeong and F. Hussain, "On the identification of a vortex," *Journal of fluid mechanics*, vol. 285, pp. 69–94, 1995.

[35] P. G. Saffman, *Vortex dynamics*. Cambridge university press, 1992.

[36] C.-S. Yao, J. C. Lin, and B. G. Allan, "Flow-field measurement of device-induced embedded streamwise vortex on a flat plate," *NASA STI/Recon Technical Report N*, vol. 3, p. 12931, 2002.

[37] A. D. Cutler and P. Bradshaw, "Strong vortex/boundary layer interactions," *Experiments in fluids*, vol. 14, no. 5, pp. 321–332, 1993.

[38] A. D. Cutler and P. Bradshaw, "Strong vortex/boundary layer interactions," *Experiments in fluids*, vol. 14, no. 5, pp. 393–401, 1993.

[39] H. Görtler, "On the three-dimensional instability of laminar boundary layers on concave walls," 1954.

[40] J. Floryan, "On the görtler instability of boundary layers," *Progress in Aerospace Sciences*, vol. 28, no. 3, pp. 235–271, 1991.

[41] C. M. Velte, V. Okulov, and I. Naumov, "Regimes of flow past a vortex generator," *Technical Physics Letters*, vol. 38, no. 4, pp. 379–382, 2012.

[42] C. M. Velte, M. O. Hansen, and V. L. Okulov, "Multiple vortex structures in the wake of a rectangular winglet in ground effect," *Experimental Thermal and Fluid Science*, vol. 72, pp. 31–39, 2016.

[43] O. Lögdberg, K. Angele, and P. H. Alfredsson, "On the robustness of separation control by streamwise vortices," *European Journal of Mechanics-B/Fluids*, vol. 29, no. 1, pp. 9–17, 2010.

[44] H. Schlichting and K. Gersten, *Boundary-layer theory.* Spring Science & Business Media, 2003.

[45] P. Dengel and H. Fernholz, "An experimental investigation of an incompressible turbulent boundary layer in the vicinity of separation," *Journal of Fluid Mechanics*, vol. 212, pp. 615–636, 1990.

[46] G. Godard and M. Stanislas, "Control of a decelerating boundary layer. part 1: Optimization of passive vortex generators," *Aerospace Science and Technology*, vol. 10, no. 3, pp. 181–191, 2006.

[47] J. C. Lin, "Review of research on low-profile vortex generators to control boundary-layer separation," *Progress in Aerospace Sciences*, vol. 38, no. 4, pp. 389–420, 2002.

[48] F. Florin, D. Alexandru, D. Horia, and P. Octavian, "Active control of separating boundary layer," *PAMM*, vol. 10, pp. 465–466, 2010.

[49] H. F. Müller-Vahl, C. Strangfeld, C. N. Nayeri, C. O. Paschereit, and D. Greenblatt, "Control of thick airfoil, deep dynamic stall using steady blowing," *AIAA Journal*, vol. 53, no. 2, pp. 277–295, 2014.

[50] M. L. Post and T. C. Corke, "Separation control using plasma actuators: dynamic stall vortex control on oscillating airfoil," *AIAA journal*, vol. 44, no. 12, pp. 3125–3135, 2006.

[51] C. M. Velte, M. O. L. Hansen, K. E. Meyer, and P. Fuglsang, "Evaluation of the performance of vortex generators on the du 91-w2-250 profile using stereoscopic piv," in *International Symposium on Energy, Informatics and Cybernetics: Focus Symposium in the 12th World Multiconference on Systemics, Cybernetics and Informatics (WMSCI 2008)*, pp. 263–267, 2008.

[52] M. Manolesos, G. Papadakis, and S. G. Voutsinas, "Assessment of the cfd capabilities to predict aerodynamic flows in presence of vg arrays," in *Journal of Physics: Conference Series*, vol. 524, p. 012029, IOP Publishing, 2014.

[53] J. C. Dudek, "Empirical model for vane-type vortex generators in a navier-stokes code," *AIAA Journal*, vol. 44, pp. 1779–1789, 2015/09/02 2006.

[54] U. Fernández-Gámiz, C. Marika Velte, P.-E. Réthoré, N. N. Sørensen, and E. Egusquiza, "Testing of self-similarity and helical symmetry in vortex generator flow simulations," *Wind Energy*, 2015.

[55] M. O. Hansen and C. Westergaard, "Phenomenological model of vortex generators," in *IEA, Aerodynamics of Wind Turbines, 9th Symposium, Stockholm*, 1995.

[56] V. Brunet, C. Francois, E. Garnier, and M. Pruvost, "Experimental and numerical investigations of vortex generators effects," *AIAA Paper*, vol. 3027, p. 2006, 2006.

[57] L. Florentie, A. Van Zuijlen, and H. Bijl, "Towards a multi-fidelity approach for cfd simulations of vortex generator arrays," in *Proceedings-WCCM XI: 11th World Congress on Computational Mechanics; ECCM V: 5th European Conference on Computational Mechanics; ECFD VI: 6th European Conference on Computational Fluid Dynamics, Barcelona, Spain, 20-25 July 2014*, 2014.

[58] M. Gaunaa, C. Bak, *et al.*, "The effect of mounting vortex generators on the dtu 10mw reference wind turbine blade," in *Journal of Physics: Conference Series*, vol. 524, p. 012034, IOP Publishing, 2014.

[59] N. Troldborg, F. Zahle, and N. N. Sørensen, "Simulation of a mw rotor equipped with vortex generators using cfd and an actuator shape model," in *33rd ASME Wind Energy Symposium*, American Institute of Aeronatuics & Astronautics, 2015.

[60] F. Menter, "Best practice: Scale-resolving simulations in ansys cfd," *ANSYS Germany GmbH*, pp. 1–70, 2012.

[61] J. Johansen, N. Sorensen, J. Michelsen, and S. Schreck, "Detached-eddy simulation of flow around the nrel phase-vi blade," in *ASME 2002 Wind Energy Symposium*, pp. 106–114, American Society of Mechanical Engineers, 2002.

[62] C. ANSYS, "Release 15.0-user manual," *Canonsburg, PA, USA*, 2013.

[63] D. C. Wilcox *et al.*, *Turbulence modeling for CFD.* DCW industries La Canada, CA, 2006.

[64] "Two equation turbulence models – cfd-wiki, the free cfd reference." `http://www.cfd-online.com/Wiki/Two_equation_turbulence_models`. (Accessed on 03/06/2016).

[65] F. G. Schmitt, “About boussinesq’s turbulent viscosity hypothesis: historical remarks and a direct evaluation of its validity,” *Comptes Rendus Mécanique*, vol. 335, no. 9, pp. 617–627, 2007.

[66] F. R. Menter, “Review of the shear-stress transport turbulence model experience from an industrial perspective,” *International Journal of Computational Fluid Dynamics*, vol. 23, no. 4, pp. 305–316, 2009.

[67] F. R. Menter, “Zonal two equation k-turbulence models for aerodynamic flows,” *AIAA paper*, vol. 2906, p. 1993, 1993.

[68] N. N. Sørensen, “Cfd modelling of laminar-turbulent transition for airfoils and rotors using the γ- model,” *Wind Energy*, vol. 12, no. 8, pp. 715–733, 2009.

[69] P. E. Smirnov and F. R. Menter, “Sensitization of the sst turbulence model to rotation and curvature by applying the spalart–shur correction term,” *Journal of Turbomachinery*, vol. 131, no. 4, p. 041010, 2009.

[70] B. Launder and M. Kato, “Modelling flow-induced oscillations in turbulent flow around a square cylinder,” *American Society of Mechanical Engineers, Fluids Engineering Division (Publication) FED*, vol. 157, pp. 189–199, 1993.

[71] F. Menter, A. Garbaruk, and Y. Egorov, “Explicit algebraic reynolds stress models for anisotropic wall-bounded flows,” in *Progress in Flight Physics*, vol. 3, pp. 89–104, EDP Sciences, 2012.

[72] S. Gamard and W. K. George, “Reynolds number dependence of energy spectra in the overlap region of isotropic turbulence,” *Flow, turbulence and combustion*, vol. 63, no. 1-4, pp. 443–477, 2000.

[73] W. K. George and M. Tutkun, “Mind the gap: a guideline for large eddy simulation,” *Philosophical Transactions of the Royal Society of London A: Mathematical, Physical and Engineering Sciences*, vol. 367, no. 1899, pp. 2839–2847, 2009.

[74] P. Catalano and M. Amato, “An evaluation of rans turbulence modelling for aerodynamic applications,” *Aerospace science and Technology*, vol. 7, no. 7, pp. 493–509, 2003.

[75] G. Kalitzin, G. Medic, G. Iaccarino, and P. Durbin, “Near-wall behavior of rans turbulence models and implications for wall functions,” *Journal of Computational Physics*, vol. 204, no. 1, pp. 265–291, 2005.

[76] C. Rhie and W. Chow, “Numerical study of the turbulent flow past an airfoil with trailing edge separation,” *AIAA journal*, vol. 21, no. 11, pp. 1525–1532, 1983.

[77] P.-E. Réthoré, P. Laan, N. Troldborg, F. Zahle, and N. N. Sørensen, “Verification and validation of an actuator disc model,” *Wind Energy*, vol. 17, no. 6, pp. 919–937, 2014.

[78] P.-E. M. Rethore and N. N. Sørensen, “Actuator disc model using a modified rhie-chow/simple pressure correction algorithm. comparison with analytical solutions,” in *2008 European Wind Energy Conference and Exhibition*, 2008.

[79] N. Niels, F. Zahle, C. Bak, T. Vronsky, *et al.*, “Prediction of the effect of vortex generators on airfoil performance,” in *Journal of Physics: Conference Series*, vol. 524, p. 012019, IOP Publishing, 2014.

[80] Y. Perivolaris and S. Voutsinas, “A cfd performance analysis of vortex generators used for boundary layer control on wind turbine blades,” in *Proceedings of the European Wind Energy Conference, Copenhagen, Denmark*, 2001.

[81] J. Schepers, O. Ceyhan, F. Savenije, M. Stettner, H. Kooijman, P. Chaviarapoulos, G. Sieros, C. S. Ferreira, N. Sørensen, M. Wächter10, *et al.*, “Avatar: Advanced aerodynamic tools for large rotors,” in *Proceedings of 33rd ASME Wind Energy Symposium*, 2015.

[82] W. L. Oberkampf, T. G. Trucano, and C. Hirsch, “Verification, validation, and predictive capability in computational engineering and physics,” *Applied Mechanics Reviews*, vol. 57, no. 5, pp. 345–384, 2004.

[83] C. M. Velte, C. Braud, S. Coudert, and J. Foucaut, “Vortex generator induced flow in a high re boundary layer,” in *Journal of Physics: Conference Series*, vol. 555, p. 012102, IOP Publishing, 2014.

[84] A. Bernard, J.-M. Foucaut, P. Dupont, and M. Stanislas, “Decelerating boundary layer: a new scaling and mixing length model,” *AIAA journal*, vol. 41, no. 2, pp. 248–255, 2003.

[85] C. Cuvier, J.-M. Foucaut, C. Braud, and M. Stanislas, “Characterisation of a high reynolds number boundary layer subject to pressure gradient and separation,” *Journal of Turbulence*, vol. 15, no. 8, pp. 473–515, 2014.

[86] C. J. Roy, "Grid convergence error analysis for mixed-order numerical schemes," *AIAA journal*, vol. 41, no. 4, pp. 595–604, 2003.

[87] C. J. Roy, "Review of discretization error estimators in scientific computing," *AIAA Paper*, vol. 126, p. 2010, 2010.

[88] P. J. Roache, "Quantification of uncertainty in computational fluid dynamics," *Annual Review of Fluid Mechanics*, vol. 29, no. 1, pp. 123–160, 1997.

[89] B. G. Allan, C.-S. Yao, and J. C. Lin, "Numerical simulations of vortex generator vanes and jets on a flat plate," *AIAA paper*, vol. 3160, p. 2002, 2002.

[90] M. Marquillie, J.-P. Laval, and R. Dolganov, "Direct numerical simulation of a separated channel flow with a smooth profile," *Journal of Turbulence*, no. 9, p. N1, 2008.

[91] A. G. Gungor and S. Menon, "Multi-scale simulation of near-wall turbulent flows," in *Direct and Large-Eddy Simulation VII*, pp. 157–162, Springer, 2010.

[92] F. Menter, M. Kuntz, and R. Langtry, "Ten years of industrial experience with teh sst turbulence model," *Turbulence, heat and mass transfer*, vol. 4, no. 1, 2003.

[93] T. J. Craft, H. Iacovides, and B. E. Launder, "Rans modelling of some strongly swirling aerospace flows," *Mécanique & Industries*, vol. 10, no. 3-4, pp. 171–174, 2009.

[94] M. Marquillie, U. Ehrenstein, J.-P. Laval, *et al.*, "Instability of streaks in wall turbulence with adverse pressure gradient," *Journal of Fluid Mechanics*, vol. 681, no. 205-240, p. 30, 2011.

[95] W. Timmer and R. Van Rooij, "Summary of the delft university wind turbine dedicated airfoils," *Journal of Solar Energy Engineering*, vol. 125, no. 4, pp. 488–496, 2003.

[96] F. Bertagnolio, N. Sørensen, and J. Johansen, *Profile catalogue for airfoil sections based on 3D computations.* Risø National Laboratory, 2006.